SISSA

Scuola
Internazionale
Superiore di
Studi Avanzati

Physics Area - PhD course in
Theory and Numerical Simulation of the Condensed Matter

Many-body systems
in and out of equilibrium

Candidate:
Mikheil Tsitsishvili

Advisors:
Dr. Marcello Dalmonte
Prof. Michele Fabrizio

Academic Year 2023-24

SCUOLA INTERNAZIONALE SUPERIORE DI STUDI AVANZATI
SISSA

DOCTORAL THESIS

Many-body systems in and out of equilibrium

Author:
Mikheil TSITSISHVILI

Supervisors:
Dr. Marcello DALMONTE,
Prof. Michele FABRIZIO

A thesis submitted in fulfillment of the requirements
for the degree of Doctor of Philosophy

in the

Condensed Matter Theory Group

2024

Abstract

In this thesis, we study many–body systems both in and out of equilibrium. Though these two setups are fundamentally different from each other, the phenomena that emerge due to interactions in the former and the effects of non–reversible dynamics in the latter share many similarities. Together with highly controllable synthetic quantum system experiments, these many–body setups are a relevant topic of research in condensed matter physics, statistical physics, and quantum information theory.

The first part of the thesis is dedicated to the many–body systems in equilibrium. Motivated by the recent experimental advances in synthetic quantum systems, we investigate the behaviour of interacting particles on ladder geometries. Specifically, the so–called Rydberg–dressing of atoms allows one to experimentally realize Hubbard–like models with highly tunable long–range interaction. The competition between these interactions and geometrical effect of the lattice (e.g. geometric frustration) can lead to interesting equilibrium phases of the system. Moreover, one might encounter scenarios where the system at the critical point has enlarged symmetry relative to its microscopic Hamiltonian – a manifestation of an emerging phenomena. Using various analytical and numerical tools, we study the phase diagram of interacting Rydberg–dressed atoms on square and triangular ladder geometries. We demonstrate that the interaction gives rise to a rich phase diagram, accommodating conventional Luttinger liquids and the so–called cluster–Luttinger liquid phases. Moreover, apart from usual Berezinskii–Kosterlitz–Thouless and Gaussian critical lines, the system hosts a supersymmetric quantum critical point with an emerging Majorana degree of freedom. These results can be relevant for experimentally studying the coupling of supersymmetric critical points on lattice geometries.

In the second part, we explore many–body systems out of equilibrium. Namely, we study the competition between the unitary evolution and dissipative effects upon the entanglement content of the many–body system. By using the so–called quantum trajectory approach to unravel the Markovian (i.e., memoryless) dynamics of the system, it has been demonstrated that depending on the dissipation strength, the scaling of entanglement undergoes a phase transition – a phenomenon known as measurement induced phase transition. Moreover, at the critical point the scaling of entanglement hosts features characteristic of conformal field theories. We generalize these considerations to memoryful dissipative setups by introducing a diagrammatic method to unravel the dynamics of non–Markovian many–body systems. Using the proposed analytical technique, corroborated by direct simulations of the quantum trajectories, we demonstrate the stability of the measurement induced phase transitions against the memory effects of the dynamics. The experimental setups that study quantum systems are inevitably affected by a memoryful environment and thus the results represent a step forward in the field of transitions induced by external baths.

Part I is based on

1. **Mikheil Tsitsishvili**, Titas Chanda, Matteo Votto, Pierre Fromholz, Marcello Dalmonte and Alexander Nersesyan
   Phase diagram of Rydberg-dressed atoms on two-leg square ladders: Coupling supersymmetric conformal field theories on the lattice
   Phys. Rev. B 105, 155159 (2022)

2. Pierre Fromholz, **Mikheil Tsitsishvili**, Matteo Votto, Marcello Dalmonte, Alexander Nersesyan and Titas Chanda
   Phase diagram of Rydberg-dressed atoms on two-leg triangular ladders
   Phys. Rev. B 106, 155411 (2022)

Part II is based on

3. Giuliano Chiriacò, **Mikheil Tsitsishvili**, Dario Poletti, Rosario Fazio and Marcello Dalmonte
   Diagrammatic method for many-body non-Markovian dynamics: memory effects and entanglement transitions
   Phys. Rev. B 108, 075151 (2023)

4. **Mikheil Tsitsishvili**, Dario Poletti, Marcello Dalmonte and Giuliano Chiriacò
   Measurement induced transitions in non-Markovian free fermion ladders
   SciPost Phys. Core 7, 011 (2024)

Not included in the thesis

5. Bachana Beradze, **Mikheil Tsitsishvili**, Emanuele Tirrito, Marcello Dalmonte, Titas Chanda and Alexander Nersesyan
   Emergence of non-Abelian SU(2) invariance in Abelian frustrated fermionic ladders
   Phys. Rev. B 108, 075146 (2023)

Contents

Part I

Rydberg atom arrays in ladder geometries: a kaleidoscope of phases

Introduction

Over the last ten years, ensembles of ground state atoms laser-coupled to Rydberg states and trapped by means of optical potentials have demonstrated impressive capabilities of realizing strongly interacting quantum dynamics under controlled and tunable experimental conditions [1, 2, 3, 4, 5, 6]. From the many-body perspectives, the opportunities offered by these settings profit from the combination of very rich interactions properties between Rydberg states, including long-range characters and spatial anisotropy, with a high degree of local control and manipulation [7]. Within such settings, inter-particle interactions are indeed sizeable even at distances of a few microns – so that, for instance, lattice potentials can be probed at the single site level with minimal experimental effort when compared to conventional cold atoms in optical lattices operating in Hubbard-like regimes.

The dynamics of Rydberg atom arrays in the case of large lattice spacing between sites is often described in terms of Ising or XY spin-1/2 models [8, 9, 10]. Starting from the observation of dynamical crystallization reported in [1, 11], a plethora of phenomena has been observed, including magnetic phases of one-dimensional (1D) systems [12], the first example of a topological phase in a cold atom experiment [13], and ordered phased of two-dimensional (2D) arrays [14, 15]. One key leitmotif of these experiments is that they are carried out in such a way that Rydberg states are populated, making the dynamics so fast that atomic motion can most often be neglected as it is slower than typical decoherence mechanism such as spontaneous decay of the Rydberg states.

An alternative, relatively unexplored setting is ground state atoms that are only weakly coupled to Rydberg states [16, 17, 18, 19]: in this regime, up to timescales that are long compared to typical sources of dissipation, the Rydberg state is only virtually populated – yet, it does have drastic effects in determining the system's coherent dynamics. In particular, it allows to engineer dynamics that is somehow intermediate between conventional Hubbard models, and frozen Rydberg gases: this results into generalized Hubbard models, where interactions combine a long-range, power-law tail (van der Waals), with a short-range plateau, that is of widespread use in classical statistical mechanics, and is often referred to as the soft-shoulder potential [9]. Even in their simplest instance of a single scalar bosonic field in 1D, these types of interactions lead to exotic critical behavior, including phases where the Luttinger theorem is inapplicable [20] and supersymmetric quantum critical points [21]. The phenomenology is equally rich in 2D systems, where soft-shoulder potentials have been linked to anomalous dynamics and glassy behavior [22, 23].

Opposite to the aforementioned cases, the transition regime between 1D and 2D systems is poorly understood. The goal of this part of the thesis is to shed light on the latter, by investigating the ground state phase diagram of soft-shoulder Hubbard models in square and triangular ladder geometries. In addition to this theoretical motivation, a recent experiment [24] has realized many-body dynamics of single-species Hubbard models with clustering interactions. In two-leg square and triangular ladders, our findings below are [25, 26], in large part, motivated by such experimental capabilities, and offer a clear theoretical pathway to investigate the effects of frustration within that platform.

Apart from aforementioned experimental setups and various advanced tools of numerical simulations, such low-dimensional many-body problems on a lattice can be amenable to continuous quantum field theoretical descriptions. For example, the so-called continuous phase transitions are extremely interesting from the theoretical point of view. In the vicinity of the critical point, the macroscopically large number of strongly correlated degrees of freedom limits the applicability

of perturbation theory. Diverging correlation length renders the microscopic details (such as lattice constant, individual interaction between the degrees of freedom) to be irrelevant and only the global properties, such as symmetries of the Hamiltonian and dimensionality of the space, dictates the properties of the system close to the criticality. This means that two different systems can exhibit both qualitatively and quantitatively similar features at the critical point, if they share symmetries and dimensionality. This phenomenon is known as the universality and the number of different universality classes for continuous critical points is much less than the number of different physical systems that can undergo continuous phase transitions. Apart from the so-called Gaussian criticality, in the following chapters we will review two additional universality classes: 1D Ising and Berezinskii-Kosterlitz-Thouless (BKT) universality classes. By implementing conformal field theoretical tools [27], Abelian bosonization and renormalization group approach [28], we will demonstrate how the universal properties emerge when the system is close to criticality. Being equipped with the understanding of these theoretical methods, we will apply the knowledge to more complex many-body setups.

Chapter 1

Quantum Ising model

In this chapter we will study the so called 1-dimensional quantum Ising model (QIM), a toy model of interacting SU(2) invariant bosonic degrees of freedom on a lattice [29]. Apart from various interesting features hosted by the model, our main goal will be to extract the underlying field theory that governs the properties of QIM in the vicinity of the critical point. To achieve this, we will map QIM onto the so-called Kitaev chain and demonstrate how quantum field theory (QFT) of massive Majorana fermions emerge as one approaches the critical point [30]. We will show that at criticality, the theory becomes scale invariant and one can implement conformal field theoretical (CFT) [27, 28] description to unravel the so-called Ising universality class. On the way to understanding the Ising universality class, we will encounter the so-called Jordan-Wigner transformation (JW), when mapping hard-core bosonic degrees of freedom on to fermionic. Another approach that demonstrates "fermion–boson equivalence" will be discussed in the next chapter, in the context of the Heisenberg XXZ model and Abelian bosonization [28].

The quantum Ising model is a paradigmatic toy model of a 1-dimensional magnetic system, where nearest-neighbouring spin-$\frac{1}{2}$ degrees of freedom interact with each other. Apart from a classical part of nearest neighbor interaction between x-projections of spin, QIM also includes a transverse magnetic field that couples linearly to a transverse component of the spin. Since these two components of spin operators do not commute with each other, the transverse magnetic field turns the model fully quantum.

Being an exactly solvable quantum model, it has been extensively studied from many different point of views and has been proven that QIM can accommodate conformal field theoretical description, topological states and etc.

The Hamiltonian of a 1D Quantum Ising model is

$$\hat{H}_{\text{QIM}} = -J\left(\sum_{n=1}^{N-1} \hat{\sigma}_n^x \hat{\sigma}_{n+1}^x + \lambda \sum_{n=1}^{N} \hat{\sigma}_n^z\right), \tag{1.1}$$

$\hat{\sigma}^x$ and $\hat{\sigma}^z$ are the Pauli matrices

$$\hat{\sigma}^x = \begin{pmatrix} 0 & 1 \\ 1 & 0 \end{pmatrix}, \quad \hat{\sigma}^y = \begin{pmatrix} 0 & -i \\ i & 0 \end{pmatrix}, \quad \hat{\sigma}^z = \begin{pmatrix} 1 & 0 \\ 0 & 1 \end{pmatrix}. \tag{1.2}$$

These matrices commute with each other if their site indices are different, however they obey standard SU(2) algebra if their spatial indices coinside

$$[\sigma_n^\alpha, \sigma_n^\beta] = 2i\epsilon_{\alpha\beta\gamma}\sigma^\gamma, \quad \{\sigma_n^\alpha, \sigma_n^\beta\} = 2\delta_{\alpha\beta}. \tag{1.3}$$

The quantum Ising hamiltonian consists of two terms - the first one favours ferromagnetically ordered configurations of spins along x direction, while the second prefers paramagnetism. The hamiltonian Eq.(1.1) possesses $\hat{\sigma}_n^x \to -\hat{\sigma}_n^x$ global $\mathbb{Z}_2$ symmetry. This transformation is generated

by the so-called spin-flip operator

$$(-1)^F = \prod_{i=1}^{N} \hat{\sigma}_i^z, \quad \left[\hat{H}_{QIM}, (-1)^F\right] = 0. \tag{1.4}$$

The hamiltonian changes the sign under $\sigma_j^z \to -\sigma_j^z$, $\sigma_{2j}^x \to -\sigma_{2j}^x$ transformation. This way, the spectrum of the system is invariant under $\hat{H}_{QIM} \to -\hat{H}_{QIM}$. This symmetry will later be identified as a particle-hole symmetry of the model. Eq.(1.1) is time-reversal symmetric, since the time-reversal operator is a complex conjugation operation $\hat{K}$ and the hamiltonian is real.

For $\lambda = 0$ we have

$$\hat{H}_{QIM} = -J \sum_{n=1}^{N-1} \hat{\sigma}_n^x \hat{\sigma}_{n+1}^x, \tag{1.5}$$

thus the global $\mathbb{Z}_2$ symmetry is spontaneously broken down and the model exhibits long-range order:

$$\lim_{|n-m|\to\infty} \langle \hat{\sigma}_n^x \hat{\sigma}_m^x \rangle = Q^2 = 1 \quad \Rightarrow \quad \langle \hat{\sigma}_n^x \rangle = \pm 1 \tag{1.6}$$

For $\lambda \ll 1$ phase of the system remains qualitatively similar. In the opposite limit of $\lambda \to \infty$, infinitely strong magnetic field polarizes the spins along z direction and hence

$$\langle \hat{\sigma}_n^x \hat{\sigma}_m^x \rangle = 0. \tag{1.7}$$

For $1 \ll \lambda < \infty$ we have

$$\lim_{|n-m|\to\infty} \langle \hat{\sigma}_n^x \hat{\sigma}_m^x \rangle \sim e^{-|n-m|/\xi}. \tag{1.8}$$

This way, since by from $\lambda \ll 1$ to $\lambda \gg 1$ regime is accompanied by a spontaneous breakdown of a global $\mathbb{Z}_2$ symmetry, one can expect a quantum phase transition for some critical point $\lambda = \lambda_c$.

1.1   The Duality Transformation and Self-Duality for QIM

We pinpoint the exact value of λ_c by implementing the concept of self-duality [28]. We introduce a duality transformation by defining $\hat{\mu}_{n+1/2}^x$ and $\hat{\mu}_{n+1/2}^z$ operators

$$\hat{\mu}_{n+1/2}^x = \prod_{j=1}^{n} \hat{\sigma}_j^z, \quad \hat{\mu}_{n+1/2}^z = \sigma_n^x \hat{\sigma}_{n+1}^x, \tag{1.9}$$

where $\hat{\mu}_{n+1/2}^{x,z}$ squares to one and satisfy Eq.(1.3) algebra. Being a highly non-local operator in original spin variables, the action of $\hat{\mu}_{n+1/2}^x$ on spin configuration is non-trivial:

$$\hat{\mu}_{n+1/2}^x | \uparrow_1; \uparrow_2; \uparrow_3; \dots \uparrow_{n-1}; \uparrow_n; \uparrow_{n+1}; \dots \uparrow_N \rangle_x = | \downarrow_1; \downarrow_2; \downarrow_3; \dots \downarrow_{n-1}; \downarrow_n; \uparrow_{n+1}; \dots \uparrow_N \rangle_x \tag{1.10}$$

where $\hat{\mu}_{n+1/2}^x$ operator is known as the disorder operator, since it creates a domain wall and thus disorders the spin configuration. Here the subscript $|\bullet\rangle_x$ denotes that we work in the basis states of $\hat{\sigma}^x$ operator. By expressing $\hat{H}_{QIM}$ in terms of the disorder operators, we get

$$\hat{H}_{QIM}[\sigma] \to \hat{H}_{QIM}[\mu] = J \left(-\lambda \sum_n \hat{\mu}_{n-1/2}^x \hat{\mu}_{n+1/2}^x - \sum_n \mu_{n+1/2}^z \right) \tag{1.11}$$

Under the duality transformation the model is mapped onto itself and one can see that

$$\hat{H}_{\text{QIM}}[\{\sigma\}; \lambda] = \lambda \hat{H}_{\text{QIM}}[\{\mu\}; 1/\lambda] \tag{1.12}$$

In the spirit of Kramers-Wannier duality, the model is self-dual and thus critical at $\lambda = \lambda_c = 1$. Thus, we conclude that

$$\begin{aligned}
\langle \sigma^x \rangle \neq 0, \quad \langle \mu^x \rangle = 0 \quad &\text{if} \quad \lambda < 1, \\
\langle \sigma^x \rangle = 0, \quad \langle \mu^x \rangle \neq 0 \quad &\text{if} \quad \lambda > 1.
\end{aligned} \tag{1.13}$$

1.2 The Jordan-Wigner Transformation

The Jordan-Wigner transformation is applicable to various one-dimensional spin problems. This transformation maps the spin-$\frac{1}{2}$ operators onto creation and annihilation operators of spinless fermions. Though the mapping is non-local, it allows one to extract the exact solution of various spin-$\frac{1}{2}$ models, including QIM [31].

Consider the Pauli matrices Eq.(1.2). The eigenstates of $\hat{\sigma}^z$ diagonal matrix are $|\uparrow\rangle$ and $|\downarrow\rangle$. The corresponding raising and lowering operators $\hat{\sigma}^\pm = \frac{\hat{\sigma}^x \pm i\hat{\sigma}^y}{2}$ act in this 2-dimensional space as

$$\begin{aligned}
\hat{\sigma}^+|\uparrow\rangle = 0, \quad \hat{\sigma}^-|\uparrow\rangle = |\downarrow\rangle, \\
\hat{\sigma}^-|\downarrow\rangle = 0, \quad \hat{\sigma}^+|\downarrow\rangle = |\uparrow\rangle.
\end{aligned} \tag{1.14}$$

Now we introduce a spinless fermion, with the creation $\hat{a}^\dagger$ and annihilation $\hat{a}$ operators that obeying the standard algebra

$$\{\hat{a}, \hat{a}^\dagger\} = 1, \quad \{\hat{a}, \hat{a}\} = \{\hat{a}^\dagger, \hat{a}^\dagger\} = 0, \tag{1.15}$$

The vacuum state $|0\rangle$ is defined as $a|0\rangle = 0$ and by acting with $\hat{a}^\dagger$ on it we get $\hat{a}^\dagger|0\rangle = |1\rangle$. This way, $|0\rangle$ and $|1\rangle$ form a basis for 2-dimensional fermionic space. $|0\rangle$ and $|1\rangle$ are eigenfunctions of the particle number operator $\hat{n} = \hat{a}^\dagger\hat{a}$: $\hat{n}|0\rangle = 0 \times |0\rangle$ and $\hat{n}|1\rangle = 1 \times |1\rangle$. As a summary, we have

$$\begin{aligned}
\hat{a}^\dagger|1\rangle = 0, \quad \hat{a}|1\rangle = |0\rangle \\
\hat{a}|0\rangle = 0, \quad \hat{a}^\dagger|0\rangle = |1\rangle.
\end{aligned} \tag{1.16}$$

The spin and fermionic cases show some similarity under the following identification

$$|\uparrow\rangle \rightleftarrows |1\rangle, \quad |\downarrow\rangle \rightleftarrows |0\rangle \quad \text{and} \quad \hat{\sigma}^+ \rightleftarrows \hat{a}^\dagger, \quad \hat{\sigma}^- \rightleftarrows \hat{a}, \quad \hat{\sigma}^z \rightleftarrows 2\hat{n} - 1. \tag{1.17}$$

This correspondence is wrong for many body-systems, since the spin operators on different lattice sites commute while the fermionic operators anti-commute. We can fix this issue by we attaching non-local pre-factors

$$\hat{\sigma}_j^+ = e^{-i\pi \sum_{k=1}^{j-1} \hat{a}_k^\dagger \hat{a}_k} \hat{a}_j^\dagger, \quad \hat{\sigma}_j^- = e^{+i\pi \sum_{k=1}^{j-1} \hat{a}_k^\dagger \hat{a}_k} \hat{a}_j, \quad \hat{\sigma}_j^z = 2\hat{a}_j^\dagger \hat{a}_j - 1. \tag{1.18}$$

The so-called "tail factor" $\hat{\mathcal{N}}_j = e^{-i\pi \sum_{k=1}^{j-1} \hat{a}_k^\dagger \hat{a}_k}$ counts the parity of fermions between sites 1 and $j-1$. Eq.(1.18) is known as the Jordan-Wigner transformation.

By employing the Jordan-Wigner transformation, we can reframe any spin-$\frac{1}{2}$ model as an equivalent model of spinless fermions. Frequently, this can significantly simplify the process of solving the model, while studying the properties of the fermionic model is equivalent to analyzing the spin model and vice versa.

1.3   Kitaev chain

In this subsection we apply Eq.(1.18) to the Quantum Ising model hamiltonian and map it onto the so-called Kitaev chain [30, 32, 33]. Since the Kitaev chain is quadratic in fermionic fields, one can diagonalize it exactly. This way, by studying the properties of the Kitaev chain, we automatically extract information about QIM.

By transforming the QIM hamiltonian according to Eq.(1.18), we get:

$$\hat{H}_{QIM} \to \hat{H}_{KC} = -\lambda J \sum_{n=1}^{N} \left(2\hat{a}_n^\dagger \hat{a}_n - 1 \right) - J \sum_{n=1}^{N-1} \left(\hat{a}_n^\dagger \hat{a}_{n+1} + \hat{a}_n^\dagger \hat{a}_{n+1}^\dagger + h.c. \right) \tag{1.19}$$

Eq.(1.19) is describing a 1D p-wave superconductor, known in the literature as Kitaev chain. The total number of particles is not conserved in Eq.(1.19), but the parity $(-1)^P = e^{-i\pi \sum_{n=1}^{N} \hat{a}_n^\dagger \hat{a}_n}$ is.

Since we are interested in bulk properties, we put periodic boundary conditions. In general, for the purpose of minimizing of the ground state energy, one imposes $\hat{a}_{N+1} = -(-1)^N \hat{a}_1$. Since we are interested in the thermodynamic limit, we can fix N to be even and work with $\hat{a}_{N+1} = -\hat{a}_1$. In momentum space, Eq.(1.19) is written in the Bogoliubov–de Gennes form

$$\hat{H}_{KC} = \sum_{k \in BZ} \hat{\Psi}_k^\dagger \hat{\mathcal{H}}_k \hat{\Psi}_k, \quad \Psi_k = \begin{pmatrix} \hat{a}_k \\ \hat{a}_{-k}^\dagger \end{pmatrix} \tag{1.20}$$

$$\hat{\mathcal{H}}_k = \mathbf{h}(k) \cdot \hat{\boldsymbol{\tau}}, \quad \mathbf{h}(k) = \begin{cases} h_x(k) = 0 \\ h_y(k) = J\sin(k\alpha_0) \\ h_z(k) = -J(\cos(k\alpha_0) + \lambda) \end{cases} \tag{1.21}$$

with $\{\hat{\tau}^\alpha\}$ being the Pauli matrices.

Since the parity operator and the Hamiltonian commute with eachother, both operators can be diagonalized simultaneously. Due to this, the state of the system falls either into odd or even sectors of the $\mathbb{Z}_2$ group. The particle-hole symmetry, generated by a charge-conjugation operator $\hat{C}$, would imply that there should exist a pair of states $\{|\Psi\rangle; \hat{C}|\Psi\rangle\}$ with energies $\{E; -E\}$. Therefore, if $\{C, \hat{H}_{KC}\} = 0$, then the system has the particle-hole symmetry. In our case

$$\hat{C} = \hat{\tau}^x \hat{K}, \tag{1.22}$$

with $\hat{K}$ being the complex-conjugation operator.

If the system has time-reversal symmetry, generated by a time-reversal operator $\hat{T}$, then there exists a pari of state $\{|\Psi\rangle; \hat{T}|\Psi\rangle\}$ with same energy E. If such symmetry exists in the model, then $[\hat{T}, \hat{H}_{KC}] = 0$ and $E(k) = E(-k)$, for all momenta k. For the case of spinless fermions, we have $\hat{T} = \hat{K}$ complex conjugation. This way, since $(\mathcal{H}_k)^* = \mathcal{H}_{-k}$, the system is time-reversal symmetric.

Since the model has both time-reversal and the particle-hole symmetry, the system is also chiral symmetric. All of these symmetries are present in the bulk spectrum, extracted from Eq.(1.20,1.21) :

$$E^{(\pm)}(k) = \pm E(k) = \pm\sqrt{h_z^2(k) + h_y^2(k)} = \pm J\sqrt{1 + \lambda^2 + 2\lambda\cos(k\alpha_0)}. \tag{1.23}$$

Due to particle-hole symmetry we have $E^+(k)$ and $E^-(k) = -E^+(k)$ branches of spectrum, while the time-reversal symmetry demands $E(k) = E(-k)$ to hold.

The phases appearing for different signs of λ are related by a particle-hole transformation $\hat{a}_n \to (-1)^n \hat{a}_n^\dagger$, resulting in $\lambda \to -\lambda$.
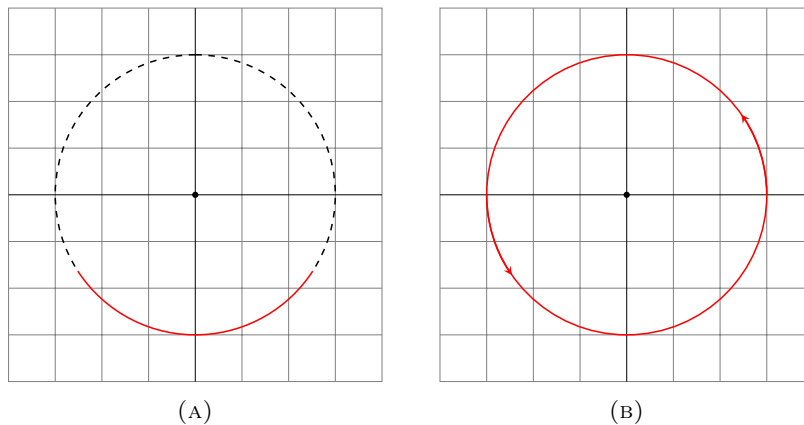
FIGURE 1.1: (A) The trajectory (red line) of the vector $\hat{\mathbf{h}}(k)$ for $|\lambda| > 1$. $\hat{\mathbf{h}}(k)$ vector traverses only an arc of the circle, therefore the winding number is 0; (B) For any $|\lambda| < 1$, the winding number is 1.

Since the Hamiltonian does not conserve the number of particles, one needs to use the the Bogoliubov transformation to diagonalize Eq.(1.20):

$$\hat{a}_k = \cos(\theta_k)\hat{c}_k - i\sin(\theta_k)\hat{c}_{-k}^{\dagger}, \qquad \tan(2\theta_k) = \frac{h_y(k)}{h_z(k)}. \tag{1.24}$$

Under Eq.(1.24) we get

$$\hat{H}_{KC} = -\sum_{k \in BZ} E(k) + \sum_{k \in BZ} E(k)\hat{c}_k^{\dagger}\hat{c}_k, \tag{1.25}$$

with the ground state of the system $|GS\rangle$ defined as $\hat{c}_k|0\rangle = 0$ for all momentum k.

As evident from Eq.(1.23), the bulk spectrum becomes gapless for $\lambda = \pm 1$. Due to the particle-hole symmetry of the model, we can say that only $|\lambda| < 1$ (weak coupling) and $|\lambda| > 1$ (strong coupling) phases are distinct. The ground state of the system can be written down exactly

$$|GS\rangle \propto \prod_{0<k<\pi} \left(1 + \varphi_{C.p}(k)c_{-k}^{\dagger}c_k^{\dagger}\right)|0\rangle, \quad \varphi_{C.p}(k) = -i\tan(\theta_k). \tag{1.26}$$

One can rewrite $\varphi_{C.p}(k)$ in the real space, and interpret it as a wavefunction of the Cooper pair. Important feature of $\varphi_{C.p}(x)$ is that it behaves differently in the weak and strong coupling cases [33]

$$|\varphi_{C.p}(x)| \sim \begin{cases} e^{-|x|/\xi}, & |\lambda| > 1 \\ \text{const.}, & |\lambda| < 1 \end{cases} \tag{1.27}$$

The fact that the Cooper-pair size is finite for $|\lambda| > 1$ and infinite for $|\lambda| < 1$ does not necessarily imply that these phases are different from each other. To distinguish these two, we use the topological characterization of the phases. From Eq.(1.21) we can define a normalized vector $\hat{\mathbf{h}}(k) = \frac{\mathbf{h}(k)}{|\mathbf{h}(k)|}$. Since $h_y(k) = -h_y(-k)$ and $h_z(k) = h_z(-k)$, the direction where $\hat{\mathbf{h}}(k)$ can point to for $k = 0$ and $k = \pi/\alpha_0$ is restricted as

$$\hat{\mathbf{h}}(0) = -\text{sgn}(1+\lambda)\hat{z} = s_0\hat{z}, \tag{1.28}$$

$$\hat{\mathbf{h}}(\pi/\alpha_0) = \text{sgn}(1-\lambda)\hat{z} = s_{\pi/\alpha_0}\hat{z} \tag{1.29}$$

where s_0 and s_{π/α_0} are the signs of the kinetic energy respectively at $k = 0$ and $k = \pi/\alpha_0$ parts of the Brillouin zone. When one varies the momentum k within the Brillouin zone, $\hat{\mathbf{h}}(k)$ vector will move along the circumference of a unit circle. If $s_0 = -s_{\pi/\alpha_0}$, then the trajectory of the unit vector
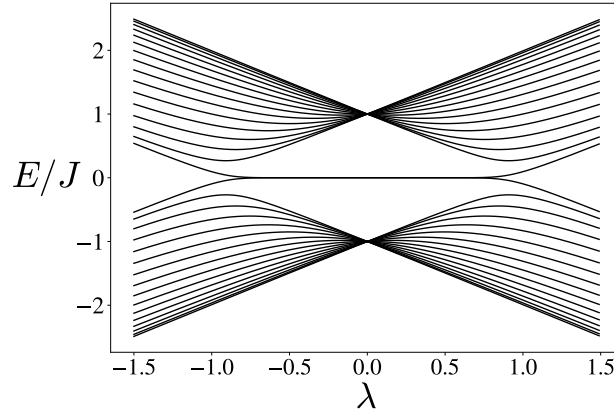
FIGURE 1.2: The figure shows the eigenstates of Eq.(1.19) for various λ parameter, with open boundary conditions. The spectrum is extracted for the system consisting of $L = 16$ sites.

will wind once around the origin (Fig.1.1b). If $s_0 = s_{\pi/\alpha_0}$, then the vector traverses a arc, without zero winding number (Fig.1.1a). Topologically these are distinct trajectories, since it is impossible to continuously deform one into the other. The $\mathbb{Z}_2$ topological invariant that distinguishes these two regimes is

$$\nu = s_0 s_{\pi/\alpha_0}. \tag{1.30}$$

To demonstrate the difference between $\nu = \pm 1$ phases, we study the Kitaev chain with *open boundary conditions*. For simplicity we set $\lambda \leq 0$ and introduce a notation

$$\mu = 1 + \lambda. \tag{1.31}$$

In terms of a new variable μ, the weak and strong coupling limits are $\mu > 0$ and $\mu < 0$, respectively. The low-energy sector of the model can be linearly approximated as $\hat{\mathcal{H}}_k$ a Dirac Hamiltonian

$$\hat{\mathcal{H}}_k \simeq \Delta k \hat{\tau}_y - \mu \hat{\tau}_z. \tag{1.32}$$

Small momenta k correspond to long-wave physics, thus we can pass from a discrete to a continuum description of the theory $n \to x$. Since the corresponding Dirac equation is massive, one should expect *zero energy* bound-states on the mass kinks [34]. Suppose that the mass depends on coordinate $\mu \to \mu(x)$ and has a kink profile

$$\mu(-\infty) < 0 \quad \text{strong pairing side} \tag{1.33}$$
$$\mu(+\infty) > 0 \quad \text{weak pairing side.} \tag{1.34}$$

We seek for a single-particle solution $|\psi(x)\rangle$ with *zero energy*, satisfying $\hat{H}_{KC}|\psi(x)\rangle = 0$. Such a solution is

$$|\psi(x)\rangle = \frac{1}{\sqrt{2}} e^{-\frac{1}{\Delta} \int_0^x dx' \mu(x')} \begin{pmatrix} 1 \\ -i \end{pmatrix}. \tag{1.35}$$

The operator $\hat{\gamma}$ that annihilates this mode is

$$\hat{\gamma} = \frac{1}{\mathcal{N}} \int dw e^{-\frac{1}{\Delta} \int_0^w dx' \mu(x')} \times \frac{1}{\sqrt{2}} \left(\hat{a}(x) - i\hat{a}(x) \right), \tag{1.36}$$

where $\mathcal{N}$ is some normalization factor. By performing a phase transformation $\gamma' = e^{i\pi/4}\hat{\gamma}$, we see that $\gamma' = \gamma'^\dagger$. Thus, the zero-energy mode localized at the mass kink is a *Majorana fermion*. Due

to the normalization, the zero-mode appears only $\mu > 0$ and vanishes if $\mu < 0$.

One can solve the model and extract the full spectrum of the model using exact diagonalization method [35], shown on Fig.(1.2). As it can be seen, for $-1 < \lambda < 1$ and zero-energy state emerges and they disappear for $|\lambda| > 1$.

For $\lambda = 1$ and $\lambda = -1$, the single-particle gap closes at $k = \pm\pi/\alpha_0$ and $k = 0$ respectively. By Taylor expanding the spectrum in the vicinity of the gap-closing momentum, one extracts a low-energy single-particle spectrum. For $\lambda \to \pm1$, we have

$$E(k) \approx J\sqrt{\tau^2 + (k\alpha_0)^2}, \quad |\tau| \ll 1, \quad |k\alpha_0| \ll 1 \tag{1.37}$$

with $\lambda = \pm1 + \tau$. As already anticipated from Eq.(1.32), the spectrum corresponds to a spectrum of a *massive relativistic fermion*, with $m(\tau) \sim |\tau|$ mass. Since the mass gap and the correlation length are related as $\xi \sim m^{-1}$, we get that

$$\xi \sim |\tau|^{-1}, \tag{1.38}$$

i.e. close to the critical point the correlation length diverges, with $\nu = 1$ critical exponent, in agreement with the exact solutions [27].

As one approaches $\tau \to 0$ critical point, ξ becomes larger relative to α_0 lattice spacing. This way, close to criticality we can pass from discrete lattice description to the continuum limit. At the critical point, the excitation spectrum becomes

$$E(k) \approx \Delta|k|, \quad \Delta = J\alpha_0. \tag{1.39}$$

1.4 Majorana fermions in Kitaev chain

In the previous subsection, we showed that the topological phase of the Kitaev chain is described by a zero-energy mode of Majorana degree of freedom. For the sake of completeness, we briefly analyze the topologicaly trivial and non-trivial phases using Majorana representation of the model. The reader can skip this section, as the present content is not relevant for our further discussions.

Majorana fermions are introduced by multiplying order and disorder operators

$$\hat{\zeta}_j = (-1)^j \hat{\sigma}_j^x \hat{\mu}_{j+1/2}^x = \hat{a}_j + \hat{a}_j^\dagger, \quad \hat{\eta}_j = i\hat{\zeta}_j \hat{\sigma}_j^z = i(\hat{a}_j - \hat{a}_j^\dagger). \tag{1.40}$$

Being hermitian field operators that square to unity, Majorana fermions obey the following algebra

$$\{\hat{\zeta}_j, \hat{\zeta}_k\} = \{\hat{\eta}_j, \hat{\eta}_k\} = 2\delta_{jk}, \quad \{\hat{\zeta}_j, \hat{\eta}_k\} = 0. \tag{1.41}$$

With open boundary conditions, the Kitaev chain in Majorana representation is

$$\hat{H}_{\text{KM}} = i\lambda J \sum_{j=1}^{N} \hat{\zeta}_j \hat{\eta}_j + iJ \sum_{j=1}^{N-1} \hat{\eta}_j \hat{\zeta}_{j+1} \tag{1.42}$$

and the corresponding parity operators is

$$(-1)^P = \prod_{j=1}^{N} (-i\hat{\zeta}_j \hat{\eta}_j). \tag{1.43}$$

A Majorana zero-energy mode $\hat{\Psi}$ is described an operator, obeying the following conditions [36]

$$[\hat{H}, \hat{\Psi}] \;=\; 0, \tag{1.44}$$

$$\{(-1)^P, \hat{\Psi}\} \;=\; 0, \tag{1.45}$$

$$\hat{\Psi}^\dagger \hat{\Psi}|_{N \to \infty} \;=\; 1. \tag{1.46}$$

According to these conditions, $\hat{\Psi}$ operator maps a state between odd and even parity sectors. Together with Eq.(1.44) and Eq.(1.46), we see that the energy spectrum of the system should be the same in both parity sectors. Since we want the zero-energy mode to be localized at the boundary of the system, the matrix elements of $\hat{\Psi}$ should decay exponentially fast with respect to l distance from the boundary. It has been shown [36] that the good candidate for the left and right edge zero modes are

$$\hat{\Psi}_{\text{left}}^{(N)} = \hat{\zeta}_1 + \lambda\hat{\zeta}_2 + \lambda^2\hat{\zeta}_3 + ... \tag{1.47}$$

$$\hat{\Psi}_{\text{right}}^{(N)} = \hat{\eta}_N + \lambda\hat{\eta}_{N-1} + \lambda^2\hat{\eta}_{N-2} + ... \tag{1.48}$$

However, these operators do not commute with Hamiltonian:

$$[\hat{H}_{\text{KM}}, \hat{\Psi}_{\text{left}}^{(N)}] = J\lambda^N\hat{\eta}_L, \quad [\hat{H}_{\text{KM}}, \hat{\Psi}_{\text{right}}^{(N)}] = J\lambda^N\hat{\zeta}_1 \tag{1.49}$$

The commutation condition is exactly satisfied only if $|\lambda| < 1$ and $N \to \infty$. In this regime, operator becomes normalized and thus the modes become exct zero-energy edge modes.

Thus, in the thermodynamic limit, for $|\lambda| < 1$ there are two exact Majorana edge zero modes and the phase is topologically non-trivial. If $|\lambda| > 1$, the edge modes disappear and the system falls in a topologically trivial phase.

1.5   Critical QIM and Relativistic Quantum Field Theory

As demonstrated in Eq.(1.37), in the vicinity of the critical point the spectrum becomes formally relativistic. In this subsection we will derive a quantum field theory of a relativistic massive Majorana fermions in 1+1 dimensions, which is a valid description of QIM close to the critical point. As already mentioned in Eq.(1.39), at the critical point the model becomes massless and thus scale-invariant.

The components of Nambu-spinor Eq.(1.20) are not mutually independent, since $\hat{\Psi}_k^\dagger = \hat{\Psi}_{-k}^T\hat{\tau}_x$. This means that $\hat{\Psi}_k$ is real and thus a Majorana fermion spinor. In the continuum limit, the lattice constant $\alpha_0 \to 0$ and the coupling constant $J \to \infty$, but their product is finite $v = 2J\alpha_0$. The Majorana field operators $\hat{\eta}_i$ and $\hat{\zeta}_i$ in the continuum limit are:

$$\hat{\eta}_i \to \sqrt{2\alpha_0}\hat{\eta}(x), \quad \hat{\zeta}_i \to \sqrt{2\alpha_0}\hat{\zeta}(x), \tag{1.50}$$

$$\hat{\eta}_{i+1} \to \sqrt{2\alpha_0}\hat{\eta}(x + \alpha_0) \approx \sqrt{2\alpha_0}\left(\hat{\eta}(x) + \alpha_0\partial_x\hat{\eta}(x) + \mathcal{O}(\alpha_0^2)\right), \tag{1.51}$$

$$\hat{\zeta}_{i+1} \to \sqrt{2\alpha_0}\hat{\zeta}(x + \alpha_0) \approx \sqrt{2\alpha_0}\left(\hat{\zeta}(x) + \alpha_0\partial_x\hat{\zeta}(x) + \mathcal{O}(\alpha_0^2)\right). \tag{1.52}$$

Using these rules, the Kitaev chain hamiltonian close to the criticality in the continuum limit is expressed as:

$$\hat{H}_{\text{KM}} \to \hat{H}_{\text{KM}} = i2\lambda J\int dx\hat{\zeta}_x\hat{\eta}_x + i2J\int dx\hat{\eta}_x\hat{\zeta}_{x+\alpha_0} \approx i\int dx\left(v\hat{\eta}\partial_x\hat{\zeta} - m\hat{\eta}\hat{\zeta}\right) + \mathcal{O}(\alpha_0^2) \tag{1.53}$$

Due to the particle-hole symmetry of the model, we can concentrate only on $\lambda > 0$ regime. In this case, the mass gap of the Majorana field is $m = 2J(\lambda - 1)$. One can pass to the chiral Majorana fields

$$\hat{\phi}_R = \frac{1}{\sqrt{2}} \left(\hat{\eta} - \hat{\zeta} \right), \quad \hat{\phi}_L = \frac{1}{\sqrt{2}} \left(\hat{\eta} + \hat{\zeta} \right) \tag{1.54}$$

to obtain the hamiltonian of a relativistic massive Majorana fermion in 1+1 dimensions [28, 27]

$$\hat{H}_{\text{KM}} = \int dx \Phi^\dagger \left(\frac{v}{2}(-i\partial_x)\hat{\sigma}_z + \frac{m}{2}\hat{\sigma}_y \right) \Phi, \quad \Phi^\dagger = \Phi^T = (\phi_R, \phi_L). \tag{1.55}$$

In this representation, the global $\mathbb{Z}_2$ transformation corresponds to $\phi_{R,L} \to -\phi_{R,L}$, while the duality transformation is $\phi_R \to -\phi_R, \phi_L \to \phi_L$ [1]. Since during the duality transformation the mass term changes the sign, the model is self-dual and thus a critical when $m = 0$:

$$\hat{\mathcal{H}}_{\text{KM}} = i\frac{v}{2} \int dx \left(\phi_L \partial_x \phi_L - \phi_R \partial_x \phi_R \right). \tag{1.56}$$

We can pass from real 1+1 Euclidean space $\mathcal{R}^2_{x,\tau}$ to a complex plane $\mathcal{C}_{z,\overline{z}}$

$$z = \tau + ix, \quad \overline{z} = \tau - ix. \tag{1.57}$$

Here we have disregarded $\frac{v}{2}$ pre-factor for convenience, as it only sets the energy scale and is irrelevant for our discussion. The derivatives in the complex representation are $\partial \equiv \partial_z = \frac{1}{2}\left(\partial_\tau - i\partial_x\right)$ and $\overline{\partial} \equiv \partial_{\overline{z}}$. In Euclidean space, the equation of motion of Majorana fields show that $\phi_R(x,t) = \phi_R(x-t)$ and $\phi_L(x,t) = \phi_L(x+t)$, meaning that they are the right and left moving fields, respectively. We identify these fields as $\phi_R(x,t) \equiv \phi(z,\overline{z})$ and $\phi_L(x,t) \equiv \overline{\phi}(z,\overline{z})$. The Euclidean action of the model at the critical point is

$$S = \int d^2z \left(\phi\overline{\partial}\phi + \overline{\phi}\partial\overline{\phi} \right), \tag{1.58}$$

which is a well-studied 2-dimensional Conformal Field Theory (CFT) [28], where ϕ and $\overline{\phi}$ are the so-called primary fields. Their scaling dimension Δ_ϕ and $\Delta_{\overline{\phi}}$ is defined as $\phi(\lambda z) = \lambda^\Delta \phi(z)$ and $\overline{\phi}(\lambda\overline{z}) = \lambda^{\Delta_{\overline{\phi}}}\overline{\phi}(\overline{z})$, where λ is the re-scaling factor of the complex space.

The equation of motion $\delta S = 0$ dictates that:

$$\overline{\partial}\phi(z,\overline{z}) = 0, \quad \phi(z,\overline{z}) = \phi(z) \quad \text{Holomorphic}, \tag{1.59}$$

$$\partial\overline{\phi}(z,\overline{z}) = 0, \quad \overline{\phi}(z,\overline{z}) = \overline{\phi}(\overline{z}) \quad \text{Anti-Holomorphic}. \tag{1.60}$$

The propagators then are [28]

$$\langle \phi(z_1)\phi(z_2) \rangle = \frac{1}{2\pi} \frac{1}{z_1 - z_2}, \quad \langle \overline{\phi}(\overline{z}_1)\overline{\phi}(\overline{z}_2) \rangle = \frac{1}{2\pi} \frac{1}{\overline{z}_1 - \overline{z}_2} \quad \langle \phi(z_1)\overline{\phi}(\overline{z}_2) \rangle = 0 \tag{1.61}$$

Consider a 2-point correlation function operators of ψ_1 and ψ_2

$$\Gamma(z_1, z_2) \equiv \langle \psi_1(z_1)\psi_2(z_2) \rangle. \tag{1.62}$$

Generally speaking, $\Gamma(z_1, z_2)$ will be diverging if $z_2 \to z_1$. The leading contribution of the singularity is determined by the corresponding scaling dimensions Δ_1 and Δ_2. Due to this, one may substitute $\psi_1(z_1)\psi_2(z_2)$ product by some combination of other operators that are allowed in the theory. If operators $\{\psi_k\}$ and their derivatives form a complete set, then $\psi_1(z_1)\psi_2(z_2)|_{z_1 \to z_2}$ product

---

[1]Alternatively one could define the duality transformation as $\phi_R \to \phi_R$ and $\phi_L \to -\phi_L$

is equivalent to

$$\lim_{z_1 \to z_2} \phi_1(z_1)\phi_2(z_2) = \lim_{z_1 \to z_2} \sum_k \frac{C_{ijk}}{|z_1 - z_2|^{\Delta_1 + \Delta_2 - \Delta_k}} \psi_k\left(\frac{z_1 + z_2}{2}\right). \tag{1.63}$$

Using this equivalence, we can extract the diverging contribution from the product of operators. Only those ψ_k fields with $\Delta_k \leq \Delta_1 + \Delta_2$ will appear in the singularity, since otherwise the contribution is regular. Eq.(1.63) is known as the Operator Product Expansion (OPE) [37] and in the literature it is frequently expressed as

$$\phi_1(z_1)\phi_2(z_2) \sim \sum_k \frac{C_{ijk}}{|z_1 - z_2|^{\Delta_1 + \Delta_2 - \Delta_k}} \psi_k\left(\frac{z_1 + z_2}{2}\right). \tag{1.64}$$

It must be noted, that the operator product expansion has a physical interpretation only if one uses while taking expectation values with respect some state in the system.

If a generic model admits CFT description, then the OPE of the (anti-)holomorphic component of energy-momentum tensor T with itself will always yield [27]

$$T(z_1)T(z_2) \sim \frac{1}{2}\frac{c}{(z_1 - z_2)^4} + \frac{2T(z_2)}{(z_1 - z_2)^2} + \frac{\partial_{z_2}T(z_2)}{z_1 - z_2}, \tag{1.65}$$

where c is the so-called *central charge*, which is theory dependent but a universal number. In the case of 2-dimensional CFT of Majorana fermions, we have

$$T(z_1) = -\pi : \phi(z_1)\partial_{z_1}\phi(z_1) : \tag{1.66}$$

with $: \bullet :$ denoting the normal ordering. Using Wick's theorem, one can calculate such OPE and show that $c = \frac{1}{2}$ [27]. Moreover, Eq.(1.61) automatically means that the OPE for ϕ with itself to be

$$\phi(z_1)\phi(z_2) \sim \frac{1}{2\pi}\frac{1}{z_1 - z_2}. \tag{1.67}$$

Generically, the OPE between $T(z_1)$ and a primary field $\phi(z_2)$ is fixed to be

$$T(z_1)\phi(z_2) \sim \frac{h}{(z_1 - z_2)^2}\phi(z_2) + \frac{1}{z_1 - z_2}\partial_{z_2}\phi(z_2), \tag{1.68}$$

where h is the so-called conformal weight of ϕ. Again, using the Wick's theorem, we have

$$T(z_1)\phi(z_2) \sim \frac{\frac{1}{2}}{(z_1 - z_2)^2}\phi(z_2) + \frac{1}{z_1 - z_2}\partial_{z_2}\phi(z_2). \tag{1.69}$$

Therefore, we get $\left(h_\phi = \frac{1}{2}; \overline{h}_\phi = 0\right)$. Identical calculations for the anti-holomorphic components give $\left(h_{\overline{\phi}} = 0; \overline{h}_{\overline{\phi}} = \frac{1}{2}\right)$. The energy density operator of our model is $\epsilon(z, \overline{z}) = i\phi(z)\overline{\phi}(\overline{z})$. Since it is proportional to the mass term, we deduce that the scaling dimension is $\Delta_\epsilon = h_\phi + \overline{h}_{\overline{\phi}} = 1$. Knowledge of the central charge and the scaling dimension of ϵ energy density operator allows us to identify the theory as the Minimal Model $\mathcal{M}(4, 3)$ [38].

In the Minimal Model $\mathcal{M}(4,3)$ with $c = \frac{1}{2}$, is is known that any correlation function that involves a primary field $\psi(z)$ must satisfies the following equation:

$$\left(\frac{3}{4} \partial^2 - \sum_{i=1}^{N} \frac{\Delta_i}{(z - z_i)^2} - \sum_{i=1}^{N} \frac{\partial_i}{z - z_i} \right) \langle \psi(z) \phi_1(z_1) \phi_2(z_2) ... \phi_N(z_N) \rangle = 0. \tag{1.70}$$

As we saw in Sec.(1.1), the critical Ising model can be described either by order $\sigma(z, \overline{z})$ or $\mu(z, \overline{z})$ disorder operators. The OPE for $\psi(z)\sigma(z_1, \overline{z}_1)$ and $\psi(z)\mu(z_1, \overline{z}_1)$ are [28]

$$\psi(z)\sigma(z_1, \overline{z}_1) \sim \frac{\mu(z_1, \overline{z}_1)}{\sqrt{z - z_1}}, \quad \psi(z)\mu(z_1, \overline{z}_1) \sim \frac{\sigma(z_1, \overline{z}_1)}{\sqrt{z - z_1}}. \tag{1.71}$$

The correponding conformal weights for σ and μ are

$$\left(h_\sigma; \overline{h}_{\overline{\sigma}} \right), \quad \left(h_\mu; \overline{h}_{\overline{\mu}} \right). \tag{1.72}$$

Due to Kramers-Wanier duality, they should be equal $h_\sigma = h_\mu = h$ and $\overline{h}_{\overline{\sigma}} = \overline{h}_{\overline{\mu}} = \overline{h}$. Plugging Eq.(1.71) in Eq.(1.70) gives

$$h = \overline{h} = \frac{1}{16}, \tag{1.73}$$

Using these conformal weight, the scaling dimension for $\sigma(z, \overline{z})$ and $\mu(z, \overline{z})$ operators are $\Delta_\mu = \Delta_\sigma = h + \overline{h} = 1/8$ and therefore we can immediately deduce following the two-point correlation functions

$$\langle \sigma(z_1, \overline{z}_1)\sigma(z_2, \overline{z}_2) \rangle \sim \langle \mu(z_1, \overline{z}_1)\mu(z_2, \overline{z}_2) \rangle \sim \frac{1}{|z_1 - z_2|^{1/4}}. \tag{1.74}$$

This way, at the critical point the spin-spin correlation function for QIM follows a power law with $\eta = 1/4$ critical exponent. This result is in agreement with an exact solution [27].

The field theory of QIM close to the criticality can emerge naturally in various setups, as anticipated from the phenomenon of universality [28, 29]. Moreover, continuous field theories such as Eq.(1.53) can be implemented as a natural phenomenological description of more exotic regimes. Such cases will be encountered in Sec.(4) and Sec.(5), where we use critical Ising field theory to describe a super-symmetric critical points.

Chapter 2

XXZ model and Abelian Bosonization

In this chapter we will study the so called Heisenberg XXZ model. Being a generalization of QIM, it is a paradigmatic exactly solvable model [29] of interacting SU(2) spins and can be studied on various lattice geometries. In this case, all three projections participate in pairwise interaction, while for simplicity the external magnetic field is absent. Similar to QIM, the XXZ model contains a single parameter $|\Delta| \leq 1$ that drives the phase transition. Referred to as an exchange anisotropy, Δ quantifies the imbalance of interaction strength along one specific direction relative to others. Instead of exploring the exact Bethe ansatz solution [28], here we will be again interested in the so-called asymptotically exact solutions. By implementing Jordan-Wigner transformation, together with Abelian bosonization and renormalization group arguments, we will demonstrate that the model remains critical for $|\Delta| \ll 1$. The criticality is governed by a Gaussian conformal field theory. We will show that the effective theory derived by bosonizing the model is compatible with exact solution and the system remains critical for whole $|\Delta| \leq 1$ regime. The bosonization tools introduced in this chapter will play a central role in extracting and analyzing the effective field theory for a more complex case discussed in Sec.(4) and Sec.(5).

The Hamiltonian for the so called spin$-\frac{1}{2}$ XXZ Heisenberg model on 1D chain with nearest neighbor interactions reads as

$$\mathrm{H}_{\mathrm{XXZ}}(\Delta) = J \sum_{i=1}^{N} \left(S_i^x S_{i+1}^x + S_i^y S_{i+1}^y + \Delta S_i^z S_{i+1}^z \right) \tag{2.1}$$

where $\mathbf{S}$ is the spin vector residing on the site i of the lattice, each represented by 2×2 Pauli matrices, $\mathbf{S} = \frac{1}{2}\boldsymbol{\sigma}$. Here we impose a periodic boundary condition $\mathbf{S}_{N+1} = \mathbf{S}_1$ and assume that there are even N number of lattice sites. By choosing z as our axis of quantization, the model can be re-written as

$$\mathrm{H}_{\mathrm{XXZ}}(\Delta) = J \sum_{i=1}^{N} \left(\frac{1}{2} \left[S_i^+ S_{i+1}^- + S_{i+1}^+ S_i^- \right] + \Delta S_i^z S_{i+1}^z \right), \tag{2.2}$$

$S^{\pm}$ being the spin raising and lowering operators. Now it is clear that S^z part of the model is responsible for (anti-)alignment of spins along z direction, while kinetic term $S^{\pm}$ takes care of the propagation of spin excitations along the chain.

An important conservation law of Eq.(2.1) is that of a total magnetization along z axis:

$$S^z = \frac{1}{N} \sum_{i=1}^{N} S_i^z, \quad [S^z, \mathrm{H}_{\mathrm{XXZ}}(\Delta)] = 0. \tag{2.3}$$

Suppose we fix J to be positive coupling constant and thus consider an anti-ferromagnetic XXZ model. The dimensionless parameter Δ quantifies the deviation from an SU(2) invariant point. For $\Delta \to +\infty$, $z - z$ interaction dominates and the ground state corresponds to the Neel state, with

$\mathbb{Z}_2$ symmetry. Conversely, for $\Delta \to -\infty$, the ground state of the system is the ferromagnetic state, again with $\mathbb{Z}_2$ symmetry. For $\Delta = 1$, the symmetry of the model is maximal, corresponding to non-Abelian SU(2) group and for $\Delta = 0$, the symmetry corresponds to Abelian O(2) group.

Another important symmetry property of Eq.(2.1) Hamiltonian is the similarity transformation: one can transform the spin operators as

$$S_i^x \to (-1)^i S_i^x, \quad S_i^y \to (-1)^i S_i^y, \quad S_i^z \to S_i^z. \tag{2.4}$$

This transformation preserves the algebra between the spin operators, however under this transformation we get

$$\mathrm{H}_{\mathrm{XXZ}}(\Delta) \to \tilde{\mathrm{H}}_{\mathrm{XXZ}}(\Delta) = -\mathrm{H}_{\mathrm{XXZ}}(-\Delta)$$

$$\tilde{\mathrm{H}}_{\mathrm{XXZ}}(\Delta) = -J\sum_{i=1}^{N} \left(S_i^x S_{i+1}^x + S_i^y S_{i+1}^y - \Delta S_i^z S_{i+1}^z \right). \tag{2.5}$$

This tells us that Hamiltonians $\mathrm{H}_{\mathrm{XXZ}}(\Delta)$ and $-\mathrm{H}_{\mathrm{XXZ}}(-\Delta)$ can be diagonalized in the same basis, thus they share the physical properties and thus the overall physics is governed by the relative sign of J and Δ. It should be noted that $\Delta = \pm 1$ points correspond to a fully is SU(2) symmetric regimes. Since we have fixed J to be positive, then we can have two possible scenarios

1. If $\Delta \gg +1$, then the system is anti-Ferromagnetic

2. If $-\Delta \gg 1$, then the system is Ferromagnetic

This two scenarios are valid both for $\mathrm{H}_{\mathrm{XXZ}}(\Delta)$ and $\tilde{\mathrm{H}}_{\mathrm{XXZ}}(\Delta)$. For convenience, we will be working with $\tilde{\mathrm{H}}_{\mathrm{XXZ}}(\Delta)$ Hamiltonian.

Before passing to the next section, we need to mention the ground state and the excitation structure in $\Delta \to \pm\infty$ limits of the theory. Suppose we take $\tilde{\mathrm{H}}_{\mathrm{XXZ}}(\Delta \to -\infty)$ case, then the effective Hamiltonian becomes

$$\tilde{\mathrm{H}}_{\mathrm{XXZ}}(\Delta) = -J|\Delta|\sum_{i=1}^{N} S_i^z S_{i+1}^z. \tag{2.6}$$

In this limit, the model reduces to classical Ferromagnet, with doubly degenerate ground state of aligned spins Fig.(2.1a). If the system absorbs a photon or a phonon, carrying $s = 1$ spin quantum number, then this will induce a flip of a single spin. If one introduces weak kinetic term, then a single excitation with spin $s = 1$ will start to propagate either to the left or to the right Fig.(2.1c). The energy cost of the propagation is zero. These excitations are known as *magnons*, since they carry spin $s = 1$.

In the opposite limit $\Delta \to +\infty$, we end up with a classical anti-Ferromagnet, where the ground state corresponds to Neél state of anti-aligned spins Fig.(2.1b). As before, if the system absorbs a photon with $s = 1$ and introduces weak kinetic term, then the spin excitation above the Neél state will decay into two $s = \frac{1}{2}$ *spinons* that will propagate to the left and to the right Fig.(2.1d).

2.1   From XXZ to interacting fermions

Using the Jordan-Wigner transformation Eq.(1.18), we can map $\tilde{\mathrm{H}}_{\mathrm{XXZ}}(\Delta)$ spin model onto the model of interacting spinless fermions:

$$\tilde{\mathrm{H}}_{\mathrm{XXZ}}(\Delta) \to \hat{\mathrm{H}}(\Delta) = \mathrm{H}_0 + \mathrm{H}_{\mathrm{int.}}, \tag{2.7}$$
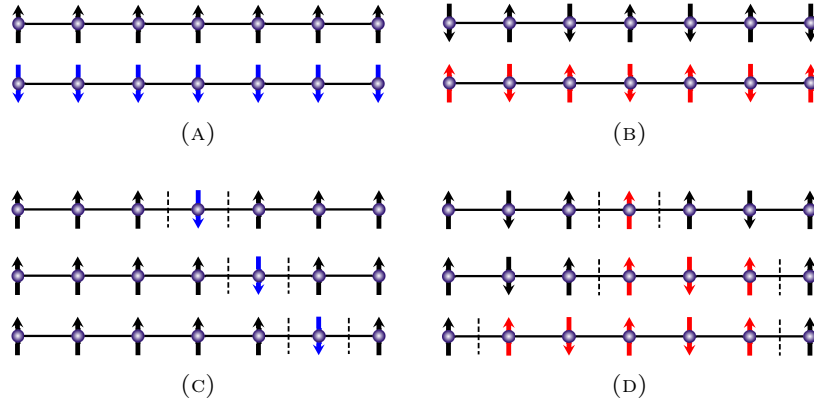
FIGURE 2.1: (a) Degenerate vacua of the ferromagnetic model; (b) Degenerate vacua of the antiferromagnetic model; (c) Magnon excitations in the ferromagnetic ground state; (d) Magnon decay into the pair of spinons in an antiferromagnet.

where the quadratic part is given by

$$\mathrm{H}_0 = -\frac{J}{2} \left(\sum_{i=1}^{N-1} \left(a_i^\dagger a_{i+1} + a_{i+1}^\dagger a_i \right) - \Delta \sum_{i=1}^{N} n_i - \Delta \frac{N}{4} \right). \tag{2.8}$$

while the interaction becomes

$$\mathrm{H}_{\mathrm{int.}} = \frac{J\Delta}{2} \sum_{i=1}^{L} n_i n_{i+1}, \tag{2.9}$$

where $n_i = a_i^\dagger a_i$. It is crucial to note that the periodic boundary conditions for the XXZ model does not necessarily translate to the same conditions for the fermionic operators. As we already saw in Sec.(1.3), due to the Jordan-Wigner string, the fermionic operators are supplemented with the boundary conditions depending on the total number of fermions N_e in the system

$$a_{i+N} = -(-1)^{N_e} a_i. \tag{2.10}$$

It is important to note that Eq.(2.7) conserves the total particle number $N_e = \sum_{i=1}^{N} n_i$, which is an immediate consequence of Eq.(2.3) conservation law.

$\Delta = 0$ case in the original spin problem would yield XX model. Due to a planar O(2) symmetry, the ground state expectation value of the total magnetization along z axis is $\langle S^z \rangle = \frac{1}{L} \sum_{i=1}^{L} \langle S_i^z \rangle = 0$. On the other hand, using Jordan-Wigner transformation we have

$$\langle S^z \rangle = \frac{1}{N} \sum_{i=1}^{N} \langle n_i \rangle - \frac{1}{2} = \frac{2N_e - N}{2N} = 0 \quad \rightarrow \quad N_e = \frac{N}{2}. \tag{2.11}$$

This means that Heisenberg XX model is equivalent to a tight binding model at half filling. Furthermore, since we typically operate in a thermodynamic limit $N \to \infty$, the boundary conditions do not play a significant role. This way, we assume N_e to be even and work with anti-periodic boundary conditions for the fermionic operators.

Passing to the momentum space as

$$a_j = \frac{1}{\sqrt{N}} \sum_{k \in BZ} e^{ijk\alpha_0} a_k, \tag{2.12}$$

we get

$$H_0 = \sum_{k \in BZ} \varepsilon(k) a_k^\dagger a_k, \quad \varepsilon(k) = -J\cos(k\alpha_0) \tag{2.13}$$

where the summation over momenta runs over the first Brillouin zone. In finite lattice limit, these momenta are

$$k = \frac{2\pi}{N}\left(n + \frac{1}{2}\right), \quad n = -\frac{N}{2}, -\frac{N}{2}+1, -\frac{N}{2}+2, ..., \frac{N}{2}-1. \tag{2.14}$$

Here the anti-periodic boundary condition Eq.(2.10) is taken into account.

As we have already seen, the half of the lattice sites are occupied by spinless fermions, $\langle n_i \rangle = \frac{1}{2}$. For the state to be the ground state at zero temperature, the spectrum must be populated from the lowest energy states first. That is the case, if all of the momenta within $k \in \left(-\frac{\pi}{2\alpha_0}, \frac{\pi}{2\alpha_0}\right)$ region are occupied. This way, the chemical potential is located at zero $\mu = \varepsilon_F = \varepsilon(\pm k_F) = 0$, with $k_F = \frac{\pi}{2\alpha_0}$.

(A)   (B)
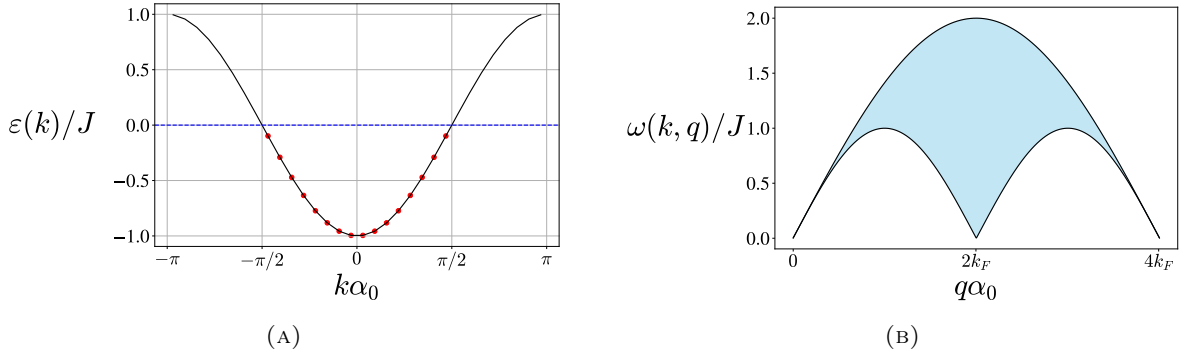
FIGURE 2.2: (a) The figure shows the single particle spectrum Eq.(2.13) for $L = 64$. The red circles correspond to the quantum states occupied by fermions. The blue line corresponds to the chemical potential, that automatically turns out to be $\mu = 0$ due to half filling of the model; (b) The figure shows the full spinon excitation spectrum of XX model, shaded in blue. The most important feature of this continuum is the linear growth of $\omega(k, q)$ for $q \approx 0$ and $q \approx 4k_F$.

Using this construction of the ground state, we can extract the spin-spin correlation function for XX model. Since $\hat{S}_n^z = \hat{a}_n^\dagger \hat{a}_n - \frac{1}{2}$, using Wick's theorem we have

$$\langle \hat{S}_n^z \hat{S}_m^z \rangle = -\langle \hat{a}_n^\dagger \hat{a}_m \rangle \langle \hat{a}_m^\dagger \hat{a}_n \rangle. \tag{2.15}$$

Using the structure of the ground state, we get

$$\langle \hat{a}_n^\dagger \hat{a}_m \rangle = \frac{1}{N} \sum_{k \in BZ} e^{-i(n-m)k\alpha_0} \langle a_k^\dagger a_k \rangle \approx -\frac{1}{\pi} \frac{\sin(\frac{\pi}{2}(n-m))}{n-m}. \tag{2.16}$$

This way, the two-point spin-spin correlation function beocmes

$$\langle \hat{S}_n^z \hat{S}_m^z \rangle = -\frac{1}{\pi^2} \frac{\sin^2(\frac{\pi}{2}(n-m))}{(n-m)^2}. \tag{2.17}$$

This correlation function has few important features. Most importantly, it exhibits a power-law decay of the correlation function and thus indicates that the theory is critical. Apart from the smooth part of the correlator, one can see a term with a staggering factor $e^{i\pi(n-m)} = e^{i2k_F(n-m)\alpha_0}$ – a signature that the microscopic constituents of the model are fermionic in nature.

The simplest excitations above the ground state correspond to the particle-hole pairs. When the system absorbs energy from the environment, these excitations propagate independently as free

particles, with well defined energy and momentum. The excitation spectrum $\omega(k;q)$ of XX model, i.e. free fermion model is gapless. For $N \gg 1$ large systems, the excitation spectrum becomes a continuum and it takes infinitesimally small energy to excite the system. Apart from $\omega(k;q)$ being continuous, another important property of $\omega(k;q)$ is that for small momentum transfer $|q| \ll k_F$ very close to fermi momentum $k \approx \pm k_F$

$$\omega(k \approx \pm k_F; q) = \varepsilon(\pm k_F + q) - \varepsilon(\pm k_F) \approx \pm v_F q, \quad v_F = J\alpha_0 \tag{2.18}$$

the excitation spectrum becomes is linear and only depends on transferred momentum q.

2.2 Continuum limit

As we have already seen, having non-zero Δ anisotropy parameter in XXZ Heisenberg model, renders the corresponding fermionic model interacting - a solvable model using Bethe Ansatz, though the solution is not trivial. Instead of attempting to seek the exact solution of the microscopic model Eq.(2.8) even for small $|\Delta| \ll 1$ anisotropy, one can try to extract the physics of the low-energy sector and analyze the properties of the model at large distances. As we already saw in Sec.(1), this type of approach turns out to be extremely insightful due to the universality classification of physical models, allows one to use mathematical tools such as Renormalization Group approach and etc. Moreover, a low-energy effective theories of many-body system is a useful guide for more exact numerical computations.

Since we are interested in the low energy sector of the model, the quantum states that are far below the Fermi energy do not participate and thus we do not need to know the full spectrum of the model. As we already saw, in the low energy sector of the excitation spectrum, only the states close to $k = \pm k_F$ participate. This way, we can linearize the single particle spectrum close to the fermi momenta: for $k = k_F$, i.e. right branch of the spectrum we have

$$\varepsilon_R(k) = v_F(k_F + k), \quad |k + k_F| < \Lambda \ll k_F \tag{2.19}$$

and similarly, for the left branch we have

$$\varepsilon_L(k) = -v_F(-k_F + k), \quad |k - k_F| < \Lambda \ll k_F. \tag{2.20}$$

Using this approach, in Eq.(2.13) we only retain the momenta that are close either to the left or the right branch of the spectrum

$$
\begin{aligned}
H_0 &\approx \sum_{|p|<\Lambda} \varepsilon(p - k_F) a^\dagger_{p-k_F} a_{p-k_F} + \sum_{|p|<\Lambda} \varepsilon(p + k_F) a^\dagger_{p+k_F} a_{p+k_F} = \\
&= \sum_{|p|<\Lambda} \varepsilon(p - k_F) a^\dagger_{p-k_F} a_{p-k_F} + \sum_{|p|<\Lambda} \varepsilon(p + k_F) a^\dagger_{p+k_F} a_{p+k_F} \approx \\
&\approx \sum_{|p|<\Lambda} (\varepsilon(-k_F) - v_F p) L^\dagger_p L_p + \sum_{|p|<\Lambda} (\varepsilon(k_F) + v_F p) R^\dagger_p R_p = \\
&= \sum_{|p|<\Lambda} v_F p \left(R^\dagger_p R_p - L^\dagger_p L_p \right).
\end{aligned}
\tag{2.21}
$$

Eq.(2.21) corresponds to a formally relativistic theory of massless fermions, which propagate with v_F velocity. By linearizing the original bounded spectrum, we ended up with an unbounded spectrum for left and right branches $\epsilon_{R/L}(p) = \pm v_F p$. We assume that all energy states with $p < 0$ for right and all states with $p > 0$ for left branches are occupied - this way we have introduced an infinitely full Fermi sea, denoting such state as $|FS\rangle$.

The corresponding spatial representation of R_p, L_p operators are

$$R(x) = \frac{1}{\sqrt{N}} \sum_{|p|<\Lambda} e^{ipx} R_p, \quad L(x) = \frac{1}{\sqrt{N}} \sum_{|p|<\Lambda} e^{ipx} L_p, \quad x = j\alpha_0 \tag{2.22}$$

Since R_p and L_p operators describe physical fermions, one must check whether $R(x)$ and $L(x)$ are physical fermionic fields or no. A straightforward way is to check the anti-commutation relations.

$$\{R^\dagger(x), R(y)\} = \frac{1}{N} \sum_{|p|<\Lambda} \sum_{|q|<\Lambda} e^{-i(px-qy)} \{R^\dagger_p, R_q\} = \frac{1}{N} \sum_{|p|<\Lambda} e^{-ip(x-y)} \approx \frac{\alpha}{\pi} \frac{1}{(x-y)^2 + \alpha^2} \tag{2.23}$$

with $\alpha \sim 1/\Lambda$ cutoff. This way, we see that the commutator, instead of being equal to the Dirac δ-function, it is given by a Lorenzian of width α. However, the important point is that the δ-function can be recovered using two *equivalent* ways:

1. The δ-function is recovered from $\frac{\alpha}{\pi} \frac{1}{(x-y)^2 + \alpha^2}$ if $|x - y| \gg \alpha$ - i.e. at large distances the fields satisfy the proper algebra

2. Remove the cutoff altogether, i.e. $\alpha \to 0$. This is equivalent to $\Lambda \to \infty$, or in other words taking the original lattice constant $\alpha_0 \to 0$, $j \to \infty$ so that $x = j\alpha_0$ stays fixed.

The second way defines the continuum limit of the theory - one takes α_0 lattice constant to be infinitesimally small, while taking J infinitely large, so that their product $v_F = J\alpha_0$ stays finite. Taking the continuum limit yields completely linear single particle spectrum at $k = \pm k_F$, while sends the top and bottom edge of the spectrum to $+\infty$ and $-\infty$, respectively and thus introduces the aforementioned infinite Fermi sea. The introduction of Dirac sea leads to important differences between the vacuum properties of linearized and non-linearized models, for example - the vacuum energy of the linearized model is $E_{FS} = \langle FS|\mathrm{H}_0|FS\rangle = -\infty$. However, since we are interested in the fluctuation above the Fermi sea, we can shift the energy scale and set $\langle FS|\mathrm{H}_0|FS\rangle$ to zero by normally ordering the Hamiltonian:

$$H_0 \to H_0 = \sum_{|p|<\Lambda} v_F p \left(: R^\dagger_p R_p : - : L^\dagger_p L_p : \right) \tag{2.24}$$

In the continuum limit, the fermionic operators are modified in the following way

$$\sum_{i=1}^N \to \frac{1}{\alpha_0} \int_0^L dx \quad a_j \to \sqrt{\alpha_0} a(x), \quad \text{with} \quad x = j\alpha_0 \tag{2.25}$$

Using these rules, we get

$$a(x) = e^{ik_F x} R(x) + e^{-ik_F x} L(x). \tag{2.26}$$

Here $R(x)$ and $L(x)$ are smoothly varying fields. Plugging the continuum version of the fermionic operators into the hamiltonian of XX model and normally ordering the result, we get

$$\mathrm{H}_0 = -\frac{J}{2} \int_0^L dx \left(e^{ik_F \alpha_0} : R^\dagger(x) R(x + \alpha_0) : + e^{-ik_F \alpha_0} : L^\dagger(x) L(x + \alpha_0) : + \text{h.c.} \right)$$
$$- \frac{J}{2} \int_0^L dx \left(e^{ik_F(2x + \alpha_0)} : L^\dagger(x) R(x + \alpha_0) : + e^{-ik_F(2x + \alpha_0)} : R^\dagger(x) L(x + \alpha_0) : + \text{h.c.} \right). \tag{2.27}$$

Since $k_F = \frac{\pi}{2\alpha_0}$, on the second line we have terms with $e^{-i\frac{\pi}{\alpha_0}x} = (-1)^{x/\alpha_0}$ rapidly oscillating pre-factors and they are dropped. This way, we have

$$\mathrm{H}_0 = -\frac{J}{2}\int_0^L dx \left(i : R^\dagger(x)R(x+\alpha_0) : -i : L^\dagger(x)L(x+\alpha_0) : +\mathrm{h.c.} \right). \qquad (2.28)$$

Expanding the fermionic fields as $R(x+\alpha_0) \approx R + \alpha_0\partial_x R$ and $L(x+\alpha_0) \approx L + \alpha_0\partial_x L$, we get

$$\mathrm{H}_0 = -iv_F \int_0^L dx \left(: R^\dagger\partial_x R : - : L^\dagger\partial_x L : \right) \equiv \mathrm{H}_0^{(R)} + \mathrm{H}_0^{(L)}. \qquad (2.29)$$

Thus we see that the Hamiltonians of L and R sectors completely decouple.

2.3   Abelian Bosonization

The field theory written in this manner, in terms of *chiral* R and L fields. The model possesses $U_L(1) \otimes U_R(1)$ *Abelian* symmetry, meaning that the number of left and right moving fermions are conserved independently. This is a larger symmetry relative to the original $U(1)$. By defining the $U_L(1)$ and $U_R(1)$ chiral currents operators as

$$J_R =: R^\dagger R :, \quad J_L =: L^\dagger L :, \qquad (2.30)$$

we see that the aforementioned chiral $U(1)$ transformations are generated

$$N_R = \int_0^L dx J_R, \quad N_L = \int_0^L dx J_L. \qquad (2.31)$$

The chiral fields, say R field in Heisenberg picture reads as

$$R(x,t) = e^{it\mathrm{H}_0^{(R)}} R(x,0) e^{-it\mathrm{H}_0^{(R)}}. \qquad (2.32)$$

Using the equation of motion $\partial_t R(x,t) = i\left[\mathrm{H}_0^{(R)}, R(x,t)\right]$, we get

$$\partial_t R(x,t) = -v_F\partial_x R(x,t). \qquad (2.33)$$

Similarly

$$\partial_t L(x,t) = +v_F\partial_x L(x,t). \qquad (2.34)$$

By passing to the so called light-cone coordinates $x_\pm = v_F t \pm x$, we get

$$\partial_- L(x,t) = 0, \quad \partial_+ R(x,t) = 0, \qquad (2.35)$$

which means that $L(x,t) = L(x+v_F t, 0) = L(x_+)$ chiral field moves to the *left* and similarly $R(x,t) = R(x-v_F t, 0) = R(x_-)$ moves to the *right*. If we include the light-cone coordinate in the Fourier representation of the chiral fields, we get

$$R(x_-) = \frac{1}{\sqrt{N}}\sum_{|p|<\Lambda} e^{-ipx_-} R_p, \quad L(x_+) = \frac{1}{\sqrt{N}}\sum_{|p|<\Lambda} e^{ipx_+} L_p, \quad x = j\alpha_0 \qquad (2.36)$$

Due to this, the chiral current satisfy identical equations of motion and therefore

$$J_L(x,t) = J_L(x_+), \quad J_R(x,t) = J_R(x_-) \tag{2.37}$$

Let us calculate two point correlation functions for the chiral currents. During the calculations, we will be taking the average with respect to the infinitely full Fermi sea, i.e. $\langle \bullet \rangle \equiv \langle FS| \bullet |FS\rangle$. First, we have a trivial correlation function

$$\langle J_L(x_+) J_R(y_-) \rangle = 0. \tag{2.38}$$

Next comes the correlations functions of the currents with the same chirality index:

$$\langle J_L(x_+) J_L(y_+) \rangle = \langle : L_{x_+}^\dagger L_{x_+} :: L_{y_+}^\dagger L_{y_+} : \rangle = \langle L_{x_+}^\dagger L_{y_+} \rangle \langle L_{x_+} L_{y_+}^\dagger \rangle \tag{2.39}$$

Here we have used Wick's theorem. The corresponding fermionic correlators can be computed easily: by using $L(x) = \frac{1}{\sqrt{N}} \sum_{|p|<\Lambda} e^{ipx} L_p$ in the correlation function we get

$$\langle L_{x_+}^\dagger L_{y_+} \rangle = \frac{1}{N} \sum_{|p|,|q|<\Lambda} e^{-i(px_+ - qy_+)} \langle L_p^\dagger L_q \rangle = \frac{1}{N} \sum_{0<p<\Lambda} e^{-ip(x_+ - y_+)} \tag{2.40}$$

By replacing the sharp cutoff with a smooth one, we get

$$\langle L_{x_+}^\dagger L_{y_+} \rangle = \frac{1}{N} \sum_{0<p<\Lambda} e^{-ip(x_+ - y_+)} \rightarrow \int_0^\infty \frac{dp}{2\pi} e^{-ip(x_+ - y_+)} e^{-\alpha p} = -\frac{i}{2\pi} \frac{1}{(x_+ - y_+) - i\alpha}. \tag{2.41}$$

Similarly, since $\langle L_{x_+} L_{y_+}^\dagger \rangle = \langle L_{y_+}^\dagger L_{x_+} \rangle$, we have

$$\langle J_L(x_+) J_L(y_+) \rangle = -\frac{1}{4\pi^2} \frac{1}{((x_+ - y_+) - i\alpha)^2}. \tag{2.42}$$

From this correlation function we can extract the average of the commutator between $J_L(x_+)$ and $J_L(y_+)$:

$$\langle [J_L(x_+), J_L(y_+)] \rangle = \frac{1}{4\pi^2} \left(\frac{1}{((x_+ - y_+) + i\alpha)^2} - \frac{1}{((x_+ - y_+) - i\alpha)^2} \right)$$
$$= \frac{i}{2\pi} \partial_{x_+} \left(\frac{\alpha}{\pi} \frac{1}{(x_+ - y_+)^2 + \alpha^2} \right) = \frac{i}{2\pi} \partial_{x_+} \delta(x_+ - y_+). \tag{2.43}$$

Similarly for right sector, we get

$$\langle J_R(x_-) J_R(y_-) \rangle = \langle R_{x_-}^\dagger R_{y_-} \rangle \langle R_{x_-} R_{y_-}^\dagger \rangle \tag{2.44}$$

with

$$\langle R_{x_-}^\dagger R_{y_-} \rangle = \langle R_{x_-} R_{y_-}^\dagger \rangle = \frac{i}{2\pi} \frac{1}{(x_- - y_-) - i\alpha} \tag{2.45}$$

and thus

$$\langle J_R(x_-) J_R(y_-) \rangle = -\frac{1}{4\pi^2} \frac{1}{((x_+ - y_+) - i\alpha)^2} \tag{2.46}$$

and this way we identically get

$$\langle [J_R(x_-), J_R(y_-)] \rangle = \frac{i}{2\pi} \partial_{x_-} \delta(x_- - y_-). \tag{2.47}$$

An important fact has to be underlined. The extracted commutators of the chiral currents correspond to the U(1) Kac-Moody algebra

$$\langle [J_L(x_+), J_L(y_+)] \rangle = \frac{i}{2\pi} \partial_{x_+} \delta(x_+ - y_+),$$
$$\langle [J_R(x_-), J_R(y_-)] \rangle = \frac{i}{2\pi} \partial_{x_-} \delta(x_- - y_-). \tag{2.48}$$

2.3.1 Sugawara Construction

One can try to re-write the free fermion Hamiltonian Eq.(2.29) in terms of chiral currents, defined in Eq.(2.30). This step it what lays as the foundation of the Abelian and non-Abelian bosonization - one starts with a fermionic theory and by implementing the Sugawara construction, rewrite the original model in terms of bosonic degrees of freedom.

To demonstrate the Sugawara construction, we concentrate on the right chiral sector first

$$J_R(x) J_R(x) =: R_x^\dagger R_x :: R_x^\dagger R_x : \tag{2.49}$$

Using point-splitting, we have

$$: R_x^\dagger R_x :: R_x^\dagger R_x := \lim_{\epsilon \to 0} : R_{x-\epsilon}^\dagger R_{x-\epsilon} :: R_{x+\epsilon}^\dagger R_{x+\epsilon} : . \tag{2.50}$$

We use Wick's theorem for the product of normal-ordered operators

$$: R_{x-\epsilon}^\dagger R_{x-\epsilon} :: R_{x+\epsilon}^\dagger R_{x+\epsilon} := : R_{x-\epsilon}^\dagger R_{x-\epsilon} R_{x+\epsilon}^\dagger R_{x+\epsilon} : - : R_{x-\epsilon}^\dagger R_{x+\epsilon} : \langle R_{x+\epsilon}^\dagger R_{x-\epsilon} \rangle$$
$$- : R_{x+\epsilon}^\dagger R_{x-\epsilon} : \langle R_{x-\epsilon}^\dagger R_{x+\epsilon} \rangle - \langle R_{x-\epsilon}^\dagger R_{x+\epsilon} \rangle \langle R_{x+\epsilon}^\dagger R_{x-\epsilon} \rangle. \tag{2.51}$$

Here we have to use the equal time correlator

$$\langle R_{x-\epsilon}^\dagger R_{x+\epsilon} \rangle = -\frac{i}{4\pi\epsilon}, \quad \langle R_{x+\epsilon}^\dagger R_{x-\epsilon} \rangle = \frac{i}{4\pi\epsilon} \tag{2.52}$$

and thus

$$: R_{x-\epsilon}^\dagger R_{x-\epsilon} :: R_{x+\epsilon}^\dagger R_{x+\epsilon} :=: R_{x-\epsilon}^\dagger R_{x-\epsilon} R_{x+\epsilon}^\dagger R_{x+\epsilon} : + \frac{i}{4\pi\epsilon} \left(: R_{x+\epsilon}^\dagger R_{x-\epsilon} : - : R_{x-\epsilon}^\dagger R_{x+\epsilon} : \right)$$
$$- \frac{2}{(4\pi\epsilon)^2}. \tag{2.53}$$

Firstly, we see that the last term is diverging as $\epsilon \to 0$. To avoid this divergence, we normally order the whole expression:

$$: \left(: R_{x-\epsilon}^\dagger R_{x-\epsilon} :: R_{x+\epsilon}^\dagger R_{x+\epsilon} : \right) :=: R_{x-\epsilon}^\dagger R_{x-\epsilon} R_{x+\epsilon}^\dagger R_{x+\epsilon} : + \frac{i}{4\pi\epsilon} \left(: R_{x+\epsilon}^\dagger R_{x-\epsilon} : - : R_{x-\epsilon}^\dagger R_{x+\epsilon} : \right). \tag{2.54}$$

The first term is vanishing, since $\lim_{\epsilon \to 0} : R_{x-\epsilon}^\dagger R_{x-\epsilon} R_{x+\epsilon}^\dagger R_{x+\epsilon} := \lim_{\epsilon \to 0} : R_{x-\epsilon}^\dagger R_{x+\epsilon}^\dagger R_{x-\epsilon} R_{x+\epsilon} := 0$. This way, we are left with

$$\int_0^L dx : J_R(x) J_R(x) := \frac{i}{4\pi} \int_0^L dx \lim_{\epsilon \to 0} \frac{1}{\epsilon} \left(: R^\dagger_{x+\epsilon} R_{x-\epsilon} : - : R^\dagger_{x-\epsilon} R_{x+\epsilon} : \right) \approx -\frac{i}{\pi} \int_0^L dx : R^\dagger \partial_x R : \tag{2.55}$$

Similarly, for the left chiral sector we have

$$\int_0^L dx : L^\dagger \partial_x L := -i\pi \int_0^L dx : J_L^2 : \tag{2.56}$$

Combining these results, we get

$$\mathrm{H}_0 = -iv_F \int_0^L dx \left(: R^\dagger \partial_x R : - : L^\dagger \partial_x L : \right) \to \pi v_F \int dx \left(: J_R^2 : + : J_L^2 : \right). \tag{2.57}$$

2.3.2   Bosonization dictionary

The striking result presented in Eq.(2.57) is that the free theory of Chiral Dirac *fermions* is equivalent to a *bosonic* theory of Chiral Currents, formally known as the Tomonaga-Luttinger liquid theory [29]. The equivalence of these two models is hidden in the fact that the correlation functions of these two models are identical, thus knowing the correlators of one model is identical to knowing the correlators of the second model and vice versa. In general, one could say that at this level the fermionic model has been completely bosonized, however Tomonaga-Luttinger model can be further expressed as a more familiar model of a quantum massless scalar field in 1+1 dimension

$$H = \frac{v}{2} \int dx \left(: (\partial_x \Theta)^2 : + : (\partial_x \Phi)^2 : \right). \tag{2.58}$$

The model of a scalar field respects the chiral decomposition

$$\Phi = \varphi_L + \varphi_R, \quad \Theta = \varphi_L - \varphi_R, \tag{2.59}$$

where the chiral fields obey the following commutation relations

$$[\varphi_R(x), \varphi_R(y)] = -[\varphi_L(x), \varphi_L(y)] = \frac{i}{4}\mathrm{sign}(x - y), \quad [\varphi_R(x), \varphi_L(y)] = \frac{i}{4} \tag{2.60}$$

then model can be written as

$$H = v \int dx \left(: (\partial_x \varphi_L)^2 : + : (\partial_x \varphi_R)^2 : \right) \tag{2.61}$$

this way, making a simple substitution $v_F \to v$ and a further identification

$$J_L =: L^\dagger L :\sim \frac{1}{\sqrt{\pi}} \partial_x \varphi_L, \quad J_R =: R^\dagger R :\sim \frac{1}{\sqrt{\pi}} \partial_x \varphi_R \tag{2.62}$$

one maps a fermionic theory to a bosonic one. Eq.(2.62) is incomplete, as it only demonstrates how one can express chiral densities in terms of bosonic fields. As we will see below, there exists other fermionic bilinears that can not be expressed using chiral densities. To see the connection between chiral fermionic operators $R(L)$ and chiral bosonic fields $\varphi_R(\varphi_L)$, one needs to implement the compactification of bosonic theory. The bosonic model Eq.(2.61) is invariant under $\varphi_{R,L} \to \varphi_{R,L} + c$ transformation, with c being a real number. On the other hand, the fermionic model respects $U(1)$ transformation in each chiral sector. Since the global symmetries (dictating such properties of the

models as topological excitations) of these two models have to be identical, one needs to compactify the bosonic theory, so that $\varphi_{R,L}$ now becomes an angular variable. Using these considerations, one deduces [27, 28, 39] that the relations between fermionic and bosonic fields are

$$R(x) \sim \frac{1}{\sqrt{2\pi\alpha}} e^{i\sqrt{4\pi}\varphi_R(x)}, \quad L(x) \sim \frac{1}{\sqrt{2\pi\alpha}} e^{-i\sqrt{4\pi}\varphi_L(x)}. \tag{2.63}$$

This way, Eqs.(2.62,2.63) form the so called *Abelian bosonization dictionary*. Using fermionic operators on the left-hand side and bosonic vertex operators on the right-hand side, this identification reproduces identical correlation functions within their respective models. It should be noted that these equations only represent a correspondence and should be used as an identity only while taking expectation values of corresponding operators. The bosonization technique will prove to be a powerful tool to solve models of interacting fermions in 1D, by mapping it to a bosonic theory. There is a wide variety of bosonic models that can emerge when bosonizing a fermionic theory, but one can use techniques such as Renormaliation Group (RG) and derive asymptotically exact result for bosonic and therefore for original fermionic theory. The bosonization technique is not restricted only to Abelian symmetry groups and can be further extended to non-Abelian groups, as demonstrated in Sec.(4) and Sec.(5)

2.3.3 Weak anisotropy case

As we have already seen, after using Jordan-Wigner transformation, the original XXZ heisenberg model maps onto a problem of interacting spinless fermions:

$$\tilde{H}_{\text{XXZ}}(\Delta) \to \hat{H}(\Delta) = H_0 + H_{\text{int.}}, \tag{2.64}$$

where the quadratic part is given by

$$H_0 = -\frac{J}{2} \sum_{i=1}^{N-1} \left(c_i^\dagger c_{i+1} + c_{i+1}^\dagger c_i \right) \tag{2.65}$$

and the interaction is

$$H_{\text{int.}} = J\Delta \sum_{i=1}^{L} \left(n_i - \frac{1}{2} \right) \left(n_{i+1} - \frac{1}{2} \right). \tag{2.66}$$

When Δ interaction is sufficiently small, we assume that the single-particle spectrum of the model is unchanged relative to the non-interacting case. Based on this assumption, one can pass to the low-energy description of the interacting model and adopt all the discussion from the previous sections:

$$H_0 = \pi v_F \int dx \left(: J_R^2 : + : J_L^2 : \right), \tag{2.67}$$

while for the interaction term we have

$$H_{\text{int}} = J\Delta\alpha_0 \int dx \left(\rho_x - \frac{1}{2} \right) \left(\rho_{x+\alpha_0} - \frac{1}{2} \right). \tag{2.68}$$

with $\rho(x) = c^\dagger(x)c(x)$. To avoid any diverging expectation values due to the infinite Fermi sea, one has to normal order the whole product. The density operator can be expressed as

$$\rho_x =: \rho_x : + \langle \rho_x \rangle =: \rho_x : + \frac{1}{2} \tag{2.69}$$

and thus we have

$$H_{\text{int}} = g \int dx : (: \rho_x :: \rho_{x+\alpha_0} :) :, \quad g \equiv J\Delta\alpha_0 = v_F\Delta \tag{2.70}$$

At this level, our goal is to rewrite H_{int} in terms of U(1) chiral currents, if possible. Using the Eq.(2.26) chiral decomposition of the continuous fermi field, we get

$$: \rho(x) := n_x + e^{2ik_F x} : L_x^\dagger R_x : + e^{-2ik_F x} : R_x^\dagger L_x : \tag{2.71}$$

where $n_x =: R_x^\dagger R_x : + : L_x^\dagger L_x :$. Using this equation, for the density-density interaction we get

$$: (: \rho_x :: \rho_{x+\alpha_0} :) :=: n_x n_{x+\alpha_0} : + \left[e^{2ik_F \alpha_0} : \left(: R_x^\dagger L_x :: L_{x+\alpha_0}^\dagger R_{x+\alpha_0} : \right) : + \text{h.c.} \right] + \mathcal{O}_{x,x+\alpha_0}^{\text{umklapp}}, \tag{2.72}$$

with

$$\mathcal{O}_{x,x+\alpha_0}^{\text{umklapp}} \equiv e^{4ik_F x} e^{2ik_F \alpha_0} : \left(: L_x^\dagger R_x :: L_{x+\alpha_0}^\dagger R_{x+\alpha_0} : \right) : + \text{h.c.}. \tag{2.73}$$

The problem with the so-called umklapp term $\mathcal{O}_{\text{umklapp}}$ is that it can not be expressed solely in terms of the chiral currents. As we have mentioned, that the pre-factor of this term is $e^{i4k_F x}$, which is *not* a rapidly oscillating term only when we are at half filling. The umklapp process describes the scattering of a pair of left(right)-movers into right(left)-moving fermions. During this process the transferred momentum is equal to $4k_F$ and should be consistent with momentum conservation. In a different setting of the model, being away from half filling ($k_F = \pi/2\alpha_0$), this would violate the momentum conservation. However, at half filling $4k_F = 2\pi/\alpha_0$, which is equal to the length of the Brillouin zone and thus the excess $4k_F$ momentum is transferred to the lattice vibrations. It is known, that for small $|\Delta| \ll 1$, the umklapp process renders to be irrelevant in the Renormalization group analysis [28]. For current discussions, we drop the umklapp term, since the case of study of this section is $|\Delta| \ll 1$. This way, we have

$$: (: \rho_x :: \rho_{x+\alpha_0} :) :=: n_x n_{x+\alpha_0} : - : \left(: R_x^\dagger L_x :: L_{x+\alpha_0}^\dagger R_{x+\alpha_0} : \right) : - : \left(: L_x^\dagger R_x :: R_{x+\alpha_0}^\dagger L_{x+\alpha_0} : \right) :$$
$$\tag{2.74}$$

The first term can be easily recognized as

$$: n_x n_{x+\alpha_0} :=: (J_L + J_R)_x (J_L + J_R)_{x+\alpha_0} : . \tag{2.75}$$

For the second term, using Wick's theorem, yields

$$: \left(: R_x^\dagger L_x :: L_{x+\alpha_0}^\dagger R_{x+\alpha_0} : \right) :=- : R_x^\dagger R_{x+\alpha_0} L_{x+\alpha_0}^\dagger L_x :$$
$$- : R_x^\dagger R_{x+\alpha_0} : \langle L_{x+\alpha_0}^\dagger L_x \rangle - : L_{x+\alpha_0}^\dagger L_x : \langle R_x^\dagger R_{x+\alpha_0} \rangle \tag{2.76}$$

Using the equal time limit of two-point correlation functions Eqs.(2.41,2.45), we get

$$: \left(: R_x^\dagger L_x :: L_{x+\alpha_0}^\dagger R_{x+\alpha_0} : \right) := - : R_x^\dagger R_{x+\alpha_0} L_{x+\alpha_0}^\dagger L_x :$$
$$+ \frac{i}{2\pi\alpha_0} \left(: R_x^\dagger R_{x+\alpha_0} : + : L_{x+\alpha_0}^\dagger L_x : \right) \tag{2.77}$$

By expanding the last term in terms of the lattice constant α_0, we get

$$: \left(: R_x^\dagger L_x :: L_{x+\alpha_0}^\dagger R_{x+\alpha_0} : \right) :\approx - : R_x^\dagger R_x L_x^\dagger L_x : - \frac{i}{2\pi} \left(: L_x^\dagger \partial_x L_x : - : R_x^\dagger \partial_x R_x : \right)$$
$$+ \frac{i}{2\pi\alpha_0} \left(L_x^\dagger L_x : + : R_x^\dagger R_x : \right) \tag{2.78}$$

Similarly, we have

$$: \left(: L_x^\dagger R_x :: R_{x+\alpha_0}^\dagger L_{x+\alpha_0} : \right) :\approx - : R_x^\dagger R_x L_x^\dagger L_x : - \frac{i}{2\pi} \left(: L_x^\dagger \partial_x L_x : - : R_x^\dagger \partial_x R_x : \right)$$
$$- \frac{i}{2\pi\alpha_0} \left(: L_x^\dagger L_x : + : R_x^\dagger R_x : \right). \tag{2.79}$$

The sum of these two terms in he chiral current representation is

$$: \left(: R_x^\dagger L_x :: L_{x+\alpha_0}^\dagger R_{x+\alpha_0} : \right) : + : \left(: L_x^\dagger R_x :: R_{x+\alpha_0}^\dagger L_{x+\alpha_0} : \right) := - : J_R^2 : - : J_L^2 : -2J_R J_L. \tag{2.80}$$

Overall, we have

$$: \left(: \rho(x) :: \rho(x+\alpha_0) : \right) := : (J_L + J_R)_x (J_L + J_R)_{x+\alpha_0} : + : J_R^2 : + : J_L^2 : +2J_R J_L$$
$$= 2\left(: J_R^2 : + : J_L^2 : \right) + 4J_R J_L \tag{2.81}$$

This way, the whole weakly interacting model, being quartic in terms of *fermionic* operators, in terms of *bosonic* the chiral currents becomes a quadratic, the so called Tomonaga-Luttinger liquid model

$$\mathrm{H} = (\pi v_F + 2g) \int dx \left(: J_R^2 : + : J_L^2 : \right) + 4g \int dx J_R J_L$$
$$= \frac{\pi v}{2} \int dx \left(K : (J_R - J_L)^2 : + \frac{1}{K} : (J_R + J_L)^2 : \right) \tag{2.82}$$

$$K \approx 1 - \frac{2\Delta}{\pi}, \quad v \approx v_F \left(1 + \frac{2\Delta}{\pi} \right) \tag{2.83}$$

Here v is the renormalized fermi velocity and K is the so-called Luttinger parameter. It should be noted that the exact value of Luttinger parameter is known from the Bethe Ansatz solution [28]

$$K = \frac{\pi}{2(\pi - \arccos \Delta)}, \tag{2.84}$$

and thus our results match the exact one in $|\Delta| \ll 1$ limit.

Using a canonical transformation that preserves the Kac-Moody algebra of the currents, one can further diagonalize the perturbed Tomonaga-Luttinger model. By parametrizing the transformation

with a single parameter θ as

$$J_L = \cosh{(\theta)}\,\tilde{J}_L + \sinh{(\theta)}\,\tilde{J}_R, \quad J_R = \sinh{(\theta)}\,\tilde{J}_L + \cosh{(\theta)}\,\tilde{J}_R, \quad \theta = \frac{1}{2}\ln(K) \approx -\frac{\Delta}{\pi} \qquad (2.85)$$

gives

$$\mathrm{H} = \frac{\pi v}{2}\int dx\left(: (\tilde{J}_R - \tilde{J}_L)^2 : + : (\tilde{J}_R + \tilde{J}_L)^2 :\right) \qquad (2.86)$$

2.3.4   Full bosonization of XXZ model

As we have shown in the previous section, the XXZ model express in terms of Chiral currents is

$$\mathrm{H} = (\pi v_F + 2g)\int dx\left(: J_R^2 : + : J_L^2(x) :\right) + 4g\int dx J_R J_L + g\int dx \mathcal{O}_{x,x+\alpha_0}^{\mathrm{umklapp}}. \qquad (2.87)$$

Using bosonization dictionary Eq.(2.62) for first two terms, we can write

$$\mathrm{H} \sim \frac{(\pi v_F + 2g)}{\pi}\int dx\left(: (\partial_x \varphi_L)^2 : + : (\partial_x \varphi_R)^2 :\right) + \frac{4g}{\pi}\int dx \partial_x \varphi_L \partial_x \varphi_R + g\int dx \mathcal{O}_{x,x+\alpha_0}^{\mathrm{umklapp}}. \quad (2.88)$$

Before dealing with the umklapp term, we pass from chiral to canonical fields Φ and Θ, which gives

$$\mathrm{H} \sim \frac{v_F}{2}\int dx\left(: (\partial_x\Theta)^2 : + \left(1 + \frac{4g}{\pi v_F}\right): (\partial_x\Phi)^2 :\right) + g\int dx \mathcal{O}_{x,x+\alpha_0}^{\mathrm{umklapp}}. \qquad (2.89)$$

Since we are at half filling, we have

$$\mathcal{O}_{x,x+\alpha_0}^{\mathrm{umklapp}} \equiv - : L_x^\dagger R_x L_{x+\alpha_0}^\dagger R_{x+\alpha_0} : - : R_x^\dagger L_x R_{x+\alpha_0}^\dagger L_{x+\alpha_0} : . \qquad (2.90)$$

By implementing the bosonization dictionary Eq.(2.63), we get

$$\mathcal{O}_{x,x+\alpha_0}^{\mathrm{umklapp}} \sim \frac{1}{(2\pi\alpha)^2}\left(: e^{i\sqrt{4\pi}(\Phi(x)+\Phi(x+\alpha_0))} : + \mathrm{h.c.}\right) \approx \frac{1}{2(\pi\alpha)^2} : \cos(\sqrt{16\pi}\Phi) : \qquad (2.91)$$

where we have used the Baker–Campbell–Hausdorff formula and Eq.(2.60) commutators. This way, the bosonized version of XXZ model is

$$\mathrm{H} \sim \frac{v_F}{2}\int dx\left(: (\partial_x\Theta)^2 : + \left(1 + \frac{4g}{\pi v_F}\right): (\partial_x\Phi)^2 :\right) + \frac{g}{2(\pi\alpha)^2}\int dx : \cos(\sqrt{16\pi}\Phi) : \qquad (2.92)$$

To bring the equation to a canonical form, we re-scale the fields as

$$\Phi = \sqrt{K}\phi, \quad \Theta = \frac{1}{\sqrt{K}}\theta \qquad (2.93)$$

which gives

$$\mathrm{H} \sim \frac{v_F}{2}\int dx\left(\frac{1}{K} : (\partial_x\theta)^2 : + K\left(1 + \frac{4g}{\pi v_F}\right): (\partial_x\phi)^2 :\right) + \frac{g}{2(\pi\alpha)^2}\int dx : \cos(\sqrt{16\pi K}\phi) : \quad (2.94)$$

If we constrain K as

$$K = \frac{1}{\sqrt{1 + \frac{4g}{\pi v_F}}} \approx 1 - \frac{2g}{\pi v_F} = 1 - \frac{2\Delta}{\pi} \tag{2.95}$$

then we get

$$\mathrm{H} \sim \frac{\tilde{v}_F}{2} \int dx \left(: (\partial_x \theta)^2 : + : (\partial_x \phi)^2 : \right) + \frac{g}{2(\pi \alpha)^2} \int dx : \cos(\sqrt{16\pi K}\phi) : \tag{2.96}$$

with renormalized Fermi-velocity

$$\tilde{v}_F = \frac{v_F}{K}. \tag{2.97}$$

This way, we see that XXZ model is mapped onto a well studied sine-Gordon model [28]. The relevancy of the cosine perturbation is dictated by the value of K Luttinger parameter, since the scaling dimension of the perturbation is

$$\Delta_{\cos} = 4K. \tag{2.98}$$

Since the anisotropy parameter of the model Δ is small, we get that the scaling dimension of the perturbation is always larger than 2 and thus is always irrelevant, unless one artificially extends the solution for larger values of Δ, where the bosonization scheme is not applicable anymore. Due to this, XXZ model for a weak anisotropy parameter Δ, positive or negative, is always critical and is described by a Gaussian model. In the language of CFT, this means that the theory is scale invariant and has a central charge of $c = 1$.

One may use the bosonizaton technique to express the order parameters in terms of bosonic fields. $S^z(x)$ component of spin in the continuum limit is equivalent to a fermion density operator Eq.(2.71):

$$S_j^z \rightarrow \alpha_0 S^z(x) \approx \alpha_0 \rho(x), \quad \rho(x) = J_R(x) + J_L(x) + (-1)^{x/\alpha_0} N(x) \equiv \rho_x^{\mathrm{smooth}} + (-1)^{x/\alpha_0} \rho_x^{\mathrm{stag.}}, \tag{2.99}$$

where we have used the fact that $k_F = \frac{\pi}{2\alpha_0}$. Using bosonization dictionary, we get

$$S^z(x) \sim \sqrt{\frac{K}{\pi}} \partial_x \phi(x) + \frac{(-1)^{x/\alpha_0}}{\pi \alpha} : \sin \sqrt{4\pi K} \phi(x) : \tag{2.100}$$

This expression can be useful, for instance, to express the spin-spin correlation function. Since the weak coupling $|\Delta| \ll 1$ theory asymptotically corresponds to a Gaussian model, the expectation values of the fields are zero, however two-point correlation functions show a power-law decays. The smooth part of the density operator gives

$$G_{x,y}^{\mathrm{smooth}} = \langle \rho_x^{\mathrm{smooth}} \rho_y^{\mathrm{smooth}} \rangle \sim \frac{1}{|x - y|^2}, \tag{2.101}$$

with a universal critical exponent 2, while the staggered part gives

$$G_{x,y}^{\mathrm{stag.}} = \langle \rho_x^{\mathrm{stag.}} \rho_y^{\mathrm{stag.}} \rangle \sim \frac{1}{|x - y|^{2K}}, \tag{2.102}$$

where the critical exponent of the staggered part depends on the anisotropy parameter Δ. The smooth and the staggered part of the correlation functions properly extend Eq.(2.17) exact result of $\Delta = 0$ to the case of small anisotropy $|\Delta| \ll 1$.

As we have already mentioned, XXZ model has been solved exactly using Bethe ansatz and the

whole phase diagram has been extracted [29]. It has been shown that XXZ model remains critical for the whole $-1 < \Delta < +1$ region and the critical line terminate with fully SU(2) points at $\Delta = \pm 1$. Moreover, when one crosses $\Delta = +1$ point, the system undergoes Berezinskii-Kosterlitz-Thouless transition to a gapped anti-Ferromagnetically ordered phase. On the other hand, crossing $\Delta = -1$ corresponds to a first order phase transition to a ferromagnetically ordered phase.

2.4   Phenomenological Bosonization

In the previous section, we have introduced the Abelian bosonization and demonstrated the predictive power of it in the context of Heisenberg XXZ, or equivalently, in the context of weakly interacting spinless fermions on 1D chain. The validity of the method strongly depends on the assumption that the weak interaction does not modify the single-particle spectrum of the non-interacting theory. One of the necessary conditions for the Abelian bosonization to be applicable is the existence of linear spectrum in the vicinity of k_F Fermi momentum (this condition also extends to non-Abelian bosonization too). This, however, is not guaranteed when one passes to the limit of strong interactions. In this regime, one has to rely on the so-called phenomenological bosonization [39, 40]

The idea of phenomenological bosonization is based on the density-phase representation of particle creation and annihilation operators. We start with bosonic fields. A bosonic field can be represented as

$$\psi(x) = e^{i\theta(x)}\sqrt{\rho(x)} \tag{2.103}$$

where $\rho = \psi^\dagger\psi$ is the particle density operator. Using this relation, one can derive the commutation relations between the density and phase variables. The commutation relation for the Bosonic field ψ is

$$\psi(x)\psi^\dagger(y) - \psi^\dagger(y)\psi(x) = \delta(x - y) \tag{2.104}$$

By multiplying both sides by $\psi^\dagger(x)$ from the right and using Eq.(2.103), we get

$$[\rho(x), e^{-i\theta(y)}] = \delta(x - y)e^{-i\theta(y)}. \tag{2.105}$$

Furthermore, by using the Taylor series for $e^{i\theta(y)}$ exponent and $[A, B^n] = nB^{n-1}[A, B]$ identity, we get

$$i\sum_{n=0}^{+\infty}\frac{i^n}{n!}\theta^n(y)[\rho(x), \theta(y)] = \sum_{n=0}^{+\infty}\frac{i^n}{n!}\delta(x - y)\theta^n(y) \tag{2.106}$$

which is satisfied only if

$$[\rho(x), \theta(y)] = i\delta(x - y). \tag{2.107}$$

This way we see that the phase and the density operator are mutually conjugate variable and satisfy canonical bosonic commutation relation.

Now we move to a concrete example, where the bosonic particles are distributed along 1D chain with α_0 lattice constant. If the position of nth particle is x_n, then the density operator of such distribution is

$$\rho(x) = \sum_n \delta(x - x_n). \tag{2.108}$$

The position x_n can be represented as $x_n = x_n^0 + \delta x_n$, where $x_n^0 = n\alpha_0$ is the equilibrium configuration and δx_n is the displacement of nth particle. If $\delta x_n = 0$ for every n, then the particles form a perfect lattice and the average density of particles is $\rho_0 = 1/\alpha_0$. Instead of working directly with the coordinate label x_n, it is more convenient to introduce a field $\phi(x)$ that takes the values $2\pi n$ when $x = x_n$. Using the new labeling of the coordinates of the particles, one can re-write the

density operator as

$$\rho(x) = \sum_n |\nabla\phi(x)|\delta(\phi(x) - 2\pi n). \tag{2.109}$$

Without loss of generality, one can choose $\nabla\phi(x) > 0$ for all x. Using the Poisson summation formula, we get

$$\rho(x) = \frac{\nabla\phi(x)}{2\pi} \sum_p e^{ip\phi(x)}, \quad p \in \mathbb{Z} \tag{2.110}$$

At this point, one can draw a similarity between Abelian bosonization and phenomenological bosonization - since we are interested in the fluctuations above the perfect configuration of particles, we single out ρ_0 contribution from $\rho(x)$ as

$$\phi(x) = 2\pi\rho_0 x - 2\varphi(x), \tag{2.111}$$

which gives

$$\rho(x) = \left(\rho_0 - \frac{\nabla\varphi(x)}{\pi}\right) \sum_p e^{i2p(\pi\rho_0 x - \varphi(x))}. \tag{2.112}$$

Plugging Eq.(2.112) in Eq.(2.107), we get

$$\left[\frac{\nabla\varphi(x)}{\pi}, \theta(y)\right] = -i\delta(x - y). \tag{2.113}$$

This way we see that, θ and $\frac{\nabla\varphi(x)}{\pi}$ are the canonically conjugate variables and by integrating the commutator, we get

$$\Pi = \frac{1}{\pi}\nabla\theta, \tag{2.114}$$

where Π is the canonically conjugate momentum to φ. This way, the phenomenological bosonization establishes the connection between bosonic field operators ψ and canonically conjugate variables θ, φ:

$$\psi(x) = e^{i\theta(x)}\sqrt{\rho_0 - \frac{\nabla\varphi(x)}{\pi}} \sum_p \alpha_p e^{i2p(\pi\rho_0 x - \varphi(x))} \tag{2.115}$$

where α_p is a non-universal constan, related to the fact that one needs to take the sqaure root of $\rho(x)$ to obtain the final result. It should be noted, that to phenomenologically bosonize the fermionic operators, one has to simply change $2p \to 2p + 1$ in the exponent in Eq.(2.115). It should be noted that the phenomenological bosonization dictionary and the Abelian bosonization dictionary Eq.(2.63) yield qualitatively the same result.

Being equipped with Eq.(2.115) equation, one can derive the corresponding field theory of the microscopic model, which will necessarily be written in terms of θ and φ fields. For the sake of demonstration, it is simple to see that the most RG-relevant contributions $(\nabla\varphi)^2$ and $(\nabla\theta)^2$ can be generated through density-density interaction and kinetic energy terms, respectively. The general symmetry considerations narrow down the allowed terms in the theory, for instance if the system has inversion symmetry $x \to -x$, then mixed terms like $\nabla\varphi\nabla\theta$ are forbidden. This way, the allowed

terms to the quadratic part of the theory is always

$$\mathrm{H}_0 \approx \frac{v}{2} \int dx \left(K(\nabla\theta)^2 + \frac{1}{K}(\nabla\varphi)^2 \right) \tag{2.116}$$

where v and K are the effective velocity and an effective Luttinger parameter of the Gaussian model. The Gaussian part is then perturbed by an infinite hierarchy of all allowed operators in the theory, corresponding to various harmonics p in Eq.(2.115). In case of a massless one-dimensional system, all of these perturbing operators are irrelevant or rapidly oscillating, thus the quadratic model remains quadratic. Since the Gaussian model is exactly solvable, one can extract all of the power-law correlation functions of the theory. However, v and K are renormalized by the aforementioned perturbing operators and thus their values strongly depend on the unknown microscopic details of the model. Due to this reason, it is impossible to determine the real values of the velocity and the Luttinger parameter and one has to rely on the numerical results. Though the result is generic and straightforward for isolated 1D chains, the phenomenological bosonization can play a crucial role to determining the possible perturbations of Gaussian model, if one couples 1D chains into 2 or multiple-leg ladders.

2.4.1   Cluster Bosonization

It should be emphasized, that the phenomenological bosonization is not bound to be used only in the context of single particle objects, as it was done in Eq.(2.108). One might encounter many-body setups, where particles group up as clusters to minimize the energy due to interaction [20, 21]. In general, the clusters can consist of different number of particles. For such scenarios, phenomenological bosonization needs to be generalize to account such composite objects. Below we review such a generalization, referred to as cluster bosinization,

To obtain the dictionary for cluster bosonization, we reformulate the density distribution $\rho(x)$ by coarse graining the particle distribution into the clusters. The corresponding cluster density distribution for is

$$\rho(x) = \sum_{m=1}^{M} f(x_m)\delta(x - x_m), \tag{2.117}$$

where M is the number of clusters in the system and x_m is the coarse grained coordinate of the cluster, while $f(x_m)$ counts the number of particles in the corresponding cluster. By construction, $\sum_{x_m} f(x_m) = N$ where N is the conserved total number of particles. As before, we define the cluster field $\phi(x)$ accounting for the quantum fluctuations of the cluster density. By construction, the cluster field is strictly monotonic and an integer multiple of π at the center of a cluster: $\phi(x_m) = \pi m$ with $m \in \mathbb{Z}$, such that

$$\rho(x) = \nabla\phi(x) \sum_{m=1}^{M} f(x_m)\delta(\phi(x) - \pi m). \tag{2.118}$$

For the system of length L and periodic boundary conditions, we extend Eq.(2.118) over all space. We set $\phi(x + L) = \phi(x) + M\pi$, such that for $j = nM + m$ with $1 \le m \le M$ and $n \in \mathbb{Z}$, we get $x_j = x_m$ modulo L, and we take $I_{\pi M}$ as the unit Dirac comb of periodicity πM. Then the L-periodic Eq.(2.118) is

$$\rho(x) = \nabla\phi(x) \sum_{j=-\infty}^{+\infty} f(x_j) I_{\pi M}(\phi(x) - \pi j) = \frac{N}{M}\nabla\phi(x) \sum_{q=-\infty}^{+\infty} \frac{A_q}{\pi} e^{-i2q\phi(x)}, \tag{2.119a}$$

where we have used Poisson's summation, and defined NA_q, $q \in \mathbb{Z}$, as the Fourier coefficients of $f(x_j)$, a function of j of period M. The coefficients $A_q = A^*_{-q}$ are not universal and depend on the microscopic details of the model.

In the density-angle variables formalism, we define the amplitude of the cluster bosonic field as the square-root of the coarse grained (or cluster) density, and the cluster angle is the associated canonical conjugate variable. To construct these fields, we introduce $\phi'(x)$ [1] as

$$\phi(x) = \pi\nu\sigma x - \sqrt{\pi}\phi'(x), \tag{2.120}$$

where $\sigma = M/N$ and $\nu = N/L$. The cluster density operator is

$$\rho(x) = \left(\nu - \frac{1}{\sqrt{\pi}\sigma}\nabla\phi'(x)\right) \sum_{q=-\infty}^{+\infty} A_q e^{-i2q(\pi x \sigma \nu - \sqrt{\pi}\phi'(x))}. \tag{2.121}$$

We define $\theta'(x)$ as the conjuguate variable of $\nabla\phi'(x)$ such that

$$\left[\theta'(y), \frac{1}{\pi}\nabla\phi'(x)\right] = i\delta(x-y). \tag{2.122}$$

We deduce the expression for the cluster bosonic field $\psi(x)$ in the density-angle formulation

$$\psi(x) = e^{-\frac{i\sqrt{\pi}}{\sigma}\theta(x)}\sqrt{\nu - \frac{1}{\sqrt{\pi}\sigma}\nabla\phi(x)} \sum_{q=-\infty}^{+\infty} \alpha_q e^{-i2q(\pi x \sigma \nu - \sqrt{\pi}\phi'(x))}, \tag{2.123}$$

where α_q are the non-universal Fourier coefficients of the square root of the sum in Eq.(2.121).

As for conventional phenomenological bosonization, using Eqs.(2.121,2.123) one can extract the effective bosonic field theory for cluster degrees of freedom. However, as before, the predictive power of cluster bosonization is also limited and can only be used to deduce the possible relevant perturbations to the theory. Once the phenomenlogical field theory is extracted, one has to supplement the results with numerical simulations. As we will see in Sec.(4) and Sec.(5), cluster bosonization can generate non-trivial perturbations to the massless bosonic theory. Moreover, using numerical simulations we will see that these perturbations can indeed be relevant within certain regimes of parameters.

It is worth concluding this chapter with few historical facts about the development of bosonization [41]. In the context of condensed matter physics, in 1933-34 Felix Bloch showed that the excitation spectrum of a 3-dimensional degenerate Fermi gas was entirely accounted by the density fluctuations [42, 43]. Due to this, he deduced that the properties of the many-body fermionic system could be approximately determined by far less number of bosonic degrees of freedom. Motivated by this and by further developments by Pascual Jordan [44, 45, 46, 47, 48, 49], Sin-itiro Tomonaga managed to fully describe the properties of a 1-dimensional Fermi gas by using only the density operators, bosonic in nature [50]. Based on the advancements by Joaquin Luttinger [51], Daniel Mattis and Elliot Lieb [52] – in 1974 Alan Luther, together with Victor Emery and Ingo Peschel, demonstrated the equivalence between the bosonic Sine-Gordon model and the fermionic backscattering Luttinger model [53, 54]. A year later, particle physicist Sidney Coleman showed that the quantum Sine-Gordon model, a theory of interacting mesons and the Thirring model of interacting massive fermions were equivalent [55]. Being unaware that the Thirring model of interacting massive fermions was known as the backscattering Luttinger model in the condensed matter physics community, he later famously wrote in his paper:

---

[1]We used the factor $\sqrt{\pi}$ in Eq.(2.120) to follow the convention chosen for Abelian bozonisation.

We (Luther and himself) are also united in our embarrassment that we were incapable of reaching this conclusion unprompted. (Our offices are on the same corridor.)

The work done by Coleman demonstrates the direct equivalence between bilinears of fermionic fields and bosonic operators. Exactly one month later, Stanley Mandelstam published a paper where he establishes direct correspondence between fermionic and bosonic field operators [56] – laying the foundation of mathematically rigorous Abelian bosonization. In the seminal work of 1984, Edward Witten developed non-Abelian bosonization [57]. For further reading, one can address some of well known review articles [58, 59, 60], and for more in-depth exploration, consider the following famous books [28, 29, 39, 41, 58, 61].

Chapter 3

Synthetic Quantum Systems

Strongly correlated many-body quantum systems can exhibit many exotic and useful features. These features can arise from various geometrical properties of the system or, most notably, due to the rich variety of interactions between the constituents of the system. However, the same interactions is what makes the problem of strongly correlated systems difficult to solve analytically. For past decades, overcoming this difficulty has attracted attention of many physicist, leading to the development of various analytical tools to find exact or approximate solutions of the corresponding problems [27, 28, 39]. However, frequently the problem becomes intractable analytically and one has to rely on numerical simulations instead, which typically becomes computationally expensive as the size of the system increases. The attempts to overcome the complication of numerical simulations has lead to the birth of different approaches, most notably Density Matrix Renormalization Group method (DMRG) [62, 63, 64, 65] which has proven to be powerful tool to study many-body physics in 1-dimensional systems and ladders. However, numerical algorithms come with limitations and only offer applicability for very specific regimes.

A straightforward but hard way to proceed would be to experimentally study a system, whose microscopic description coincides with the many-body quantum model of our interest. However, it is easy to guess, that such systems rarely exist. An interesting and useful alternative is to experimentally synthesize a quantum system and fine tune it's the microscopic details, so that it simulates the desired many-body system. Recent advances in modern experimental physics and quantum information has lead to the creation of the so-called quantum simulators [66]. One of the famous and successful representatives of such simulators are the Rydberg atoms trapped in optical potentials [1, 2, 3, 4, 5, 6].

In this chapter, we introduce basic concepts of Rydberg atom quantum simulators, and discuss some of the many-body problems that can be addressed in these experiments.

3.1 Rydberg atoms

A natural building block of a many-body system is an atom, which in turn is a many-body system itself. However, there are certain elements that can be further simplified and described with a reasonable accuracy as hydrogen-like atoms. These elements are the so-called Alkali metals, where the outer shell is occupied by a single electron, while the core electrons partially screen the nucleus of the atom. This way, one may think of an Alkali metal atom as a Hydrogen-like atom. The Hydrogen atom problem has been solved nearly a century ago, thus one can use the results straightforwardly. The deviations from Hydrogen-like properties can be accounted for using the framework of quantum defect theory [67].

The energy spectrum of a Hydrogen-like atom consists of two regions - for $E > 0$, the continuum of energy states correspond to ionized atom, while for $E < 0$, electron is in a bound state with the atom, with quantized energy states

$$E_n = -\frac{R_{\text{atom}}}{n^2}, \quad n \in \mathbb{N} \tag{3.1}$$

with $R_{\text{atom}} = R_\infty/(1 + m_e/m_{\text{atom}}) \simeq R_\infty \sim 10^7 \text{meter}^{-1}$, were m_e and m_{atom} are the electron and the atom masses, respectively. The energy spectrum only depends on n principal quantum number, while it does not depend on azimuthal quantum number l and m the magnetic quantum number.

An important property of hydrogen-like atoms is that the orbital radius r_{eff}, i.e. effective size of an atom, scales as $\sim n^2$. If one manages to excite the system to the state with relatively large n, called the Rydberg state, then the effective size of an atom can become macroscopically large, of order of $10 - 100nm$ [68]. The Rydberg states are essential building block of modern quantum simulators, due to their large dipole moments and the controlability.

The atom can possess an angular momentum $\mathbf{I}$, which can have three different origins: orbital angular momentum $\mathbf{L}$, electron spin $\mathbf{S}$ and the spin of the nucleus $\mathbf{J}$. The Hamiltonian of the simplified atom model commutes with all three types of angular momentum operators, thus leading to a degeneracy of the energy of the state with respect to corresponding quantum numbers - for the case of orbital angular momentum $\mathbf{L}$, that is l and m quantum numbers. This degeneracy can be lifted if one introduces the relativistic corrections to the model, lifting the degeneracy related to l and m [69], or introduce external symmetry breaking terms such as magnetic field that splits the energy degeneracy with respect to electronic and nuclear spin. Suppose we apply the external magnetic field along z direction $\mathbf{B} = B\mathbf{z}$, then additional term to the Hamiltonian will be

$$\text{H}' = -\mu_B \left(g_J S_z - g_N J_z \right) B \tag{3.2}$$

where μ_B is the Bohr magneton, while g are the Landé g-factors [70]. If the external field is small, then one obtains the Zeeman splitting of the degenerate energy levels. Taking the advantage of the level splitting, one can precisely address the desired energy states and use them for quantum simulations.

3.2 Jaynes–Cummings model

As we have seen in the previous chapter, by applying an external magnetic fields, one may obtain even richer energetic spectrum of an atom. Accessing individual states and driving transitions among them can turn an atom into a useful playground for quantum simulations.

Suppose than one applies an external driving force (e.g. electro-magnetic field) to an atom in a way that it amplifies the transitions between the ground state $|g\rangle$ and some excited state $|e\rangle$, while all the transitions between other states are strongly suppressed. In this regime, the atom can be approximated as a two level system. This is possible in a single-mode cavity, where a radiation mode with frequency ω drives an atomic transitions with a Rabi frequency Ω. This simplified model has to be supplemented with an assumption, that the motion of atom is negligible, i.e. the average kinetic energy of the atom is much smaller than $\hbar\Omega$. If this assumption is violated, then the atomic motion can strongly influence the dynamics of coherent atom-light interaction. Suppose that the kinetic energy of the atom is purely thermal energy $E_{\text{kin.}} \sim k_B T$. In a typical setups, the Rabi frequency is of order $\Omega \sim 10^6$ Hz. This way, if we need the average kinetic energy of the atom to be smaller than $\hbar\Omega$, than one needs to cool down the system $T \ll T^*$, with $T^* \sim 10^{-5}K$ being the upper threshold temperature when $k_B T^* \sim \hbar\Omega$. In this model, the Hamiltonian splits into three parts:

$$\text{H} = \text{H}_{\text{atom}} + \text{H}_{\text{int.}} + \text{H}_{\text{field}}. \tag{3.3}$$

By setting the ground state energy of the atom to zero, one gets

$$\text{H}_{\text{atom}} = \hbar\omega_e |e\rangle\langle e|. \tag{3.4}$$

The field Hamiltonian consist of the photon creation $a^\dagger$ and annihilation a operators:

$$H_{\text{field}} = \hbar\omega a^\dagger a. \tag{3.5}$$

Since we want to the most simple case of study of $H_{\text{int.}}$, we limit ourselves with the interaction of the electric field in the cavity, that is $E \sim a + a^\dagger$, with the electric dipole moment of the atom $\mu = |e\rangle\langle g| + |g\rangle\langle e|$. In this limiting case, the interaction hamiltonian will be

$$H_{\text{int.}} = \frac{\hbar\Omega}{2}\left(|e\rangle\langle g|(a + a^\dagger) + \text{h.c.}\right). \tag{3.6}$$

The interaction hamiltonian contains two types of processes: $|e\rangle\langle g|a^\dagger$ describes the process when a photons is emitted and the atom decays to the ground state (combined with the hermitian conjugate process) and $|e\rangle\langle g|a$, where the photon is absorbed and the system relaxes to the ground state. The second kind of processes is strongly suppressed, since the energy cost is $\Delta E = \hbar\omega_e + \hbar\omega$ and thus in the rotating wave approximation $\Omega \ll \omega_e + \hbar\omega$ we can completely neglect it. This approximation is valid if one couples the atom to optical radiation - in this case $\omega \sim 10^{14}$ Hz and $\Omega \sim 10^6$ Hz. These assumptions lead to the so called Jaynes-Cummings model, described by the following hamiltonian

$$H_{\text{JC}} = \hbar\omega_e\frac{1 + \sigma^z}{2} + \frac{\hbar\Omega}{2}\left(\sigma^+ a + \sigma^- a^\dagger\right) + \hbar\omega a^\dagger a \tag{3.7}$$

with

$$\mathbb{I} = |e\rangle\langle e| + |g\rangle\langle g|, \quad \sigma^z = |e\rangle\langle e| - |g\rangle\langle g|, \quad \sigma^+ = |e\rangle\langle g|, \quad \sigma^- = |g\rangle\langle e|. \tag{3.8}$$

3.3 Rydberg atom quantum simulators

Over the last ten years, ensembles of ground-state atoms laser-coupled to Rydberg states in optical lattices have shown outstanding aptitudes for realizing strongly interacting quantum dynamics under controlled and tunable experimental conditions [1, 2, 3, 4, 5, 6, 7]. For example, a weak coupling between the ground state and the Rydberg states [16, 17, 18, 19] (the Rydberg-dressing) generates an effective long-range two-body interaction with a short-range plateau (the soft-shoulder potential [9]) and a power-law tail (van der Waals). The range of the plateau may reach a few microns such that probing the single-site level is easier than conventional cold atoms systems operating in Hubbard-like regimes. For a single scalar bosonic field in 1D, such an interaction induces exotic critical behaviour such as cluster Luttinger liquids (CLL) where the Luttinger theorem is inapplicable [20] and supersymmetric (SUSY) quantum critical points [21]. In 2D systems, it is associated with anomalous dynamics and glassy behavior [22, 23].

The atom in the Rydberg state has orders of magnitude larger dipole moment, compared to the one in the ground state. One may take the advantage of this fact and try to synthetically engineer quantum systems, where the strong and long-range dipole-dipole interaction between electrically neutral atoms in the Rydberg state gives the possibility to simulate exotic many-body systems. A typical experimental setup would be cold atoms trapped in optical lattices, where one can carefully access and select the suitable Rydberg states within each atom by shining them with lasers.

In what follows, we discuss two possible setups of Rydberg atom quantum simulators. Though constituents of these two setups are the same, the different operational regimes yields qualitatively different behavior of atoms.

3.3.1 Rydberg atoms in the frozen regime

Suppose that one deals with a many-atom setup, were each atoms is held in place by optical tweezers, thus strongly suppressing the spatial delocalization. Then one can shine a laser to each atom, with Rabi frequency Ω and detuning $\Delta = \omega_e - \omega$, coupling the ground state and the desired Rydberg state. This setup can be effectively described by the Jaynes–Cummings model, where the photonic part is in a coherent state. This way, the corresponding Hamiltonian for non-interacting atoms becomes

$$\mathrm{H}_0 = \hbar \sum_i \left(\Delta n_i + \Omega \sigma_i^x \right), \quad n_i = \frac{1 + \sigma_i^z}{2}. \tag{3.9}$$

For simplicity we assume that every atom is coupled to the same Rydberg state. Apart the single-particle contribution, one includes the interactions between the atoms as well. As we already know, for hydrogen-like atoms (e.g. alkali metals), the average distance between the nucleus and the electron scales as $r_{\mathrm{eff}} \sim n^2$, n being the principal quantum number of the state, leading to large dipole moments for $n \gg 1$ Rydberg states. Due to this, two atoms in the Rydberg state can interact with eachother via dipole-dipole interaction, that extends over the distances much larger than the typical lengthscales associated with electronic wavefunctions. The interaction term in the hamiltonian would be

$$\mathrm{H}_{\mathrm{int}} = \sum_{i,j} V_{i,j} \frac{\hat{\mu}_i \hat{\mu}_j}{R_{ij}^3}, \tag{3.10}$$

where R_{ij} is the distance between i^{th} and j^{th} atoms and V_{ij} is some coupling constant between these two atoms. Since the fully interacting model is not exactly solvable, we rely on the perturbative approach instead. The interaction gives vanishing contribution at the first order, since the average dipole moment of an atom is zero. Passing to the second order correction, the effective interaction between the two atoms i and j in the Rydberg state becomes

$$V_{i,j} = \frac{V_0}{|i - j|^6}, \quad V \sim n^{11}, \tag{3.11}$$

which leads to the strong coupling Hamiltonian

$$\mathrm{H} = \mathrm{H}_0 + \sum_{i \neq j} \frac{V_0}{|i - j|^6} n_i n_j. \tag{3.12}$$

In Eq.(3.12), one may recognize the Van der Waals interaction, that decays as $1/R^6$ with respect to the interaction distance.

3.3.2 Rydberg dressing

Starting from the frozen regime, one can make a step further and introduce a large detuning Δ, to weakly couple a non-Rydberg state, say the ground state $|g\rangle$, to some Rydberg state $|r\rangle$. In this way, one virtually populates the Rydberg state, meaning that at the first order in the perturbation theory, the $|g\rangle$ ground state of the system will be modified and will acquire a small admixture of the Rydberg state [7, 16, 17]:

$$|\tilde{g}\rangle \sim |g\rangle + \frac{\Omega}{\Delta} |r\rangle. \tag{3.13}$$

We will be referring to $|\tilde{g}\rangle$ as the Rydberg-dressed state. Before talking about the interaction between Rydberg-dressed atoms, it is worth mentioning that one will inevitably encounter dissipation in such setups. Without Rydberg-dressing, one of the dissipative processes could be the decay of

Rydberg state. The advantage of Rydberg-dressing is that it greatly enhances the lifetime of the state and thus reduces the dissipative effects. To unravel the properties of interaction between the atoms in Rydberg-dress states, we carry out perturbation theory up to the fourth order in Ω/Δ. For time being, we limit our discussion with two-atom scenario, but the arguments stay valid for many-atom setup. For a pair of atoms, in the fourth order approximation there are two processes when both atoms are in the Rydberg state and thus interact with each other. By neglecting the numerical constant contributions that simply shift the energy scale, the effective interaction between two particles r distance apart will be

$$V_{\text{int}} \approx \frac{\Omega^4}{\Delta^3} \frac{1}{1 + \left(\frac{r}{r_c}\right)^6}, \quad r_c = \left(\frac{2\Delta}{V_0}\right)^{1/6}. \tag{3.14}$$

In the literature Eq.(3.14) is known as the Soft-shoulder potential. Such an interaction had an interesting and useful property: at short distances $r \ll r_s$, the interaction strength shows a plateau, while for large distances $r \gg r_s$ it decays as Van der Waals interaction Eq.(3.12). As we will see in the following sections, such an interaction can be useful to experimentally realize Hubbard-like models, where the density-density interactions are extended over many lattice sites. Long-range interactions within low dimensional quantum systems can exhibit exotic quantum phases.
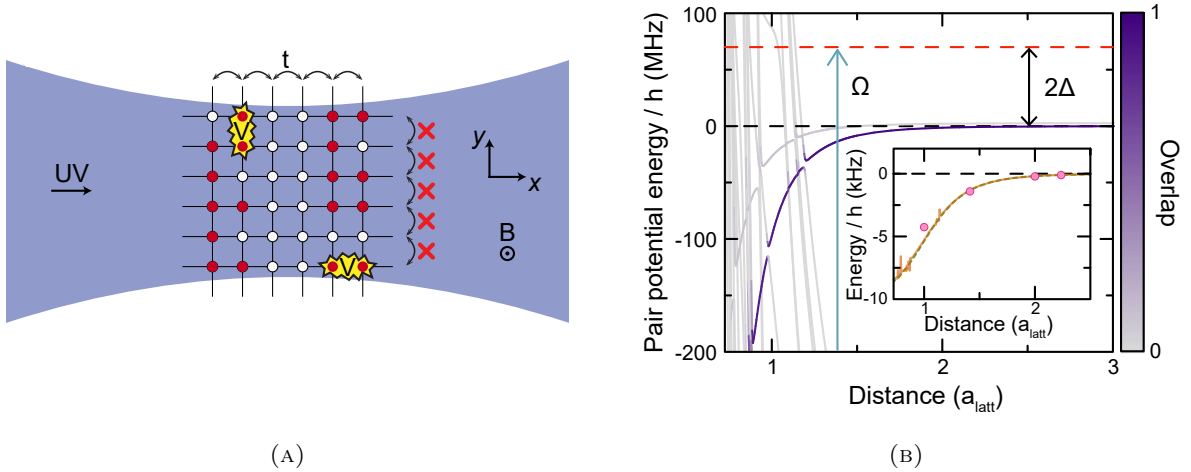
FIGURE 3.1: (A) A pictorial representation of the experimental setup; (B) Experimentally measured attractive potential, engineered by Rydberg dressing. Figure extracted from [24].

3.3.3 Experimental realisations

The setup presented in [24], experimentally studied the emerging physics using Rydberg-dressed ^{6}Li atoms populated on a 2D optical lattice with $\alpha_0 = 752nm$ lattice spacing, see Fig(3.1a). An external magnetic field of $B_z \approx 591G$ is applied perpendicularly to the optical lattice plane. The spin polarized ^{6}Li atoms are initially prepared to be in $|nl, m_l, m_s, m_I\rangle = |2S, 0, -1/2, 1\rangle \equiv |g\rangle$ state. The ground state is coupled to the Rydberg state $|r\rangle \equiv |28P, 0, -1/2\rangle$ by shining $231nm$ laser along the x direction, linear along B_z direction. Thus, these two states form the two dimensional space of states $|g\rangle$ and $|r\rangle$. By changing the intensity and the detuning of the dressing light, one has a full control over the soft-core interaction potential Eq.(3.14). This way, one has an experimental setup

to simulate the dynamics of hard-core bosons governed by the following hamiltonian

$$\mathrm{H}_{\mathrm{full}} = -t \sum_{\langle i,j \rangle} \left(c_i^\dagger c_j + \mathrm{h.c} \right) + \frac{1}{2} \sum_{i,j} V_{i,j} n_i n_j + \sum_i \delta_i n_i. \qquad (3.15)$$
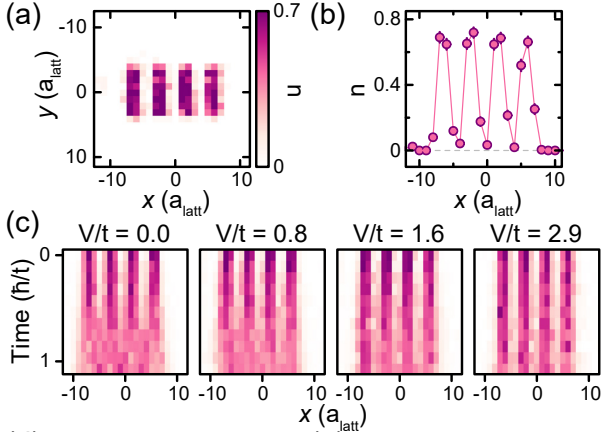

FIGURE 3.2: (a) Initially prepared CDW order. Tunneling along y direction is suppressed. (b) Density variation along x axis in the initial CDW ordered state. (c) The quench dynamics of initial CDW state. Figure extracted from [24].

Here δ_i are the so-called single-particle light-shifts, that originates from the lattice and Rydberg-dressing light beams. By narrowing the dressing beam and focusing it with $16.1\mu m$ waist, the variation of δ_i along y direction becomes larger compared to t - typically greater than $3t$. On the other hand, the variation of δ_i along x direction becomes negligible. This way, to the first order approximation, we can drop the light-shift term and neglect the tunneling processes along y direction. This reduces the effective hamiltonian to

$$\mathrm{H}_{\mathrm{eff}} = -t \sum_{\langle i,j \rangle_x} \left(c_i^\dagger c_j + \mathrm{h.c} \right) + \frac{1}{2} \sum_{i,j} V_{i,j} n_i n_j, \qquad (3.16)$$

Therefore, this setup allows one to study experimentally study the physics of coupled 1-dimensional $t - V$ models with long-range interactions, with strongly suppressed tunneling between the chains.

Within this setup, an interplay between the tunneling and the interaction was studied. By fine tuning the the single-particle light shift δ_i and the detuning Ω, a nearest-neighbor repulsive interaction was obtained $V_{i,j} = V\delta_{i,i+1}$. To examine the competition between the tunneling and the repulsion of the atoms, an initial charge-density wave (CDW) was prepared – with period $\lambda = 4\alpha_0$ and width $w = 7\alpha_0$. The density of particles in the peaks of CDW was chosen to be $n \sim 0.7$, see Figs.(3.2a,b). By observing the quench dynamics of the charge density wave for various ratios V/t, it was determined that for non-interacting case the phase of CDW inverts at a times $\sim \hbar/t$. This is an expected outcome, due a coherent evolution of the system. On the other hand, for sufficiently strong repulsion $V/t \approx 2.9$, CDW order remains for larger times – an immediate effect of the repulsion on the dynamics, Fig.(3.2c).

In a more recent setup [71], the authors experimentally realized an effective 1D extended Bose-Hubbard model, by implementing Rydberg-dressed atoms in an optical lattice. In this case, ^{87}Rb atoms are pumped in a single plane of an optical lattice. Each atom is prepared in $|g\rangle = |F = 2, m_F = 2\rangle$ ground state. By using the folded lattice approach [72] with $\alpha_0 = 752nm$, a 2D Bose-Hubbard model is realized, with tunable J hopping amplitude and fixed $U/\hbar \approx 35.8Hz$ on-site interaction strength. Above this, by single-site addressing, up to three parallel and non-interacting one-dimensional systems can be prepared. The separation between each chain can be up to 3
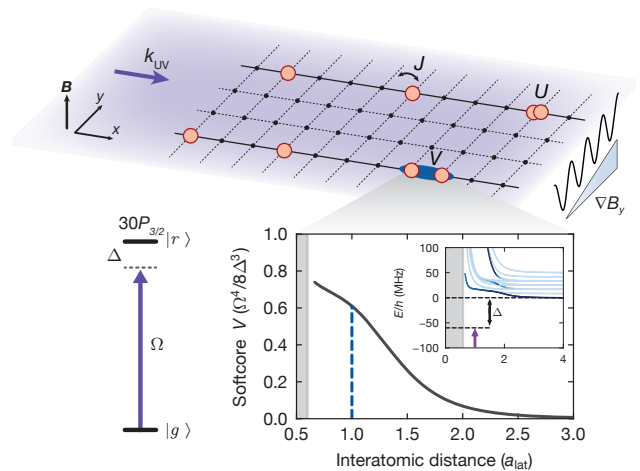

FIGURE 3.3: Pictorial representation of the experimental setup. Figure extracted from [71].
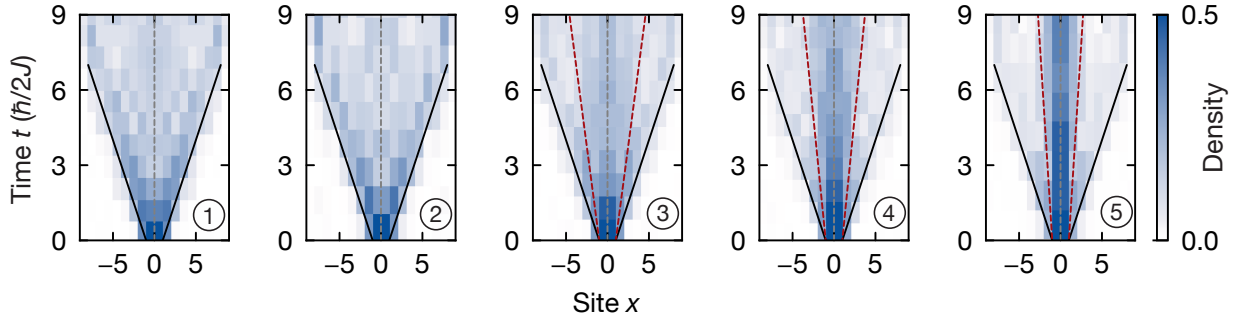
FIGURE 3.4: The figure shows the dynamics of the symmetrized two-particle density for $V/J = 0, 1.0(1), 2.0(2), 3.3(1), 4.9(2)$ (cases 1 to 5 , respectively) post-selected on two particles being present. Evidently, below the critical value of V_c (figures 1 and 2) the particles spread independently, following a ballistic light-cone with group velocity $2J\alpha_0/\hbar$. Above the critical point (figures 3 to 5), a slower light-cone emerges (highlighed with red dashed lines) – corresponding to the bound pair's expansion. Figure extracted from [71].

lattice sites, as shown on Fig.(3.3a). Each 1D chain contains experimentally tunable number of atoms. As already mentioned, the tunneling along each chain happens with rate J, while inter-chain tunneling is suppressed by applying a magnetic field along y direction with $\nabla B_y \approx 350Hz/\alpha_0$ gradient. As a next step, one off-resonantly shines the system with $297nm$ laser light along 1D chains, thus inducing the coupling between the local ground states $|g\rangle$ to corresponding Rydberg state $|r\rangle = |30P_{3/2}, m_j = 3/2\rangle$. The off-resonance Δ is fine tuned in a way, that the effective dressed interaction V extends over two nearest neighboring sites, as shown on Fig.(3.3a). In this manner, the one experimentally realises a synthetic quantum system, where the dynamics is described by the so-called extended Bose-Hubbard model

$$\text{H} = -J \sum_{\langle ij \rangle_x} a_i^\dagger a_j + \frac{U}{2} \sum_i n_i(n_i - 1) + V \sum_i n_i n_{i+1}. \tag{3.17}$$

In this scenario, the authors tune the setup to $U/J \gtrsim 11$ and thus operate in the hard-core regime, while also manage to reach relatively strong $V/J \simeq 6 - 10$ repulsion strength. In Ref.[73], it was theoretically predicted predict that bound states of atoms start to populate the system if the interaction strength is sufficiently strong $V > V_c$, with $V_c = 2J$. By quenching the tunnel coupling of the lattice, bound states of atoms has been detected (see Fig.(3.4)), as predicted by the theory. Apart from the agreement with theoretical results, the group has applied stroboscopic sequence of pulses to enhance the control over the interaction V. Such an approach for dressing has also enhanced the expected Rydberg lifetime by one order of magnitude.

Chapter 4

Phase diagram of Rydberg-dressed atoms on two-leg square ladders: Coupling supersymmetric conformal field theories on the lattice

In this section we investigate the phase diagram of hard-core bosons in two-leg ladders in the presence of soft-shoulder potentials. We show how the competition between local and non-local terms gives rise to a phase diagram with liquid phases with dominant cluster, spin-, and density-wave quasi-long-range ordering. These phases are separated by Berezinskii-Kosterlitz-Thouless, Gaussian, and supersymmetric (SUSY) quantum critical transitions. For the latter, we provide a phenomenological description of coupled SUSY conformal field theories, whose predictions are confirmed by matrix-product state simulations. Our results are motivated by, and directly relevant to, recent experiments with Rydberg-dressed atoms in optical lattices, where ladder dynamics has already been demonstrated, and emphasize the capabilities of these setups to investigate exotic quantum phenomena such as cluster liquids and coupled SUSY conformal field theories.

By utilizing a combination of field theoretical approaches based on bosonization [28, 39], and numerical simulations based on exact diagonalization [74] and tensor networks [75, 76], we find that two-leg soft-shoulder Hubbard models support a rich phase diagram (schematically depicted in Fig.(4.1b)). In the weakly interacting regime, the system supports a fully gapless and a spin-density wave phase, that are well captured via an Abelian bosonization field theory. In the limit of strong intra-chain interactions, the system is effectively described by chains that are subjected to clustering: remarkably, in such limit, despite the already strong nature of fractionalization due to the inapplicability of the Luttinger theorem, finite inter-chain interactions immediately lock clusters, giving rise to a single, 'spin-locked' cluster Luttinger liquid. We capture this regime utilizing a phenomenological cluster bosonization field theory [40, 20, 21, 77].

Close to the (decoupled) single chain critical point, the models we consider offer an almost unique possibility of investigating the controlled coupling of two supersymmetric (SUSY) conformal field theories [78, 27]. This happens at intermediate interactions, where we are unable to construct a microscopically justified quantum field theory. To describe such scenario, we instead propose a phenomenological field theory. The emerging picture is that, for the case of square ladders, the mutual interactions between the SUSY theories lead to the opening of a gapless phase with density-wave quasi-long-range order that is absent in any interaction limit. This phase is separated from the weak coupling phase by a Gaussian transition, and from the strong coupling phase by a conformal critical line with central charge $c = 3/2$. We confront these predictions against extensive tensor network simulations, including an analysis of entanglement properties as well as experimentally observable correlation functions.

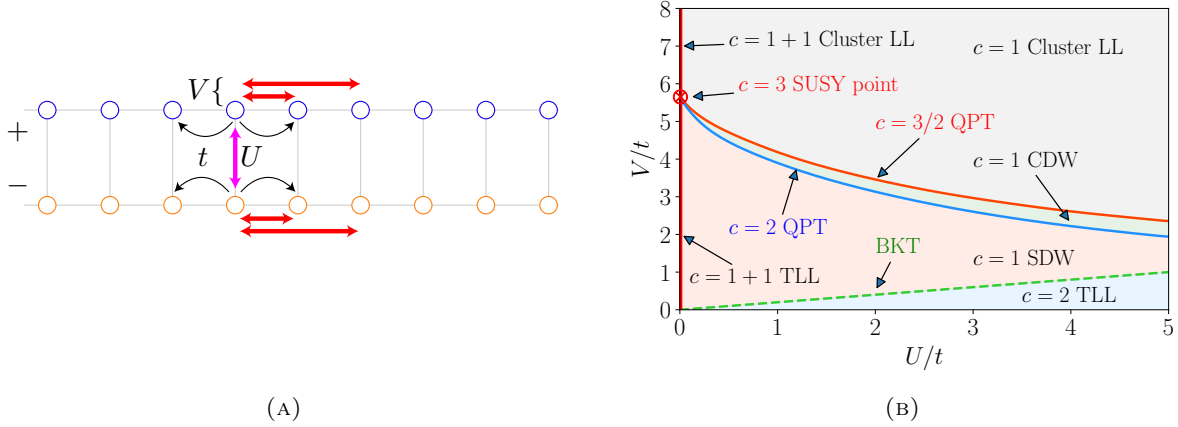## 4.1   Model Hamiltonian and overview of the phase diagram

FIGURE 4.1: (A) Representation of the soft-shoulder (V) Hubbard (U) square ladder of Rydberg hard-core bosons. They hop (t) within a same leg of the ladder only. We depict a range of 2 for the soft-shoulder interaction. (B) Phase diagram of the model. The weak coupling regime displays a gapless phase composed of two Tomonaga-Luttinger liquids (TLLs) in both charge and spin (mapped from the leg index) sectors (2TLL). Upon increasing V, first, the spin sector undergoes a Berezinskii-Kosterlitz-Thouless (BKT) transition (green line) onto a spin-density wave (SDW); then, a Gaussian transition (blue line) drives the system to a charge-density wave phase (CDW). At large interactions, a $c = 3/2$ transition (red line) separates the CDW from a 'spin-locked' cluster Luttinger liquid (CLL). The transitions lines at intermediate couplings relate to the effective field theory emerging from the two superposed supersymmetric (SUSY) conformal critical points at $U = 0$ (red crossed-dot). At $U = 0$, the two legs are independent and display TLL (1+1 TLL) and CLL (1+1 CLL) phases separated by the $c = 3$ SUSY point.

We study a square ladder of spinless hard-core bosons at $\nu = 2/5$ filling (on average two filled sites for every five sites in each chain). The system Hamiltonian is schematically depicted in Fig.(4.1a), and reads:

$$H = -t \sum_{i,\ell} \left(b_{i,\ell}^{\dagger} b_{i+1,\ell} + H.c. \right) + U \sum_{i} n_{i,+} n_{i,-} + V \sum_{i,\ell} \sum_{j=1}^{r_C} n_{i,\ell} n_{i+j,\ell}. \tag{4.1}$$

where $b_{i,\ell}^{\dagger}$ is the creation operator for hard-core bosons on site i of chain $\ell = +, -$ and $n_{i,\ell} = b_{i,\ell}^{\dagger} b_{i,\ell}$. t is the intra-chain hopping, U is the nearest neighbor inter-chain interaction amplitude, V is the longer-ranged intra-chain interaction amplitude, and $r_C \in \mathbb{N}$. The density $\nu = 2/5$ is chosen in such a manner that, in the classical limit, the model supports clustering. In this model, the U(1) charges of the two legs are conserved separately, making the Hamiltonian a U(1)×U(1) symmetric system. There is no inter-chain tunneling but the two legs interact.

The model in Eq.(4.1) is directly inspired by the Rydberg experiments performed in Ref.[16]. There, a gas of atoms was weakly coupled to Rybderg p-state in the Paschen-Bach regime, resulting in pairwise interactions of the type:

$$V(r) = \frac{V_{\max}}{1 + \frac{r^6}{r_S^6}}, \tag{4.2}$$

with both $V_{\max} > 0$ and r_S easily tunable in both the transversal and longitudinal directions. Tunneling between tubes was instead strongly suppressed leveraging on the comparatively large quadratic Zeeman shifts from tube to tube. An alternative way to prevent inter-wire tunneling is

to suppress it utilizing a higher potential barrier between the wires. Densities could be tuned via changing the atom loading scheme.

The potential in Eq.(4.2) is connected to the model Hamiltonian above as follows. In a lattice, when $r_S \sim a_0$ with a_0 being the lattice spacing, such potential is well approximated by a Heaviside step function stepping down at $r = r_C a_0 = \text{Floor}(r_S/a_0)a_0$. We take $r_C = 2$ in Eq.(4.1) along the legs and $r_C = 1$ along the rungs. Note that anisotropic potentials could be generated in various ways – either changing the relative lattice spacing along and perpendicular to the wire, or utilizing dressing via p- and d-states under specific directions. The influence of longer-range terms (for V) is known to affect clustering only at the quantitative level [20], so, throughout the work, we will solely employ Eq.(4.1) with $r_C = 2$ for the sake of clarity.

The red line ($U = 0$) of Fig.(4.1b) corresponds to two decoupled chains of known behavior [20, 21]. The phase diagram of a single chain displays a Tomonaga-Luttinger liquid (TLL) for $0 < V/t \lesssim 5.7$, and a cluster Luttinger liquid (CLL) for $V/t \gtrsim 5.7$. A CLL behaves like a regular TLL, with its elementary excitations behaving as propagating waves of local (over a few sites) *clusters* of filled and empty sites. For $\nu = 2/5$ such clusters minimizes the energy cost in V. Two semi-classical cluster configurations are represented in Fig.(4.2a) and involve two clusters A and B in a ratio 1:2. Both the TLL and the CLL have a central charge $c = 1$. They are separated by a SUSY conformal phase transition point of central charge $c = 3/2$ at $V/t \simeq 5.7$ identified numerically [21]. The low-energy field theory for this point is described by a combination of a compactified boson and a real Majorana fermion.

By adding an interaction between two of these chains, we infer the rest of the phase diagram Fig.(4.1b). We map the leg index to a SU(2) spin-1/2 degree of freedom. We show that a partial spin gap opens as soon as $U > 0$ (and $V > 0$). At weak coupling ($V/t \lesssim 5.7$) the leading instability is a spin-density wave (SDW). At strong coupling ($V/t \gtrsim 5.7$), it is the CLL that is spin-locked. In both cases, the central charge is $c = 1$. When $V = 0$, the ladder is equivalent to the fully gapless Hubbard model described by a TLL with $c = 2$ (2TLL). At $t < U \lesssim V$, we find a charge-density Wave (CDW) leading instability (with $c = 1$) between the SDW and the CLL. We understand the existence of this instability here as the consequence of the inversion of the sign of the mass of the spin degree of freedom before clusterization when starting from the SDW and increasing both U and V. We provide a cartoon picture of the dominant instabilities in Fig.(4.2).
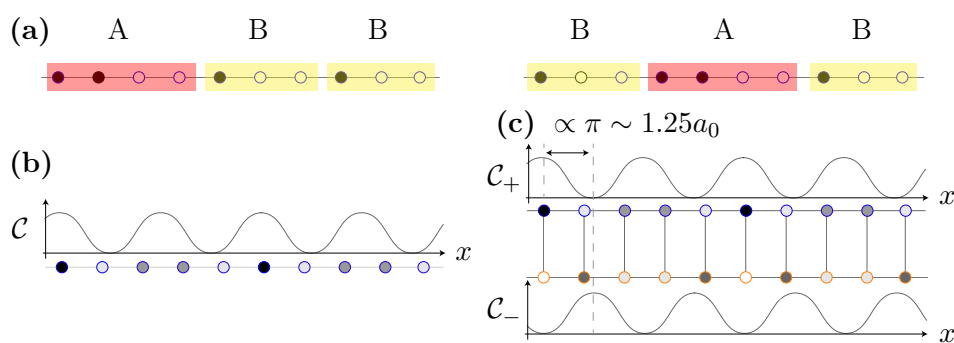

FIGURE 4.2: Cartoon pictures of the leading instability of the various phases in the single chain and ladder model (for 2/5 filling). (a) Two of the possible semi-classical configurations of the two clusters of hard core bosons A and B in a ratio 1:2. (b) TLL for only one chain. $\mathcal{C}$ is the density-density correlations without the algebraic damping. (c) Spin density wave along z-direction for the square lattice for a gapped spin sector. Such a wave propagates with a momentum of $\pm 2k_F$.

The SDW and CDW phases are separated by the Gaussian phase transition with $c = 2$. When $U = 0$, the phase transition point at $V/t \simeq 5.7$ is the superposition of the two SUSY conformal phase transition of each independent chain, hence $c = 3/2 + 3/2 = 3$. The CDW and the CLL are

separated by the generalization of the supersymetric phase transition point existing at ($V/t \simeq 5.7$, $U = 0$). This transition has $c = 3/2$ and may not be supersymmetric. The SDW and 2TLL phases are separated by a Berezinskii-Kosterlitz-Thouless (BKT) transition (green dashed line in Fig.(4.1b)). Note that the location of this BKT transition is predicted from the analytical results at weak coupling regime and hard to locate precisely for the entire parameter range using numerical tools used in this study.

We establish these results analytically in Sec.(4.2) starting from the two independent chain coupled by the perturbative interaction U. We use Abelian bosonization in the weak coupling regime or provide a phenomenological explanation using cluster bosonization for $V/t \gg 5.7$. Moreover, we predict possible outcomes for the coupling between two SUSY conformal field theories close to ($V/t \simeq 5.7$, $U \gtrsim 0$) using a phenomenological field theoretic approach in Sec.(4.3). We use exact diagonalization and infinite density matrix renormalization group (iDMRG) method in Sec.(4.4) to corroborate our theoretical results and predictions, and to uncover the phase diagram of Fig.(4.1b) for large U/t.

We note that Ref. [79] studied a similar model as Eq.(4.1) but with an inter-leg interactions (U) of range two (in diagonal) instead of zero like we do. This corresponds to a very different classical limit, and reflects onto the fact that the phase diagrams, apart from weak coupling regions, are generically distinct. In particular, there appears to be no similar scenario close to the SUSY point.

4.2 Analytical & phenomenological approach of weakly coupled legs

In this section, we derive our analytical results on the ladder model by starting from the two decoupled chains that are either describe by massless single-particles ($V \ll t$) or cluster liquids ($V \gg t$), to which we add the interaction U perturbatively. In the weak coupling regime ($U, V \ll t$), we use Abelian bosonization to predict the SDW phase, the 2TLL phase, and the BKT phase transition in between (the dashed line in Fig.(4.1b)). In the strong V regime, we use cluster bosonization to describe the properties of two interacting CLL, and how the interaction induces a partial gap, leading to $c = 1$ CLL in the ladder geometry.

4.2.1 Weak intra-chain interactions: Abelian bosonization

In the weak coupling, we predict the existence of two phases: the 2 Tomonaga-Luttinger liquid when $V = 0$ and the holonic phase with spin density wave leading instability when $V > 0$ (c.f. Figs.(4.2b,c) for a cartoon picture). Formulated as a soft-shoulder Hubbard model of spinful fermions and using Abelian bosonization, we show that the model in Eq.(4.1) describes a TLL with a mass term for the spin degree of freedom which is relevant as soon as $V > 0$ at first loop of renormalization and irrelevant when $V = 0$ (for the filling $\nu = 2/5$). When $U = 0$, the model is gapless for both degrees of freedom.

We obtain these predictions by bosonizing the Hamiltonian in Eq.(4.1) and obtaining explicit formulae for the parameters of the low-energy field theory. Indeed, when both $U = 0$ and $V = 0$, Eq.(4.1) describes two chains of free spinless fermions (via, e.g., a pair of Jordan-Wigner transformations) with an emerging conformal symmetry when taking the continuous limit. We therefore study the weak-coupling low-energy properties of the system using standard Abelian bozonisation techniques as detailed in Refs. [27, 39, 28]. We use the same conventions as in Ref. [28]:

$$c_{i,\ell} \sim \psi_{R,\ell}(x = i) + \psi_{L,\ell}(x = i), \tag{4.3a}$$

$$\psi_{r,\ell} = \frac{1}{\sqrt{2\pi a_0}} U_{r,\ell} e^{irk_F x} e^{i\sqrt{\frac{\pi}{2}}(r\phi_c - \theta_c + \ell(r\phi_s - \theta_s))}. \tag{4.3b}$$

Here, $c_{i,\ell}$ is the fermionic annihilation operator obtained from $b_{i,\ell}$ after a Jordan-Wigner transformation, $\psi_{r,\ell}$ is the associated right ($r = R$) and left ($r = L$) moving fermionic field in the continuous limit close to the Fermi points, $\ell = +, -$ denotes the chain index, $a_0 = 1$ is the lattice spacing, $U_{r,\ell}$ are the Klein factors such that $\{U_{r,\ell}, U_{r',\ell'}\} = 2\delta_{r,r'}\delta_{\ell,\ell'}$, and $k_F = \pi\nu/a_0$ is the Fermi momentum with $\nu = 2/5$ being the filling factor for each chain. The bosonic fields ϕ_c, ϕ_s, θ_c, and θ_s are the charge and spin fields and their respective dual fields.

The Hamiltonian in Eq.(4.1) in terms of the bosonic fields can be written as

$$
\begin{aligned}
H \sim \frac{u_c}{2} \int \mathrm{d}x \left(K_c : (\partial_x \theta_c)^2 : + \frac{1}{K_c} : (\partial_x \phi_c)^2 : \right) \\
+ \frac{u_s}{2} \int \mathrm{d}x \left(K_s : (\partial_x \theta_s)^2 : + \frac{1}{K_s} : (\partial_x \phi_s)^2 : \right) - \frac{g_\perp}{4\pi^2} \int \mathrm{d}x \cos(\sqrt{8\pi}\phi_s),
\end{aligned}
\tag{4.4}
$$

where ∂_x is the first derivative with respect to the spatial coordinate x, the colon denotes normal ordering, and a_0 is the lattice spacing (taken equal for both the x and y directions for simplicity). The quantities

$$
v_F = 2t \sin(2\pi/5), \tag{4.5a}
$$
$$
u_s K_s = u_c K_c = v_F, \tag{4.5b}
$$
$$
g_\perp = -2U, \tag{4.5c}
$$
$$
g_\parallel = -2(U - 5V), \tag{4.5d}
$$
$$
K_c = \frac{1}{\sqrt{1 + \frac{U+5V}{\pi v_F}}}, \tag{4.5e}
$$
$$
K_s = \frac{1}{\sqrt{1 + \frac{g_\parallel}{2\pi v_F}}}, \tag{4.5f}
$$

are the Fermi velocity v_F, bare charge velocity u_c, charge Luttinger parameter K_c at first order in U/t and V/t, spin velocity u_s and spin Luttinger parameter K_s at first order. Expressions for generic k_F and r_C can be found in the Appendix. The renormalization equations at first loop of renormalization are

$$
\frac{dg_\perp}{dl} = \frac{1}{2\pi} g_\perp g_\parallel \tag{4.6a}
$$
$$
\frac{dg_\parallel}{dl} = \frac{1}{2\pi} g_\perp^2, \tag{4.6b}
$$

which predict a BKT phase transition when $g_\parallel = -|g_\perp|$, i.e., when $V = 0$ for $U > 0$ [28].

Solving Eqs.(4.6) shows that the spin sector is gapped when $V > 0$, and gapless when $V = 0$ [28]. As the extended interaction breaks the SU(2) symmetry, the renormalization flow may introduce a gap in the spin sector without commensurability effect. As $m = -g_\perp/(4\pi^2) > 0$, this gap fixes $\phi_s = \sqrt{\pi/8}$ (modulo $\sqrt{\pi/2}$) such that the order parameter $\mathcal{O}_{\text{triplet}_0}$ is the "triplet 0" [80]:

$$
\mathcal{O}_{\text{triplet}_0} = \sin(\sqrt{2\pi}\phi_s). \tag{4.7}
$$

This order parameter describes the spin sector contribution in the "$2k_F$" spin density wave along the z-direction (SDW^z) whose order parameter $\mathcal{O}_{\mathrm{SDW}}^z$ [1] can be defined as follows [81]:

$$\mathcal{O}_{\mathrm{SDW}}^z = S^z(x) - \frac{1}{\sqrt{2\pi}}\partial_x\phi_s(x) = \cos(\sqrt{2\pi}\phi_c + 2k_F x)\sin(\sqrt{2\pi}\phi_s). \tag{4.8}$$

where $S^z(x)$ the continuous limit of the spin operator

$$\frac{1}{2}\sum_{\ell,\ell'=\pm} b_{x,\ell}^\dagger \sigma_{\ell\ell'}^z b_{x,\ell'} \sim S^z(x), \tag{4.9}$$

with $\sigma_{\ell\ell'}^z$ the Pauli matrix along the z-direction. The associated correlator is

$$\langle \mathcal{O}_{\mathrm{SDW}}^z(x)\mathcal{O}_{\mathrm{SDW}}^z(y)\rangle \sim \cos(2k_F|x-y|)|x-y|^{-K_c}, \tag{4.10}$$

which is also the correlator with the longest range, such that the SDW^z is the dominant instability in the system. The cartoon picture of the low energy states of the phase at low filling is a set of right or left moving particles of momentum close to $2k_F$ distributed equally between the two legs. When two particles from different legs scatter, they exchange momentum.

When $V = 0$, the phase is fully gapless as in the Hubbard model. Both the CDWs with momentum $2k_F$ and SDWs instabilities are in competition. We define the order parameter associated with CDW with

$$\mathcal{O}_{\mathrm{CDW}} = \rho(x) - \sqrt{\frac{2}{\pi}}\partial_x\phi_c(x), \tag{4.11}$$

where $\rho(x)$ is the continuous limit of the density operator

$$\sum_{\ell=\pm} b_{x,\ell}^\dagger b_{x,\ell} \sim \rho(x). \tag{4.12}$$

The correlation functions associated with both CDW and SDW^z are

$$\langle \mathcal{O}_{\mathrm{CDW}_{2k_F}}(x)\mathcal{O}_{\mathrm{CDW}_{2k_F}}(y)\rangle \sim \cos(2k_F|x-y|)|x-y|^{-(K_c+K_s^*)},$$
$$\langle \mathcal{O}_{\mathrm{SDW}}^z(x)\mathcal{O}_{\mathrm{SDW}}^z(y)\rangle \sim \cos(2k_F|x-y|)|x-y|^{-(K_c+K_s^*)}, \tag{4.13}$$

with $K_s^* = 1$, the renormalized Luttinger parameter as the SU(2) symmetry emerges asymptotically. As a comparison, the CDW correlation function in the SDW phase decays exponentially as

$$\langle \mathcal{O}_{\mathrm{CDW}}(x)\mathcal{O}_{\mathrm{CDW}}(y)\rangle \sim \cos(2k_F|x-y|)|x-y|^{-K_c}e^{-|x-y|/\xi}, \tag{4.14}$$

where $\xi \sim \frac{1}{M}$ and M is the dynamically generated mass gap [28] defined as

$$M = \Lambda\exp\left(-\left(g_\perp^2 - g_\parallel^2\right)^{-\frac{1}{2}}\right), \tag{4.15}$$

with Λ being the ultra-violet cutoff.

When $0 < V < U/5$, the partial gap of the SDW is more fragile than when $V > U/5$. Indeed, the scaling dimension of the mass operator in the sine-Gordon model in Eq.(4.4) is larger than two when $K_s > 1$, i.e., when $U = 5V$. In this zeroth loop approach, the mass operator is therefore irrelevant when $0 < V < U/5$ such that the spin gap opens only because of first-loop corrections.

---

[1] The contribution also appears in the bond-spin density wave along the z-direction (BSDW^z) order parameter. As the charge sector is gapless, SDW^z and BSDW^z leading instabilities are indistinguishable.

This feature of the BKT phase transition hints at the difficulty to precisely pinpoint the phase transition line within the regime $0 < V < U/5$ seen in our later numerical approach.

Long-range intra-leg interaction potential $V(\mathbf{r})$ at weak coupling

Using the Abelian bosonization approach discussed in Sec.(4.2.1), the weak coupling effective field theory is derived for a generic case of the intra-leg soft-shoulder potential range r_C. Away from half-filling, the bosonized Hamiltonian has exactly the same form as Eq.(4.4). The charge sector is gapless. The bare parameters describing the spin sector at weak coupling are

$$u_s K_s = u_c K_c = v_F, \tag{4.16a}$$

$$K_s = \frac{1}{\sqrt{1 + \frac{g_\parallel}{2\pi v_F}}}, \tag{4.16b}$$

$$g_\parallel = -2\left(U - V\left(2r_c + 1 - \frac{\sin([2r_c + 1]k_F)}{\sin(k_F)}\right)\right), \tag{4.16c}$$

$$K_c = \frac{1}{\sqrt{1 - \frac{g}{2\pi v_F}}}, \tag{4.16d}$$

$$g = -2\left(U + V\left(2r_C + 1 - \frac{\sin([2r_C + 1]k_F)}{\sin(k_F)}\right)\right). \tag{4.16e}$$

while $g_\perp = -2U$ remains unaffected. For $k_F = 2\pi/5$, the changes in parameters Eqs.(4.16) narrows the location of the BKT phase transitions for $V < U/5$ but leaves the first loop prediction ($V = 0$) unchanged.

4.2.2 Strong intra-chain interactions and the clustering limit: cluster bosonization

In the strong coupling regime $V \gg t, U$, we show that the phase is a CLL: to minimize the shoulder potential V, the hard-core bosons on each leg group up in clusters separated by r_C empty sites. Both the number of particle per cluster and the variety of clusters depend on the filling and r_C. For $\nu = 2/5$ and $r_C = 2$, two clusters A and B emerges with ratio 1:2 and are represented in Fig.(4.2a). In the CLL, it is the collective modes of these clusters A and B that propagate freely, similarly to the holons of Sec.(4.2.1). We show that the inter-leg interaction U may lead to the equivalent of a spin gap for these clusters, forcing the clusters from both legs to propagate in a correlated manner. When this cluster spin gap is present, the central charge is $c = 1$, and $c = 2$ otherwise. Numerical simulations conclude $c = 1$ in Sec.(4.4).

To derive the results, we use cluster bosonization. As already demonstrated in Eq.(2.123), one can use a generalized phenomenological bosonization to take into account the fact that the clusters are composite objects. For the present case, since we are dealing with two chains, one simply needs to attach extra chain index $l = \pm$ to Eq.(2.123) and all corresponding commutators. Since in our case $\sigma = M/N = 3/4$ and $\nu = N/L = 2/5$, we have

$$\rho_\ell(x) = \left(\frac{2}{5} - \frac{1}{\sqrt{\pi}\sigma}\nabla\phi'_\ell(x)\right)\sum_{q=-\infty}^{+\infty} A_{q,\ell} e^{-i2q(3\pi x/10 - \sqrt{\pi}\phi'_\ell(x))}, \tag{4.17}$$

with

$$\left[\theta'_\ell(y), \frac{1}{\pi}\nabla\phi'_{\ell'}(x)\right] = i\delta_{\ell,\ell'}\delta(x - y), \tag{4.18}$$

while the expression for the cluster bosonic field $\psi_\ell(x)$ in the density-angle formulation is

$$\psi_\ell(x) = e^{-\frac{i\sqrt{\pi}}{\sigma}\theta_\ell'(x)}\sqrt{\frac{2}{5} - \frac{1}{\sqrt{\pi}\sigma}\nabla\phi_\ell'(x)}\sum_{q=-\infty}^{+\infty}\alpha_{q,\ell}e^{-i2q(3\pi x/10 - \sqrt{\pi}\phi_\ell'(x))},\qquad(4.19)$$

where $\alpha_{q,\ell}$ are the non-universal Fourier coefficients.

Using the cluster density (see Eq.(4.17)) and the cluster bosonic field (see Eq.(4.19)), we write the effective continuous Hamiltonian describing the low-energy behavior of the clusters. For $U = 0$, this Hamiltonian is [20, 21]

$$H = \sum_{\ell=\pm}\frac{v_\ell}{2}\int dx\left(K_\ell(\nabla\theta_\ell')^2 + K_\ell^{-1}(\nabla\phi_\ell')^2\right),\qquad(4.20)$$

where the cluster velocities and Luttinger parameters include the (unknown) Jacobian of the coarse graining. By symmetry both $v_\ell = v$ and $K_\ell = K$ for the two chains. The Hamiltonian in Eq.(4.20) describes two CLL (2CLL), with central charge $c = 1$ each ($c = 2$ in total) [20, 21]. The inter-leg interaction in the cluster bosonic field variables is

$$U\int dx\rho_+(x)\rho_-(x) \sim g_0\int dx\nabla\phi_+'\nabla\phi_-' + g_\perp\int dx\cos(\sqrt{4\pi}(\phi_+' - \phi_-'))$$
$$+ g_2\int dx\sin(\sqrt{4\pi}(\phi_+' - \phi_-')) + ...\qquad(4.21)$$

with $g_0 = \frac{UA_{0,+}A_{0,-}}{\pi\sigma^2}$, $g_\perp = 8U\,\text{Re}[A_{1,+}A_{-1,-}]/25$ and $g_2 = -8U\,\text{Im}[A_{1,+}A_{-1,-}]/25$. In Eq.(4.21), we have only written the slowly oscillating terms at least as relevant as $\cos(\sqrt{4\pi}\phi')$. By symmetry, at zeroth order in perturbation of U, the coefficient $A_{q,\ell}$ are independent of the leg index. In this case, we expect $g_0 > 0$, $g_\perp > 0$ and $g_2 = 0$. We define the cluster spin and charge bosonic field ϕ_s and ϕ_c as

$$\phi_c' = \frac{\phi_+' + \phi_-'}{\sqrt{2}},\qquad\qquad\phi_s' = \frac{\phi_+' - \phi_-'}{\sqrt{2}},\qquad(4.22a)$$

$$\theta_c' = \frac{\theta_+' + \theta_-'}{\sqrt{2}},\qquad\qquad\theta_s' = \frac{\theta_+' - \theta_-'}{\sqrt{2}}.\qquad(4.22b)$$

Using Eqs.(4.20–4.22), we derive the Hamiltonian in Eq.(4.1) with inter-leg interaction as follows:

$$H \sim \frac{v_c}{2}\int\left(K_c(\nabla\theta_c')^2 + K_c^{-1}(\nabla\phi_c')^2\right)$$
$$+ \frac{v_s}{2}\int\left(K_s(\nabla\theta_s')^2 + K_s^{-1}(\nabla\phi_s')^2\right) + g_\perp\int dx\cos(\sqrt{8\pi}\phi_s'),\qquad(4.23)$$

where

$$K_c = \frac{K}{\sqrt{1 + \frac{g_0 K}{v}}}, \tag{4.24a}$$

$$K_s = \frac{K}{\sqrt{1 - \frac{g_0 K}{v}}}, \tag{4.24b}$$

$$v_c = v\sqrt{1 + \frac{g_0 K}{v}}, \tag{4.24c}$$

$$v_s = v\sqrt{1 - \frac{g_0 K}{v}}. \tag{4.24d}$$

According to this phenomenological picture, we expect the cluster charge sector to be gapless, while the spin sector may be gapped or gapless. The partial gap depends on the value of K_s, and leads to a CLL with $c = 1$ or $c = 2$. As the inter-leg interaction (U) does not involve the cluster charge bosonic field, Eq.(4.23) displays spin-charge separation with is no gap opening when $U = 0$ [20, 21]. When $K_s > 1$, the cluster spin mass is irrelevant. In both of these cases, both the charge and the spin sectors are gapless such that the system describes a 2CLL with $c = 2$ at zero loop of renormalization. When $K_s < 1$, the cluster spin gap is relevant. Like for the SDW of Sec.(4.2.1) we expect the mass to be positive. Unlike the SDW, the coarse grained nature of the cluster degree of freedom prevents an easy interpretation of the microscopic correlation functions obtained numerically. Given the repulsive nature of U, we nonetheless can expect an anti-alignment of the clusters along the rung. Then the phase is a spin-locked 1CLL with $c = 1$. The numerical simulations of Sec.(4.4) differentiates the 2CLL from the 1CLL, and show that the phase is indeed the spin-locked CLL with $c = 1$ as soon as $U > 0$.

4.3 Coupling SUSY conformal field theories: a phenomenological approach

In the intermediate coupling regime that captures the transition between weak and strong coupling, none of the above approaches is reliable. In particular, close to the transition point at $U = 0$, $V/t \simeq 5.7$, each chain is separately described by a $c = 3/2$ supersymmetric conformal field theory, composed of a compactified boson and a real fermion field with the same speed of sound. Coupling two chains thus presents a very rare opportunity to investigate the coupling of supersymmetric theories – something that, to the best of our knowledge, is not achievable in other cold gas settings.

In order to provide a qualitative understanding of the system dynamics in the vicinity of the SUSY point, we first recap what is known about the single chain, and then develop an effective, phenomenological field theory for the ladder. The latter theory results in two possible scenarios for the phase diagram. We resolve such dichotomy by means of tensor network simulations in the next section. It is important to note that we are interested here in the intermediate-interaction parameter regime, so that our approach is complementary to hard-constrained models [82].

4.3.1 Brief recap: SUSY critical point at $U = 0$

For a single chain, the vicinity of the SUSY phase transition point at $V/t \simeq 5.7$ can be phenomenologically described by the field theory of a massless compact bosonic field with $c = 1$ and a real fermion (with $c = 1/2$ when massless). Specifically, the effective Hamiltonian around the SUSY

conformal point reads

$$H^{\text{1SCF}} = \frac{v_{\text{B}}}{2} \int dx \left((\partial_x \varphi)^2 + (\partial_x \vartheta)^2 \right) + i \int dx \left(v_M \eta \partial_x \zeta + m_M \eta \zeta \right), \tag{4.25}$$

where φ and ϑ are the two conjugate compact bosonic fields of associated velocity v_B. The fields are not the microscopic bosonic field nor the cluster fields: in fact, their relation to the microscopic operators has not been determined. Over the transition regime, they do not acquire a mass. η and ζ are a pair of Majorana operators of velocity v_M and mass m_M. At the SUSY conformal point $m_M = 0$: at that point, $v_F = v_B$, and the Luttinger parameter of the bosonic field is fixed by the SUSY [82].

Based on a level spectroscopy analysis, one can interpret the phase transition towards the CLL as an inversion of the sign of m_M [21]. At the phenomenological level, one can interpret the real fermion as an Ising field, that is 'ordered' in the CLL phase, and 'disordered' in the TLL phase. It is thus a field that indicates the presence of composite particles as fundamental objects. It is worth mentioning that the appearance of a critical point with central charge larger than one, while certainly unusual for a single-species model, is not fully unexpected: indeed, it is known that by considering quantum dynamics beyond nearest-neighbor, even free theories can display phases with more than one-gapless channel - one paradigmatic example being tight-binding models where NN and NNN tunnelings are of the same order.

4.3.2   Coupling two SUSY critical points

Starting from the above picture, we develop a description to the ladder scenario. In the ladder, there are two compact bosonic degrees of freedom: their charge combination acts as an underlying field that remains gapless over the transition regime, while the spin combination shall be gapped to account for the presence of the SDW. The real fermion theory is also doubled.

Based on these two observations, the effective Hamiltonian in the vicinity of the SUSY conformal phase transition point $U = 0, V/t \simeq 5.7$ reads:

$$\begin{aligned} H^{\text{2SCF}} = \,&\frac{v_{\text{B},c}}{2} \int dx \left((\partial_x \varphi_c)^2 + (\partial_x \vartheta_c)^2 \right) \\ &+ \frac{v_{B,s}}{2} \int dx \left((\partial_x \varphi_s)^2 + (\partial_x \vartheta_s)^2 \right) + g \int dx \cos(\sqrt{8\pi K_s} \varphi_s) \\ &+ i \int dx \left(v_{M,S} \eta_S \partial_x \zeta_S + m_{M,S} \eta_S \zeta_S \right) + i \int dx \left(v_{M,A} \eta_A \partial_x \zeta_A + m_{M,A} \eta_A \zeta_A \right), \end{aligned} \tag{4.26}$$

where the indices c, S, s, and A stand for charge, symmetric, spin and anti-symmetric respectively. The charge (resp. spin) boson and symmetric (resp. anti-symmetric) Majorana fermions are symmetric (resp. anti-symmetric) combinations of the fields of the two legs. By consistency with our results in Sec.(4.2.1), $g > 0$ in the SDW phase and the sine-Gordon interaction is relevant. There is no umklapp term here as neither the weak or strong coupling regimes support an insulting phase.

In principle, other terms could be included in the low-energy theory. Those could either couple the bosonic fields to the fermions, or the two fermions. The latter are likely not relevant to our description: since the system is symmetric under chain inversion, a coupling between anti-symmetric and symmetric clustering real fermionic fields is unlikely. It is instead hard to justify, in general, the absence of terms coupling fermions to bosons. In fact, with the possible exception at the vicinity of the $U = 0$ critical point, there is no microscopic reason that suggests not to include them: however, the lack of an exact lattice-to-field operator mapping prevents us from having a clear idea on their possible functional form. We will thus proceed under the assumption that those terms are irrelevant, and verify this a posteriori in the next section.

Under these assumptions, we can treat the bosonic and fermionic sectors of the theory in a modular manner:

- charge field φ_c: this field is always gapless, and describes collective density fluctuations (either starting from a single particle description, or from a cluster one);

- spin field φ_s: this field is strongly pinned in the SDW phase, owing to the value of the spin-Luttinger parameter $K_s \ll 1$. In such regime of the sine-Gordon model, it is still possible for the system to undergo a Gaussian transition at $g = 0$: this transition is described by a $c = 1$ CFT, and separates two phases with opposite pinning of the spin field;

- symmetric fermionic field: we expect this field to undergo an Ising transition, separating a regime where microscopic degrees of freedom are clusters, from the one where those are single particle fields;

- anti-symmetric fermionic field: this field might lead to interesting dynamics in case of unbalanced chains (for instance, including clusterization only in one of them). However, since such imbalance is not present in the strong coupling limit if the U(1)×U(1) symmetry is preserved, we do not expect this sector of the theory to be of relevance here.

The aforementioned considerations open two possibilities for the quantum criticality. We illustrate these two scenarios moving from weak to strong coupling by, e.g., increasing V and $U > 0$, in the following.

P.1 In the first one, the spin field undergoes a Gaussian transition first into a CDW phase, and then clustering occurs via an Ising transition. The sequence of central charges here is $c = 1$ (SDW), $c = 2$ (Gaussian critical line), $c = 1$ (CDW), $c = 3/2$ (Ising critical line), $c = 1$ (spin-locked CLL).

P.2 The second scenario would instead see first cluster forming, and subsequently, a Gaussian transition in the spin sector. The sequence of central charges here is $c = 1$ (SDW), $c = 3/2$ (Ising critical line), $c = 1$ (cluster liquid that we cannot fully characterize), $c = 2$ (Gaussian transition), $c = 1$ (spin-locked CLL).

Here, we rule out the scenario where both transitions happen along the same line, as this will require fine tuning (to the best of our understanding). We note that, while hard to diagnose, it may be possible under both scenarios to recover SUSY along the critical $c = 3/2$ line.

Since we are lacking even a phenomenological functional form for the effective parameters in Eq.(4.26) as a function of (U, V), it is not possible to determine which of the two scenarios of SUSY-breaking is actually taking place. We will thus scrutinize our prediction against numerical simulations in the next section.

4.4 Numerical results

To validate the analytical approaches and extend the prediction to larger U, we now use exact diagonalization (ED) for small system-sizes and tensor-network (TN) numerical simulations to tackle larger systems sizes. ED (see Sec.(4.4.1)) hints at the phase diagram Fig.(4.1b). The picture is completed Sec.(4.4.2) by the infinite Density Matrix Renormalization Group method (iDMRG), a variational methods to obtain a matrix-product state (MPS) approximation of the ground state directly in the thermodynamic limit. Using iDMRG, we compute the central charges and useful correlation functions of all phases and transitions.
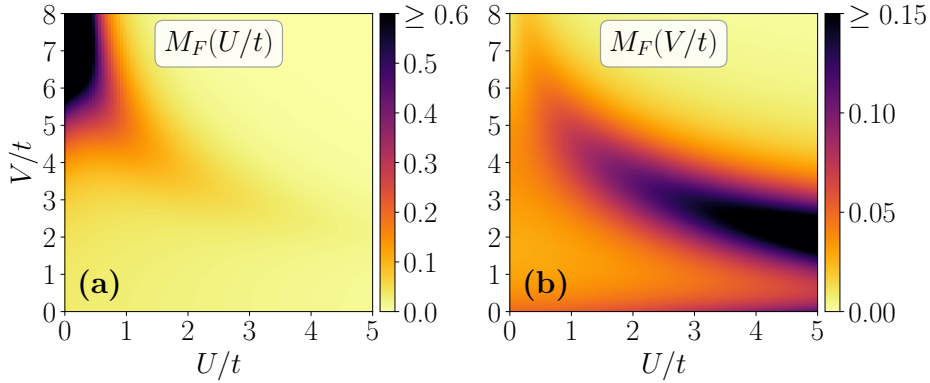
FIGURE 4.3: The fidelity-susceptibility M_F (see Eq.(4.28)) in the $(U/t, V/t)$-plane while varying the parameters (a) U/t and (b) V/t. Results are obtained via exact diagonalization of a system of size $L = 10$ with density $\nu = 2/5$. In (a), large values of $M_F(U/t)$ near the $U/t = 0$ line for $V/t \gtrsim 5.7$ could signal a phase transition between two decoupled CLL (2CLL), that appears for $U/t = 0$, to the spin-locked 1CLL phase for $U/t > 0$ (see the text for details). On the other hand, in (b) a transition between the SDW phase and the CLL phase can be seen. Moreover, for small V/t, a weak signature of 2TLL-SDW transition, pertaining to the BKT transition predicted in Sec.(4.2.1), is visible.

4.4.1   Exact diagonalization

The first step in the numerical analysis of the considered model relies on the exact diagonalization (ED) of the quantum Hamiltonian for small systems-sizes. This method will give access to the physics of the whole phase diagram with accuracy limited only by the finite size of the system [74].

Since the model has an internal U(1)×U(1) symmetry, we fix the symmetry sector in which we want to analyze the ground state, i.e., the constant filling ν_ℓ, $\ell = \pm$, for each chain. This restricts us to diagonalize the Hamiltonian for system-sizes such that the total particle number in each chain $N_\ell = \nu_\ell L$ is an integer. Furthermore, since we want to understand the effect of interactions in the CLL phase, we also need to consider fillings and system sizes which are commensurate with this phenomenon. The smallest system size that fulfills these constraints is $L = 10$ for $\nu_\pm = 2/5$ and $r_C = 2$. Indeed, 10 sites are needed for $U = t = 0$ and $V > 0$ to represent the classical ground states on one chain that are combined together in a CLL ground state by second order perturbation theory in t (see Fig.(4.2a)).

An useful tool to verify the overall structure of the phase diagram is provided by the fidelity, defined as

$$F(h, \delta h) = |\langle gs(h)|gs(h + \delta h)\rangle| \tag{4.27}$$

with h being either U/t or V/t, as a probe of the phase diagram at different values of U/t and V/t. It is known that the fidelity displays a minimum in a finite-size system when crossing what would be a quantum phase transition in the thermodynamic limit [83]: this is due to the fact that transition lines typically correspond to parameter regimes where the (finite-size) ground state wave function changes very rapidly with respect to changes in the microscopic parameters. At the quantitative level, this is typically better detected by considering the fidelity-susceptibility [84], defined as:

$$M_F(h) = \lim_{\delta h \to 0} \frac{-2\ln F(h, \delta h)}{(\delta h)^2}. \tag{4.28}$$

It shows a maximum near the transition (and diverges in the thermodynamic limit at the transition), and is more commonly considered in the literature since it displays universal features at quantum critical points [85].

The scans of the fidelity-susceptibility M_F in the $(U/t, V/t)$-plane while varying either U/t or V/t are presented in Fig.(4.3). The fidelity-susceptibility plots suggest the presence of three transitions, which we summarize in the following observations:

1. The scan of $M_F(U/t)$ in Fig.(4.3a) suggests that for $V/t \gtrsim 5.7$ there is a transition between the decoupled 2CLL phase at $U/t = 0$ to an another phase for $U/t > 0$;

2. The trends of $M_F(V/t)$ in Fig.(4.3b) clearly shows a transition between the SDW and the CLL phase also for $U/t > 0$, as predicted by the theory. At large $U/t > 3$, an intermediate phase seems to appear;

3. Furthermore, there is a weak signal near small V/t in Fig.(4.3b).

All of the observations above are consistent with the weak coupling theory presented in Sec.(4.2). In fact, not only the strongest signal confirms the presence of a phase transition between a liquid regime (the SDW phase) and a clustering regime, but there is also a weak signal for the transition from the 2TLL phase to the SDW phase predicted at small V/t, and finite U/t. The weakness of the signal could be related to the BKT behavior of this transition [86].

At strong coupling in V/t, the simulations suggest that there might be one transition from 2CLL phase (with $c = 2$) to 1CLL phase (with $c = 1$) for $U/t \neq 0$ if the cluster spin-gap is relevant when $K_s < 1$ (see Eqs.(4.23,4.24)). In the regime of intermediate V and finite U, the transition between SDW and CLL seems to split and give rise to an intermediate phase, as predicted by both the scenarios in Sec.(4.3).

However, since we are only restricted to one small system-size of $L = 10$ for the ED calculations, the above observations should be interpreted with caution. Moreover, the ED results are unable to draw any conclusions about the two possibilities coming out of the phenomenological model near the SUSY point given in Sec.(4.3), as the horizontal signal in Fig.(4.3b) is very broad and can not distinguish between one or two transitions.

4.4.2 Tensor network analysis

In this part, we report the results of a numerical analysis using tensor networks (TN) for the system at hand. First we map out the topology of the entire phase diagram of the system in terms of the entanglement entropy, in order to determine the existence of different phases and phase transitions. Specifically, we show the existence of a charge-density wave (CDW) phase sandwiched between the SDW and the CLL phases. Then we characterize different phase transitions and phases by means of central charges and correlation functions.

The numerical analysis is based on the widely successful density matrix renormalization group (DMRG) [62, 63, 64, 65] method using the matrix-product state (MPS) ansatz [75, 76]. This ansatz relies on the truncation of the Schmidt spectrum, keeping only the χ (which will be referred to as the bond dimension) largest values, therefore approximating the target state with a quantum state that has area-law entanglement [75], and which admits an efficient representation for one-dimensional gapped systems even at large (as well as infinite) sizes.

For our purpose, we probe the system directly at the thermodynamic limit using the infinite DMRG (iDMRG) [87, 88] method in translationally invariant infinite MPS (iMPS) representation [89] (see Ref. [90] for an introduction). One advantage of considering iDMRG over the standard finite-size DMRG for our purpose is that it allows us to circumvent the strong boundary effects that clustering potentials induce at finite-sizes (see e.g., Refs. [20, 91]), as they do not occur in iDMRG simulations.

Since our system Hamiltonian enjoys global U(1)×U(1) symmetry corresponding to the conservation of both the densities ν_+ and ν_-, we employ U(1)×U(1) symmetric iMPS ansatz for our

simulations [92, 93]. Moreover, as mentioned in the previous subsection 4.4.1, to capture the onset of the CLL phase with densities $\nu_\pm = 2/5$ and $r_C = 2$, the iMPS representation needs a unit cell of $L = 10m$ sites with $m \in \mathbb{N}$. In our analysis, we have verified that the results remain unaltered for $m \geq 1$, so that we can faithfully restrict ourselves to the lowest possible unit cell of size $L = 10$ sites in the iMPS representation.

For the characterization of different phases and phase transitions of the system, we consider two quantities, namely the system correlation length ξ and the von Neumann entanglement entropy $\mathcal{S}$. The correlation length $\xi_{\mathcal{O}}$ corresponding to any local operator $\mathcal{O}_j$ is defined by the length scale associated with the correlation function $\langle \mathcal{O}_j \mathcal{O}_{j+R} \rangle - \langle \mathcal{O}_j \rangle \langle \mathcal{O}_{j+R} \rangle \sim \exp\left(-R/\xi_{\mathcal{O}}\right)$. Then the correlation length ξ of the quantum state is given by the maximum of them as $\xi = \max(\xi_{\mathcal{O}_1}, \xi_{\mathcal{O}_2}, \xi_{\mathcal{O}_3}, ...)$. On the other hand, a given pure quantum state $|\psi\rangle$ belonging to a Hilbert space $\mathcal{H}_{AB} = \mathcal{H}_A \otimes \mathcal{H}_B$ can be written as $|\psi\rangle = \sum_k \lambda_k |e_k^A\rangle \otimes |e_k^B\rangle$, where λ_k's are the Schmidt coefficients and $|e_k^{(A)B}\rangle$'s form orthonormal basis in $\mathcal{H}_{A(B)}$. The von Neumann entanglement entropy across the bipartition $A : B$ is then defined as

$$\mathcal{S} = -\sum_k \lambda_k^2 \ln \lambda_k^2. \tag{4.29}$$

It is to be noted that both the Schmidt coefficients and the entanglement entropy across any bond can be calculated very efficiently in the MPS or iMPS representation [75].

The theoretical prediction suggests us that all the possible phases in the system are described by conformal field theories, where both the correlation length ξ and the entanglement entropy $\mathcal{S}$ diverge in the thermodynamic limit. Of course, such divergences cannot be captured by the iMPS ansatz with finite bond dimension χ. Instead, the finite value of χ will impose a length scale given by a finite value of the correlation length ξ_χ [2] that scales as $\xi_\chi \propto \chi^\kappa$ with κ being a scaling exponent [94, 95, 96]. The χ-dependent entanglement entropy $\mathcal{S}_\chi$ is then follow the following well-known scaling formula [97, 98, 99]:

$$\mathcal{S}_\chi = \frac{c}{6} \ln \xi_\chi + b', \tag{4.30}$$

where c is the central charge for the underlying conformal field theory and b' is a non-universal constant.

By varying the iMPS bond dimension in the range $[64, 1280]$, we use Eq.(4.30) to characterize different phases and phase transitions in terms of the central charge c. We refine the characterization by computing the correlation functions of the form

$$\mathcal{C}_{\mathcal{O}}(R) = \langle \mathcal{O}_j \mathcal{O}_{j+R} \rangle - \langle \mathcal{O}_j \rangle \langle \mathcal{O}_{j+R} \rangle, \tag{4.31}$$

where $\mathcal{O}_j$ is a local operator. When $R > \xi_\chi$ all correlations will trivially decay exponentially, restricting the extension of the correlation function to $R \approx \xi_\chi$ at maximum.

4.4.3   The phase diagram: a glimpse from the von Neumann entropy

We present the pattern of the entanglement entropy $\mathcal{S}$ and its derivatives with respect to the system parameters U/t and V/t in the $(U/t, V/t)$-plane in Fig.(4.4) for the iMPS bond dimension of $\chi = 256$. Interestingly, all the scans clearly pick up the signature of the phase transition between the SDW and the CLL phases with increasing V/t for all values of the coupling strength U/t. Moreover, similar to the feature of Fig.(4.3a) the derivative of $\mathcal{S}$ with respect to U/t (see Fig.(4.4b)) also

---

[2]For an iMPS with finite bond dimension χ, the correlation length ξ_χ can be defined as

$$\xi_\chi = -1/\ln|\epsilon_2|$$

where ϵ_2 is the second largest eigenvalue of the iMPS transfer matrix [90].
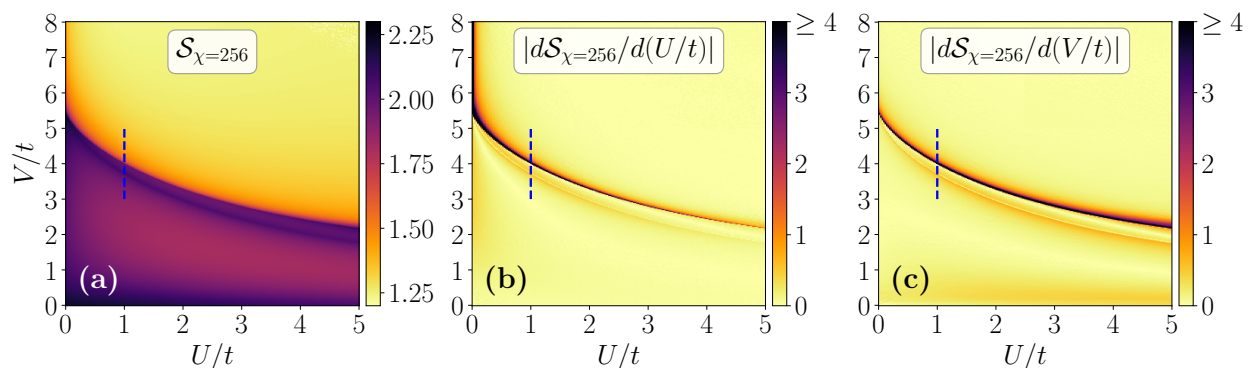
FIGURE 4.4: (a) The entanglement entropy $\mathcal{S}$ and its derivatives with respect to the system parameters (b) U/t and (c) V/t in the $(U/t, V/t)$-plane. The quantities are computed by the iDMRG algorithm with bond dimension $\chi = 256$. The blue dashed lines represent the cut along which the analyses of Fig.(4.5) are performed.

shows the sign of the phase transition between the decoupled 2CLL phase at $U/t = 0$ for $V/t \gtrsim 5.7$ to a coupled CLL phase at $U/t > 0$.

However, on a closer inspection of the scans (specifically, Figs.(4.4a,c)) another signal of a second phase transition at $U/t > 0$ and appearance of another phase sandwiched between the SDW and CLL phases become apparent. This transition and the phase at $U/t > 0$ originates from the $c = 3$ SUSY point at $U/t = 0$ and $V/t \simeq 5.7$. These observations of having another phase transition line and existence of a sandwiched phase corroborate the phenomenological analysis presented in Sec.(4.3).

From the analysis of Fig.(4.4), it is also clear that the signature of the BKT transition between the 2TLL and the SDW phases at low V/t values cannot be quantitatively captured from such numerical analysis, similarly to what has been observed from the ED results. What we can estimate is a lower bound for the $c = 1$ phase based on the study of the central charge, as the latter typically overestimates the extent of critical phases (in our case, the $c = 2$ one).

4.4.4 Coupling SUSY conformal field theories: a numerical perspective

Based solely on the entanglement entropy analysis, it is already possible to discern whether one of the two proposed scenarios of coupled-SUSY theories presented in Sec.(4.3) is describing the vicinity of the $c = 3$ critical point.

In Figs.(4.5a,b), we present the entanglement entropy $\mathcal{S}_\chi$ and the correlation length ξ_χ respectively as functions of V/t for fixed $U/t = 1$ with different bond dimensions in the range $\chi \in [128, 640]$. The variations of both $\mathcal{S}_\chi$ and ξ_χ display sharp non-analytic kinks in their profile signalling the presence of two phase transitions – coherent with both scenarios of Sec.(4.3). The location of the transitions change with respect to the bond dimension χ (or more precisely with the correlation length ξ_χ) following the standard power-law scaling:

$$(V_c/t)_\chi = (V_c/t)_{\chi \to \infty} + a\xi_\chi^{-\Xi}, \tag{4.32}$$

where V_c denotes the transition point and Ξ is a scaling exponent with a being a constant. While Ξ in Eq.(4.32) appears to be analogous to the inverse of the thermodynamic critical exponent ν, the two quantities are a priori unrelated. The first is associated with an entanglement-based length scale introduced by the numerical method, whereas the second is associated with a length scale imposed by the inverse of the smallest gap in the system (which is zero at every point of the phase diagram at this filling). In Figs.(4.5a,b), the locations of the transitions for different bond dimensions are present by the dashed lines. Importantly, the size of the intermediate phase is sufficiently large so
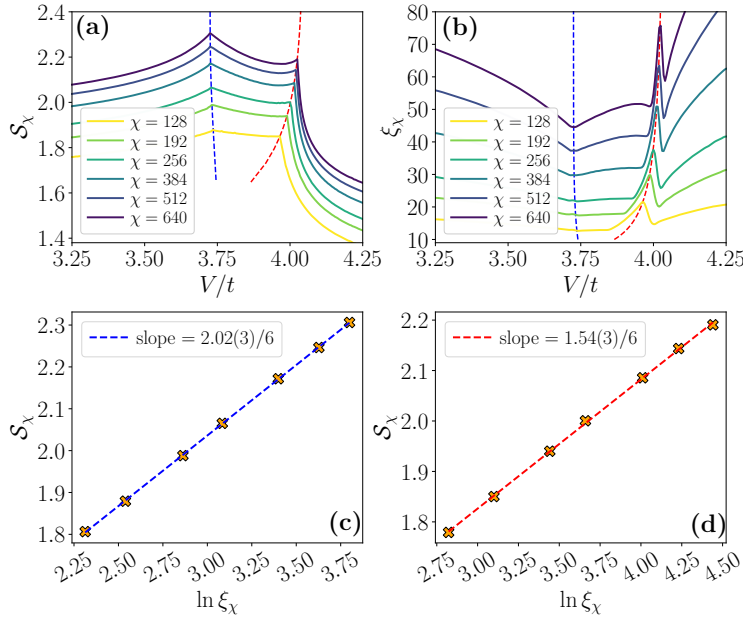
FIGURE 4.5: The variations of (a) the entanglement entropy $\mathcal{S}_\chi$ and (b) the correlation length ξ_χ with respect to V/t for fixed $U/t = 1$ and for different bond dimensions χ. The blue dashed lines in (a) and (b) represent the SDW-CDW transition, while the red dashed lines are for the CDW-CLL transition. (c)-(d) The scaling of the entanglement entropy according to Eq.(4.30) across the χ-dependent transition points for (c) the SDW-CDW and (d) the CDW-CLL phase transitions. The central charges that we obtain from the scaling for these transitions are respectively $c = 2.02(3)$ and $c = 1.54(3)$.

that a finite-size characterization will be possible via correlation functions: we will come back to this point below.

To precisely obtain the central charges of these transitions, instead of using Eq.(4.30) for fixed values of U/t and V/t, we perform the same scaling of the entanglement entropy across the χ-dependent transition points (marked by the blue and red dashed lines in Figs.(4.5a,b)) as prescribed in Ref. [90]. Figs.(4.5c,d) show such scaling across these two phase transitions. Interestingly, the central charges that we obtain from these scaling are compatible at the percent level with $c = 2$ for the SDW-CDW transition and $c = 3/2$ for the CDW-CLL transition (see Figs.(4.5c,d)). This numerical finding confirms the scenario P.1 presented in Sec.(4.3).

4.4.5 Characterization of the phases: entanglement properties

We now characterize the SDW, CDW, CLL, and 2TLL phases that appear in the system for $U/t > 0$ by the scaling of the entanglement entropy against the bond dimension, extracting the corresponding central charges. Specifically, here we show that all these phases – except the one at weak intra-chain and strong inter-chain coupling – have $c = 1$.

Our theoretical analysis using the Abelian bosonization in Sec.(4.2.1) tells that the spin sector in the SDW phase is gapped, while the charge sector is not, thereby suggesting that the phase is of $c = 1$. The phase is adjacent to a BKT transition that requires too large bond dimensions to be sharply demarcated. Thus, any points in its vicinity cannot be sharply identified by deducing their central charge, unless very large bond dimension is taken that may not be always possible in practical simulations. In Figs.(4.6a,b), we show the variations of the entanglement entropy $\mathcal{S}_\chi$ with the correlation length ξ_χ in two points in the SDW phase respectively with bond dimensions in the wide range of $[64, 1280]$. By fitting the scaling formula of Eq.(4.30) to the data in different

ranges of χ, we observe that the slopes of the curves reduce with higher values of χ and slowly approach to the expected value of $1/6$.

The similar trend in the behavior of the entanglement entropy is observed in the sandwiched CDW phase, where the slope of the curve reduces from $\sim 1.5/6$ to $\sim 1.3/6$ with increasing bond dimension (see Fig.(4.6c)). This is due to the fact that there are two very nearby transitions with central charge $c > 1$, and we need very large bond dimensions to resolve the CDW phase properly. However, since, in lattice models, quantum phases with only integer values of central charges are stable, the data of Fig.(4.6c) confirms that the CDW phase is of $c = 1$.

On the other hand, deep in the CLL phase with $U/t > 0$ (see Fig.(4.6d)), we can faithfully obtain the central charge of $c = 1$. For the entire range of $\chi \in [64, 1280]$, the slopes of the curves stay stick to $1/6$ in the CLL phase. This proves that the cluster spin-gap in this CLL phase in non-zero ($K_s < 1$ in Eqs.(4.23,4.24)), and the cluster excitations from both the chains are coupled (i.e., a spin-locked CLL).

Figs.(4.6e,f) show the same scaling of entanglement entropy in two points deep in the 2TLL phase. The central charge of $c = 2$, as predicted by the Abelian bosonization method, can be faithfully extracted by the scaling for the entire range of bond dimension considered here.
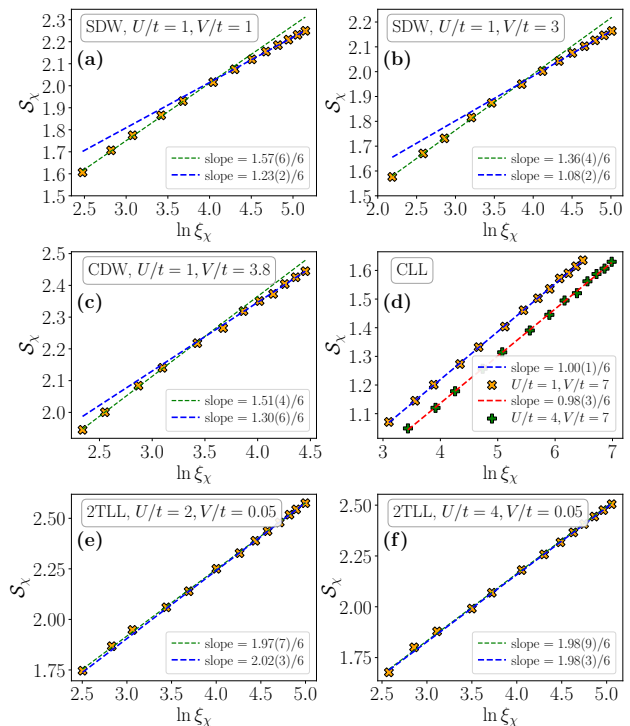
FIGURE 4.6: The behavior of the entanglement entropy $\mathcal{S}_\chi$ with respect to the correlation length ξ_χ in different phases for the iMPS bond dimension $\chi \in [64, 1280]$ ($\chi \in [96, 1280]$ for CDW phase). (a) and (b) correspond to two points in the SDW phase, (c) and (d) are for the CDW and the CLL phases respectively, while (e) and (f) correspond to the 2TLL phase. In (a)-(c), (e), and (f) the thin green dotted lines correspond to the fits in the range $\chi \in [64, 384]$ ($\chi \in [96, 384]$ for the CDW phase in (c)), while the blue dashed lines correspond to the fits for $\chi \in [512, 1280]$.

4.4.6 Correlation functions in the SDW and CDW phases

We now move on to analyze correlation functions (see Eq.(4.31)) in the SDW and CDW phases. Specifically, we first consider the spin correlation function

$$\mathcal{C}_{S^z}(R) = \langle S^z_j S^z_{j+R} \rangle - \langle S^z_j \rangle \langle S^z_{j+R} \rangle, \tag{4.33}$$

with $S^z_j = (n_{j,+} - n_{j,-})/2$, and the charge correlation function

$$\mathcal{C}_n(R) = \langle n_j n_{j+R} \rangle - \langle n_j \rangle \langle n_{j+R} \rangle, \tag{4.34}$$

with $n_j = (n_{j,+} + n_{j,-})$, in the SDW and in the CDW phases. However, as mentioned before, these correlation functions can be faithfully interpreted only when $R \lesssim \xi_\chi$, and in these two phases we have $\xi_\chi \sim 100$ for the largest bond dimension ($\chi = 1280$) at our disposal.

Figs.(4.7a,b) depict the correlation functions $\mathcal{C}_{S^z}(R)$ and $\mathcal{C}_n(R)$ in the SDW and CDW phases for $R \leq 100$.

We remark that for this small range of R differentiating the power-law decay with the exponential decay is possible only under the assumption of a correlation length shorter that ξ_χ. Still, the trends
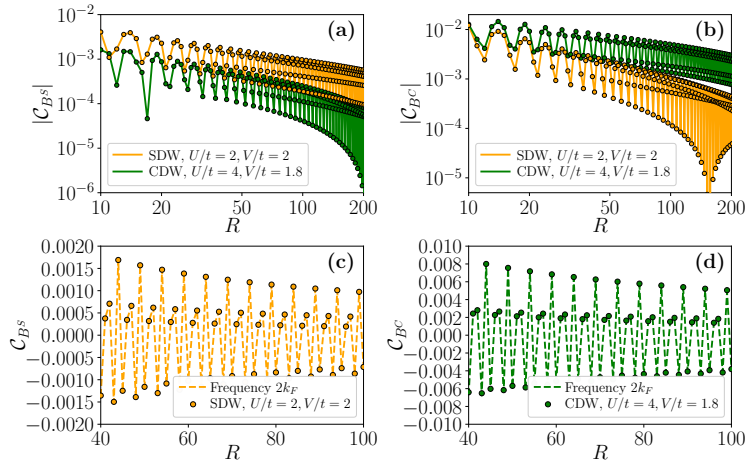
FIGURE 4.7: The behaviors of (a) the spin correlation function $\mathcal{C}_{S^z}(R) = \langle S_j^z S_{j+R}^z \rangle - \langle S_j^z \rangle \langle S_{j+R}^z \rangle$ and (b) the charge correlation function $\mathcal{C}_n(R) = \langle n_j n_{j+R} \rangle - \langle n_j \rangle \langle n_{j+R} \rangle$ as functions of the distance R in the SDW and CDW phases. Here both axes are in the logarithmic scale. (c)-(d) The fits (according to Eq.(4.35)) of the spin and charge correlations respectively in the SDW and CDW phases.

of correlations in Fig.(4.7) are quite distinctive from each other. Specifically, we observe slow power-law decay of the spin correlation and fast (exponential) decay of the charge correlation in the SDW phase, numerically confirming the spin-density wave nature of the phase. Exactly opposite is seen in the CDW phase, that has oscillating slow (power-law) decay of the charge correlation. This provides convincing proof that this sandwiched phase is indeed a CDW.

To correctly get the proper frequencies of the oscillations in the algebraically decaying correlations, we numerically fit them using the following formula:

$$\mathcal{C}(R) \sim \cos{(kR)}\, R^{-\beta}. \tag{4.35}$$

In Figs.(4.7c,d) we show such fits for the spin and the charge correlations respectively in the SDW and CDW phases. In both the cases, the numerical fits show that the frequency of oscillations are $k = 2k_F$ as expected from Eqs.(4.10,4.13,4.14).

4.4.7 Correlation functions in the spin-locked CLL phase

By analyzing the spin and charge correlation functions in the spin-locked CLL phase, we observe that, unlike the SDW and CDW phases, both the correlations follow power-law behavior (see Figs.(4.8a,b)). Both the numerical fits using Eq.(4.35) and their Fourier transformation Fig.(4.8c) suggests that the frequencies of the oscillations are $k = 3k_F/2 = 3\pi/5$ for the spin correlation function and $k = 2k_F = 4\pi/5$ for the charge correlation. $k = 3k_F/2$ is the cluster Fourier momentum as it appears in Eq.(4.17) and translates the specific cluster instability of the Luttinger liquid. Surprisingly, this feature is absent in the charge correlation function, and is instead replaced by a peak at $2k_F$. Since we lack a controlled operator mapping between lattice and underlying fields, it is not clear what is the origin of such property. Still, we point out that single chain correlations do show a strong peak at the clustering point. Indeed, the correlation function for the single-chain density $n_\ell, \ell = \pm$, is

$$\mathcal{C}_{n_\ell}(R) = \langle n_{j,\ell} n_{j+R,\ell} \rangle - \langle n_{j,\ell} \rangle \langle n_{j+R,\ell} \rangle. \tag{4.36}$$

Fig.(4.8d) shows the Fourier transform of the correlation function $\mathcal{C}_{n_+}$. This Fourier transform shows both – a peak at the frequencies $k = 3\pi/5$ corresponding to the cluster instability and
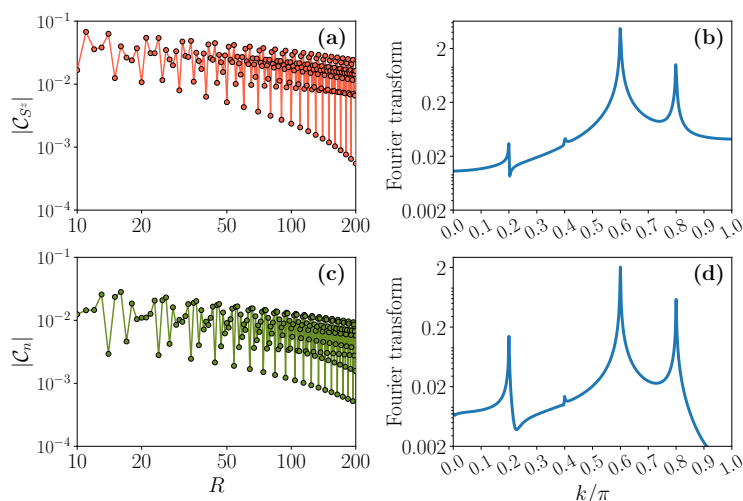
FIGURE 4.8: (a) The spin correlation $\mathcal{C}_{S^z}(R)$ and (b) the charge correlation $\mathcal{C}_n(R)$ as functions of the distance R in the CLL phase. The dashed lines show the numerical fits according to Eq.(4.35). The subplot (c) depicts the Fourier transform of the correlations $\mathcal{C}_{S^z}(R)$ and $\mathcal{C}_n(R)$, while (d) shows the same for the correlation function of the single-chain density n_+.

$k = 4\pi/5$ corresponding to the possible rivalling density wave instability. This observation suggests that one possible explanation for the lack of cluster peaks in the CDW correlator is that inter-leg correlations are out of phase with respect to intra-leg ones.

4.4.8 The complete picture from the numerical analysis

The above numerical investigations using both ED and TN methods provide us the full picture about the system phase diagram and different phases. Here we summarize the details of the phase diagram with increasing V/t in the following (compare the schematic phase-diagram in Fig.(4.1b)):

1. At small values of $V/t \sim 0$, the ground state of the system is in standard 2TLL phase (with $c = 2$).

2. With increasing V/t, a BKT transition appears and the system goes into the $c = 1$ SDW phase where quasi-long-range order in the spin sector exists. In the phase, the spin sector becomes gapped while the charge sector remains gapless. The precise determination of this BKT transition, predicted by Abelian bosonization in the weak coupling regime, is beyond the scope of the numerical tools used here.

3. There exists a $c = 2$ Gaussian transition that separates the SDW phase from the CDW phase. Across this transition the spin-gap closes, so that both the charge and the spin sectors are gapless resulting in $c = 2$.

4. In the CDW phase, the spin sector again becomes massive with disordered paramagnetic nature, while the charge sector remains gapless with a charge density wave order giving us $c = 1$.

5. After the CDW phase, a $c = 3/2$ phase transition appears, where one part $c = 1$ is again from the gapless charge sector, and the another part $c = 1/2$ comes from the Ising type transition same as in the single-chain SUSY point.

64

Chapter 4. Phase diagram of Rydberg-dressed atoms on two-leg square ladders: Coupling supersymmetric conformal field theories on the lattice

6. At high values of V/t and $U/t > 0$, a $c = 1$ CLL phase exists. However, unlike the 2CLL phase (with $c = 2$) at $U/t = 0$, the clusters in both the chains are coupled, and the cluster spin-gap is non-vanishing that results into $c = 1$.

Chapter 5

Phase diagram of Rydberg-dressed atoms on two-leg triangular ladders

In the previous chapter we considered square ladder lattices for dressed Rydberg atoms at filling $\nu = 2/5$, with the two legs interacting, and without inter-leg hopping. Such geometry effectively couples two SUSY theories at a fine-tuned point separating a Tomonaga Luttinger liquid (TLL) and a CLL. All phases and transitions involved in the phase diagram surprisingly appear as soon as the two chains interact. Both the TLL and CLL are 'spin-locked' and the critical point extends into a Gaussian phase transition line, a possibly SUSY conformal transition, and a partially gapped phase in between.

In this chapter we extend this exploration to triangular lattice geometries. Such a setting is the minimal geometry where geometric frustration, interaction clustering, and kinetic dynamics can compete. Our main result is the phase diagram of the system that is schematically depicted in Fig.(4.1: it is considerably richer than - and fundamentally different from - the square lattice case. The ability to manipulate the coupling of the two SUSY conformal field theories by *e.g.*, increasing the range of the inter-leg interaction would be useful to investigate SUSY phenomenology [78, 27]. By using a triangular geometry, we show that as soon as the range is extended, only a single, potentially SUSY, transition exists between the 'spin-locked' TLL and CLL. In contrast, we show the existence of three phases exclusive to strong coupling, establishing the setup as a promising platform to study commensurability in extended Hubbard models.

5.1 The Triangular ladder model

We study a triangular ladder of spinless hard-core bosons at $\nu = 2/5$ filling (on average two filled sites for every five sites in each chain, see Fig.(5.1a)). Such a filling supports clustering in the classical limit. The Hamiltonian of the system reads:

$$ H = - t \sum_{i,\ell} \left(b_{i,\ell}^\dagger b_{i+1,\ell} + \text{H.c.} \right) + U \sum_i n_{i,+} n_{i,-} + U_1 \sum_i n_{i,+} n_{i+1,-} + V \sum_{i,\ell} \sum_{j=1}^{r_C} n_{i,\ell} n_{i+j,\ell}. \quad (5.1) $$

where $b_{i,\ell}^\dagger$ is the creation operator for hard-core bosons on site i of chain $\ell = \pm$ and $n_{i,\ell} = b_{i,\ell}^\dagger b_{i,\ell}$. t is the intra-chain hopping, U and U_1 are the anisotropic nearest-neighbor inter-chain interaction amplitude, V is the intra-chain interaction amplitude of range $r_C \in \mathbb{N}$. As there is no inter-chain tunneling, the U(1) charge of each leg is conserved separately such that the Hamiltonian Eq.(5.1) is U(1)×U(1) symmetric. Densities are tuned by the loading scheme. For simplicity, we take $r_C = 2$ and $U_1 = U$ unless otherwise stated.

We now briefly summarize the phase diagram at weak-coupling, that is obtained using both weak-coupling bosonization, cluster bosonization. These approaches follows closely previous works [20,
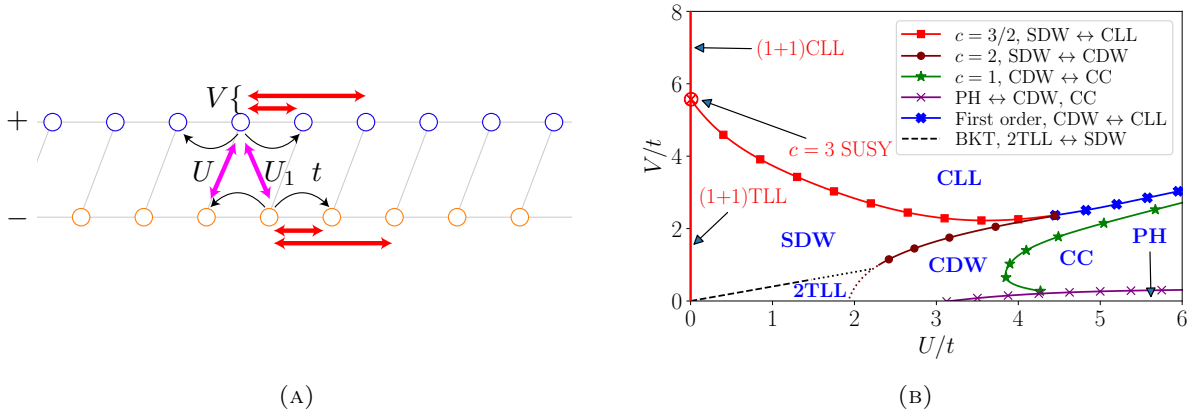
(A)   (B)

FIGURE 5.1: (A) The system of Rydberg-dressed hardcore bosons on a two-leg triangular lattice with intra-leg soft-shoulder interaction (V) of range 2, anisotropic inter-leg interactions (U, U_1), and intra-chain nearest-neighbor hopping (t). (B) The reach landscape of the phases of the triangular ladder system for a filling of $2/5$ with $U_1 = U$. For $U/t > 0$, the phase diagram consists of $c = 2$ Tomonaga-Luttinger liquid (2TLL), $c = 1$ spin density wave (SDW), $c = 1$ charge density wave (CDW), $c = 1$ cluster Luttinger liquid (CLL), polarized holonic (PH) phases, and fully-gapped cluster crystal (CC) (see text) as marked in the figure. Different lines correspond to different phase transitions as depicted in the legend. At $U = 0$ (red line) the two legs are independent and display $c = 1 + 1$ TLL and $c = 1 + 1$ CLL phases separated by $c = 3$ supersymmetric point (red crossed-dot).

21, 25]. We thus refer to the Appendices A and B for the analytical details of the approach, and only present its results below.

The red line ($U = 0$) in Fig.(5.1b) corresponds to two decoupled chains [20, 21]. The phase diagram of a single chain displays a TLL for $0 < V/t \lesssim 5.7$, and a CLL for $V/t \gtrsim 5.7$. Both the TLL and the CLL have a central charge $c = 1$. They are separated by a SUSY conformal phase transition point of central charge $c = 3/2$ at $V/t \simeq 5.7$ identified numerically [21].

By adding the interaction (U) between two of these chains, we obtain the rest of the phase diagram as shown in Fig.(5.1b). We map the leg index to a SU(2) spin-$1/2$ degree of freedom to use the Hubbard model formalism and vocabulary [8, 9, 10]. When $U > 0$, the phase diagram displays a Spin Density Wave (SDW) TLL with $c = 1$ and a fully gapless TLL with $c = 2$ (2TLL) at weak coupling when $U/t \leq 5V/2t \ll 1$ and $5V/2t \leq U/t \ll 1$ respectively. These two are separated by a Berezinskii-Kosterlitz-Thouless (BKT) transition.

For strong shoulder potential ($V/t \gtrsim 5.7$), we show that the phase is a spin-locked CLL with $c = 1$ for $U \neq 0$. We predict the separation of the SDW and the CLL by a single phase transition line of central charge $c = 3/2$ extending from the $c = 3$ SUSY critical point. The value of this central charge hints that this phase transition line might itself be supersymmetric. This behavior contrasts with the square ladder geometry [25] where the SDW and CLL are separated by two transitions and one Luttinger liquid phase instead. As we will now show, the separation by a single transition occurs as soon as $U, U_1 > 0$. Furthermore, the phase diagram Fig.(5.1b) near the SUSY point is qualitatively unchanged for any $U_1/U > 0$ justifying focusing on $U_1 = U$ for simplicity.

5.2   Numerical simulations

We confirm these predictions and explore the large U/t regime using both exact diagonalization (ED) [74] for a system of 10 sites with periodic boundary condition and infinite density matrix renormalization group (iDMRG) techniques [62, 63, 64, 65, 88, 75, 76, 90].
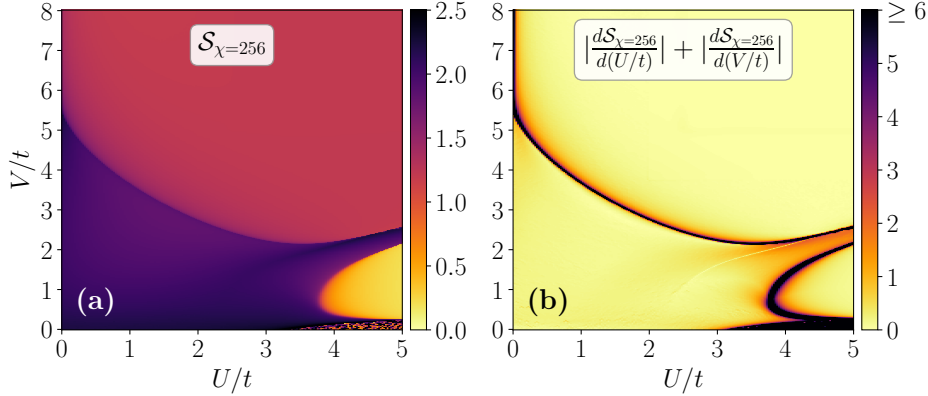
FIGURE 5.2: (a) The entanglement entropy $\mathcal{S}$ and (b) the sum of the absolute values of derivatives with respect to the system parameters U/t and V/t in the $(U/t, V/t)$-plane. The quantities are computed by the iDMRG algorithm with bond dimension $\chi = 256$. The BKT and 2TLL $\leftrightarrow$ CDW transitions are too narrow to stand out when $\chi = 256$.

5.2.1 Phase diagram of the regime $U = U_1$

We first characterize the system using iDMRG to effectively access the system directly at the thermodynamic limit. The set χ-th value of the bond dimension of the matrix-product state ansatz for the iDMRG simulation introduces a maximal length-scale (sometimes referred to as correlation length [1]) ξ_χ beyond which any correlation decays exponentially [94, 95, 96]. By computing the bipartite von Neumann entanglement entropy S_χ, we obtain the phase diagram in Fig.(5.2).

Besides contours compatible with the weak U/t predictions (when visible), the simulation predicts three additional phases at larger U/t. Anticipating their identification, we find a Charge Density Wave (CDW) TLL phase at intermediate U/t. When $U/t \gg 1$ and $V/t \gtrsim 0.34$, we find a fully gapped cluster crystal (CC). When $U/t \gtrsim 3.1$ and $V/t \lesssim 0.34$, we find a polarized holonic (PH) phase.

To identify and characterize the (gapless) phases and phase transitions, we compute the central charges c of each by evaluating how S_χ scales with ξ_χ using [97, 98, 99]:

$$\mathcal{S}_\chi = \frac{c}{6} \ln \xi_\chi + b',$$

(5.2)

where b' is a non-universal constant. We thereby extract $c = 1$ for the CLL, SDW, and CDW phases, while $c = 2$ for the 2TLL phase. We refer to Ann.(C) for both the associated scalings of entanglement entropy and correlation functions characterizing these phases by their leading instabilities.

Moreover, following the method used in Refs. [25, 90], we identify the $c = 3/2$ SDW $\leftrightarrow$ CLL, Gaussian $c = 2$ SDW $\leftrightarrow$ CDW, and the $c = 1$ CDW $\leftrightarrow$ CC phase transitions (see Fig.(5.3a)). We expect the BKT phase transition between the SDW and the 2TLL phases by analogy with the square case. The sudden discontinuities in $\mathcal{S}_\chi$ seen in Fig.(5.3b) indicate that the direct CDW $\leftrightarrow$ CLL transition is of the first order type.

As the iDMRG simulations do not converge properly in the PH phase due to frustrations originating from strong repulsive interaction in the triangular geometry, we cannot characterize the PH phase or the PH $\leftrightarrow$ CC and PH $\leftrightarrow$ CDW phase transitions from the iDMRG results. Therefore, to characterize both the PH and the CC phases, we use a semi-classical strong-coupling approach, completed by exact diagonalization when possible.

---

[1]We stress to the reader that this length-scale is an artifact introduced by the matrix-product state ansatz in iDMRG simulations and is not linked to any energy scale of the system. It characterizes the size after which the algorithm truncates the correlations.
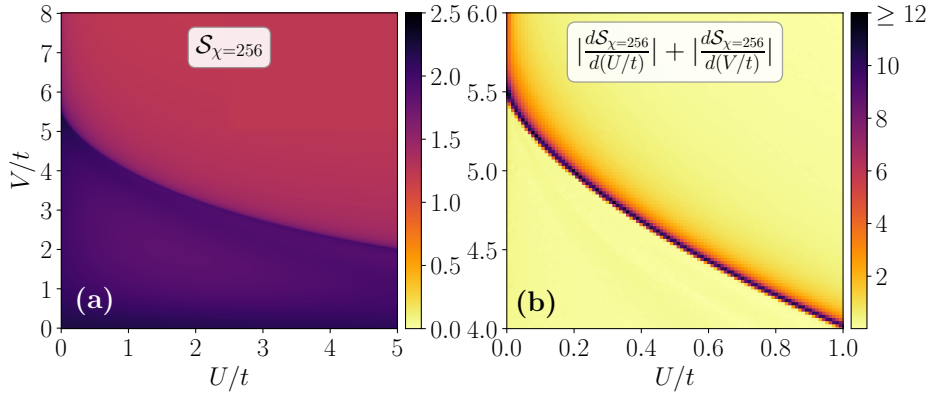
FIGURE 5.5: (a) The entanglement entropy $\mathcal{S}$ and (b) sum of the absolute values of its derivative with respect to the system parameters U/t and V/t in the $(U/t, V/t)$-plane for $U_1 = U/10$. The $c = 3/2$ phase transition is clearly visible while only an imprint of the Gaussian transition, existing for $U_1 = 0$, is present. The quantities are computed by the iDMRG algorithm with bond dimension $\chi = 256$.
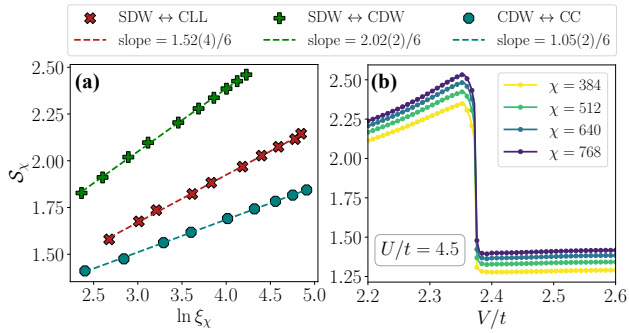

FIGURE 5.3: (a) The scaling of the entanglement entropy $\mathcal{S}_\chi$ with the correlation length ξ_χ according to Eq.(5.2) for different phase transitions. We have tracked the transitions by fixing $U/t = 1$ (for SDW ↔ CLL), $U/t = 3.5$ (for SDW ↔ CDW), $U/t = 4.5$ (for CDW ↔ CC), and varying V/t (see Ref. [25]). (b) The variations of the entanglement entropy $\mathcal{S}_\chi$ across the CDW ↔ CLL transition for different bond dimensions χ. The sudden jumps in $\mathcal{S}_\chi$ suggest the the transition to be first order.

We note that the 2TLL ↔ CDW transition is too narrow to be well studied numerically. It is also too deep in the intermediate interaction regime to be approached by perturbative techniques, hence the dotted lines in Fig.(5.1b) represent extrapolations of the analytical and numerical results.

5.2.2   Anisotropic regime $U > U_1$ close to the supersymmetric critical point

We now study the phase diagram in the vicinity of the supersymmetric (SUSY) $c = 3$ critical point at $V/t \sim 5.7$ and $U = U_1 = 0$ as U_1 is tuned from 0 (square geometry) to $U > 0$. We observe that as soon as $U_1 > 0$ ($U_1 = U/10$ in our simulation), the Charge Density Wave (CDW) phase existing in the square geometry [25] vanishes (see Fig.(5.5)). Along with the phase, the $c = 2$ Gaussian phase transition existing between the Spin Density Wave (SDW) and the CDW vanishes as well. We interpret this result as the non-zero triangular term being relevant for these parameters, preventing the phase transition and deforming the SDW phase into the SDW(α) (see Ann.(A)).

While no Gaussian transition appears in our simulation, a more detailed study in its vicinity shows that a remnant of it still exists (see Fig.(5.4)). Such observation is compatible with a spin gap reaching a local *finite* minimum corresponding to both a correlation length ξ_χ and entanglement entropy $\mathcal{S}_\chi$ reaching a local maximum. The absence of a sharp peak (present for the transition in the square case, see Ref. [25]) confirms the absence of the transition.

The $c = 3/2$ phase transition between the spin-locked Cluster Luttinger Liquid (CLL) and the SDW phases remains. The phenomenological understanding of this phase transition as the sign inversion of the mass of an effective Majorana field existing at the SUSY point for the square geometry [25] holds as well for the triangular geometry.

5.3 Strong intra-chain coupling

To provide analytical predictions for the large U regime, we use a perturbative strong coupling approach where t/U is the perturbation. Semi-classically in the limit $U \to \infty$, both the geometry and the strong intra-chain interaction segment the ladder into polarized domains. Each domain sees one leg of the ladder hosting atoms while the opposite leg is empty. States displaying such domains as in Figs.(5.6a,b) generate the effective Hilbert space at strong-coupling. The filled leg of the ladder within a domain may host (quasi-)holes, that we call polarized holons: these holons freely propagate within the domain, and may hop from one domain to the next at no energy cost. The density of such holons f_h and the density of domain walls f_w is fixed by the filling ν, such that

FIGURE 5.4: The variations of the entanglement entropy $\mathcal{S}$ with respect to V/t for various U/t and $U_1 = U/10$. The quantities are computed by the iDMRG algorithm with bond dimension $\chi = 512$. The SDW to CLL phase transition is sharp, whereas the remnant of the Gaussian phase transition is not (compared to e.g., Fig. 5 in Ref. [25]).

$$f_w + 2f_h = 2 - 4\nu, \tag{5.3a}$$

$$0 \le f_w \le \mathrm{Min}(2\nu, 2 - 4\nu). \tag{5.3b}$$

When V/t is negligible, configurations that maximize the density of holons and minimize the number of domains are favored energetically as the holons can delocalize both within and beyond a domain. It is the polarized holonic (PH) liquid. Instead, for larger V, small but numerous domains (i.e., clusters in that case) are energetically favored. Deprived of the propagating holons, the system is fully gapped. We denote this regime as the cluster crystal. When $V \geqslant 2U$, the strong U coupling approach breaks down.

To derive these results, we first obtain the perturbative Hamiltonian at second order in perturbation in t^2/U with $V = 0$. Restricted to the effective Hilbert space of the strong coupling, the perturbative Hamiltonian is

$$H|_{\mathrm{res}} = t \sum_{i=1}^{L} \sum_{\ell} (b_{i,\ell}^{\dagger} b_{i+1,\ell} + \mathrm{h.c.}) - \frac{2t^2}{U} \sum_i (n_{i,+} n_{i+2,-} + n_{i,-} n_{i+1,+}). \tag{5.4}$$

In this Hilbert space, the first term of Eq.(5.4) corresponds to the hopping of one particle *two* sites further along the zigzag if there are immediately at least three consecutive empty sites in the direction of the hopping (see Fig.(5.6(a))). These three consecutive holes constitute the holon. When a holon is immediately followed by other holons (its cohort), each of these extra holons adds two holes along the zigzag. In this formulation, the first term of Eq.(5.4) simply describes the hopping of free holons. The second term of Eq.(5.4) is a chemical potential for succession of exactly two empty sites. The polarization of the ladder changes across such a structure: it is a domain wall. A domain wall can also accompany a cohort of consecutive holons, each of them adding two holes along the zigzag. By convention, we consider that the domain wall is always at the left of the cohort.

To rewrite the effective model in terms of holons and domain walls, we require a creation and annihilation operator for both the holons ($h_i^{\dagger}$ and h_i) and the domain walls ($w_i^{\dagger}$ and w_i). It is possible to derive the explicit expression for both the densities of holons (n_{hi}) and domain walls (n_{wi}) (see Ann.(D)). The existence of these densities implies the existence of the associated creation
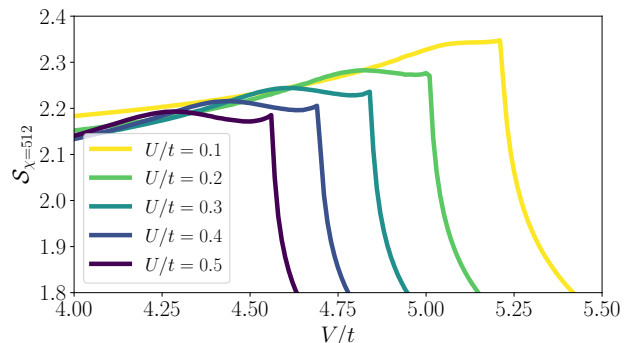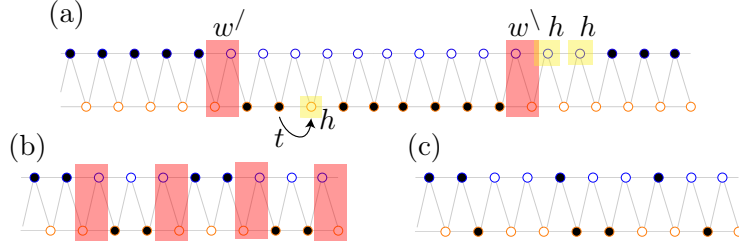
FIGURE 5.6: (a) The cartoon picture of the PH phase and example of a semi-classical state of the effective Hilbert space when $U \to \infty$. The ladder is divided into polarized segments (here, only two with periodic boundary conditions). These segments are separated by domain walls (in red). Holes in the segments are holons (in yellow). Holons can belong to the cohort of a domain wall, like for the left domain wall on the picture. Arrow: example of hopping. (b) The cartoon picture of the CC phase. (c) One semi-classical configuration of the CLL phase.

and annihilation operators. Using these operators, we define the basis of the effective Hilbert space such that

$$h_i^\dagger |0_i\rangle = |1_i\rangle, \qquad\qquad\qquad h_i |1_i\rangle = |0_i\rangle, \qquad (5.5a)$$

$$h_i^\dagger |1_i\rangle = 0, \qquad\qquad\qquad h_i |0_i\rangle = 0, \qquad (5.5b)$$

$$w_i^\dagger |X_i\rangle = |w_i X_i\rangle, \qquad\qquad\qquad w_i |w_i X_i\rangle = |X_i\rangle, \qquad (5.5c)$$

with $X = 0$ or 1, and $\{h_i, h_i^\dagger\} = \{w_i, w_i^\dagger\} = 1$. For simplicity, we assume that the holonic and domain walls operators commute, essentially treating them as decoupled degrees of freedom. Such approximation is justified a posteriori, by comparing our findings to numerics.

Using these operators, we obtain a phenomenological expression for the perturbative Hamiltonian from which we deduce an estimate of the energy levels as a function of the average density of domain walls and holon. The Hamiltonian is

$$H|_{\text{res}} \sim t \sum_{i=1}^{L} \left[w_i^\dagger h_{i+1}^\dagger w_{i+1} h_i + h_i^\dagger w_{i+1}^\dagger h_{i+1} w_i + h_i^\dagger h_{i+1} \left(1 - n_{w,i+1}\right) + h_{i+1}^\dagger h_i \left(1 - n_{w,i+2}\right) \right]$$
$$\qquad\qquad\qquad\qquad\qquad\qquad\qquad\qquad\qquad\qquad - \frac{2t^2}{U} \sum_i w_i^\dagger w_i h_i h_i^\dagger. \qquad (5.6)$$

In Eq.(5.6), the first four terms describe the hopping of holons depending on the proximity of a wall. When no wall is nearby, the hopping holon is unimpeded. When a holon hops across a wall, the holon and wall exchange places. The last term in Eq.(5.6) counts the number of walls without cohort. As a consequence, a wall effectively moves only through scattering with a holon. All walls hop one site when a holon propagates along the entire ladder. Due to this difference in scale of the two momenta, we work under the assumption that the two variables are independent to estimate the spectrum of the Hamiltonian. We take $\langle n_{hi} \rangle = f_h L$ and $\langle n_{wi} \rangle = f_w L$. We find

$$\langle H|_{\text{res}}\rangle / 2tL = \frac{t}{U} f_w (f_h - 1) - \frac{1}{\pi}(1 - f_w)\sin(\pi f_h) - \frac{2}{\pi^2}\sin(\pi f_h)\sin(\pi f_w / 2). \qquad (5.7)$$

Eq.(5.7) highlights competition between holons and domain walls. When $U/t > 2\pi/(5\sin(\pi/5)) \sim 2.14$, the phase is the polarized holonic liquid with $c = 1$. Such a small value of U/t is beyond the validity of the strong-coupling approach which explains the difference with the value of ~ 3.1 observed in Fig.(5.2). Third order corrections in U/t and higher allow the transformation of two domain walls of small domains into one holon and vice-versa.
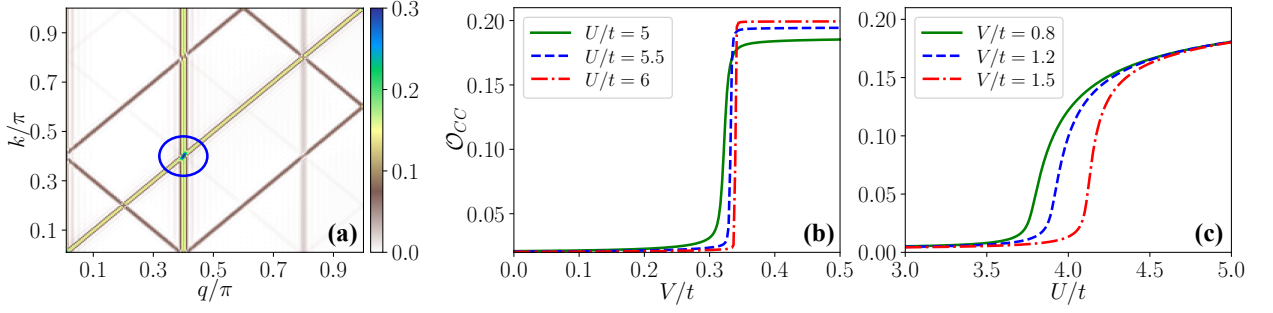
FIGURE 5.7: (a) The structure factor $S(q,k)$ (see Eq.(5.9)) in the CC phase ($U/t = 5, V/t = 1.5$) as a function of the momenta q and k. $S(q,k)$ attains a sharp peak at $q = 2\pi/5, k = 2\pi/5$ as highlighted by the blue circle. (b)-(c) The order parameter $\mathcal{O}_{CC}$ (see text) along the the CC $\leftrightarrow$ PH and the CC $\leftrightarrow$ CDW phase transitions respectively. The figures (a) and (c) have been obtained from iDMRG simulations with bond dimension $\chi = 256$, while (b) is obtained from ED calculations for a system with 10 sites.

Similarly, we obtain the contribution of the shoulder potential to the estimated energy levels using the holons and domain walls reformulation. We find (see Ann.(D))

$$\langle H_{\text{Shoulder}}\rangle/VL = 2 - 4f_h - 4f_w + 2f_h^2 - \frac{1}{\pi^2}\sin^2(\pi f_h)$$
$$- \frac{1}{2\pi^2}\sin(\pi f_h)\sin(2\pi f_h) + 4f_h f_w + \frac{1}{2}f_w^2. \tag{5.8}$$

The full estimate of the energy levels is the sum of Eqs.(5.7,5.8). Because of Eq.(5.3a), the maximal domain wall density is twice the maximal holon density, such that Eq.(5.8) unilaterally favours the domain walls over the holons. A transition thus occurs when the contribution of Eq.(5.8) dominates over the contribution from Eq.(5.7). When $U \to \infty$, this transition is predicted at $V/t \sim 0.33$ and observed at $V/t \sim 0.34$ on Fig.(5.2). Higher order corrections effectively introduce a repulsion between domain walls. When the density of domain walls is maximized, a pattern spontaneously breaking the translation symmetry emerges, and the system goes into the CC phase.

By comparing the energy of semi-classical configuration of the CC pattern as in Fig.(5.6b) $E_{CC} = 2V$ and of a CLL state minimizing U as in Fig.(5.6c) (not included in the restricted Hilbert space) $E_{CLL} = V + 2U$ when $t = 0$, we predict the end of the CC phase at $V = 2U$. Due to the existence of the CDW phase (CDW are not included in the restricted Hilbert space), the transition occurs at smaller $V < 2U$ for finite U.

We extract the order parameter $\mathcal{O}_{CC}$ associated with the CC phase using the structure factor:

$$S(q,k) = \frac{1}{L^2}\sum_{j,j'}\sum_{\ell,\ell'}\langle n_{j,\ell}n_{j',\ell'}\rangle e^{-i(q+k(\ell-\ell'))(j-j')}. \tag{5.9}$$

In the CC phase at $\nu = 2/5$, $S(q,k)$ displays a sharp peak at momenta $q = 2\pi/5, k = 2\pi/5$ (see Fig.(5.7a)). Subtracting the disconnected contribution from $S(q,k)$, we define the order parameter $\mathcal{O}_{CC} = S(2\pi/5, 2\pi/5) - 4/25$ of the CC phase. Figs.(5.7b,c) show the variation of the order parameter along the CC $\leftrightarrow$ PH and the CC $\leftrightarrow$ CDW phase transitions respectively. The sharp changes in $\mathcal{O}_{CC}$ across the CC $\leftrightarrow$ PH transition, even for small system-size as $L = 10$, strongly hint that this transition might be first order in nature.

Appendix

A   Weak coupling approach

Using the Abelian bosonization [28, 39] method we study the phase diagram of the triangular ladder model in the weak coupling regime. Specifically, after reformulating the description of the system in terms of fermions using a Jordan-Wigner transformation, we take the continuous limit of the discrete model, and linearize it around the Fermi points. To the obtained chiral Dirac fermions, we then apply the standard Abelian bosonization relations to finally derive the sine-Gordon model of two compact bosons. Using a conformal renormalization scheme at first loop, we deduce the asymptotes of the renormalization group equations depending on the initial conditions. We therefore obtain the outline of the phase diagram at weak coupling. By computing correlation functions associated to each asymptote, we identify each phase of this diagram. Using this approach, we predict the gapless 2TLL and the SDW_α^z phases separated by a BKT phase transition.

We perform a Jordan-Wigner transformation to use fermionic degrees of freedom and notions associated with Hubbard-like models:

$$b_{i,l} = \left(\delta_{l,+} e^{i\pi \sum_{j=1}^{i-1} n_{j,+}} c_{i,+} + \delta_{l,-} e^{i\pi \sum_{k=1}^{N} n_{k,+}} e^{i\pi \sum_{j=1}^{i-1} n_{j,-}} c_{i,-} \right), \tag{A.1}$$

where $b_{i,\ell}$ is the hard-core bosonic annihilation operator on site i and leg $\ell = \pm$. The fermionic annihilation operators $c_{i,\ell}$ obey the standard anti-commutation relations. The particle number operators are $n_{i,\ell} = c_{i,\ell}^\dagger c_{i,\ell} = b_{i,\ell}^\dagger b_{i,\ell}$. After the transformation, the triangular ladder Hamiltonian Eq.(5.1) is unchanged:

$$H = H_0 + H_U + H_{U_1} + H_V, \tag{A.2}$$

with

$$H_0 = -t \sum_{l=\pm} \sum_i \left(c_{i,l}^\dagger c_{i+1,l} + \text{h.c.} \right), \tag{A.3}$$

$$H_U = U \sum_i n_{i,+} n_{i,-}, \tag{A.4}$$

$$H_{U_1} = U_1 \sum_i n_{i,+} n_{i+1,-}, \tag{A.5}$$

$$H_V = V \sum_{l=\pm} \sum_{r=1}^{r_c} n_{i,l} n_{i+r,l}, \tag{A.6}$$

where we take $r_C = 2$ unless otherwise specified.

We then linearize the model Eq.(A.2) around the Fermi points (at momentum $\pm k_F$) in the weak coupling regime after taking the continuum limit by introducing the right- and left-moving Dirac

fermion fields

$$c_{i,\ell} \sim \psi_{R,\ell}(x = i) + \psi_{L,\ell}(x = i), \tag{A.7a}$$

$$\psi_{r,\ell} = \frac{1}{\sqrt{2\pi a_0}} U_{r,\ell} e^{irk_F x} e^{i\sqrt{\frac{\pi}{2}}(r\phi_c - \theta_c + \ell(r\phi_s - \theta_s))}. \tag{A.7b}$$

$\psi_{r,\ell}$ is the associated right ($r = R$ as an index, $r = +1$ when in the exponential) and left ($r = L$, $r = -1$ respectively) moving fermionic field in the continuous limit close to the Fermi points, $a_0 = 1$ is the lattice spacing, $U_{r,\ell}$ are the Klein factors such that $\{U_{r,\ell}, U_{r',\ell'}\} = 2\delta_{r,r'}\delta_{\ell,\ell'}$, and $k_F = \pi\nu/a_0$ is the Fermi momentum with $\nu = 2/5$ being the filling factor for each chain. The bosonic fields ϕ_c, ϕ_s, θ_c, and θ_s are the charge and spin fields and their respective dual fields. After bosonization, each term in Eq.(A.3-A.6) splits into the spin and charge sector as

$$H_0 \sim \frac{v_F}{2} \int dx \left((\partial_x\theta_c)^2 + (\partial_x\phi_c)^2\right) + \frac{v_F}{2} \int dx \left((\partial_x\theta_s)^2 + (\partial_x\phi_s)^2\right), \tag{A.8a}$$

$$H_U \sim \frac{U}{2\pi} \int dx \left((\partial_x\phi_c)^2 - (\partial_x\phi_s)^2\right) + \frac{U}{2\pi^2} \int dx \cos(\sqrt{8\pi}\phi_s), \tag{A.8b}$$

$$H_{U_1} \sim \frac{U_1}{2\pi} \int dx \left((\partial_x\phi_c)^2 - (\partial_x\phi_s)^2\right)$$
$$+ \frac{U_1(1 + \cos(2\pi\nu))}{2\pi^2} \int dx \cos(\sqrt{8\pi}\phi_s) + \frac{U_1 \sin(2\pi\nu)}{2\pi^2} \int dx \sin(\sqrt{8\pi}\phi_s), \tag{A.8c}$$

$$H_V \sim \frac{V(2 - \cos(2\pi\nu) - \cos(4\pi\nu))}{\pi} \int dx \left((\partial_x\phi_c)^2 + (\partial_x\phi_s)^2\right), \tag{A.8d}$$

with $v_F = 2t\sin(\pi\nu)$. The full Hamiltonian displays the spin-charge separation:

$$H = H_c + H_s, \tag{A.9a}$$

$$H_c = \frac{v_c}{2} \int dx \left(K_c(\partial_x\theta_c)^2 + \frac{1}{K_c}(\partial_x\phi_c)^2\right), \tag{A.9b}$$

$$H_s = \frac{v_s}{2} \int dx \left(K_s(\partial_x\theta_s)^2 + \frac{1}{K_s}(\partial_x\phi_s)^2\right) - \frac{g_0}{4\pi^2} \int dx \cos(\sqrt{8\pi}\phi_s - \alpha), \tag{A.9c}$$

where H_c is the bosonized Hamiltonian of the charge sector, and H_s is the sine-Gordon Hamiltonian of the spin sector. We find

$$K_s = \frac{1}{\sqrt{1 + \frac{g_\parallel}{2\pi v_F}}}, \tag{A.10a}$$

$$v_s = v_F \sqrt{1 + \frac{g_\parallel}{2\pi v_F}}, \tag{A.10b}$$

$$v_s K_s = v_F, \tag{A.10c}$$

$$K_c = \frac{1}{\sqrt{1 + \frac{2g}{\pi v_F}}}, \tag{A.10d}$$

$$v_c = v_F \sqrt{1 + \frac{2g}{\pi v_F}}, \tag{A.10e}$$

$$v_c K_c = v_F, \tag{A.10f}$$

and

$$g = \frac{U + U'}{2} + V(2 - \cos(2\pi\nu) - \cos(4\pi\nu)), \tag{A.11a}$$

$$g_\parallel = -2U - 2U_1 + 4V(2 - \cos(2\pi\nu) - \cos(4\pi\nu)), \tag{A.11b}$$

$$g_0 = -2\sqrt{(U + U_1)(U + U_1 + 2U_1\cos(2\pi\nu)) + U_1^2}, \tag{A.11c}$$

$$\alpha = \arctan\left(\frac{U_1\sin(2\pi\nu)}{U + U_1(1 + \cos(2\pi\nu))}\right) \quad \text{modulo } 2\pi. \tag{A.11d}$$

Based on the zeroth loop approach, the cosine perturbation in Eq.(A.9c) is irrelevant as soon as $K_s > 1$ (i.e. $g_\parallel < 0$). In this regime the spin gap nonetheless opens because of the first-loop corrections to the renormalization group equations [28]

$$\frac{dg_\parallel}{dl} = \frac{1}{2\pi}g_0^2, \qquad \frac{dg_0}{dl} = \frac{1}{2\pi}g_0 g_\parallel, \qquad \frac{d\alpha}{dl} = 0, \tag{A.12}$$

which predict a BKT phase transition from gapless 2LL to SDW$^z(\alpha)$ with a spin-gap, when $g_\parallel > -|g_0|$. In other words, the zero-th loop predicts the 2TLL $\leftrightarrow$ SDW transition at $V = 5U/2$, whereas the first loop renormalization predicts the transition at $V = \frac{4 - 2\sqrt{4 - \sqrt{5}}}{10}U$. Such a result means that the characterization of each phase should be sharp above and below both predicted transition line, but more arduous in between as the partial gap is weaker. Such a phenomena explains why the detection of the BKT phase transition is more difficult in numerical simulations. We draw the $V = 5U/2$ line on the phase diagram as it is below this line that a simulation likely mistakenly confuses the SDW for the 2TLL.

In the SDW$^z(\alpha)$ phase the spin field is fixed at $\phi_s(\alpha) = \frac{\alpha}{\sqrt{8\pi}} + \sqrt{\frac{\pi}{8}}$ modulo $\left(\sqrt{\frac{\pi}{8}}\right)$ by the spin gap. The corresponding order parameter is

$$\mathcal{O}_\alpha = \sin(\sqrt{2\pi}\phi_s - \alpha/2) = \mathcal{O}_{\text{triplet}_0}\cos(\alpha/2) - \mathcal{O}_{\text{singlet}}\sin(\alpha/2), \tag{A.13a}$$

with $\alpha \in [0; 2\pi/5]$ as $U_1/U \in [0; \infty)$ and where $\mathcal{O}_{\text{triplet}_0}$ is the "triplet 0" and $\mathcal{O}_{\text{singlet}}$ is the singlet order parameter [80]. When $\alpha = 0$ ($U_1 = 0$), this order parameter corresponds to the contribution of the spin sector to the $2k_F$ spin-density-wave operator

$$\mathcal{O}_{\text{SDW}}^z = S^z(x) - \frac{1}{\sqrt{2\pi}}\partial_x\phi_s(x) = \cos(\sqrt{2\pi}\phi_c + 2k_Fx)\sin(\sqrt{2\pi}\phi_s), \tag{A.14}$$

where $S^z(x)$ the continuous limit of the spin operator

$$\frac{1}{2}\sum_{\ell,\ell'=\pm}c_{x,\ell}^\dagger\sigma_{\ell\ell'}^z c_{x,\ell'} \sim S^z(x), \tag{A.15}$$

with $\sigma_{\ell\ell'}^z$ the Pauli matrix along the z-direction. The associated correlation function in SDW$^z(\alpha)$ phase is

$$\langle\mathcal{O}_{\text{SDW}}^z(x)\mathcal{O}_{\text{SDW}}^z(y)\rangle \sim \sin^2\left(\sqrt{2\pi}\phi_s(\alpha)\right)\cos(2k_F|x-y|)|x-y|^{-K_c}, \tag{A.16}$$

which is also the correlator with the longest range, such that the SDW$^z(\alpha)$ is the dominant instability in the system.

In 2TLL phase, both $2k_F$ momentum CDWs and SDWs instabilities are in competition. The order parameter associated with CDW is defined as

$$\mathcal{O}_{\text{CDW}} = \rho(x) - \sqrt{\frac{2}{\pi}}\partial_x\phi_c(x), \tag{A.17}$$

where $\rho(x)$ is the continuous limit of the density operator

$$\sum_{\ell=\pm} c^\dagger_{x,\ell}c_{x,\ell} \sim \rho(x). \tag{A.18}$$

The correlation functions associated with both CDW and SDW^z are

$$\langle \mathcal{O}_{\text{CDW}}(x)\mathcal{O}_{\text{CDW}}(y)\rangle \sim \cos(2k_F|x-y|)|x-y|^{-(K_c+K_s^*)}, \tag{A.19a}$$

$$\langle \mathcal{O}^z_{\text{SDW}}(x)\mathcal{O}^z_{\text{SDW}}(y)\rangle \sim \cos(2k_F|x-y|)|x-y|^{-(K_c+K_s^*)}, \tag{A.19b}$$

with $K_s^* = 1$, the renormalized Luttinger parameter as the SU(2) symmetry emerges asymptotically.

B   Cluster bosonization approach

The low-energy effective theory of a single chain ($U = U_1 = 0$) at strong coupling $V \gg t$ is effectively described by cluster bosonic fields, *i.e.* density fluctuations of perfect cluster configuration of particles. To derive this result, we use the Cluster bosonization approach. In the continuum limit, the bosonic field operators are expressed as [21, 25]

$$\psi_l(x) = e^{-\frac{i\sqrt{\pi}}{\sigma}\theta'_l(x)}\sqrt{\nu - \frac{1}{\sqrt{\pi}\sigma}\nabla\phi'_l(x)}\sum_{q=-\infty}^{+\infty}\alpha_{q,l}e^{-i2q(\pi x\nu\sigma - \sqrt{\pi}\phi'_l(x))} \tag{B.1}$$

and the particle density operator as

$$\rho_\ell(x) = \left(\nu - \frac{1}{\sqrt{\pi}\sigma}\nabla\phi'_\ell(x)\right)\sum_{q=-\infty}^{+\infty}A_{q,\ell}e^{-i2q(\pi x\sigma\nu - \sqrt{\pi}\phi'_\ell(x))}. \tag{B.2}$$

$\phi'_\ell(x)$ is the fluctuation above a perfect cluster configuration on chain ℓ. $\theta'_\ell(x)$ is defined as the conjugate variable of $\nabla\phi'_\ell(x)$ such that

$$\left[\theta'_\ell(y), \frac{1}{\pi}\nabla\phi'_{\ell'}(x)\right] = i\delta_{\ell,\ell'}\delta(x-y). \tag{B.3}$$

$A_{q,\ell} = A^*_{-q,\ell}$ and $\alpha_{q,\ell}$ are the non-universal constants that strongly depend on the microscopic details of the system. $\sigma = M/N$ with M and N being the number of clusters and particles respectively.

In the absence of the inter-chain interactions U and U_1, we have two decoupled chains with the soft-shoulder interaction V acting within each chain. Using the cluster bosonization, the Hamiltonian of each chain is mapped to the Hamiltonian of free massless cluster bosons [20, 21]

$$H_{V,t} \sim \sum_{\ell=\pm}\frac{v}{2}\int dx\left(K(\nabla\theta'_\ell)^2 + \frac{1}{K}(\nabla\varphi'_\ell)^2\right), \tag{B.4}$$

where K is the cluster-Luttinger parameter. Since the top and bottom chains are identical, we have $K_+ = K_- = K$ and $v_+ = v_- = v$. By dropping the constants and only keeping the most relevant

terms, the mapping for the U interaction is [25]

$$H_U \sim U \int dx \rho_+(x)\rho_-(x) \approx g_U^{(0)} \int dx \nabla\varphi'_+(x)\nabla\varphi'_-(x) + g_U^{(1)} \int dx \cos(\sqrt{4\pi}[\varphi'_+(x) - \varphi'_-(x)]),$$

(B.5)

with $g_U^{(0)} = \frac{U|A_0|^2}{\pi\sigma^2}$ and $g_U^{(1)} = 2\nu^2 U|A_1|^2$. Similar calculations for U_1 interaction gives

$$H_{U_1} \sim U_1 \int dx \rho_+(x)\rho_-(x + a_0) \approx g_{U_1}^{(0)} \int dx \nabla\varphi'_+(x)\nabla\varphi'_-(x)$$
$$+ g_{U_1}^{(1)} \int dx \cos(\sqrt{4\pi}[\varphi'_+(x) - \varphi'_-(x)]) - g_{U_1}^{(2)} \int dx \sin(\sqrt{4\pi}[\varphi'_+(x) - \varphi'_-(x)]),$$

(B.6)

with

$$g_{U_1}^{(0)} = \frac{U_1|A_0|^2}{\pi\sigma^2}, \quad g_{U_1}^{(1)} = 2\nu^2 U_1|A_1|^2 \cos(2\pi n\sigma a_0), \quad g_{U_1}^{(2)} = 2\nu^2 U_1|A_1|^2 \sin(2\pi n\sigma a_0)$$

(B.7)

Using the spin and charge cluster bosonic fields

$$\varphi'_\ell = \frac{\varphi'_c + \ell\varphi'_s}{\sqrt{2}}, \qquad\qquad \theta'_\ell = \frac{\theta'_c + \ell\theta'_s}{\sqrt{2}},$$

(B.8)

with $\ell = \pm$, the total hamiltonian for the triangular ladder $H = H_{V,t} + H_U + H_{U_1}$ is

$$H = \frac{v_c}{2} \int dx \left(K_c (\nabla\theta'_c)^2 + \frac{1}{K_c}(\nabla\varphi'_c)^2 \right) + \frac{v_s}{2} \int dx \left(K_s(\nabla\theta'_s)^2 + \frac{1}{K_s}(\nabla\varphi'_s)^2 \right)$$
$$+ g \int dx \cos(\sqrt{8\pi}\varphi'_s - \alpha),$$

(B.9)

with

$$g = \sqrt{\left(g_U^{(1)} + g_{U_1}^{(1)}\right)^2 + \left(g_{U_1}^{(2)}\right)^2}, \quad \alpha = \arctan\left(\frac{-g_{U_1}^{(2)}}{g_U^{(1)} + g_{U_1}^{(1)}}\right),$$

(B.10)

$$K_c = \frac{K}{\sqrt{1 + \frac{\left(g_U^{(1)}+g_{U_1}^{(1)}\right)K}{v}}}, \quad v_c = v\sqrt{1 + \frac{\left(g_U^{(1)} + g_{U_1}^{(1)}\right)K}{v}}.$$

(B.11)

$$K_s = \frac{K}{\sqrt{1 - \frac{\left(g_U^{(1)}+g_{U_1}^{(1)}\right)K}{v}}}, \quad v_s = v\sqrt{1 - \frac{\left(g_U^{(1)} + g_{U_1}^{(1)}\right)K}{v}}.$$

(B.12)

As the effective cluster Hamiltonian Eq.(B.9) is formally similar to the bosonized Hamiltonian Eq.(A.9), we conclude that two phases are possible ($g > 0$). If the spin mass is irrelevant, then one possible phase is a CLL with $c = 2$. If instead the mass is relevant, then the second possible phase is a 'spin-locked' CLL with $c = 1$. The microscopic details of the coarse-graining realized with the Cluster bosonization are hidden within the $A_{\ell,q}$ and $\alpha_{\ell,q}$ coefficients, preventing their estimations. In consequence, the relevancy of the mass is only accessible by the numerical simulations. The simulations we perform show that $c = 1$ and therefore that the mass is relevant.
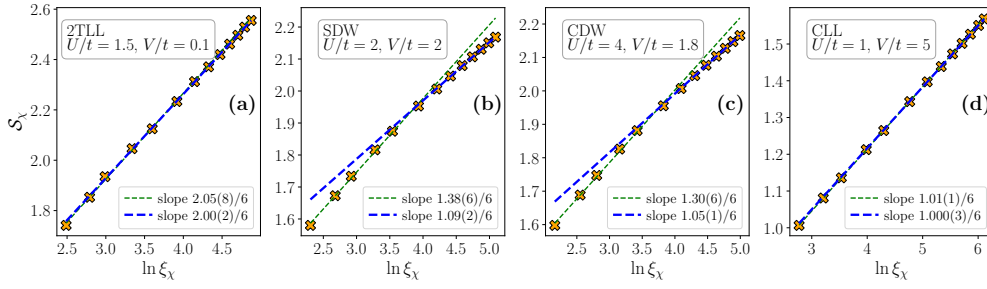
FIGURE 5.8: The behavior of the entanglement entropy $\mathcal{S}_\chi$ with respect to the correlation length ξ_χ for the bond dimensions $\chi \in [64, 1280]$ in different phases, namely (a) 2TLL, (b) SDW, (c) CDW, and (d) CLL. The thin green lines correspond to the fits (see Eq.(5.2))in the range $\chi \in [64, 384]$, while the thick blue lines correspond to the fits for $\chi \in [512, 1280]$.

C Numerical results on the phases at weak and intermediate inter-chain coupling strengths

By the means of iDMRG simulations, we now numerically analyze different phases that appear at weak and intermediate inter-chain coupling (U/t) strengths, i.e., the 2TLL, the SDW, the CDW, and the CLL phases. To this end, we first extract the central charge c for these phases by fitting the bond dimension χ-dependent entanglement entropy $\mathcal{S}_\chi$ as a function of the χ-dependent correlation length ξ_χ using the relation[97, 98, 99] Eq.(5.2). In Fig.(5.8), we plot the scaling of $\mathcal{S}_\chi$ with respect to ξ_χ in these phases as we increase the bond dimension from $\chi = 64$ to 1280. Clearly, all these phases, except the 2TLL, have central charge $c = 1$ indicating gapped spin-sectors while the charge-sectors remain gapless as in the case for square geometry [25]. In the 2TLL phase, $c = 2$ signifies that the both sectors are gapless.

We characterize each phases with $c = 1$ phases by analyzing correlation functions of the form

$$\mathcal{C}_\mathcal{O}(R) = \langle \mathcal{O}_j \mathcal{O}_{j+R} \rangle - \langle \mathcal{O}_j \rangle \langle \mathcal{O}_{j+R} \rangle, \tag{C.1}$$

where $\mathcal{O}_j$ is a local operator. When the distance R is greater than the correlation length ξ_χ all correlations trivially decay exponentially, restricting the validity of the computed correlation function to $R \approx \xi_\chi$ at maximum.

Instead of considering the spin correlation function $\mathcal{C}_{S^z}$ (where $S_j^z = (n_{j,+} - n_{j,-})/2$) and the charge correlation function $\mathcal{C}_n$ (where $n_j = (n_{j,+} + n_{j,-})$), we find that the bond-spin correlation $\mathcal{C}_{B^S}$ and the bond-charge correlation $\mathcal{C}_{BC}$ are more suitable to characterize the SDW and the CDW phases. Within each of the pairs $(\mathcal{C}_{S^z}, \mathcal{C}_{B^S})$ and $(\mathcal{C}_n, \mathcal{C}_{BC})$, the correlation are largely indistinguishable in theory when the charge sector is not gapped [80]. The bond operators are defined as

$$B_j^S = \left((b_{j,+}^\dagger b_{j+1,+} + \text{H.c.}) - (b_{j,-}^\dagger b_{j+1,-} + \text{H.c.}) \right) /2, \tag{C.2a}$$

$$B_j^C = \left(b_{j,+}^\dagger b_{j+1,+} + b_{j,-}^\dagger b_{j+1,-} + \text{H.c.} \right). \tag{C.2b}$$

Figs.(5.9a,b) show these bond correlation functions in the SDW and the CDW phases for $R \leq 200 < \xi_{\chi=2048}$. Clearly, in the SDW phase, the bond-spin correlation function $\mathcal{C}_{B^S}$ follows power-law and the bond-charge correlation $\mathcal{C}_{BC}$ decays exponentially with the distance R. The opposite is observed in the CDW phase. The frequencies of the oscillations in the algebraically decaying
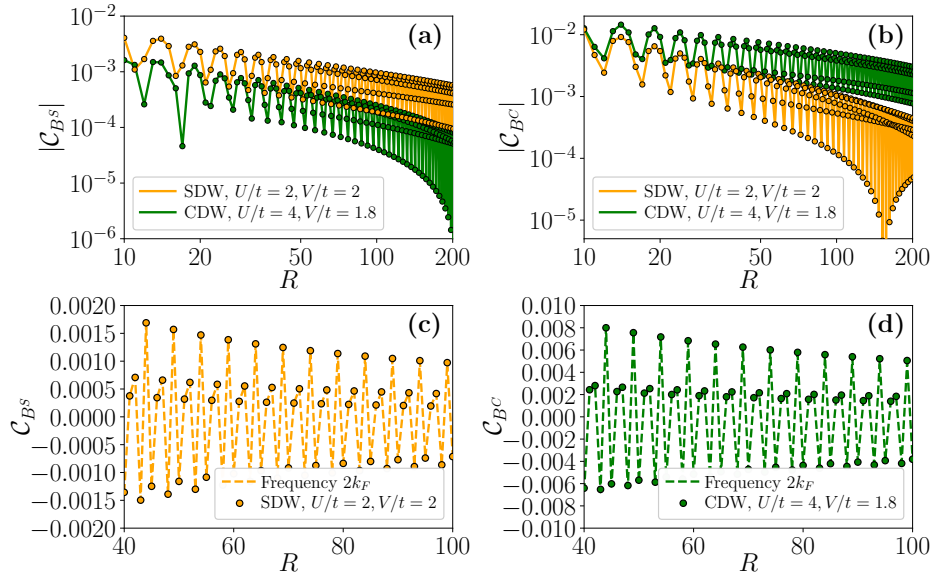
FIGURE 5.9: The behaviors of (a) the bond-spin correlation function $\mathcal{C}_{BS}(R) = \langle B_j^S B_{j+R}^S \rangle - \langle B_j^S \rangle \langle B_{j+R}^S \rangle$ and (b) the bond-charge correlation function $\mathcal{C}_{BC}(R) = \langle B_j^C B_{j+R}^C \rangle - \langle B_j^C \rangle \langle B_{j+R}^C \rangle$ as functions of the distance R in the SDW and CDW phases. Here both axes are in the logarithmic scale. (c)-(d) The power-law fits (according to Eq.(C.3)) of the bond-spin and bond-charge correlations respectively in the SDW and CDW phases.

correlations can be obtained by fitting the the data to the following formula:

$$\mathcal{C}(R) \sim \cos(kR)\, R^{-\beta}. \tag{C.3}$$

Figs.(5.9c,d) show such fits for the bond-spin and the bond-charge correlations respectively in the SDW and CDW phases. In both the cases, the numerical fits show that the frequency of oscillations are $k = 2k_F = 2\pi/5$ as expected from the analysis of Ann.(A).

In the case of the CLL phase, since the leading instabilities are clustered, we look at the spin correlation $\mathcal{C}_{S^z}$ and charge correlation $\mathcal{C}_n$ functions. Fig.(5.10) shows the evolution of these correlation functions with respect to the distance R together with their Fourier transform. As expected in the CLL phase, both the correlation functions decay following a power-law. By analyzing the Fourier transforms, we extract the two primary frequencies of the oscillations as $k = 2k_F = 4\pi/5$ and $k = 3k_F/2 = 3\pi/5$. $k = 3k_F/2$ is the cluster Fourier momentum appearing in Eq.(B.2) that translates the specific cluster instability of the Luttinger liquid. Like in the square ladder [25], we interpret the other major frequencies such as $k = 2k_F$ as due to the pollution of the signal by subdominant SDW or CDW instabilities. Interestingly and unlike the square geometry, these frequencies are present in both spin and charge correlation functions, translating the deformation due to the added range of U.

D Strong U coupling theory in the triangular ladder.

We present here the details of the semi-classical approach to the holonic polarized and the cluster crystal phases.
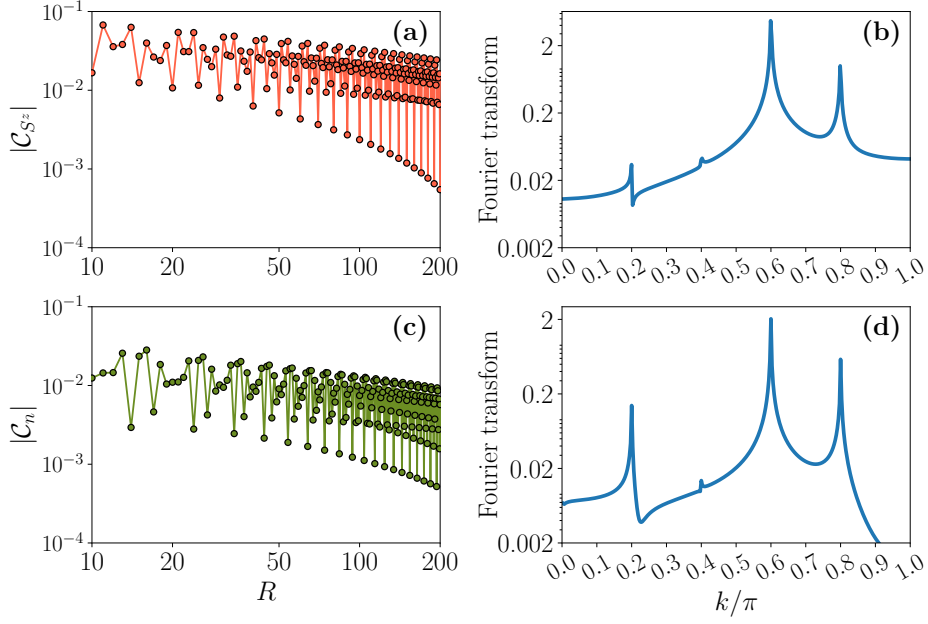
FIGURE 5.10: The behaviors of (a) the spin correlation function $\mathcal{C}_{S^z}(R) = \langle S_j^z S_{j+R}^z \rangle - \langle S_j^z \rangle \langle S_{j+R}^z \rangle$ and (c) the charge correlation function $\mathcal{C}_n(R) = \langle n_j n_{j+R} \rangle - \langle n_j \rangle \langle n_{j+R} \rangle$ as functions of the distance R in the CLL phase ($U/t = 1, V/t = 5$). The subplots (b) and (d) depict the Fourier transform of the spin correlation and charge correlation functions respectively.

D.1   Densities of holons and domain walls

It is possible to get formulae for both the domain walls and holon densities. Because holons can form cohorts, these densities are non-local operators preventing the formulae from being easily used. To obtain them, we define the projectors:

$$P_{i-} = n_{i-}(1 - n_{i+}), \tag{D.1a}$$
$$P_{i+} = n_{i+}(1 - n_{i+1+}), \tag{D.1b}$$
$$M_{i-} = (1 - n_{i-})(1 - n_{i+}), \tag{D.1c}$$
$$M_{i+} = (1 - n_{i+})(1 - n_{i+1-}), \tag{D.1d}$$
$$D_{i-} = (1 - n_{i-})n_{i+}, \tag{D.1e}$$
$$D_{i+} = (1 - n_{i+})n_{i+1-}. \tag{D.1f}$$

Using Eqs.(D.1), we define the quasi-local projector $\mathcal{P}_i$ and the total projector $\mathcal{P}$ onto the effective Hilbert space of strong U coupling as

$$\mathcal{P}_i = (M_{i-1+} + D_{i-1+} + P_{i-1+})(M_{i+} + D_{i+} + P_{i+}) - P_{i-1+}P_{i+}, \tag{D.2a}$$
$$\mathcal{P} = \otimes_i \mathcal{P}_i. \tag{D.2b}$$

Using Eqs.(D.1), we obtain the density of domain walls by summing over the projectors on one domain wall state for all cohorts. We note $w_i^{/}$ (resp. $w_i^{\backslash}$) a domain wall with its first empty site on rung i and separating a domain with the leg $+$ populated on the left (resp. right) and the leg $-$

populated on the right (resp. left). Their respective density operator are

$$
\begin{aligned}
n_{wi}^{/} &= P_{i-1+}D_{i+} + P_{i-1+}M_{i+}D_{i+1+} + \dots \\
&= P_{i-1+}\left(D_{i+} + \sum_{k=0}^{L-4} M_{i+}M_{i+1+}\dots M_{i+k+}D_{i+k+1+}\right),
\end{aligned}
\tag{D.3a}
$$

$$
\begin{aligned}
n_{wi}^{\backslash} &= P_{i-}D_{i+1-} + P_{i-}M_{i+1-}D_{i+2-} + \dots \\
&= P_{i-}\left(D_{i+1-} + \sum_{k=0}^{L-5} M_{i+1-}M_{i+2-}\dots M_{i+k+1-}D_{i+k+2-}\right),
\end{aligned}
\tag{D.3b}
$$

for periodic boundary conditions. We also define the total density of domain walls

$$
n_{w,i} = n_{wi}^{/} + n_{wi-1}^{\backslash}.
\tag{D.4}
$$

We obtain the holon densities in a similar manner. We define the two quantities

$$
n_{hi+} = P_{i-1+}(1-n_{i+})D_{i+1-} + P_{i-1+}(1-n_{i+})M_{i+1-}D_{i+2-} + P_{i-2+}M_{i-1+}(1-n_{i+})D_{i+1+} + \dots
\tag{D.5a}
$$

$$
+ \frac{1}{2}\left[P_{i-1+}M_{i+}D_{i+1+} + P_{i-1-}M_{i-}D_{i+1-} + \dots\right],
$$

$$
= \sum_{k=0}^{\infty}\sum_{l=0}^{k} P_{i-1-l+}\prod_{m=1}^{l} M_{i-m+}(1-n_{i+})\prod_{r=1}^{k-l} M_{i+r-}D_{i+(k-l)+1-}
\tag{D.5b}
$$

$$
+ \frac{1}{2}\left[\sum_{k=0}^{\infty}\sum_{l=0}^{k} P_{i-1-l+}\prod_{m=0}^{k} M_{i-l+m+}D_{i+(k-l)+1+} + \sum_{k=0}^{\infty}\sum_{l=0}^{k} P_{i-1-l-}\prod_{m=0}^{k} M_{i-l+m-}D_{i+(k-l)+1-}\right],
$$

$$
n_{hi-} = \sum_{k=0}^{\infty}\sum_{l=0}^{k} P_{i-1-l-}\prod_{m=1}^{l} M_{i-m+}(1-n_{i-})\prod_{r=1}^{k-l} M_{i+r-1+}D_{i+(k-l)+}
\tag{D.5c}
$$

$$
+ \frac{1}{2}\left[\sum_{k=0}^{\infty}\sum_{l=0}^{k} P_{i-1-l-}\prod_{m=0}^{k} M_{i-l+m-}D_{i+(k-l)+1-} + \sum_{k=0}^{\infty}\sum_{l=0}^{k} P_{i-2-l+}\prod_{m=0}^{k} M_{i-l+m-1+}D_{i+(k-l)+}\right].
$$

that would correspond to the densities of holons in a domain polarized on leg $+$ and $-$ respectively. When the holon belongs to the cohort of a domain wall, there is an ambiguity in these definition. This ambiguity explains the factor $1/2$ (chosen conventionally). This ambiguity is lifted when defining holons independently of the leg (as it should) *e.g.* for $n_{h,i} = n_{hi+} + n_{hi-}$ when the holon belongs to the cohort of a domain wall $\backslash$ or no cohort of a domain wall and $n_{h,i} = n_{hi-1+} + n_{hi-}$

otherwise. The holon density is then

$$
\begin{aligned}
n_{hi} = &\sum_{k=0}^{\infty}\sum_{l=0}^{k} P_{i-1-l+} \prod_{m=1}^{l} M_{i-m+}(1-n_{i+}) \prod_{r=1}^{k-l} M_{i+r-} D_{i+(k-l)+1-} \\
&+ \sum_{k=0}^{\infty}\sum_{l=0}^{k} P_{i-1-l-} \prod_{m=1}^{l} M_{i-m+}(1-n_{i-}) \prod_{r=1}^{k-l} M_{i+r-1+} D_{i+(k-l)+} \\
&+ \sum_{k=0}^{\infty}\sum_{l=0}^{k} P_{i-1-l+} \prod_{m=0}^{k} M_{i-l+m+} D_{i+(k-l)+1+} \\
&+ \sum_{k=0}^{\infty}\sum_{l=0}^{k} P_{i-2-l-} \prod_{m=0}^{k} M_{i-l+m-1-} D_{i+(k-l)-}.
\end{aligned}
\tag{D.6}
$$

From the densities Eqs.(D.3,D.6), we deduce the existence of the (non-local) creation and annihilation operator for both holons ($h_i^\dagger$ and h_i) and domain walls ($w_i^\dagger$ and w_i).

D.2   Estimation of the energy level

We rewrite the perturbative Hamiltonian Eq.(5.4) using $h_i^\dagger$, h_i, $w_i^\dagger$, and w_i to estimate the energy levels as a function of the average densities f_h and f_w. The perturbative Hamiltonian is

$$
\begin{aligned}
H = t\sum_{i=1}^{L} &\left[h_i^\dagger h_{i+1}\left(1-n_{w\backslash,i}\right) + h_i^\dagger w_{i+1}^{\backslash\dagger} h_{i+1} w_i^{\backslash} + h_i^\dagger h_{i+1}\left(1-n_{w/,i+1}\right) + h_i^\dagger w_{i+2}^{/\dagger} h_{i+2} w_{i+1}^{/} \right. \\
&\left. + h_{i+1}^\dagger h_i\left(1-n_{w\backslash,i+1}\right) + w_i^{\backslash\dagger} h_{i+1}^\dagger w_{i+1}^{\backslash} h_i + h_{i+1}^\dagger h_i\left(1-n_{w/,i+2}\right) + w_{i+1}^{/\dagger} h_{i+2}^\dagger w_{i+2}^{/} h_i \right] \\
&- \frac{2t^2}{U}\sum_i \left[n_{w\backslash,i}(1-n_{h,i+1}) + n_{w/,i}(1-n_{h,i+1}) \right],
\end{aligned}
\tag{D.7}
$$

leading to the phenomenological Eq.(5.6) when simplifying the details concerning the range that have no influence on the estimation. For simplicity, we consider holons independent from domain walls to obtain an effective Hamiltonian for each by averaging over the holons or the domain walls separately. We have

$$
H_h \simeq |\alpha| \sum_{i=1}^{L}\left(e^{i\theta} h_i^\dagger h_{i+1} + \text{H.c.}\right) + \beta \sum_i (n_{h,i}-1),
\tag{D.8a}
$$

$$
H_w \simeq |\gamma| \sum_{i=1}^{L}\left(e^{i\phi} w_i^\dagger w_{i+1} + \text{H.c.}\right) + \delta \sum_i n_{w,i} + 2tL\,\text{Re}(\gamma),
\tag{D.8b}
$$

with

$$
\alpha = t\left(\langle 1 - n_{w,i+1}\rangle + \langle w_{i+1}^\dagger w_i\rangle\right) = |\alpha|e^{i\theta},
\tag{D.9a}
$$

$$
\beta = \frac{2t^2}{U}\langle n_{w,i}\rangle,
\tag{D.9b}
$$

$$
\begin{aligned}
\gamma &= t\langle h_{i+1}^\dagger h_i\rangle, \\
&= |\gamma|e^{i\phi},
\end{aligned}
\tag{D.9c}
$$

$$
\delta = -t\left(\langle h_{i-1}^\dagger h_{i-2}\rangle + \langle h_{i-1}^\dagger h_i\rangle\right) - \frac{2t^2}{U}\langle 1 - n_{h,i}\rangle.
\tag{D.9d}
$$

By diagonalizing the Hamiltonian Eqs.(D.8) and building the eigenstates as a product state of holonic and domain wall mode, we get the hopping averages (*e.g.* $\langle w_{i+1}^{\dagger} w_i \rangle$) such that

$$\alpha = t\left(1 - f_s\right) + \frac{2t}{L} e^{i(\phi - \pi - \frac{\pi}{L})} \frac{\sin(\frac{\pi}{2} f_w)}{\sin(\frac{\pi}{L})}, \tag{D.10a}$$

$$\beta = \frac{2t^2 f_w}{U}, \tag{D.10b}$$

$$\gamma = \frac{t}{L} e^{i(\theta - \pi - \frac{\pi}{L})} \frac{\sin(\pi f_h)}{\sin(\frac{\pi}{L})}, \tag{D.10c}$$

$$\delta = -\frac{2t}{L} \cos(\theta - \pi - \frac{\pi}{L}) \frac{\sin(\pi f_h)}{\sin(\frac{\pi}{L})} - \frac{2t^2}{U}\left(1 - f_h\right), \tag{D.10d}$$

$$\phi = \theta - \pi - \pi/L \ [2\pi], \tag{D.10e}$$

$$\tan(\theta) = \frac{\sin(\theta - \frac{2\pi}{L})}{\cos(\theta - \frac{2\pi}{L}) + \frac{L \sin(\pi/L)}{\sin(\pi f_w)}\left(1 - f_w\right)}. \tag{D.10f}$$

Eqs.(D.10e,D.10f) always (only) admit $\theta = \phi + \pi = 0 \ [2\pi]$ as a solution when $L \to \infty$. We then obtain Eq.(5.7) by averaging Eq.(5.6) over both holons and domain walls successively and using Eqs.(D.10) in the limit $L \to \infty$.

D.3 Phenomenological shoulder potential

We provide the expression of the shoulder potential and its contribution to the estimate of the energy level for $r_c = 3$. The method is identical to Sec.(D.2), but must be carried term by term. It is diagonal in the basis of domain walls and holons so there are no higher order corrections in V. Starting with

$$H_{\text{Shoulder}} = \sum_{i,\ell} \sum_{r=1}^{r_c} V_r n_{i,\ell} n_{i+r,\ell}, \tag{D.11}$$

the shoulder potential is rewritten as

$$\begin{aligned}
H_{\text{Shoulder}} - L(V_1 + V_2 + V_3) = &-(V_1 + 2V_2 + 3V_3)\sum_i n_{w,i}^{\backslash} - (2V_1 + 3V_2 + 4V_3)\sum_i n_{w,i}^{/} \\
&- 2(V_1 + V_2 + V_3)\sum_i n_{h,i} + V_1 \sum_i n_{h,i} n_{h,i+1} + V_2 \sum_i n_{h,i} n_{h,i+2} + V_3 \sum_i n_{h,i} n_{h,i+3} \\
&+ (V_1 + V_2 + V_3)\sum_i n_{w,i}^{/} n_{h,i+1} + (V_1 + V_2 + V_3)\sum_i n_{w,i}^{\backslash} n_{h,i+1} + (V_2 + V_3)\sum_i n_{w,i}^{/} n_{h,i+2} \\
&+ (V_2 + V_3)\sum_i n_{w,i}^{\backslash} n_{h,i+2} + (V_2 + V_3)\sum_i n_{h,i} n_{w,i+2}^{/} + (V_2 + V_3)\sum_i n_{h,i} n_{w,i+1}^{\backslash} \\
&+ V_3 \sum_i n_{w,i}^{/} n_{h,i+3} + V_3 \sum_i n_{w,i}^{\backslash} n_{h,i+3} + V_3 \sum_i n_{h,i} n_{w,i+3}^{/} + V_3 \sum_i n_{h,i} n_{w,i+2}^{\backslash} \\
&+ (V_2 + 2V_3)\sum_i (n_{w,i}^{/} n_{w,i+1}^{\backslash} + n_{w,i}^{\backslash} n_{w,i+2}^{/}) + V_3 \sum_i (n_{w,i}^{/} n_{w,i+2}^{\backslash} + n_{w,i}^{\backslash} n_{w,i+3}^{/})
\end{aligned} \tag{D.12}$$

$$\sim -\frac{1}{2}\sum_{i,l}(1+2l)V_l n_{w,i} - 2\sum_{i,l}V_l n_{h,i} + \sum_{i,l}V_l n_{h,i}n_{h,i+l} + 2\sum_{i,l}\sum_{m=l}^{\infty}V_m n_{w,i}n_{h,i\pm l}$$

$$+ (V_2 + 2V_3)\sum_i(n^{/}_{w,i}n^{\backslash}_{w,i+1} + n^{\backslash}_{w,i}n^{/}_{w,i+2}) + V_3\sum_i(n^{/}_{w,i}n^{\backslash}_{w,i+2} + n^{\backslash}_{w,i}n^{/}_{w,i+3}),$$

(D.13)

where Eq.(D.13) is the phenomenological approximation of Eq.(D.12). The contribution of the shoulder potential to the energy levels follows:

$$\langle H_{\text{Shoulder}}\rangle = L\sum_l V_l - \frac{L}{2}\sum_l(1+2l)V_l f_w - 2L\sum_l V_l f_h + L\sum_l V_l\left(f_h^2 - \frac{1}{l\pi^2}\sin(\pi f_h)\sin(l\pi f_h)\right)$$

$$+L\sum_l(2l-1)V_l f_m f_w + L(V_2 + 3V_3)f_w^2/2.$$

(D.14)

When $V_1 = V_2 = V$ and $V_3 = 0$, we find Eq.(5.8). Within the scope of the approximation, we see that longer-range interactions than next-to nearest neighbors or a more realistic potential for V_ℓ fitting e.g. $V/(1 + (\ell/r_c)^6)$ would not qualitatively change Eq.(D.14) and hence Eq.(5.8).

Chapter 6

Conclusion

In this part of the thesis we studied quantum phase transitions in many-body systems. Specifically, we analyzed various many-body setups whose asymptotically exact solutions can be obtains by using conformal field theoretical approach and bosonization techniques. As a recap, we have analyzed previously known results regarding 1-dimensional Quantum Ising model (QIM). By introducing the duality transformation, we showed that QIM undergoes a quantum phase transition from ordered to disordered phase, while the transition is driven by an external transverse magnetic field. By implementing the Jordan-Wigner transformation, QIM was mapped onto the so-called Kitaev chain model and it was demonstrated that the model hosts topologically non-trivial phase. By analyzing the topological phase, it was shown that zero-energy edge-modes correspond to Majorana fermions. Using this fact as a motivation to rewrite the whole model in terms of Majorana fermions, we demonstrate that the underlying field theory of QIM close to the criticality is a quantum field theory of massive Majorana fermions. At the critical point, Majorana field becomes massless and thus low-energy sector of QIM at the critical point is described a by 2-dimensional conformal field theory (CFT) of Majorana fermions. By using well established techniques of CFT, we demonstrate how the critical exponents and various correlation functions of QIM can be extracted, this solving the model exactly.

We have also re-derived and demonstrated the predictive power of the so-called Bosonization technique, being a closely related idea to the aforementioned Jordan-Wigner transformation. By presenting the detailed derivation and the application of Abelian variant of Bosonization in the context of XXZ Heisenberg model. We demonstrate how the exact solution of XX Heisenberg model and asymptotically exact solution for XXZ Heisenberg model for vanishing z-axis anisotropy differ from each other. By referring to the Bethe ansazt exact solution of XXZ Heisenberg model, we observed that the bosonization solution predicts correct physical properties of the model.

Motivated by recent advances in the experimental setups of synthetic quantum systems, analyze the phase diagram of hard-core bosons on a square and triangular lattices. Most important feature of the model is that the range of density-density interaction between bosons extends over 2 lattice sites. The extended range of interaction leads to novel phases of the system and can be experimentally realized by populating ultra-cold and Rydberg-dressed atoms on optical lattices. The Rydberg-dressing technique allows one to generate the interaction between two atoms characterized by the so-called soft-shoulder potential. The advantage of this approach is that the range and strength of soft-shoulder potential is easily tunable.

We provided and characterized the phase diagram of a system of spinless hard-core bosons in a square ladder geometry at filling $\nu = 2/5$, interacting via soft-shoulder potentials, and in the absence of inter-chain tunneling. The hard core bosons are allowed to tunnel within each chain with tunneling amplitude t, while the soft-shoulder repelling potential is assumed to extend only on two lattice site within each chain and has a fixed value of V. Additionally, if bosons are occupying nearest neighboring sites but reside on different legs of the lattice, then they are allowed to repel each other with strength U.

To obtain the phase diagram, we used analytical arguments close to the regime of weak coupling between the legs ($U \ll t, V$). Our analytical predictions were corroborated and extended to larger coupling using numerical simulations. Specifically, for $V \ll t$ and $U = 0$, each chain is described by a gapless Tomonaga-Luttinger liquid (TLL) with central charge $c = 1$. As soon as $U > 0$, the degree of freedom relative to the leg of the ladder, called spin, becomes gapped. The resulting gapless phase displays a leading spin-density wave (SDW) instability of momentum $2k_F$ well seen in the simulations. When $V \lesssim U/5$, and particularly when $V = 0$, the system transits across a Berezinskii-Kosterlitz-Thouless (BKT) phase transition predicted by the Abelian bosonization and hinted by the exact diagonalization. Past the transition, the description of the system is equivalent to the standard Hubbard model described by two Luttinger liquids with $c = 2$ in total.

For $V \gg t$ and $U = 0$, each chain displays an exotic cluster Luttinger liquid (CLL) with $c = 1$ described by cluster bosonization and seen by iDMRG. As soon as $U > 0$, the cluster equivalent of the spin degree of freedom is gapped, leading to a 'spin-locked' cluster with $c = 1$. The corresponding cluster density wave has a momentum $(3/4) \times 2k_F$, the clearest consequence of the clusterization of the microscopic degree of freedom into cells of 3 clusters of 4 particles in total for this filling and the range of V. Such emergent clustering is also reflected in both single chain and spin correlation functions.

In the vicinity of the single-chain transition point, we develop an effective field theory describing the ladder system that is obtained via coupling two supersymmetric conformal field theories – a scenario that is, to the best of our knowledge, not accessible in any other cold atom setup. The SUSY phase transition point at $U = 0$ and $V/t \simeq 5.7$ extends into a gapless phase with $c = 1$ and leading charge-density wave instability (CDW) of momentum $2k_F$ when $U > 0$ and $V/t \sim 5.7$. The CDW is separated from the SDW by a Gaussian phase transition with $c = 2$ and from the spin-locked CLL by a critical line with $c = 3/2$. Both the phase and the transitions are sharply seen by iDMRG. The critical line $c = 3/2$ may also be supersymmetric conformal phase transitions, but it is not possible to conclude this based on the present analysis. In fact, such proof may require a true quantum simulator, as the more direct way of probing this is studying the long-time dynamics of large chains. Indeed, it is possible to obtain the low-energy band structure of time-independent, translation-symmetric Hamiltonian by computing the time and space Fourier transform of correlation functions of various observables after a quench [100, 101]. The system therefore provides a unique platform to study interactions between two SUSY conformal field theories.

For the triangular geometry of the ladder, we have seen that the extension of the range of the inter-leg interaction immediately redesigns the vicinity of the supersymmetric point with respect to the square ladder case. In particular, a single phase transition line, likely to be a supersymmetric one, separates the weak and strong intra-chain interacting regimes at weak inter-chain interaction. The extra range only deforms the neighboring SDW and spin-locked CLL instead. Such results illustrate the difficulty in controlling the coupling between two supersymmetric field theories like in the square case as power-law tails always exist in realistic systems. Instead, the CLL phenomenology is robust to the inter-leg interaction range extension.

The strong coupling limit is also richer in the triangular geometry: a CDW appears at intermediate U/t, and the PH and gapped translation symmetry breaking CC emerge at large U/t, compared to the square case. The gapless PH is qualitatively unchanged by varying the range of the interaction or the filling. Instead, the CC disappears as soon as the filling ($2/5$ here) is changed or the interaction range is further extended akin to gapped phases in half-filled Hubbard models. We thus expect a plethora of other CC patterns for other ranges of V and matching commensurate filling, separated at incommensurate filling by both standard and cluster Luttinger liquid phases. The phenomenology of the extended Hubbard model at any filling and at strong coupling is thus more complex than the sole clusterization of the degrees of freedom but involves instead the co-existence of phases with both clustered and Luttinger bosonic excitations separated by uncommon (*e.g.,* supersymmetric) phase transitions.

Beyond observability in experiments, there are several research directions that one can pursue starting from the understanding of the present model. The onset of CLLs require a range of soft-shoulder interaction of at least 2. They are generally not modified by longer range, so that we do not expect a qualitative change of the phase diagram for longer ranges. Other commensurate fillings (above 1/3 but below 1/2 for range 2) may display CLL physics leading to similar phase diagrams. Different fillings for both chains are instead likely to lead to richer arrangements between the CLL on the two legs and decouple the SUSY points on one leg and the other, enriching the phase diagram once more. Other CLL arrangements may also appear when changing the sign of U, or extending the interaction U over more rungs. Besides exploring these various regimes theoretically and experimentally, it would also be interesting to stack more chains above the ladder and approach the 2D regime. It is indeed not known if the clusterization vanishes or if it becomes the local order of a fully gapped phase and how. Finally, it would be interesting to investigate regimes where the ladder displays a genuine SU(2) "spin"-symmetry, in analogy to electronic systems. Such interactions are not available when dressing atoms via s-states, but could be at least approximately realized utilizing a combination of dressing to p-states [102] and lattice spacing tuning.

Part II

Many-body systems with non-Markovian dynamics: memory effects and entanglement transitions

Introduction

Quantum systems in the real world are subject to their own coherent evolution as well as interactions with the environment. The interplay between these two gives rise to complex and rich physics that has great relevance in the context of quantum technologies, and has consequently been extensively studied in recent years. It is the case of many solid state, cold atoms or trapped ions systems, where environmental effects can strongly alter the state of the system [103, 104, 105, 106, 107, 108, 109, 110, 111, 112, 113, 114, 115, 116, 117, 118], such as in dissipative phase transitions tuned by the dissipation strength, or induce new relaxation regimes [119, 120, 121, 122, 123, 124, 125, 126, 127]. This interplay is important also in the context of quantum information where, for example, systems can decouple from the incoherent action of the environment and form dissipative free subspace with important error-preventing properties [128, 129, 130, 131, 132, 133, 134, 135, 136].

Dissipative phase transitions occur at the level of the average state – i.e. manifest themselves in the properties of the density matrix of the system – but new phases may emerge also at the level of single quantum trajectories, as highlighted by a series of recent works [137, 138, 139, 140, 141, 142, 143, 144, 145, 146, 147, 148, 149, 150, 151, 152, 153, 154, 155, 156, 157, 158, 159, 160, 161, 162, 163, 164, 165, 166, 167, 168, 169]. Focusing mainly on systems amenable to be realized in cold atoms or quantum computing platforms, these works have shown that the competition between quantum measurements and coherent dynamics also gives rise to transitions of the entanglement that manifest themselves in specific observables - such as von Neumann entropies, negativities, or two-time correlation functions. These transitions are often referred to as "measurement induced" phase transitions (MIPT).

The MIPT [170, 171, 137, 138, 139, 140, 141, 142, 143, 144, 145, 149, 148, 146, 151, 152, 153, 154, 156, 157, 158, 163, 164, 166, 167, 165, 162, 169, 172, 173] have been the subject of intense research in recent years. They appear at the level of the scaling behavior of the entanglement with the size of the system, and are caused by the action of random measurements that collapse the entanglement of the system, and counteract the correlation spreading action of the unitary dynamics. Even at a finite rate of measurement, this interplay leads to a transition between phases with extensive (or critical) scaling of the entanglement, and phases with low entanglement. Indeed, entanglement transitions have been observed in many different settings and models, including random circuits [139, 140, 138, 174, 175, 176], stabilizer and Clifford circuits [146, 151, 177, 178, 179, 155, 180, 181], Ising-like models with either short-range or long-range interactions [164, 182, 150, 183], and systems of free fermions [165, 162, 169, 184, 185, 186, 187]. In all these works, the studied systems are coupled to Markovian environments, which cause memory-less measurements – i.e. the probability of a random measurement occurring is completely independent of the history of the system. Opposite to this, the setup where the system is coupled to memoryful, i.e. non-Markovian measuring apparatus is largely unexplored. This is due to a complex interplay between entanglement destruction due to measurements and memory effect of the environment – lost coherences of the system can be recovered at later times.

The study of non-Markovian systems is broad and challenging [188]. Even at the level of the density matrix, it is not always possible to describe the dynamics through a Lindblad equation. This subject has been extensively studied in the literature, including its many connections to complexity and entanglement [189, 190, 191], and how to quantify the degree of non-Markovianity etc. [192, 193, 189, 194, 195]. One can choose to work with a paradigmatic model, in which the dynamics of

the system is described by a master equation of the type

$$\dot{\rho}(t) = \mathcal{L}_t \rho(t). \tag{6.0.1}$$

The time dependent Liouvillian $\mathcal{L}_t$ depends on the details of the unitary evolution and on a time dependent dissipation rate, which may be either positive or negative depending on the direction of the information flow. Information flows from the system to the environment and the decay rate is positive for Markovian regions, while it goes from the bath to the system (with an associated negative rate) when the evolution is non-Markovian.

Another difficulty of studying the many-body non-Markovian systems is the need to consider the quantum trajectories of its dynamics, and so far no clear and general protocol to unravel such non-Markovian dynamics exists. Unlike in Markovian systems, where the unraveling is performed in a straightforward way using methods such as Monte Carlo wave function (MCWF) [196, 197, 198], or Quantum State Diffusion (QSD) [199], unraveling recipes have proven to be much harder to implement for non-Markovian systems.

While in recent years a protocol implementing the unraveling through quantum jumps has been proposed for single-body systems [200, 201], still no general approach to many-particle systems exists. Indeed, extending the method of non-Markovian quantum jumps to many-body systems is not trivial, since the interplay between unitary evolution and measurements (or equivalently - interaction with the environment) makes this task very complicated at a conceptual level, and exponentially complex at a computational level. Just to cite an example, the quantum trajectories of a non-Markovian system are inter-dependent of each other, due to the memory of the bath, and a statistical sampling of the trajectory ensemble similar to the Markovian case is not possible anymore.

In the following chapters, after reviewing the foundations of open quantum systems and quantum information, we will try to bridge the gap between single- and many-body quantum jump approach for non-Markovian dynamics. To do this, we introduce a diagrammatic approach and demonstrate how non-Markovianity renormalizes the probability of following a certain quantum trajectory [202]. By applying the diagrammatic method to random unitary circuit model with non-Markovian measurements, we show that the measurement induced phase transition is stable against non-Markovian dynamics. Moreover, by directly simulating the quantum trajectories of partially monitored free fermionic ladder, we again confirm that MIPT can be resilient against the memory effects [203].

Chapter 7

Decoherence in open quantum systems

It is a nearly century old and as of today a well tested idea, that quantum mechanical systems can exhibit features such as superposition principle. Namely, if the system is allowed to be in either of $|\varphi_1\rangle$ and $|\varphi_2\rangle$ states, then the it is also allowed to be in any linear superposition of these two $\alpha_1|\varphi_1\rangle + \alpha_2|\varphi_2\rangle$. This, in turn, can result in various exotic states of matter, most notably entangled states [204].

Evidently, macroscopically large systems rarely appear in such states and typically exhibit properties that can be described using classical physics. Moreover, if one tries hard enough to prepare a mesoscopically large system in, let's say, an entangled state, the quantum effects of such a state will fade away almost instantaneously. Considering the importance of such states for fundamental research directions, quantum information theory and technology, it is natural to ask how the "quantumness" of the system is washed away as soon as one tries to consider realistic macroscopic systems.

A key insight is that such states of matter are robust by construction when the system itself is isolated from the environment. If one considers more realistic scenario and allows the system to interact with the environment, then the resulting exchange of information will strongly entangle the constituents of the system with vast number of environmental degrees of freedom. This effect, known as quantum decoherence [205, 206, 207, 208], will rapidly and strongly suppress the characteristic quantum behavior of the system to the measuring apparatus, thus effectively rendering the system classical for the observer.

7.1 Decoherence via interaction

Suppose that a system of interest is described by $\hat{\rho}_{\text{sys}}$ density matrix, that operates in the $\mathcal{H}_{\text{sys}}$ Hilbert space. For simplicity, suppose that the environment consists of a single quantum degree of freedom. Here we assume that initially the environment is in a pure state $\hat{\rho}_{\text{env}}(t_0) = |\psi_{\text{env}}(t_0)\rangle\langle\psi_{\text{env}}(t_0)|$, belonging to $\mathcal{H}_{\text{env}}$ Hilbert space. The system is brought in contact with the environmental degree of freedom for some time. Since in our setup the environment and the system constitute a closed quantum system, the interaction can be fully described by some scattering operator $\hat{S}$.

Before the interaction, the system and the environment are in a product state [205, 208]

$$\hat{\rho}(t_0) = \hat{\rho}_{\text{sys}}(t_0) \otimes \hat{\rho}_{\text{env}}(t_0), \tag{7.1.1}$$

which after the interaction transforms to

$$\hat{\rho}(t_1) = \hat{S}\left[\hat{\rho}_{\text{sys}}(t_0) \otimes \hat{\rho}_{\text{env}}(t_0)\right]\hat{S}^\dagger. \tag{7.1.2}$$

Let the set of orthogonal states of the system be denoted as $|m\rangle \in \mathcal{H}_{\text{sys}}$. If we assume that the scattering off the environmental degrees of freedom does not cause any $|m\rangle \to |m'\rangle$ transitions

between the states within the system, then this means that the scattering matrix commutes with the environmental states and thus can be expanded as

$$\hat{S} = \sum_n |n\rangle\langle n| \otimes \hat{S}_n \tag{7.1.3}$$

where $\hat{S}_n$ are the parts of the scattering operator that act only on the environment. This automatically leads to

$$\begin{aligned}
\hat{\rho}(t_1) &= \sum_{m,n} |m\rangle\langle m| \otimes \hat{S}_m \left[\hat{\rho}_{\text{sys}}(t_0) \otimes \hat{\rho}_{\text{env}}(t_0) \right] |n\rangle\langle n| \otimes \hat{S}_n^\dagger \\
&= \sum_{m,n} \langle m|\hat{\rho}_{\text{sys}}(t_0)|n\rangle \times |m\rangle\langle n| \otimes \left(\hat{S}_m \hat{\rho}_{\text{env}}(t_0) \hat{S}_n^\dagger \right) \\
&= \sum_{m,n} \langle m|\hat{\rho}_{\text{sys}}(t_0)|n\rangle \times \left[|m\rangle\langle n| \otimes |\psi_{\text{env}}^{(m)}(t_1)\rangle\langle\psi_{\text{env}}^{(n)}(t_1)| \right].
\end{aligned} \tag{7.1.4}$$

Integrating out the environmental degrees of freedom, i.e. reducing the density matrix over the system states only, we get the state of the system after the interaction

$$\hat{\rho}(t_1)_{\text{sys}} = \text{Tr}_{\text{env}}\left(\hat{\rho}(t_1) \right) = \sum_{m,n} \langle m|\hat{\rho}_{\text{sys}}(t_0)|n\rangle\langle\psi_{\text{env}}^{(n)}(t_1)|\psi_{\text{env}}^{(m)}(t_1)\rangle \times |m\rangle\langle n|. \tag{7.1.5}$$

Since $\hat{S}$ scattering matrix is unitary, we get the diagonal elements of $\hat{\rho}(t_1)_{\text{sys}}$ system density matrix are unaffected

$$[\hat{\rho}(t_1)_{\text{sys}}]_{m,m} = \langle m|\hat{\rho}_{\text{sys}}(t_0)|m\rangle. \tag{7.1.6}$$

However, the off-diagonal elements are modified as

$$[\hat{\rho}(t_1)_{\text{sys}}]_{m,n} = \langle m|\hat{\rho}_{\text{sys}}(t_0)|n\rangle \times \langle\psi_{\text{env}}^{(n)}(t_1)|\psi_{\text{env}}^{(m)}(t_1)\rangle, \tag{7.1.7}$$

where the absolute value of the second multiplier is always smaller than one, thus reducing the coherence of the state after the interaction. The reduction of the coherence is due to the information exchange between the system and the environment during the interaction, which gets discarded while taking the partial trace. The more information gets transferred from the system to environment, the smaller $\langle\psi_{\text{env}}^{(n)}(t_1)|\psi_{\text{env}}^{(m)}(t_1)\rangle$ becomes. Typically the decoherence occurs on a very short timescales.

Let us pass to a more generic case and assume that the environment is in an arbitrary mixed state. In the environmental eigen-basis, the mixed state is expressed as

$$\hat{\rho}_{\text{env}}(t_0) = \sum_n p_n |\psi_{\text{env}}^{(n)}(t_0)\rangle\langle\psi_{\text{env}}^{(n)}(t_0)|. \tag{7.1.8}$$

Moreover, for a generic $\hat{S}$ scattering matrix (not necessarily separable as $\hat{S} = \hat{S}_{\text{sys}} \otimes \hat{S}_{\text{env}}$) we have

$$\hat{\rho}(t_1) = \hat{S}\left[\hat{\rho}_{\text{sys}}(t_0) \otimes \hat{\rho}_{\text{env}}(t_0)\right]\hat{S}^\dagger = \sum_n p_n \hat{S}\left[\hat{\rho}_{\text{sys}}(t_0) \otimes |\psi_{\text{env}}^{(n)}(t_0)\rangle\langle\psi_{\text{env}}^{(n)}(t_0)|\right]\hat{S}^\dagger. \tag{7.1.9}$$

Tracing over the environmental degrees of freedom gives

$$\begin{aligned}
\hat{\rho}_{\text{sys}}(t_1) &= \sum_{m,n} p_n \langle\psi_{\text{env}}^{(m)}(t_0)|\hat{S}\left[\hat{\rho}_{\text{sys}}(t_0) \otimes |\psi_{\text{env}}^{(n)}(t_0)\rangle\langle\psi_{\text{env}}^{(n)}(t_0)|\right]\hat{S}^\dagger|\psi_{\text{env}}^{(m)}(t_0)\rangle \\
&\equiv \sum_{m,n} p_n \langle\psi_{\text{env}}^{(m)}(t_0)|\hat{S}|\psi_{\text{env}}^{(n)}(t_0)\rangle \times \hat{\rho}_{\text{sys}}(t_0) \times \langle\psi_{\text{env}}^{(n)}(t_0)|\hat{S}^\dagger|\psi_{\text{env}}^{(m)}(t_0)\rangle.
\end{aligned} \tag{7.1.10}$$

It should be emphasized, that $\langle\psi_{\text{env}}^{(m)}(t_0)|\hat{S}|\psi_{\text{env}}^{(n)}(t_0)\rangle$ and $\langle\psi_{\text{env}}^{(n)}(t_0)|\hat{S}^\dagger|\psi_{\text{env}}^{(m)}(t_0)\rangle$ are operators - they represent the matrix elements of the *total* scattering operator only on the environmental subspace, while still act as operators in the system hilbert space. The expression can be re-written as

$$\hat{\rho}_{\text{sys}}(t_1) = \sum_k \hat{K}_k \hat{\rho}_{\text{sys}}(t_0) \hat{K}_k^\dagger \tag{7.1.11}$$

where

$$\hat{K}_k = \sqrt{p_{n_k}}\langle\psi_{\text{env}}^{(m_k)}(t_0)|\hat{S}|\psi_{\text{env}}^{(n_k)}(t_0)\rangle \tag{7.1.12}$$

are the so-called *Kraus operators*. Due to the unitarity of $\hat{S}$, we have

$$\begin{aligned}
\sum_k \hat{K}_k^\dagger \hat{K}_k &= \sum_k p_{n_k}\langle\psi_{\text{env}}^{(n_k)}(t_0)|\hat{S}^\dagger|\psi_{\text{env}}^{(m_k)}(t_0)\rangle\langle\psi_{\text{env}}^{(m_k)}(t_0)|\hat{S}|\psi_{\text{env}}^{(n_k)}(t_0)\rangle \\
&= \sum_k p_{n_k}\langle\psi_{\text{env}}^{(n_k)}(t_0)|\hat{S}^\dagger\hat{S}|\psi_{\text{env}}^{(n_k)}(t_0)\rangle \\
&= \sum_k p_{n_k} = \mathbb{I},
\end{aligned} \tag{7.1.13}$$

where the second line is due to the completeness of the environmental basis and the third line is due to the unitarity of $\hat{S}$ operator. In Sec.(7.3). we will elaborate on the significance of the Kraus operators and Eq.(7.1.13) normalization condition.

7.2 Decoherence as measurement

As we saw in the previous section, the interaction between the system and the environment is equivalent to the information exchange between these two. Subsequent loss of this information in the environment leads to the reduction of the coherences in the system – suppressing the ability of the system to exhibit entangled states. Another mechanism of such suppression is the measurement. By perturbing the system with a probe and extracting information, the inevitable collapse of the state of the system will result in a similar reduction of the coherences. After briefly reviewing some aspects of the measurement theory, we will make a connection between the decoherence due interactions with the system and decoherence due to the measurement [205, 206, 207, 208].

7.2.1 Projective measurements

A projector operator $\hat{\Pi}_\alpha$, associated to an idealistic measuring process with an outcome α is

$$\hat{\Pi}_\alpha = |\alpha\rangle\langle\alpha|. \tag{7.2.1}$$

Crucial property of the projector operator is the resolution of identity

$$\sum_\alpha \hat{\Pi}_\alpha = \mathbb{I}.^{1} \tag{7.2.2}$$

The probability of measuring an outcome α in a quantum state ρ is given by a standard Born rule

$$p_\alpha = \text{Tr}\left(\hat{\Pi}_\alpha\hat{\rho}\right) = \langle\alpha|\hat{\rho}|\alpha\rangle. \tag{7.2.3}$$

---

[1] If α is a continuous outcome, then for the normalization have integral over projector-valued measure $\int d\hat{\Pi}(\alpha) = \mathbb{I}$. The projector-valued measures will be useful in Sec.9.1

Since the measurement is projective, the density matrix $\hat{\rho}'$ has to be normalized after every application of the measurement operator

$$\hat{\rho} \rightarrow \hat{\rho}' = \frac{\hat{\Pi}_\alpha \hat{\rho} \hat{\Pi}_\alpha}{\mathrm{Tr}\left(\hat{\Pi}_\alpha \hat{\rho}\right)}. \tag{7.2.4}$$

7.2.2   Generalized measurement

Suppose that an outcome α corresponds to some positive *measurement element* operator $\hat{F}_\alpha$, where the operators sum up to unity

$$\sum_\alpha \hat{F}_\alpha = \mathbb{I} \tag{7.2.5}$$

As already mentioned, the probability of observing an outcome α is

$$p_\alpha = \mathrm{Tr}\left(\hat{F}_\alpha \hat{\rho}\right). \tag{7.2.6}$$

Using this kind of measurement, the effect on the state $\hat{\rho}$ can be written as

$$\hat{\rho} \rightarrow \hat{\rho}' = \frac{\sum_k \hat{M}_\alpha^k \hat{\rho} (\hat{M}_\alpha^k)^\dagger}{\mathrm{Tr}(F_\alpha \hat{\rho})}, \tag{7.2.7}$$

The normalization condition of the so-called *measurement operators* $\hat{M}_\alpha^k$ is

$$\sum_k \hat{M}_\alpha^k (\hat{M}_\alpha^k)^\dagger = \hat{F}_\alpha. \tag{7.2.8}$$

It should be noted that the transformation Eq.(7.2.7) contains a positive map in the numerator. However, since $\sum_k \hat{M}_\alpha^k (\hat{M}_\alpha^k)^\dagger < \mathbb{I}$, the map is norm-decreasing. As we will see in Sec.(7.3), Eq.(7.2.7) is closely related to the so-called dynamical maps.

7.2.3   Efficient measurement

A special case of the generalized measurement is the so called *efficient measurement*. The measurement is said to be efficient, if the measurement element $\hat{F}_\alpha$ contains only one measurement operator $\hat{M}_\alpha$. In this case, the non-linear transformation of the density matrix becomes

$$\hat{\rho} \rightarrow \hat{\rho}' = \frac{\hat{M}_\alpha \hat{\rho} \hat{M}_\alpha^\dagger}{\mathrm{Tr}(F_\alpha \hat{\rho})}, \tag{7.2.9}$$

which implies that the a pure state $\hat{\rho}$ will be mapped onto another pure state $\hat{\rho}'$. Moreover, since the normalization condition demands that $\hat{M}_\alpha \hat{M}_\alpha^\dagger = \hat{F}_\alpha$, one can split the measurement operator as

$$\hat{M}_\alpha = \hat{U}_\alpha \hat{F}_\alpha^{1/2}, \quad \hat{U}_\alpha^\dagger \hat{U}_\alpha = \mathbb{I}. \tag{7.2.10}$$

Using this decomposition, we can express the efficient measurement as

$$\hat{\rho} \rightarrow \hat{\rho}' = \hat{U}_\alpha \frac{\hat{F}_\alpha^{1/2} \hat{\rho} \hat{F}_\alpha^{1/2}}{\mathrm{Tr}(F_\alpha \hat{\rho})} \hat{U}_\alpha^\dagger. \tag{7.2.11}$$

In this representation, we see that the transformation of the state splits into the so-called *raw measurement* $\hat{F}_\alpha^{1/2} \hat{\rho} \hat{F}_\alpha^{1/2} / \text{Tr}(F_\alpha)$, sandwiched by unitary $\hat{U}_\alpha$ *measurement back-action* operator [205, 207].

7.2.4 Indirect Measurement

Instead of directly measuring and thus strongly perturbing the state of the system, one can perform the measurement mediated by a probe. During this approach, we let a probe and the system interact with eachother and then perform a projective measurement on the probe, while minimally perturbing the state of the system. Mathematically, the procedure goes along the following steps: suppose the system is in some $\hat{\rho}_{\text{sys}}$ state, while the probe is initially prepared in $\hat{\rho}_{\text{probe}}$ state. After the interaction, a total $\hat{\rho} = \hat{\rho}_{\text{sys}} \otimes \hat{\rho}_{\text{probe}}$ state transforms using the aformentioned S scattering matrix [205, 208]

$$\hat{\rho}' = \hat{S} \left[\hat{\rho}_{\text{sys}} \otimes \hat{\rho}_{\text{probe}} \right] \hat{S}^\dagger. \tag{7.2.12}$$

After the interaction, the state of the probe is

$$\hat{\rho}'_{\text{probe}} = \text{Tr}_{\text{sys}} \left(\hat{S} \left[\hat{\rho}_{\text{sys}} \otimes \hat{\rho}_{\text{probe}} \right] \hat{S}^\dagger \right). \tag{7.2.13}$$

Probability of performing a measurement on $\hat{\rho}'_{\text{probe}}$ and finding α outcome is

$$p_{\alpha,\text{probe}} = \text{Tr}_{\text{probe}} \left(\Pi_\alpha \hat{\rho}'_{\text{probe}} \right) = \text{Tr}_{\text{probe}} \left(\Pi_\alpha \text{Tr}_{\text{sys}} \left(\hat{S} \left[\hat{\rho}_{\text{sys}} \otimes \hat{\rho}_{\text{probe}} \right] \hat{S}^\dagger \right) \right). \tag{7.2.14}$$

Since Π_α acts only on the probe Hilbert space, we can extend the operator as $\Pi_\alpha = \mathbb{I}_{\text{sys}} \otimes \Pi_{\alpha,\text{probe}}$ and thus

$$p_{\alpha,\text{probe}} = \text{Tr}_{\text{probe}} \left(\left[\mathbb{I}_{\text{sys}} \otimes \Pi_{\alpha,\text{probe}} \right] \text{Tr}_{\text{sys}} \left(\hat{S} \left[\hat{\rho}_{\text{sys}} \otimes \hat{\rho}_{\text{probe}} \right] \hat{S}^\dagger \right) \right). \tag{7.2.15}$$

Since the second trace affects only the system degrees of freedom we can swap the positions of Tr_{sys} and $\left[\mathbb{I}_{\text{sys}} \otimes \Pi_{\alpha,\text{probe}} \right]$:

$$
\begin{aligned}
p_{\alpha,\text{probe}} &= \text{Tr} \left(\hat{S}^\dagger \left[\mathbb{I}_{\text{sys}} \otimes \Pi_{\alpha,\text{probe}} \right] \hat{S} \left[\hat{\rho}_{\text{sys}} \otimes \hat{\rho}_{\text{probe}} \right] \right) = \\
&= \text{Tr} \left(\hat{S}^\dagger \left[\mathbb{I}_{\text{sys}} \otimes \Pi_{\alpha,\text{probe}} \right] \hat{S} \left[\mathbb{I}_{\text{sys}} \otimes \hat{\rho}_{\text{probe}} \right] \cdot \hat{\rho}_{\text{sys}} \right) \\
&= \text{Tr}_{\text{sys}} \left(\text{Tr}_{\text{probe}} \left(\hat{S}^\dagger \left[\mathbb{I}_{\text{sys}} \otimes \Pi_{\alpha,\text{probe}} \right] \hat{S} \left[\mathbb{I}_{\text{sys}} \otimes \hat{\rho}_{\text{probe}} \right] \right) \cdot \hat{\rho}_{\text{sys}} \right) \\
&= \text{Tr}_{\text{sys}} \left(\hat{F}_\alpha \hat{\rho}_{\text{sys}} \right)
\end{aligned}
\tag{7.2.16}
$$

with

$$\hat{F}_\alpha \equiv \text{Tr}_{\text{probe}} \left(\hat{S}^\dagger \left[\mathbb{I}_{\text{sys}} \otimes \Pi_{\alpha,\text{probe}} \right] \hat{S} \left[\mathbb{I}_{\text{sys}} \otimes \hat{\rho}_{\text{probe}} \right] \right). \tag{7.2.17}$$

It is evident that $\sum_\alpha \hat{F}_\alpha = \mathbb{I}_{\text{sys}}$ normalization is satisfied, due to unitarity of $\hat{S}$.

Since after the interaction we have $\hat{\rho}' = \hat{S} \left[\hat{\rho}_{\text{sys}} \otimes \hat{\rho}_{\text{probe}} \right] \hat{S}^\dagger$, the after performing the projective measurement on the probe, we have

$$
\begin{aligned}
\hat{\rho}''_\alpha &= \frac{\left(\mathbb{I}_{\text{sys}} \otimes \hat{\Pi}_{\alpha,\text{probe}}\right) \hat{\rho}' \left(\mathbb{I}_{\text{sys}} \otimes \hat{\Pi}_{\alpha,\text{probe}}\right)}{\text{Tr}\left[\left(\mathbb{I}_{\text{sys}} \otimes \hat{\Pi}_{\alpha,\text{probe}}\right) \hat{\rho}'\right]} = \frac{\left(\mathbb{I}_{\text{sys}} \otimes \hat{\Pi}_{\alpha,\text{probe}}\right) \hat{S} \left[\hat{\rho}_{\text{sys}} \otimes \hat{\rho}_{\text{probe}}\right] \hat{S}^\dagger \left(\mathbb{I}_{\text{sys}} \otimes \hat{\Pi}_{\alpha,\text{probe}}\right)}{\text{Tr}\left[\hat{S}^\dagger \left(\mathbb{I}_{\text{sys}} \otimes \hat{\Pi}_{\alpha,\text{probe}}\right) \hat{S} \left[\hat{\rho}_{\text{sys}} \otimes \hat{\rho}_{\text{probe}}\right]\right]} \\
&= \frac{\left(\mathbb{I}_{\text{sys}} \otimes \hat{\Pi}_{\alpha,\text{probe}}\right) \hat{S} \left[\hat{\rho}_{\text{sys}} \otimes \hat{\rho}_{\text{probe}}\right] \hat{S}^\dagger \left(\mathbb{I}_{\text{sys}} \otimes \hat{\Pi}_{\alpha,\text{probe}}\right)}{\text{Tr}_{\text{sys}}\left(\hat{F}_\alpha \hat{\rho}_{\text{sys}}\right)}.
\end{aligned}
$$
$$(7.2.18)$$

In this expression of $\hat{\rho}''_\alpha$, tracing out the probe gives the final state of the system:

$$
\hat{\rho}''_{\text{sys},\alpha} = \frac{\text{Tr}_{\text{probe}}\left[\left(\mathbb{I}_{\text{sys}} \otimes \hat{\Pi}_{\alpha,\text{probe}}\right) \hat{S} \left[\hat{\rho}_{\text{sys}} \otimes \hat{\rho}_{\text{probe}}\right] \hat{S}^\dagger \left(\mathbb{I}_{\text{sys}} \otimes \hat{\Pi}_{\alpha,\text{probe}}\right)\right]}{\text{Tr}_{\text{sys}}\left(\hat{F}_\alpha \hat{\rho}_{\text{sys}}\right)}.
$$
$$(7.2.19)$$

Suppose that the probe is in a mixed state $\hat{\rho}_{\text{probe}} = \sum_k p_{k,\text{probe}} |\psi^{(k)}_{\text{probe}}\rangle \langle \psi^{(k)}_{\text{probe}}|$, then

$$
\begin{aligned}
\hat{\rho}''_{\text{sys},\alpha} &= \sum_k \frac{\text{Tr}_{\text{probe}}\left(\left[\sqrt{p_{k,\text{probe}}}\left(\mathbb{I}_{\text{sys}} \otimes \hat{\Pi}_{\alpha,\text{probe}}\right) \hat{S}\right] \left[\hat{\rho}_{\text{sys}} \otimes |\psi^{(k)}_{\text{probe}}\rangle \langle \psi^{(k)}_{\text{probe}}|\right] \left[\sqrt{p_{k,\text{probe}}} \hat{S}^\dagger \left(\mathbb{I}_{\text{sys}} \otimes \hat{\Pi}_{\alpha,\text{probe}}\right)\right]\right)}{\text{Tr}_{\text{sys}}\left(\hat{F}_\alpha \hat{\rho}_{\text{sys}}\right)} \\
&= \sum_k \frac{\hat{M}_{\alpha,k,\text{sys}} \hat{\rho}_{\text{sys}} \hat{M}^\dagger_{\alpha,k,\text{sys}}}{\text{Tr}_{\text{sys}}\left(\hat{F}_\alpha \hat{\rho}_{\text{sys}}\right)}.
\end{aligned}
$$
$$(7.2.20)$$

If we take $\hat{\Pi}_{\alpha,\text{probe}} = |\alpha_{\text{probe}}\rangle \langle \alpha_{\text{probe}}|$, then

$$
\sum_k \frac{\hat{M}_{\alpha,k,\text{sys}} \hat{\rho}_{\text{sys}} \hat{M}^\dagger_{\alpha,k,\text{sys}}}{\text{Tr}_{\text{sys}}\left(\hat{F}_\alpha \hat{\rho}_{\text{sys}}\right)} = \sum_k \frac{\left[\sqrt{p_{k,\text{probe}}} \langle \alpha_{\text{probe}}| \hat{S} |\psi^{(k)}_{\text{probe}}\rangle\right] \hat{\rho}_{\text{sys}} \left[\sqrt{p_{k,\text{probe}}} \langle \psi^{(k)}_{\text{probe}}| \hat{S}^\dagger |\alpha_{\text{probe}}\rangle\right]}{\text{Tr}_{\text{sys}}\left(\hat{F}_\alpha \hat{\rho}_{\text{sys}}\right)}
$$
$$(7.2.21)$$

and this way we have

$$
\hat{M}_{\alpha,k,\text{sys}} \equiv \sqrt{p_{k,\text{probe}}} \langle \alpha_{\text{probe}}| \hat{S} |\psi^{(k)}_{\text{probe}}\rangle
$$
$$(7.2.22)$$

It is important to stress, that if the probe is initially in the pure state, then only one measurement operator $\hat{M}_{\alpha,k',\text{sys}}$ survives, while rest vanish due to $p_{k \neq k',\text{probe}} = 0$. This way, if the probe is prepared in the pure state, then the indirect measurement becomes efficient.

Moreover, if one performs an indirect measurement, but skips the readout process, then we rely on a probabilistic description:

$$
\hat{\rho}''_{\text{sys}} = \sum_{\alpha,k} \hat{M}_{\alpha,k,\text{sys}} \hat{\rho}_{\text{sys}} \hat{M}^\dagger_{\alpha,k,\text{sys}}
$$
$$(7.2.23)$$

which very closely resembles Eqs.(7.1.11,7.1.12). This is what allows us to interpret decoherence as information transfer from the system to the environment.

7.3 Markovian Dynamics of Open Quantum System

In last two sections we have introduced and briefly studied a setup, where a quantum system interacts with the environment, or equivalently with the measuring apparatus. Using considerations from scattering theory, we deduced that the interaction inevitably leads to decoherence in the system. In what follows, we will study the same problem, but from more generic point of view. Instead of using the scattering theory, we will employ much larger class of mappings for the density matrix, referred to as quantum dynamical semi-groups. Using this approach, we will derive the Lindblad master equation – equation of motion for the state of the system which interacts with the environment. Implementing the Markovian and non-Markovian quantum trajectory methods, we will demonstrate how to unravel many-body Markovian and single-body non-Markovian master equations, respectively.

Suppose that an isolated system is in some mixed state $\hat{\rho}$ and the dynamics is governed by some Hamiltonian $\hat{H}$, then the temporal evolution of $\hat{\rho}$ is governed by the von Neumann equation [205]:

$$\partial_t \hat{\rho} = \frac{1}{i}\left[\hat{H}, \hat{\rho}\right], \quad \hbar \equiv 1. \tag{7.3.1}$$

The system under consideration is referred to as closed, since the temporal evolution is unitary and thus reversible

$$\hat{\rho}(t) = \hat{U}(t)\hat{\rho}(0)\hat{U}^\dagger(t), \quad \hat{U}(t) = e^{i\hat{H}t}. \tag{7.3.2}$$

If we trace out some part of the system, then the dynamics of a subsystem becomes open and thus non-reversible. One might pose the question from a different point of view and ask what is the equation of motion for a system that is coupled to the environment. Integrating out the environmental degrees of freedom leads to

$$\hat{\rho}_{\text{sys}}(t) = \text{Tr}_{\text{env}}\left[\hat{U}(t)\hat{\rho}(0)\hat{U}^\dagger(t)\right] \quad \rightarrow \quad \partial_t \hat{\rho}_{\text{sys}}(t) = \frac{1}{i}\text{Tr}_{\text{env}}\left(\left[\hat{H}, \hat{\rho}\right]\right) \tag{7.3.3}$$

The equation above is exact, but offers barely any practical use, therefore we need some further assumptions to extract some useful information about the dynamics of the system.

Eq.(7.3.3), respecting causality principle, is non-local in time and in general $\hat{\rho}_{\text{sys}}(t)$ depends on the state of the system at all previous times $t' < t$. For a generic case, the evolution of the state is governed by a generalized master equation. The equation can be specified using linear operators that takes in $\hat{\rho}_{\text{sys}}(t')$ state of the system for all $t' < t$ and maps them to an infinitesimal change of the state at time t:

$$\hat{\rho}_{\text{sys}}(t + dt) = \hat{\rho}_{\text{sys}}(t) + dt\mathcal{P}\left[\{\hat{\rho}_{\text{sys}}(t') : t' < t\}\right]. \tag{7.3.4}$$

A temporal non-locality of Eq.(7.3.4) can be interpreted as a memory effect – both system and environment have memory of their past state and of the system-environment interaction. A way to circumvent this issue is to coarse-grain the time to scales much larger than the characteristic time of the environment, so that the memory effects become negligible. After a proper coarse-graining, the master equations becomes local in time and thus the change in $\hat{\rho}_{\text{sys}}$ at some time t now solely depends on the state at that same instant. The time-local equation itself can be represented by a Liouville super-operator as

$$\partial_t \hat{\rho} = \mathcal{L}\hat{\rho}. \tag{7.3.5}$$

Master equations of this type are called Markovian, due to absence of memory of state. Both Markovian and non-Markovian master equations will be reviewed in details in what follows.

The evolution of a quantum state has to respect certain properties, for the state of the system to remain physical. One has to double-check if these properties are also respected after the coarse-graining of the time-scales. Below we will review these properties and, consequently, the imposed

constraints on the Liouville super-operator.

7.3.1   Quantum Dynamical Semi-Groups

To properly formulate the Markovianity assumption, one can use the quantum dynamical semigroup approach. We start of with few ideas from the open quantum system theory [198, 205, 207].

A dynamical map is a one parameter (in our case time t) map, that maps the system at time $\hat{\rho}(0)$ to a state at later time $\hat{\rho}(t)$

$$\mathcal{W}(t) : \hat{\rho}(0) \to \hat{\rho}(t), \tag{7.3.6}$$

where, of course, the parameters t is non-negative, corresponding to the forward propagation of the state. For $t = 0$, the map corresponds to an identity $\mathcal{W}(0) \equiv \mathbb{I}$. For the dynamical map to be physical, the initial state $\hat{\rho}(0)$ has to be mapped on to a valid state $\hat{\rho}(t)$. This requirement narrows down the properties of $\mathcal{W}(t)$. Firstly, the dynamical map has to be *trace preserving*, which guarantees that the state remains normalized after the evolution. Secondly, the transformation of the mixed states of the systems demand that the map to be *convex linear*. Thirdly, the map $\mathcal{W}_t(\rho_0)$ must be *completely positive*. Complete positivity ensures that the dynamical map, when applied to small part of a larger system, does not lead to the subsystem being in an un-physical (non-positive) state. This is crucial when considering entangled systems where the map might act only on a subsystem.

The framework of dynamical semi-groups has many mathematical advantages in analyzing a complex dynamics of the system coupled to environment.

Any dynamical map can be written in Kraus representation, in terms of an operator-sum form

$$\mathcal{W}_t(\rho_0) = \sum_{\alpha=1}^{N} K_\alpha(t)\rho_0 K_\alpha^\dagger(t), \tag{7.3.7}$$

where $K_\alpha(t)$ are the Kraus operators already introduced in Eqs.(7.1.11,7.1.12), with the resolution of identity,

$$\sum_{\alpha=1}^{N} K_\alpha^\dagger(t)K_\alpha(t) = \mathbb{I}. \tag{7.3.8}$$

The choice of the Kraus operator is not unique, but the number of Kraus operators N in the theory is limited by $N \leq d^2$, where d is the size of the Hilbert space of the system under consideration.

We go a step further and assume that the map $\mathcal{W}_t$ forms a dynamical semigroup:

$$\mathcal{W}_{t_1}(\mathcal{W}_{t_2}(\rho)) = \mathcal{W}_{t_1+t_2}(\rho) \tag{7.3.9}$$

which is assumed to be valid for any non-negative $t_{1,2}$. This assumptions seems to be valid after the coarse-graining the time, as during times longer than typical timescales of the environment, all the memory of the environment is erased. The reason why we are dealing with a semigroup and not a group is due to the absence of the inverse element.

For a dynamical semigroup, there exists a superoperator $\mathcal{L}$ that acts as a generator and satisfies

$$\mathcal{W}_t = e^{\mathcal{L}t}. \tag{7.3.10}$$

This way, $\mathcal{W}_t(\rho)$ becomes a formal solution of the Markovian master equation

The dynamics of a closed/isolated quantum systems can be formulated in various ways, two of them being known as Schrödinger and Heisenberg picture. By far, we have been working using Schrödinger picture, where the state of the system evolves unitarily in time, while the operators do not depend on time at all. Now we reformulate our discussion following Heisenberg picture, where

the state of the system does not evolve in time, but the operators do change. Suppose we have an operator $\hat{O}$, then the map

$$\tilde{\mathcal{W}}_t : \hat{O}_0 \to \hat{O}_t \qquad (7.3.11)$$

is called a dual map (dual with respect to $\mathcal{W}_t$). The maps $\mathcal{W}_t$ and $\tilde{\mathcal{W}}_t$ are related to eachother by

$$\text{Tr}\left[\hat{O}\mathcal{W}_t\left(\hat{\rho}\right)\right] = \text{Tr}\left[\hat{\rho}\tilde{\mathcal{W}}_t\left(\hat{O}\right)\right], \qquad (7.3.12)$$

meaning that the expectation value of $\langle\hat{O}\rangle$ should be independent of the picture on chooses to work in. As for $\mathcal{W}_t$, for a dynamical semigroup $\tilde{\mathcal{W}}_t = e^{\tilde{\mathcal{L}}t}$, the equation of motion for operator $\hat{O}$ takes the form

$$\partial_t \hat{O} = \tilde{\mathcal{L}}\hat{O}, \qquad (7.3.13)$$

where $\tilde{\mathcal{L}}$ now is a dual Liouville operator. $\mathcal{L}$ and dual $\tilde{\mathcal{L}}$ operators are related to eachother by

$$\text{Tr}\left[\hat{O}\mathcal{L}\left(\hat{\rho}\right)\right] = \text{Tr}\left[\hat{\rho}\tilde{\mathcal{L}}\left(\hat{O}\right)\right]. \qquad (7.3.14)$$

7.3.2 The Lindblad Form Of The Master Equation

Using the notions presented in the previous subsection, we are in shape to derive the general form of $\mathcal{L}$ generator constrained by the dynamical semigroup assumption [205]. Here we additionally assume that the system of interest has a finite $d < \infty$ Hilbert space $\mathcal{H}$ and define the scalar product of operators acting in $\mathcal{H}$ as $(\hat{O}, \hat{O}') = \text{Tr}\left(\hat{O}^\dagger \hat{O}'\right)$, we get a d^2 dimensional Hilbert space $\mathcal{H}'$.

In $\mathcal{H}'$ Hilbert space, one can find an orthonormal vector (operator) basis E_β with $\beta = 1, 2, ..., d^2$. Using this basis, any operator K_α can be expanded as

$$K_\alpha = \sum_{\beta=1}^{d^2} (E_\beta, K_\alpha) E_\beta. \qquad (7.3.15)$$

We are free to choose the basis $\{E_\beta\}$ in a way, that one of the elements is proportional to identity operator. Suppose that the label for such an operator is $\beta = d^2$, thus

$$E_{d^2} = \frac{1}{\sqrt{d}}\mathbb{I}, \qquad (7.3.16)$$

meaning that the trace of E_{d^2} operator is normalized to $\sqrt{d}$, while all the other operators are traceless.

Using this operator, we can re-write Kraus representation of dynamical map as (dropping t time label temporarily)

$$\mathcal{W}_t\left(\rho_0\right) = \sum_{\alpha=1}^{N}\left(\sum_{\beta=1}^{d^2}(E_\beta, K_\alpha)E_\beta\right)\rho_0\left(\sum_{\beta'=1}^{d^2}E_{\beta'}^\dagger(E_{\beta'}, K_\alpha)^*\right) = \sum_{\beta,\beta'=1}^{d^2}c_{\beta\beta'}E_\beta\rho_0 E_{\beta'}^\dagger \qquad (7.3.17)$$

with

$$c_{\beta\beta'} = \sum_{\alpha=1}^{N}(E_\beta, K_\alpha)(E_{\beta'}, K_\alpha)^*. \qquad (7.3.18)$$

Here $c_{\beta\beta'} = c_{\beta\beta'}(t)$ are elements of a positive matrix. We can derive the semigroup generator $\mathcal{L}$, defined as

$$\mathcal{L}\rho = \partial_t \rho = \lim_{\Delta t \to 0} \frac{\rho(t + \Delta t) - \rho(t)}{\Delta t} = \lim_{\Delta t \to 0} \frac{1}{\Delta t} \left(\mathcal{W}_{\Delta t} \rho - \rho \right) \tag{7.3.19}$$

Using this expansion derived above, we have

$$
\begin{aligned}
\mathcal{W}_{\Delta t}\rho - \rho &= \sum_{\beta,\beta'=1}^{d^2} c_{\beta\beta'} E_\beta \rho E_{\beta'}^\dagger - \rho = \\
&= c_{d^2,d^2} E_\beta \rho E_{\beta'}^\dagger - \rho + \sum_{\beta=1}^{d^2} \left(c_{d^2,\beta} E_{d^2} \rho E_\beta^\dagger + c_{\beta,d^2} E_\beta \rho E_{d^2}^\dagger \right) + \sum_{\beta,\beta'=1}^{d^2-1} c_{\beta\beta'} E_\beta \rho E_{\beta'}^\dagger = \\
&= \frac{c_{d^2,d^2} - d}{d} \rho + \rho \left(\sum_{\beta=1}^{d^2} \frac{c_{d^2,\beta}}{\sqrt{d}} E_\beta^\dagger \right) + \left(\sum_{\beta=1}^{d^2} \frac{c_{\beta,d^2}}{\sqrt{d}} E_\beta \right) \rho + \sum_{\beta,\beta'=1}^{d^2-1} c_{\beta\beta'} E_\beta \rho E_{\beta'}^\dagger \equiv \\
&\equiv \Delta t \left(c_0 \rho + \rho B^\dagger + B\rho + \sum_{\beta,\beta'=1}^{d^2-1} \alpha_{\beta\beta'} E_\beta \rho E_{\beta'}^\dagger \right).
\end{aligned}
\tag{7.3.20}
$$

Plugging this expression in Eq.(7.3.19), we get

$$\mathcal{L}\rho = c_0 \rho + \rho B^\dagger + B\rho + \sum_{\beta,\beta'=1}^{d^2-1} \alpha_{\beta\beta'} E_\beta \rho E_{\beta'}^\dagger. \tag{7.3.21}$$

By splitting B operator into Hermitian and anti-Hermitian parts as

$$B = G - \frac{c_0}{2} - iH, \tag{7.3.22}$$

we get

$$\mathcal{L}\rho = \frac{1}{i}[H, \rho] + \{G, \rho\} + \sum_{\beta,\beta'=1}^{d^2-1} \alpha_{\beta\beta'} E_\beta \rho E_{\beta'}^\dagger. \tag{7.3.23}$$

Since the dynamical map is trace preserving $\mathrm{Tr}\,(\mathcal{L}\rho) = 0$, this gives

$$\mathrm{Tr}\left[\left(2G + \sum_{\beta,\beta'=1}^{d^2-1} \alpha_{\beta\beta'} E_{\beta'}^\dagger E_\beta \right) \rho \right] = 0 \tag{7.3.24}$$

which must be valid for all ρ and thus we see that operator G and matrix α are related to eachother as

$$G = -\frac{1}{2} \sum_{\beta,\beta'=1}^{d^2-1} \alpha_{\beta\beta'} E_{\beta'}^\dagger E_\beta. \tag{7.3.25}$$

This relation yields

$$\mathcal{L}\rho = \frac{1}{i}[H, \rho] + \sum_{\beta,\beta'=1}^{d^2-1} \alpha_{\beta\beta'} \left(E_\beta \rho E_{\beta'}^\dagger - \frac{1}{2}\{E_{\beta'}^\dagger E_\beta, \rho\} \right). \tag{7.3.26}$$

To transform Eq.(7.3.26) to a standard Lindblad form, we need to diagonalize positive matrix α. Suppose that one finds such unitary matrix U, that yields

$$U\alpha U^\dagger = \text{diag}(\gamma_1, \gamma_2, .., \gamma_{d^2-1}), \tag{7.3.27}$$

then by transforming the basis operators as

$$E_j = \sum_{k=1}^{d^2-1} L_k U_{kj} \tag{7.3.28}$$

we get

$$\mathcal{L}\rho = \frac{1}{i}[H, \rho] + \sum_{\beta=1}^{N} \gamma_\beta \left(L_\beta \rho L_\beta^\dagger - \frac{1}{2}\{L_\beta^\dagger L_\beta, \rho\} \right), \quad N \le d^2 - 1. \tag{7.3.29}$$

This way we see, that the temporal evolution of the density matrix is governed by a hermitian operator H and set of jump operators $\{L_\beta\}$. It should be noted that H appearing in the unitary part of the Lindblad equation can be different from the Hamiltonian of the isolated system. The coefficients γ_β associated to each jump operator are positive γ_β and are frequently referred to as the decay rates, while indices β are known as the decay channels. The fact that the decay rates are positive is tightly connected to the fact that the dynamics of the system is assumed to be Markovian. As we will see later, for negative decay rates the dynamics becomes effectively non-Markovian.

7.4 Quantum Trajectories

Extracting valuable information from the master equation is not an easy task. One way to tackle this complication is based on the so-called quantum trajectory method. Based on this approach, one imagines the evolution of the system as a sequence of processes when quantum jumps do or do not occur. These processes are frequently referred to as click and no-click events and the sequence of them is referred to as a quantum trajectory. Every distinct quantum trajectory has a corresponding probability of occurring. By rewriting the evolution of the state of the system in terms of these probabilities, one can unravel the master equation and reformulate it in a stochastic form. Apart from the numerical advantage of simulating stochastic equation of motion, quantum trajectory approach also gives a deep insight regarding the physical processes. Below we will review the quantum trajectory approach in the context of Markovian dynamics [198, 205, 207].

We can split the Liouville superoperator $\mathcal{L}$ into two parts $\mathcal{L}_0$ and $\mathcal{L}_*$, then the formal solutions of the master equations can be written as

$$\begin{aligned} \mathcal{W}_t = e^{t\mathcal{L}} = e^{t(\mathcal{L}_0 + \mathcal{L}_*)} &= \sum_{n=0}^{\infty} \frac{t^n}{n!}(\mathcal{L}_0 + \mathcal{L}_*)^n \\ &= \sum_{n=0}^{\infty} \sum_{\{k_n=0\}}^{\infty} \frac{t^{n+\sum_j k_j}}{(n+\sum_j k_j)!} \mathcal{L}_0^{k_n} \mathcal{L}_* \mathcal{L}_0^{k_{n-1}} \mathcal{L}_* \times ... \times \mathcal{L}_* \mathcal{L}_0^{k_1} \mathcal{L}_* \mathcal{L}_0^{k_0} \end{aligned} \tag{7.4.1}$$

To obtain the second line, we used the binomial formula for non-commuting operators [209]. One can use the following integral identity

$$\frac{t^{n+\sum_j k_j}}{(n+\sum_j k_j)!} = \int_0^t dt_n \int_0^{t_n} dt_{n-1} ... \int_0^{t_2} dt_1 \frac{(t-t_n)^{k_n}}{k_n!} \times \frac{(t_n - t_{n-1})^{k_{n-1}}}{k_{n-1}!} \times ... \times \frac{t_1^{k_0}}{k_0!} \tag{7.4.2}$$

and further simplify Eq.(7.4.1) as

$$
\mathcal{W}_t = \sum_{n=0}^{\infty} \sum_{\{k_n=0\}}^{\infty} \int_0^t dt_n \int_0^{t_n} dt_{n-1}... \int_0^{t_2} dt_1 \frac{(t-t_n)^{k_n} \mathcal{L}_0^{k_n} \mathcal{L}_*}{k_n!} \times \frac{(t_n - t_{n-1})^{k_{n-1}} \mathcal{L}_0^{k_{n-1}} \mathcal{L}_*}{k_{n-1}!} \times ... \times \frac{t_1^{k_0} \mathcal{L}_0^{k_0}}{k_0!}
$$

$$
= e^{t\mathcal{L}_0} + \sum_{n=1}^{\infty} \int_0^t dt_n \int_0^{t_n} dt_{n-1}... \int_0^{t_2} dt_1 e^{(t-t_n)\mathcal{L}_0} \mathcal{L}_* e^{(t_n - t_{n-1})\mathcal{L}_0} \mathcal{L}_* ... \times \mathcal{L}_* e^{t_1 \mathcal{L}_0}.
$$

$$(7.4.3)$$

This way, we obtain a Dyson-like expansion of an evolution of the system [70]. One can think of $\mathcal{L}_0$ as an unperturbed evolution of the state, while $\mathcal{L}_*$ corresponds to the perturbations. This way, the evolution of the state from time 0 up to time t can be imagined as unperturbed steps of evolution interspersed with perturbations $\mathcal{L}_*$.

Going back to the Lindblad form of the master equation Eq.(7.3.29), one introduce a set of new super-operators, defined as

$$
\mathcal{L}_\beta \rho = \gamma_\beta L_\beta \rho L_\beta^\dagger \tag{7.4.4}
$$

and supplement it with a non-Hermitian operator $\tilde{\mathrm{H}}$:

$$
\tilde{\mathrm{H}} = \mathrm{H} - \frac{i}{2} \sum_{\beta=1}^N \gamma_\beta L_\beta^\dagger L_\beta. \tag{7.4.5}
$$

Using these two new operators, Eq.(7.3.29) can be expressed as

$$
\mathcal{L}\rho = \frac{1}{i} \left(\tilde{\mathrm{H}}\rho - \rho\tilde{\mathrm{H}}^\dagger \right) + \sum_{\beta=1}^N \gamma_\beta L_\beta \rho L_\beta^\dagger \equiv \mathcal{L}_0 \rho + \sum_{\beta=1}^N \mathcal{L}_\beta \rho. \tag{7.4.6}
$$

Here we have introduced new two types of operators, $\mathcal{L}_0$ and $\{\mathcal{L}_\beta\}$. Regardless the fact that none of these super-operators generate a dynamical semi-group, they still are useful constructions to interpret non-unitary evolution of quantum systems. The operators $\{\mathcal{L}_\beta\}$ describe an instantaneous quantum jumps in the system, that occur randomly in time with corresponding probability γ_β. Suppose that at time t_j the system undergoes a quantum jump along β_j channel, then some realization of the evolution of the system for time t, containing n quantum jumps can be labeled as

$$
T_n^t = \{t_1, \beta_1 | t_2, \beta_2 | ... | t_n, \beta_n\}. \tag{7.4.7}
$$

We will refer to T_n^t as record of evolution. This way, a generic non-unitary evolution $\mathcal{W}_t$ can be expressed as free evolution $e^{t\mathcal{L}_0}$ renormalized by all possible superoperators corresponding to T_n^t record

$$
\mathcal{W}_t = e^{t\mathcal{L}_0} + \sum_{n=1}^{\infty} \int_0^t dt_n \int_0^{t_n} dt_{n-1}... \int_0^{t_2} dt_1 \sum_{T_n^t} \mathcal{M}_{T_n^t},
$$

$$
\mathcal{M}_{T_n^t} \equiv e^{(t-t_n)\mathcal{L}_0} \mathcal{L}_{\beta_n} e^{(t_n - t_{n-1})\mathcal{L}_0} \mathcal{L}_{\beta_{n-1}}... \times \mathcal{L}_{\beta_0} e^{t_1 \mathcal{L}_0}. \tag{7.4.8}
$$

In this expression, $e^{t\mathcal{L}_0}$ term contains only a single T_0^t record, where no quantum jumps have occurred.

Since $\tilde{\text{H}}$ has a negative complex part $\text{Im}\left(\tilde{\text{H}}\right) = -\frac{1}{2}\sum_{\beta=1}^{N}\gamma_\beta L_\beta^\dagger L_\beta$, $e^{t\mathcal{L}_0}$ renders to be trace decreasing:

$$\text{Tr}\left[e^{t\mathcal{L}_0}\rho\right] = \text{Tr}\left[e^{-t\sum_\beta \gamma_\beta L_\beta^\dagger L_\beta}\rho\right] \quad \rightarrow \quad \frac{d}{dt}\text{Tr}\left[e^{t\mathcal{L}_0}\rho\right] = -\sum_{\beta=1}^{N}\text{Tr}\left[\gamma_\beta L_\beta^\dagger L_\beta e^{t\mathcal{L}_0}\rho\right] =$$
$$= -\sum_{\beta=1}^{N}\text{Tr}\left[\mathcal{L}_\beta\left(e^{t\mathcal{L}_0}\rho\right)\right] < 0. \tag{7.4.9}$$

Since $\mathcal{L}_0$ super-operator is related to an evolution with no-jump record, it is natural to interpret $\text{Tr}\left[e^{t\mathcal{L}_0}\rho\right]$ as the probability $\mathcal{P}(T_0^t)$ of realisation of such a record. Due to this, the non-Hermitian operator $\tilde{\text{H}}$ is frequently referred to as as a no-click Hamiltonian. Moreover, the fact that $\frac{d}{dt}\text{Tr}\left[e^{t\mathcal{L}_0}\rho\right] < 0$ means that the probability of quantum jump occurring is increased after every subsequent time step. Similarly, $\text{Tr}\left[\mathcal{M}_{T_n^t}\rho\right]$ gives the probability $\mathcal{P}(T_n^t)$ observing T_n^t record of quantum jumps after evolving the system for time t.

Using the record operators $\mathcal{M}_{T_n^t}$ and the corresponding probabilities of realizing them $\mathcal{P}(T_n^t)$, we can define normalized the so-called quantum trajectory operators

$$\mathcal{C}(\rho|T_n^t) \equiv \frac{\mathcal{M}_{T_n^t}\rho}{\mathcal{P}(T_n^t)}. \tag{7.4.10}$$

Using this quantum trajectory formalism, one can formally write down the exact solution of the Lindblad equations

$$\rho(t) = \mathcal{P}(T_0^t)\mathcal{C}(\rho|T_0^t) + \sum_{n=1}^{\infty}\int_0^t dt_n \int_0^{t_n} dt_{n-1}...\int_0^{t_2} dt_1 \sum_{\{T_n^t\}}\mathcal{P}(T_n^t)\mathcal{C}(\rho|T_n^t). \tag{7.4.11}$$

This stochastic unraveling of the master equations once shows how the evolution of the system consists of multiple quantum trajectories, each occurring with corresponding probability.

Moreover, since we have

$$e^{t\mathcal{L}_0}\rho = e^{-it\tilde{\text{H}}}\rho e^{it\tilde{\text{H}}^\dagger}, \quad \mathcal{L}_\beta\rho = \gamma_\beta L_\beta \rho L_\beta^\dagger \tag{7.4.12}$$

one can re-write Eq.(7.4.10) as

$$\mathcal{C}(\rho|T_n^t) = \frac{M_{T_n^t}\rho M_{T_n^t}^\dagger}{\text{Tr}\left(M_{T_n^t}^\dagger M_{T_n^t}\rho\right)} \tag{7.4.13}$$

with

$$M_{T_n^t} = e^{-i(t-t_n)\tilde{\text{H}}}L_{\beta_n} \times e^{-i(t_n-t_{n-1})\tilde{\text{H}}}L_{\beta_{n-1}} \times ... \times e^{-it_1\tilde{\text{H}}}L_{\beta_1}. \tag{7.4.14}$$

A close resemblance between Eq.(7.4.13) and Eq.(7.2.9) again demonstrates that the dynamics of an open quantum system generated by $\mathcal{L}$ Liouville superoperator can be viewed as an effective continuous monitoring of the system by the environment.

7.5 Non-Markovian Dynamics of Open Quantum System

As we have derived in Sec.(7.3), by introducing appropriate set of jump operators $\{L_\beta\}$, supplemented with $\gamma_\beta > 0$ decay rates, one may fully describe the temporal evolution of a system that is coupled to the bath with a master equation Eq.(7.3.29). The validity of this approach is based on the assumption that the temporal evolution of the state is governed by the dynamical map and

thus the Eq.(7.3.7) Kraus decomposition of the map holds. One can go a step further and show that even by neglecting the Markov approximation, the density matrix of the system interacting with the environment obeys a time-local master equation if the dynamical map is invertible and differentiable [210]. To demonstrate this, we take the time derivative of the Kraus representation of the dynamical map Eq.(7.3.7), which yield

$$\frac{d\rho_t}{dt} = \sum_\alpha \left(\frac{dK_\alpha(t)}{dt}\rho_0 K_\alpha^\dagger(t) + K_\alpha(t)\rho_0\frac{dK_\alpha^\dagger(t)}{dt} \right). \tag{7.5.1}$$

If the map is invertible, then the initial density matrix ρ_0 can always be expressed as

$$\rho_0 = \sum_m F_m(t)\rho_t Q_m(t). \tag{7.5.2}$$

Plugging this expression back into Eq.(7.5.1) gives

$$\frac{d\rho_t}{dt} = \sum_{\alpha,m} \left(\frac{dK_\alpha(t)}{dt}F_m(t)\rho_t Q_m(t)K_\alpha^\dagger(t) + K_\alpha(t)F_m(t)\rho_t Q_m(t)\frac{dK_\alpha^\dagger(t)}{dt} \right) =$$
$$= \sum_{\alpha,m} \left(A_{1,\alpha,m}(t)\rho_t B_{1,\alpha,m}^\dagger(t) + A_{2,\alpha,m}(t)\rho_t B_{2,\alpha,m}^\dagger(t) \right), \tag{7.5.3}$$

where $k \equiv \{\sigma, \alpha, m\}$

$$A_{1,\alpha,m}(t) = \frac{dK_\alpha(t)}{dt}F_m(t), \quad A_{2,\alpha,m}(t) = K_\alpha(t)F_m(t),$$
$$B_{1,\alpha,m}^\dagger(t) = Q_m(t)K_\alpha^\dagger(t), \quad B_{2,\alpha,m}^\dagger(t) = Q_m(t)\frac{dK_\alpha^\dagger(t)}{dt}. \tag{7.5.4}$$

By introducing a shorthand notation k for the collective set of indices $\{1, \alpha, m\}$ and $\{2, \alpha, m\}$, we get

$$\frac{d\rho_t}{dt} = \sum_k A_k(t)\rho_t B_k^\dagger(t). \tag{7.5.5}$$

Just like in Eq.(7.3.15,7.3.16), we can introduce a complete basis of operators and expand A_k and B_k as

$$A_k(t) = \sum_i a_{ik}(t)G_i, \quad B_k(t) = \sum_i b_{ik}(t)G_i, \tag{7.5.6}$$

which leads to a similar construction as we got with a Markov approximation Eq.(7.3.20). Repeating identical the calculations as in Sec.(7.3), finally yields

$$\mathcal{L}(t)\rho = \frac{1}{i}[H(t), \rho] + \sum_{\beta=1}^N \gamma_\beta(t)\left(L_\beta(t)\rho L_\beta^\dagger(t) - \frac{1}{2}\{L_\beta^\dagger(t)L_\beta(t), \rho\} \right), \tag{7.5.7}$$

which is a non-Markovian generalization of Eq.(7.3.29). Here, complete positivity of the map is guaranteed only if $\gamma_\beta(t) \geq 0$ for all β and any t. This means, that the overall dynamics is Markovian if all of the decay rates are non-negative for all times [188, 211] and it becomes Non-Markovian if at least one of the decay rate becomes negative during some time interval Δt. The reason why the dynamics becomes non-Markovian for negative decay rates will be examined in Sec.(7.7).

In order to study the dynamics of the system where the decay rates can become negative, one

has to unravel the corresponding master equation as it was done in Eq.(7.4.11)– i.e. follow the evolution of the state along a single trajectory corresponding to a particular realization of the random quantum jumps. A standard technique is the Monte Carlo wave function (MCWF) method [196, 197]. This method can be summarized in the following way [212]:

1. Extract the probability of performing a jump along a channel s:

$$p^{s,+} = \gamma_s(t)\delta t \langle \psi(t)|L_s^\dagger L_s|\psi(t)\rangle. \tag{7.5.8}$$

2. Generate a random number $0 \geq p \geq 1$ and compare it with $p^{s,+}$. The outcome decides whether the jump happens or no;

3. If $p < p^{s,+}$, then a quantum jump occurs and the state of the system gets updated as

$$|\psi\rangle \to |\psi'\rangle = \frac{L_s|\psi\rangle}{||L_s|\psi\rangle||}; \tag{7.5.9}$$

4. If $p > p^{s,+}$, then a quantum jump does not occur and the system evolves according to a corresponding no-click Hamiltonian Eq.(7.4.5).

5. Inject the resulting state back to step 1 and repeat to obtain a quantum trajectory.

6. Take the average these wave functions at any time to extract the density matrix of the system.

We see that adapting this recipe to non-Markovian systems presents some problems. An evident issue is that for the times when $\gamma_s(t) < 0$ the jump probability would become negative, which has no physical meaning.

Another issue is that the back-flow of information from the environment to the system restores not only the population of the excited states, but also coherences, i.e. the off-diagonal elements in the density matrix, as can be seen by solving the master equation [200, 201]. This cannot be implemented through an "opposite" jump operator that connects two states in the opposite direction of the corresponding normal jump operator. Fig.(7.1) shows the simple example of a spin pair that loses its entanglement upon the application of a normal jump operator; applying the inverse operator does not result in retrieving the lost entanglement. This is true even for single body systems: take for example a two level system with $a = \sigma^-$; one may be tempted to use σ^+ to reverse the effect of the quantum jump, but it can be seen that the application of σ^+ leads to an increase of the population in the excited state, which still results in a decay of coherences. Restoring quantum coherence is an operation that requires memory of the past evolution of the system, a property that a simple implementation in terms of Kraus operators does not have.
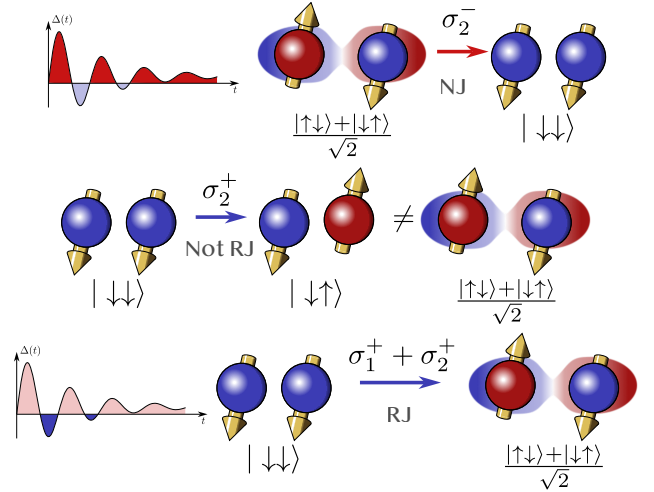
FIGURE 7.1: (a) Scheme of an entangled spin pair undergoing a normal jump (NJ) through the jump operator σ_2^-. (b) Trying to implement the reverse jump (RJ) through σ_2^+ re-excites the second spin, but does not take the spins into the initial entangled state, and the system stays separable. (c) Instead, in order to restore the original entanglement one has to apply $\sigma_1^+ + \sigma_2^+$ even though the NJ knew nothing about the presence of spin 1.

7.6   Non-Markovian quantum jumps of single body systems
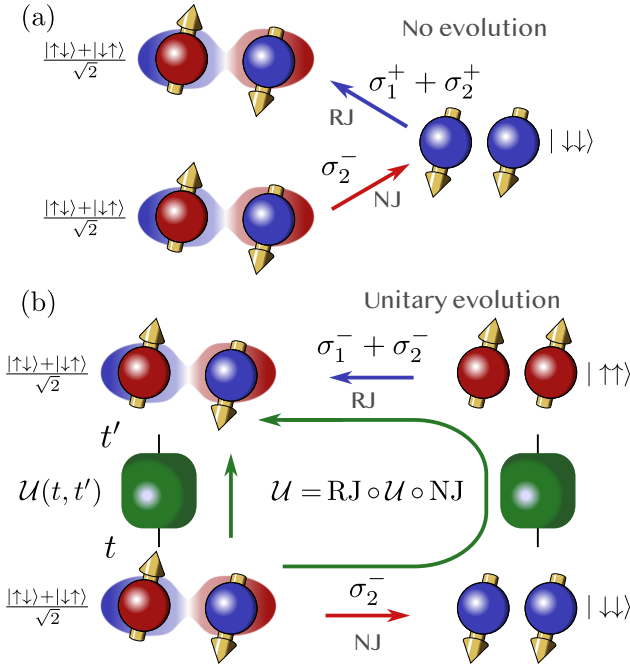
FIGURE 7.2: (a) Simple example of the dependence of the reverse jump (RJ) operator on the time at which is performed. A system starts in an entangled Bell pair state and normal jumps (NJ) into the separable state through σ_2^-. (a) If the RJ occurs immediately, the original state is restored through $\sigma_1^+ + \sigma_2^+$. (b) If the system evolves from time t to t' through the unitary operator $\mathcal{U} = \sigma_1^x \sigma_2^x$, the separable state is now flipped and the RJ operator that restores the original state is now $\sigma_1^- + \sigma_2^- = \mathcal{U}(\sigma_1^+ + \sigma_2^+)\mathcal{U}^\dagger$.

In this section we will review in detail what is known about one- (or few-) body systems. This is instructive to highlight the conceptual differences with respect to Markovian dynamics, as well as to identify the major technical challenges that we will address in the many-body case below.

A technique to unravel non-Markovian dynamics has been proposed in Ref. [200, 201], in the form of the non-Markovian quantum jumps (NMQJ) method. This prescription allows to describe each interaction with the environment (either Markovian or non-Markovian) in terms of a quantum jump process, and gives back the correct starting master Eq.(7.5.7) when averaged over the stochastic ensemble of quantum trajectories. For simplicity, we can assume that the jump operators are independent of time.

The main feature of the NMQJ method is the introduction of two different types of quantum jumps in the stochastic evolution of the state: a "normal jump" (NJ) occurring during the Markovian regions of the dynamics ($\gamma(t) \geq 0$), and a "reverse" quantum jump (RJ) acting during the non-Markovian regions ($\gamma(t) < 0$). A reverse jump essentially brings the quantum state back to what it was prior to the last Markovian normal jump, effectively cancelling out its effects on the system. More formally, this is described by stating explicitly the probability of performing a jump (either normal or reverse) in the Markovian and non-Markovian regions, and the corresponding initial and final quantum state before and after the jump, similar to Eq.(7.5.9).

Similarly to the MCWF method, the evolution of the state $|\psi(t)\rangle$ along a trajectory is deterministic, until a random quantum jump occurs. We discretize the evolution of the system, so that the probability that more than one jump occurs within each time interval δt is negligible, and assume the jumps to occur instantaneously. The average over the stochastic ensemble gives back the density matrix: $\rho(t) = \sum_{\{|\psi\rangle\}} \frac{N_{|\psi\rangle\langle\psi|}(t)}{N} |\psi(t)\rangle \langle\psi(t)|$, where $N_{|\psi\rangle\langle\psi|}(t)$ is the population of the trajectory $|\psi(t)\rangle$ and N is the total population of the states in the ensemble – i.e. the ratio $\frac{N_{|\psi\rangle\langle\psi|}(t)}{N}$ is the stochastic probability of realizing the trajectory $|\psi(t)\rangle$.

Let us now consider a time t for which a particular channel s has a positive rate $\gamma_s(t) > 0$. The system may perform a normal jump from a state $|\psi\rangle$ to a state $|\psi'\rangle$ with probability $p^{s,+}$, according to Eqs.(7.5.8,7.5.9).

During a non-Markovian region a RJ may occur cancelling out the effect of the last normal jump:

$$|\psi'(t)\rangle \leftarrow |\psi(t)\rangle = \frac{L_s|\psi'(t)\rangle}{||L_s|\psi'(t)\rangle||}; \tag{7.6.1}$$

$$p^{s,-}_{|\psi\rangle \to |\psi'\rangle} = \frac{N'(t)}{N(t)}|\gamma_s(t)|\delta t \langle\psi'(t)|L_s^\dagger L_s|\psi'(t)\rangle. \tag{7.6.2}$$

The $\leftarrow$ means that the system performs the reverse jump starting from the initial state $|\psi(t)\rangle$, which is the result of applying the NJ operator L_s to the final state $|\psi'(t)\rangle$ after the RJ. This corresponds to effectively erasing the last NJ, and the initial states eligible to reverse jump are the ones that have previously performed (at least) one normal jump. This is also reflected in the expectation value of $L_s^\dagger L_s$, which expresses the probability that a certain state is eligible to jump, and that for a reverse jump is calculated on the target state but using the normal jump operators.

The process in Eq.(7.6.1) cannot be described using a Kraus operator, but is formally obtained by applying the (state dependent) jump operator $|\psi'(t)\rangle\langle\psi(t)|$. This is a fundamental difference with the MCWF method and a consequence of the memory of the non-Markovian dynamics: the operator corresponding to a RJ depends on the current quantum state and on the target state, see Fig.(7.2).

Another consequence is the presence of the ratio $N'(t)/N(t)$ in the jump probability: it corresponds to the ratio between the probability of being in the target state and the probability of being in the initial state. This ratio ensures that the evolution averaged over trajectories is described by the master equation Eq.(7.5.7).

In Refs. [200, 201] the number of inequivalent trajectories – in the sense that they correspond to different quantum states (we explain it more in detail later on) – is finite and very small, due to the single body nature of the considered systems. This makes a numerical simulation of the system dynamics viable, since one only has to follow those few trajectories and update the ensemble statistics based on the type of quantum jump performed by the system.

The situation is very different for a many-body system: if the jump operators take the system into states that are not eigenstates of the unitary evolution given by H, then the time at which a jump is performed becomes important, resulting in different trajectories. The number of trajectories is then very large, being exponential in the time of the evolution. For example, this occurs when the many-body Hamiltonian contains terms that counteract the action of the jump operators, since at any time the system may or may not decay, and after a decay it may be excited again by the unitary evolution. A very simple example is a two spin-1/2 system with jump operators $\sigma^-_{1/2}$ and unitary evolution operator $\sigma^x_1\sigma^x_2$: the steady state for the jump operator has both spins down in the z direction; this is not an eigenstate of the Hamiltonian, which can move back the spins to be both up in the z direction, thus effectively counteracting the action of the jump operators, see Fig.(7.2).

As noted in Ref. [213, 201], the dynamics corresponding to this unraveling [200, 201] do not have an immediate physical representation in terms of a measurement protocol. For example, probing the bath to check if a jump occurred may destroy the information lost by the system and stored in the bath, and prevent the possibility of successively restoring such information. Nevertheless, this method provides key qualitative insights on non-Markovian dynamics, and rigorously illustrates how information back-flow from the environment to the system can be captured utilizing pure state dynamics only. Moreover we can still treat the trajectories as well defined mathematical objects, each with a quantum state that solely determines the physical properties, and a stochastic probability of realizing that trajectory. In Sec.(10.2), we will finally show how, under certain conditions, the inequivalent trajectories we discuss *do* describe the evolution of a realistic system (albeit corresponding to a master equation that differs from the one we start from).

From these considerations, it is evident that the application of the NMQJ method as described in Ref. [200, 201] to many-body systems is not viable. One needs a new formulation that incorporates the conceptual understanding gathered from single body problems with the non-trivial many-body dynamics, in a mathematically coherent manner. This is question will be addressed in Chap.(10).

7.7   Trace-distance as a measure of non-Markovianity

In previous sections we argued that non-Markovian behavior in quantum systems can be thought as the restoration of the lost coherences in the past dynamics, being equivalent to the memory effect [200]. In this chapter we will review how to quantify non-Markovianity in a quantum system. To keep the measure of non-Markovianity as generic as possible, one may constrain the map of the density matrix to be physical and work in the language of dynamical semi-group. This way, it is possible to avoid any further assumptions regarding the master equation and the corresponding structure of evolution [201].

Suppose that we have two quantum systems A and B that are isolated from eachother. These systems can be initiated to be in some states $\rho_A(0)$ and $\rho_B(0)$. These states can be chosen to be arbitrary and in general different from eachother $\rho_A(0) \neq \rho_B(0)$. Within this setup, a crucial difference between Markovian and non-Markovian processes is that after some time t, in the former case the distinguishability between $\rho_A(t)$ and $\rho_B(t)$ is reduced, while for the latter it can be enhanced. To understand this, one can interpret Markovianity as a non-reversible loss of information from the system to the environment. This, in turn, leads to states $\rho_A(0)$ and $\rho_B(0)$ to flow towards a mutually non-distinguishable steady state. Opposite to this, during non-Markovian dynamics, the information flows back from the environment to the system which leads to $\rho_A(t)$ and $\rho_B(t)$ states being distinguishable. The fact that during non-Markovian dynamics the system retains the memory of the past, renders the non-Markovian evolution to violate the divisibility Eq.(7.3.9).

To quantify the distinguishability between two states, we construct the so-called trace-distance between two states, a metric in the space of states:

$$d_\rho(\rho_A, \rho_B) = \frac{1}{2}\mathrm{Tr}\left(|\rho_A - \rho_B|\right), \quad |\rho| \equiv \sqrt{\rho^\dagger \rho}. \tag{7.7.1}$$

An important feature of such construction is that all completely positive and trace-preserving (CPT) maps $\mathcal{W}_t = e^{\mathcal{L}t}$, such as Eq.(7.3.29) with positive decay rates, are contractions for this metric

$$d_\rho(\rho_A, \rho_B) \geq d_\rho(\mathcal{W}_t\rho_A, \mathcal{W}_t\rho_B) \tag{7.7.2}$$

meaning that any CPT dynamical map can only reduce or at most leave the distinguishability between ρ_A and ρ_B intact.

We can generalize this statement for a broader class of maps. Suppose that we are dealing with a quantum map described by a time-dependent but time-local master equation Eq.(7.5.7). For time being, we assume that all decay rates $\gamma_s(t)$ are always positive. Even though this class of quantum processes does not correspond to dynamical semi-group, $\gamma_s(t) > 0$ constraint leads the dynamics to be time-dependent Markovian. Using the time-ordering operator $\mathcal{T}$, we can define a two parameter $\mathcal{W}(t_2, t_1)$ CPT map as

$$\mathcal{W}(t_2, t_1) = \mathcal{T}\left(e^{\int_{t_1}^{t_2} d\tau \mathcal{L}(\tau)}\right). \tag{7.7.3}$$

$\mathcal{W}(t_2, t_1)$ dynamical map has the property of divisibility, in the sense that, for instance, $\mathcal{W}(t_2 + t_1, 0)$ dynamical map can be decomposed as

$$\mathcal{W}(t_2 + t_1, 0) = \mathcal{W}(t_2 + t_1, t_1)\mathcal{W}(t_1, 0). \tag{7.7.4}$$

Since in Eq.(7.7.4), all three maps are CPT, we can say that

$$d_\rho(\rho_A(t), \rho_B(t)) \geq d_\rho(\rho_A(t+dt), \rho_B(t+dt)). \tag{7.7.5}$$

It is then natural to distinguish Markovian from non-Markovian dynamics based on whether d_ρ always decreases or may also increase, and to quantify the degree of non-Markovianity of a map $\mathcal{W}_t$ with how much the distance between two density matrices increases over time. Following Ref. [192], we define the time derivative $\sigma_{\mathcal{W}}$ at time t of the trace distance for a given map, and for two initial density matrices $\rho_A(0)$ and $\rho_B(0)$, as

$$\sigma_{\mathcal{W}}(t, \rho_{A,B}(0)) = \frac{d}{dt} d_\rho(\mathcal{W}_t \rho_A(0), \mathcal{W}_t \rho_B(0)) \tag{7.7.6}$$

For a Markovian map $\sigma_{\mathcal{L}}$ is always negative, while it may become positive for finite time intervals for a non-Markovian map.

The non-Markovianity measure $\mathcal{N}(\mathcal{W})$ is then defined as the maximum over all possible initial conditions of the integral of $\sigma_{\mathcal{W}}$ over the times where it is positive

$$\mathcal{N}(\mathcal{W}) = \max_{\rho_{A,B}(0)} \int_{\sigma_{\mathcal{W}}>0} dt \sigma_{\mathcal{W}}(t, \rho_{A,B}(0)). \tag{7.7.7}$$

A simple example to demonstrate non-Markovian dynamics is a two-level system interacting with cavity modes [192, 207]. The master equation that describes the dynamics of the density matrix of the system is

$$\dot{\rho} = \mathcal{L}(t)\rho = \gamma(t)\left(\sigma^- \rho \sigma^+ - \frac{1}{2}\{\sigma^+ \sigma^-, \rho\}\right), \quad H(t) = 0 \tag{7.7.8}$$

where we only have a single decay channel with $L = \sigma^-$ time-independent jump operator, with a time-dependent decay rate $\gamma(t)$. Suppose at time $t = 0$ we initiate two copies of the system in states $\rho_A = |0\rangle\langle 0|$ and $\rho_B = |0\rangle\langle 0|$. The trace-distance between these two states is

$$d_\rho(0) = \frac{1}{2}\text{Tr}\left(\sqrt{|0\rangle\langle 0| + |1\rangle\langle 1|}\right) = 1 \tag{7.7.9}$$

After dt time of evolution, the states $\rho_A(t)$ and $\rho_B(t)$ become

$$\rho_{A,B}(t+dt) = \rho_{A,B}(t) + \gamma_{t+dt} dt \left(\sigma^- \rho_{A,B}(t)\sigma^+ - \frac{1}{2}\left[\sigma^+\sigma^- \rho_{A,B}(t) + \rho_{A,B}(t)\sigma^+\sigma^-\right]\right) \tag{7.7.10}$$

Starting at $t = 0$ gives

$$\begin{aligned}
\rho_A(dt) &= |0\rangle\langle 0| \\
\rho_B(dt) &= |0\rangle\langle 0| - (1 - \gamma_{dt} dt)(|0\rangle\langle 0| - |1\rangle\langle 1|) \\
&\approx |0\rangle\langle 0| - e^{-\gamma_{dt} dt}(|0\rangle\langle 0| - |1\rangle\langle 1|)
\end{aligned} \tag{7.7.11}$$

The further evolution of ρ_A state is trivial and it always remain in the ground state. The evolution of ρ_B for the next time-step dt is

$$\begin{aligned}
\rho_B(2dt) &= \rho_B(dt) + \gamma_{2dt} dt\left(\sigma^- \rho_B(dt)\sigma^+ - \frac{1}{2}\left[\sigma^+\sigma^- \rho_B(dt) + \rho_B(dt)\sigma^+\sigma^-\right]\right) \\
&= |0\rangle\langle 0| - e^{-(\gamma_{dt} + \gamma_{2dt})dt}(|0\rangle\langle 0| - |1\rangle\langle 1|)
\end{aligned} \tag{7.7.12}$$

It is easy to check that this trend remains to be valid for any ndt time-step:

$$\rho_B(ndt) = |0\rangle\langle 0| - e^{-\sum_{j=1}^{n} \gamma_j dt\, dt} \left(|0\rangle\langle 0| - |1\rangle\langle 1|\right) \tag{7.7.13}$$

By taking $dt \to 0$ and $n \to \infty$, so that $ndt = t$, we get

$$\begin{aligned}
\rho_A(t) &= |0\rangle\langle 0|, \\
\rho_B(t) &= |0\rangle\langle 0| - e^{-G(t)} \left(|0\rangle\langle 0| - |1\rangle\langle 1|\right); \\
G(t) &= \int_0^t d\tau \gamma(\tau).
\end{aligned} \tag{7.7.14}$$

Using this result, we can calculate the exact time dependence of the trace distance

$$d_\rho(t) = e^{-G(t)} \tag{7.7.15}$$

and thus the measure of non-Markovianity Eq.(7.7.6) for the two-level system becomes

$$\sigma_{\mathcal{W}}(t, \rho_{A,B}(0)) = -\gamma(t) e^{-G(t)} \tag{7.7.16}$$

which starts to increase only if $\gamma(t)$ becomes negative.

As we already saw in Sec.(7.6), during times when the decay rates become negative, the lost coherence of the system are effectively recovered due to the information back-flow. This effect, in certain cases, can violate the complete positivity of the dynamical map $\mathcal{W}_t$. However, a necessary and sufficient condition for $\mathcal{W}_t$ map to be regarded as completely positive is $G(t) \geq 0$ for all times. In some realistic physical setups this condition can be satisfied, for example we can assume the decay rate $\gamma(t)$ originates from a bath whose spectral density is described by a Lorentzian centered around ω and with bandwidth Γ. Within the time-convolutionless approximation [214, 201], the decay rate becomes

$$\gamma(t) = \gamma_0 \left[\frac{\Gamma}{\omega} + e^{-\Gamma t} \left(\sin(\omega t) - \frac{\Gamma}{\omega} \cos(\omega t) \right) \right]. \tag{7.7.17}$$

For such a decay rate, $\gamma(t)$ can become negative for certain times, while $G(t) > 0$ condition is always satisfied.

It should be noted that one is not bound to work exclusively with $\mathbb{L}_1$ trace distance $\sim \mathrm{Tr}\left(|\rho_A - \rho_B|\right)$. Any generalization from $\mathbb{L}_1$ to $\mathbb{L}_d$ $d-$trace distance can be used to characterize non-Markovianity. For instance, in Sec.(11.3) we will demonstrate that $\mathbb{L}_2$ square trace distance defined as

$$d_2(\rho_1, \rho_2) = \sqrt{\mathrm{Tr}|\rho_1 - \rho_2|^2} \tag{7.7.18}$$

has advantage over d_ρ, when considering non-Markovian dynamics in fermionic Gaussian states [215].

Apart from the trace distance, there are other measures of non-Markovianity [216, 217, 218]. One of them, see Ref.[189], is taking the advantage of the dynamics of quantum correlations during trace-preserving completely-positive (CP) map.

Suppose that we prepare the system in a way, that it is maximally entangled with an ancilla. We assume that the system undergoes some undetermined dynamics, while the ancilla remains isolated from the environmental effects. It is known that entanglement can not increase by local trace-preserving CP maps [219]. Since such maps admit the composition rule Eqs.(7.3.9,7.7.4), then decay of the entanglement of the system with ancilla should monotonically decrease. This condition can break down if the dynamics of the system is non-Markovian, since environmental correlations can enhance and suppress the entanglement. This way, a simple way to determine whether the unknown dynamics of the system is Markovian or non-Markovian is to check if the monotonicity condition is

satisfied during some interval of time $t \in [t_{\min}, t_{\max}]$. This way, if $M(\rho_{\text{sys.+anc.}}(t)) \equiv M(t)$ is some measure of entanglement between the system and the ancilla at some time t, then one can define an alternative measure of non-Markovianity as

$$I_M = \int_{t_{\min}}^{t_{\max}} dt \left| \frac{dM}{dt} \right| - (M(t_{\min}) - M(t_{\max})). \tag{7.7.19}$$

If the dynamics within the system is Markovian and thus $\frac{dM}{dt} < 0$ at all times, then $I_M = 0$ by construction. On the other hand, I_M becomes non-zero only if the dynamics is non-Markovian.

Even though some non-Markovian evolution still may remain undetected, using I_M can still be advantageous when one has to study infinite-dimensional systems. For other measures of non-Markovianity, one might need to know precise form of the dynamics of the system, while I_M does not require such knowledge.

Chapter 8

Measures of Quantum Entanglement

As mentioned in Sec.(7), the principle of superposition allows systems to be in exotic states, such as entangled states. In past decades, the understanding of entanglement has strongly developed and helped to establish a whole separate line of research known as the quantum information theory [204, 212, 220]. As of today, experimental progress lead us to the possibility to create, manipulate and measure various properties of entangled states of many-body systems. Moreover, the possibility to precisely control such correlations at will has boosted the research in quantum technologies, having the goal of developing quantum computers to perform computational tasks orders of magnitude more efficiently than their classical analogues.

Having the fundamental and technological importance of the quantum entanglement in mind, one should also be able to mathematically quantify it. Below we will list so-called *postulates for axiomatic entanglement measures* [212, 221, 219]. Any measure of entanglement $M(\rho)$ can be regarded as a good measure, if it satisfies the following conditions

1. A bipartite measure $M(\rho)$ maps the density matrix onto positive real numbers: $M(\rho) \in R^+$.

2. If a state ρ is separable, i.e. not entangled, then $M(\rho) = 0$.

3. The system is in a pure state $\rho = |\psi\rangle\langle\psi|$, the M is equivalent to the entanglement entropy $E\left(|\psi\rangle\langle\psi|\right) = \left(S \circ \mathrm{Tr}_B\right)\left(|\psi\rangle\langle\psi|\right)$

Additionally to this, E is said to be an *entanglement monotone* if

$$E(\rho) \geq \sum_\alpha p_\alpha E\left(\frac{M_\alpha \rho M_\alpha^\dagger}{\mathrm{Tr}\left[M_\alpha \rho M_\alpha^\dagger\right]}\right), \quad p_\alpha = \mathrm{Tr}\left[M_\alpha \rho M_\alpha^\dagger\right]$$

where M_α is the Kraus operators of the so called *Local Operations and Classical Communication*.

Using these definitions, below we will present few of well known entanglement measures and discuss their properties in the context of CFT.

8.1 Entanglement Entropy and Mutual Information

One of many witnesses of quantum entanglement is the so called Entanglement entropy. Entanglement entropy is a valid witness of bipartite entanglement only when the whole system is in the pure state. For time being, one can completely forget about the environment and discuss the entanglement entropy in the context of an isolated system.

Suppose that an isolated system is in some pure quantum state $\rho = |\psi\rangle\langle\psi|$. If one further partitions the system into A and B subsystems, then the information about a bipartite entanglement is fully included in the spectrum of the reduced density matrix

$$\rho_A = \mathrm{Tr}_B\left(\rho\right). \tag{8.1.1}$$

By studying the scaling properties of the the Rényi entropies

$$S_A^{(n)} = \frac{1}{1-n} \ln \left(\mathrm{Tr}_A \left(\rho_A^n \right) \right) \tag{8.1.2}$$

one can recover the properties entanglement spectrum. The index n is the so-called Rényi index and for $n \to 1$ one obtains the von Neumann entropy

$$S_A = \lim_{n \to 1} S_A^{(n)} = -\mathrm{Tr}_A \left(\rho_A \ln \rho_A \right). \tag{8.1.3}$$

(A)

(B)
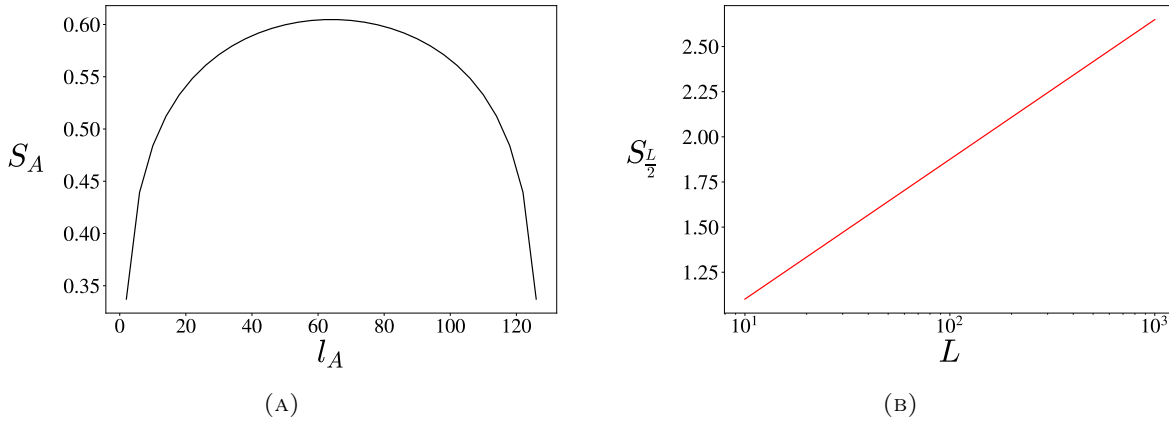
FIGURE 8.1: A) The scaling of von Neumann entropy for QIM Eq.(1.19) at criticality with periodic boundary conditions and $L = 128$ lattice sites. The scaling is with respect to the bipartition size l_A. By fitting the data to Eq.(8.1.5), the extracted central charge is $c \approx 0.527$, in agreement with an exact result $c = \frac{1}{2}$. B) The scaling of von Neumann entropy for XX model (i.e. Eq.(2.7) with $\Delta = 0$) with periodic boundary conditions. Here we instead fix the ratio $l_A = L/2$ and analyze the scaling of entanglement entropy at half-partitioning, i.e. $S_{L/2}$. Again, by fitting the data to Eq.(8.1.5), the extracted central charge is $c \approx 1.008$, in a perfect agreement with an exact result $c = 1$.

For special cases, the Rényi entropies can accommodate universal features: suppose we are dealing with a 1+1 dimensional CFT theory at zero temperature. Using the replica trick, one can show that the nth bipartite Rényi entropy will scale as

$$S_A^{(n)} = \frac{c}{6} \frac{n+1}{n} \log \left(\frac{l_A}{a} \right) + \mathrm{const.}, \tag{8.1.4}$$

where l_A is the linear size of the bipartition A, a is some microscopic length scale of the model, while c is the central charge of the underlying CFT [99]. Eq.(8.1.4) can be further generalized for the systems with periodic boundary conditions. For $n = 1$ case, the entanglement entropy for the systems periodic boundary conditions scales as

$$S_A = \frac{c}{3} \log \left(\frac{L}{\pi a} \sin \left(\frac{\pi l_A}{L} \right) \right) + \mathrm{const.}, \tag{8.1.5}$$

where L is the linear size of whole system. Eq.(8.1.4,8.1.5) are frequently used as a method to check whether the state of the system has some underlying CFT characteristics and to extract corresponding central charge of the theory.

Another quantifier of quantum correlations, closely related to the entanglement entropy, is the so-called mutual information. Similarly to the entanglement entropy, the bipartite mutual information

$\mathcal{I}_{A,B}$ is a measure of correlations between two sub-systems A and B. It is defined as

$$\mathcal{I}_{A,B} = \mathcal{S}_A + \mathcal{S}_B - \mathcal{S}_{A\cup B}. \tag{8.1.6}$$

In some cases mutual information turns out to be more useful measure of correlations relative to the entanglement entropy, since it is less prone to finite size effects.

Mutual information hosts few important features that is useful to characterize the system in and out of criticality. Suppose that a system of size L with periodic boundary conditions is tri-partitioned into A, B and C (to be integrated out). The linear sizes of A and B are chosen to be $l_A = l_B = L/8$ and with $r_{AB} = L/2$ distance between the centers of them. If the system out of the critical point, then the long-range correlations are absent and thus the mutual information scales as

$$\mathcal{I}_{A,B}(L) \sim e^{-L/\xi}, \tag{8.1.7}$$

where ξ is the correlation length of the system. As one approaches the critical point, the diverging correlation length enhances the correlations between disconnected segments A and B and thus $\mathcal{I}_{A,B}$ is enhanced.

Just like the entanglement entropy, at conformally invariant critical point the mutual information shows universal scaling properties [140]. In conformal field theory, it is known that any 4-point correlation function of primary or quasi-primary fields [27] depend on a single number η, referred to as the cross-ratio. From the point of view of the mutual information, these operators are known to be the boundary condition changing operators [99, 222] and the 4 points under question are the left and right boundary coordinates of A (labeled as x_1 and x_2) and B (labeled as x_3 and x_4). The cross ratio for these coordinates are

$$\eta = \frac{x_{12}x_{34}}{x_{13}x_{24}}, \quad \text{with} \quad x_{ij} = \frac{L}{\pi}\sin\left(\frac{\pi}{L}|x_i - x_j|\right). \tag{8.1.8}$$

As already mentioned, at the critical point, the bipartite mutual information only depends on η and for small enough $\eta \ll 1$ we have

$$\mathcal{I}_\eta \sim \eta^\Delta, \tag{8.1.9}$$

were Δ is some scaling exponent. To understand the origin of Δ, we analyze $l_A = l_B = 1$ case with $1 \ll r_{AB} \ll L$. In this case $\eta \sim r_{AB}^{-2}$ and therefore

$$\mathcal{I}_\eta \sim r_{AB}^{-2\Delta}. \tag{8.1.10}$$

Since the $l_{A(B)} = 1$, it means that the boundaries of A (B) are very close to each other. This allows us to use the operator product expansion introduced in Sec.(1.5) and transform the 4-point correlation function into the sum of 2-point correlation functions between operators that are present in the OPE. The dominant term, with the lowest scaling dimension Δ, is the one which appears as the leading contribution in Eq.(8.1.10).

8.2 Logarithmic Negativity

As we have already mentioned, entanglement entropy is not a valid witness of entanglement for mixed states. To properly characterize the entanglement content of the systems in mixed states, one switches to the so-called entanglement negativity [223, 224, 225, 226]. To separate classical and quantum correlations from eachother, a possible way is to implement the partial transpose of the density matrix ρ^{T_A}, where partial transposition is defined as

$$\langle nm|\rho^{T_A}|n'm'\rangle = \langle nm'|\rho_A|n'm\rangle. \tag{8.2.1}$$

Here $\{n\}$ and $\{m\}$ are the the the basis states of A and B parts of the whole system. Using the partial transpose of the density matrix, one defines the so-called logarithmic negativity as

$$\mathcal{E} = \log\left(\sqrt{\rho^{T_A}(\rho^{T_A})^\dagger}\right). \tag{8.2.2}$$

As for the the Rényi entropies, the possible scaling properties of the logarithmic negativity is strongly narrowed down by the symmetries when one considers conformal field theories. As an example, for two disjoint intervals A and B embedded in a infinite system with open boundary conditions (see Fig.(8.2)), the scaling of the logarithmic negativity depends

A   **B**

FIGURE 8.2

$$\mathcal{E} = \frac{c}{2}\ln(l_A) + \text{const.} \tag{8.2.3}$$

with c being the central charge of the theory. If one instead considers two joint intervals A and B that share a boundary, then the negativity scales as

$$\mathcal{E} = \frac{c}{4}\ln\left(\frac{l_A l_B}{l_A + l_B}\right) + \text{const.} \tag{8.2.4}$$

As a rule of thumb, to extract the scaling equations for the system of finite size L, one had to substitute $l_{A(B)}$ by the corresponding chord length $l_{A(B)} \to \frac{L}{\pi}\sin\left(\frac{\pi l_{A(B)}}{L}\right)$. One should keep in mind that the above definition of logarithmic negativity is only valid for bosonic systems, i.e. for the particles obeying a commutation relations. For fermions, one should track the sign change when the bra and ket states are swapped during the partial transpose. In Sec.(11.2.2) we will generalize the definition appropriately for fermionic case, using the so-called partial time-reversal transpose.

8.3   Monogamy of Entanglement

In previous sections we have reviewed two entanglement measures and discussed some of they useful scaling properties in the context of conformal field theories. The important point is that both entanglement entropy and logarithmic negativity are measures of bipartite entanglement. It is natural to pose the question regarding how the entanglement can be shared over multiple constituents of the system. Below we address this question and review the so-called entanglement monogamy.

One of many fundamental differences between classical correlations and quantum entanglement, is that the latter can not be arbitrarily shared among various parts of the system. This constraint is known as the entanglement monogamy [204, 227, 228, 229, 230, 231, 232]. The most simple setup to demonstrate the monogamy of entanglement is a tripartite system $A \cup B \cup C$, each consisting of a qubit with states labeled $\{|0\rangle, |1\rangle\}_{A,B,C}$. We start by defining another measure of entanglement, the so-called concurrence. Suppose that the pair of qubits A and B is described by a density matrix ρ_{AB}. One may define a spin-flipped density matrix $\tilde{\rho}_{AB}$ as

$$\tilde{\rho}_{AB} = \left(\sigma_A^y \times \sigma_B^y\right)\rho_{AB}^*\left(\sigma_A^y \times \sigma_B^y\right), \tag{8.3.1}$$

where ρ_{AB}^* is the complex conjugate of ρ_{AB}. Since both ρ_{AB} and $\tilde{\rho}_{AB}$ have only positive eigenvalues, so does $\rho_{AB}\tilde{\rho}_{AB}$. Suppose these eigenvalues are $\mu_{1,2,3,4}$, with $\mu_1 \geq \mu_2 \geq \mu_3 \geq \mu_4$. Using these

eigenvalues, the concurrence $\mathcal{C}_{AB}$ of the state ρ_{AB} is defined as

$$\mathcal{C}_{AB} = \max\left(\sqrt{\mu_1} - \sqrt{\mu_2} - \sqrt{\mu_3} - \sqrt{\mu_4}, 0\right). \qquad (8.3.2)$$

Suppose $A \cup B$ system is in a pure state and disentangled, say

$$|\psi\rangle_{AB} = |0\rangle_A \otimes |1\rangle_B \quad \rightarrow \quad \rho_{AB} = \begin{pmatrix} 0 & 0 & 0 & 0 \\ 0 & 0 & 0 & 0 \\ 0 & 0 & 1 & 0 \\ 0 & 0 & 0 & 0 \end{pmatrix}, \qquad (8.3.3)$$

then the spin flipped state is

$$\tilde{\rho}_{AB} = \begin{pmatrix} 0 & 0 & 0 & 0 \\ 0 & 1 & 0 & 0 \\ 0 & 0 & 0 & 0 \\ 0 & 0 & 0 & 0 \end{pmatrix} \qquad (8.3.4)$$

and thus the concurrence of such state is zero, since all of the elements of $\rho_{AB}\tilde{\rho}_{AB}$ is zero. Now suppose that the system is in a pure but maximally entangled state

$$|\psi\rangle_{AB} = \frac{1}{\sqrt{2}}\left(|0\rangle_A \otimes |0\rangle_B + |1\rangle_A \otimes |1\rangle_B\right) \quad \rightarrow \quad \tilde{\rho}_{AB} = \frac{1}{2}\begin{pmatrix} 1 & 0 & 0 & 1 \\ 0 & 0 & 0 & 0 \\ 0 & 0 & 0 & 0 \\ 1 & 0 & 0 & 1 \end{pmatrix}. \qquad (8.3.5)$$

This way, the eigenvalues of $\rho_{AB}\tilde{\rho}_{AB}$ are $\{1, 0, 0, 0\}$ and thus $\mathcal{C}_{AB} = 1$. One can formulate these cases in a more general way: if the system is in some pure state, then the concurrence of the state is $\mathcal{C}_{AB} = 2\sqrt{\det(\rho_A)}$, where ρ_A is the reduced density matrix over system A.

Going back to the original setup of tripartite system $A \cup B \cup C$, one may ask what are the relations between C_{AB} and C_{AC} when the whole system is in a pure state. Such a state, where two qubits are entangled with a third one is described by a density matrix ρ that has at most two non-zero eigenvalues. Due to this, $\rho_{AB}\tilde{\rho}_{AB}$ also shares the same property, with $\rho_{AB} = \text{Tr}_C(\rho_{ABC})$. These constraints allows as to write C_{AB} concurrence as

$$\begin{aligned} C_{AB}^2 &= (\sqrt{\mu_1} - \sqrt{\mu_2})^2 = \mu_1 + \mu_2 - 2\sqrt{\mu_1\mu_2} \\ &= \text{Tr}\left(\rho_{AB}\tilde{\rho}_{AB}\right) - 2\sqrt{\mu_1\mu_2} \leq \text{Tr}\left(\rho_{AB}\tilde{\rho}_{AB}\right). \end{aligned} \qquad (8.3.6)$$

Once can identically deriving C_{AC}^2 and C_{BC}^2, we get

$$C_{AB}^2 + C_{AC}^2 \leq \text{Tr}\left(\rho_{AC}\tilde{\rho}_{AC}\right) + \text{Tr}\left(\rho_{BC}\tilde{\rho}_{BC}\right). \qquad (8.3.7)$$

If the system is in some pure state $|\psi\rangle_{ABC} = \sum a_{\psi_A, \psi_B, \psi_C}|\psi_A, \psi_B, \psi_C\rangle$, we get that

$$\text{Tr}\left(\rho_{AB}\tilde{\rho}_{AB}\right) = 2\det(\rho_A) - \text{Tr}\left(\rho_B^2\right) + \text{Tr}\left(\rho_C^2\right) \qquad (8.3.8)$$

Since $\rho_{A/B/C}$ are the reduced 2×2 density matrices over qubit A,B and C with $\text{Tr}\left(\rho_{A/B/C}\right) = 1$ one, we have $\text{Tr}\left(\rho_{B/C}^2\right) = -2\det\left(\rho_{B/C}\right) - 1$ and thus

$$\begin{aligned} \text{Tr}\left(\rho_{AB}\tilde{\rho}_{AB}\right) &= 2\left(\det(\rho_A) + \det(\rho_B) - \det(\rho_C)\right), \\ \text{Tr}\left(\rho_{AC}\tilde{\rho}_{AC}\right) &= 2\left(\det(\rho_A) + \det(\rho_C) - \det(\rho_B)\right), \\ \text{Tr}\left(\rho_{BC}\tilde{\rho}_{BC}\right) &= 2\left(\det(\rho_B) + \det(\rho_C) - \det(\rho_A)\right). \end{aligned} \qquad (8.3.9)$$

Using these identities, we get

$$C_{AB}^2 + C_{AC}^2 \leq 4\det(\rho_A). \tag{8.3.10}$$

Let us think of combination of BC as a single composite object, then we can discuss the concurrence between qubit A and (BC) composite object. This is a valid interpretation, since only 2-dimensional subspace of full 4-dimensional $\{|\psi_B, \psi_C\rangle\}$-space of state is needed to express $|\psi\rangle_{ABC} = \sum a_{\psi_A, \psi_B, \psi_C}|\psi_A, \psi_B, \psi_C\rangle$ state of the system. Due to this, one can view $A \cup (BC)$ as a pair of 2-dimensional qubits in a pure state. Since for such a state $C_{A,(BC)} = 2\sqrt{\det(\rho_A)}$, we get

$$C_{AB}^2 + C_{AC}^2 \leq C_{A(BC)}^2. \tag{8.3.11}$$

For a 3 qubit case, Eq.(8.3.11) inequality sets the limit regarding how the entanglement can be shared among constituents of a tripartite system. Suppose that qubit A is entangled with the pair of qubits BC, measured by concurrence $C_{A(BC)}$. As a result of the inequality Eq.(8.3.11), $C_{A(BC)}$ limits the entanglement that can be shared individually between A and B and A and C, while the part of entanglement belonging to B can not be shared with C.

The monogamy of entanglement can have non-trivial consequences in many-body systems. As it will be demonstrated in Chap.(11), entanglement monogamy can lead to counterintuitive effects, such as enhancement of entanglement in the system that is projectively measured.

Chapter 9

Measurement induced phase transitions

As we have seen in previous chapters, the dynamics of an open quantum system can be notoriously complex. Nevertheless, there have been advances in studying the dynamics and properties of the system under persistent interaction with the environment. For example, by using the Lindblad master equation, one may study the dissipative phase transitions in many-body systems with one, or many particle loss processes. Apart from numerical simulations, it is possible to extract various analytical solutions [207, 233, 234, 235]. On the other hand, it can be extremely insightful to study the properties of the system along individual quantum trajectories, or even the trajectory averaged observables. Typically, trajectory averaged observables linear in the density matrix carry insignificant physical information. Instead, one can study observables that are non-linear in the density matrix. A good candidates for such observables are various measures of quantum entanglement, introduced in Sec.(8.1).

Since one can interpret the decoherence by interaction with environment as decoherence by measurement, the dynamics of the system that is coupled to the bath can be thought as a sequence of unitary evolution and corresponding type of measurements. In terms of quantum entanglement, the evolution of the system consists of two competing operators. In a typical setups, the unitary evolution tends to increase the entanglement content of the system. On the other hand, the measurement part of the evolution collapses the state of the system and thus reduces the entanglement. By controlling the coupling between the system and the environment, one can effectively drive the system from weakly to strongly entangled states.

By implementing the quantum trajectory approach and tracking the trajectory averaged measures of entanglement of the system, one can capture the so called *measurement induced phase transitions* MIPT for various coupling constants. Conceptually, this class of phase transitions is different from the ones described by Landau's theory of phase transitions (i.e. the transitions discussed in Part I of the thesis). In the previous cases, the passage through a critical point was accompanied by a breakdown or recovery of some symmetry of the system. In our case, the symmetry breaking part of the transition is absent, while the ensemble averaged measures of entanglement behaves differently on either side of the transition points. A common feature between these two classes of phase transitions is the scaling of the measures of entanglement at the critical point. In both cases, the underlying conformal field theory constraints, for example, the entanglement entropy to necessarily scale logarithmically with the subsystem size and follow Eq.(8.1.5).

9.1 Random Unitary Circuit

An interesting setup that can host a measurement induced phase transition is the so-called Random Unitary Circuit (RUC) model [145]. The temporal dynamics of RUC models is a sequence of unitary evolution and projective measurements. However, the unitary, or hamiltonian part of the evolution is featureless and consists of random Haar gates.

Let us consider a 1D array of qudits. As we have already mentioned, the temporal evolution is split into a sequence of unitary evolution and measurements. The unitary part of the evolution
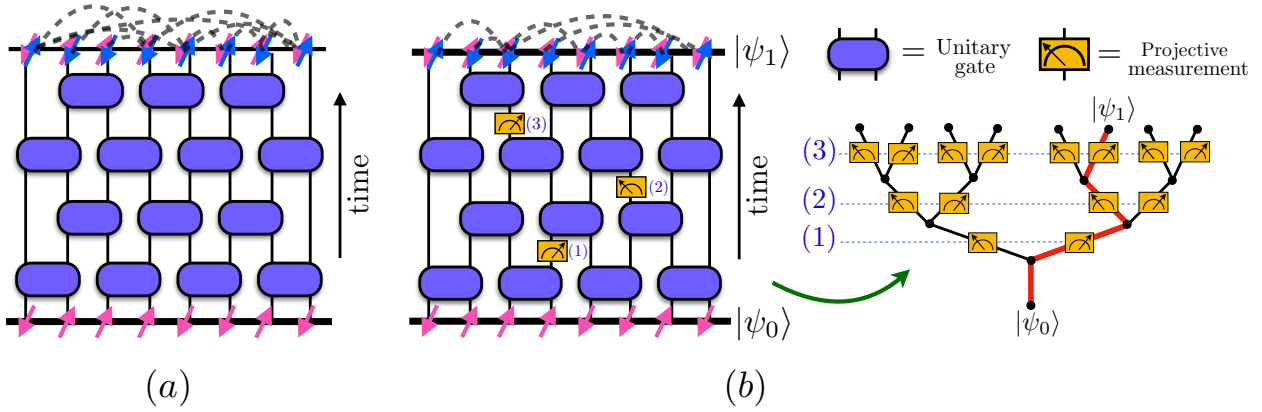
FIGURE 9.1: Pictorial representation of a random unitary circuit. Figures (a) and (b) corresponds to the evolution in time without and with projective measurements. The system is initiated in a random product state $|\psi_0\rangle$. After some time of evolution, the unitary part of the evolution entangled the qubits and the initial pure state evolves to final $|\psi_1\rangle$ entangled state. The right-hand-side of figure (b) pictorially presents the branching of quantum trajectories, based on the measurement outcome. The red line corresponds to one of the possible trajectories that the system can follow. Figure extracted from [236].

is taken to be a brick-wall configuration of Haar-random unitary gates, acting on nearest neighbor two qudits, see Fig.(9.1). The selection of unitary gates from the set of Haar-random gates is chosen to be completely decorrelated in spatial and temporal directions. The subsequent step is to insert random projective measurements after every layer of unitary evolution. The measurement happens with a probability p and the occurrence of such projectors is completely random in space and in time. In such a way, the absence of correlations between random unitaries and the projective measruements renders the overall dynamics of the system to be Markovian.

It is useful to formulate the problem using the quantum channel and quantum trajectory approach, presented in Sec.(7.4). Suppose we label the states within an on-site Hilbert state as $\mathcal{H}_d = \{|1\rangle, |2\rangle, ..., |d\rangle\}$. The on-site projective measurement with respect to $\mathcal{H}_d$ can be described by the quantum channel with the set of Kraus operators

$$M = \{K_j\} = \{|j\rangle\langle j|\}, \quad \omega_j = 1, \quad j = 1, ..., d, \tag{9.1.1}$$

where ω_j is the corresponding weight of K_j Kraus operator. In the RUC scenario, there is a probability p that one of $\{K_j\}$ will act on a local Hilbert space and probability $1 - p$ that the measurement will not occur, i.e. $\mathbb{I}$ identity will act on the state. This way, one may extend the set of Kraus operators to include the measurement and no-measurement channels together:

$$M \to M_p = \{\mathbb{I}, K_j\}, \quad \omega_{\mathbb{I}} = 1 - p, \quad \omega_{K_j} = p \quad \forall j. \tag{9.1.2}$$

Another related set of generalized measurement Kraus operators is

$$M'_p = \{\mathbb{I}\} \cup \{\sqrt{d}K_U | U \in U(d)\}, \quad K_U = U^\dagger K_1 U. \tag{9.1.3}$$

The infinite subset consisting by $\sqrt{d}K_U$ operators is parametrized by a single unitary matrix $U(d)$ and the corresponding weights are given by the Haar measure $w(\sqrt{d}K_U) = pdU$, where dU is the Haar measure on $U(d)$, normalized as $\int_{U \in U(d)} dU = \mathbb{I}$. All three sets of Kraus operators M, M_p and M'_p are normalized to $\mathbb{I}$.

Before choosing any specific set of measurements, i.e. Kraus operators, we rephrase our problem in terms of quantum trajectories. As explained in Sec.(7.4), a quantum trajectory consists of a specific realization of the sequence of measurement operators and unitary gates. Each trajectory

can be labeled by a corresponding circuit realization operator C, as defined in Eq.(7.4.10). Suppose we initialize the system in a pure state $|\psi\rangle\langle\psi|$, then the statistical average of some observable $\mathcal{O}$ can thus be defined as

$$\overline{\mathcal{O}} = \langle\mathcal{O}\rangle = \mathbb{E}_C \text{Tr}\left(C|\psi\rangle\langle\psi|C^\dagger\right) \cdot \frac{\langle\psi|C^\dagger\mathcal{O}C|\psi\rangle}{\langle\psi|C^\dagger C|\psi\rangle} = \mathbb{E}_C \text{Tr}\left(\langle\psi|C^\dagger\mathcal{O}C|\psi\rangle\right) \tag{9.1.4}$$

where the first factor is the probability $\mathcal{P}(C)$ of realization of a trajectory described by an operator C, while the second factor is the expectation value of observable $\mathcal{O}$ at the end of the trajectory. $\mathbb{E}_C$ denotes the average over all trajectories, that is average over all Haar-random gates and measurement operators. As before, the observable of our interest are the nth Rényi entropies for a bipartite system with a reduces density matrix ρ_A. Instead of directly using Eq.(8.1.2), one can reformulate it in a more convenient manner

$$S_A^{(n)}(\rho) = \frac{1}{1-n}\ln\left[\text{Tr}\left(\rho^{\otimes n}P_{n,A}\right)\right], \tag{9.1.5}$$

where $P_{n,A}$ is a permutation operator in the replica space n and satisfies the following constraint

$$P_{n,A} = \prod_j \tau_{g_j}, \quad g_j = \begin{cases} (123...n) & \text{if } j \in A \\ e & \text{if } j \notin A \end{cases} \tag{9.1.6}$$

while τ_{g_j} is the representation of g_j on the replicated Hilbert space

$$\tau_{g_x} = \sum_{[i]} |i_{g_x(1)}...i_{g_x(n)}\rangle\langle i_1...i_n|. \tag{9.1.7}$$

This way, the average bipartite n^{th} Rényi entropy will be

$$\overline{S}_A^{(n)}(\rho) = \mathbb{E}_C \text{Tr}\left(C|\psi\rangle\langle\psi|C^\dagger\right) \times S_A^{(n)}\left(\frac{C|\psi\rangle}{\sqrt{\langle\psi|C^\dagger C|\psi\rangle}}\right) =$$

$$= \frac{1}{1-n}\mathbb{E}_C \text{Tr}\left(C|\psi\rangle\langle\psi|C^\dagger\right) \times \ln\left(\frac{\text{Tr}\left(\langle\psi|C^\dagger C|\psi\rangle^{\otimes n}P_{n,A}\right)}{\text{Tr}\left(\langle\psi|C^\dagger C|\psi\rangle^{\otimes n}\right)}\right) = \tag{9.1.8}$$

$$= \lim_{m\to 0}\frac{1}{m(1-n)}\mathbb{E}_C \text{Tr}\left((C|\psi\rangle\langle\psi|C^\dagger)^{\otimes nm+1}(P_{n,A}^{\otimes m}-1)\right).$$

By introducing a notation $Q = nm+1$, then

$$\overline{S}_A^{(n)}(\rho) = \frac{1}{1-n}\lim_{m\to 0}\frac{\mathcal{Z}_A - \mathcal{Z}_0}{m} \tag{9.1.9}$$

with

$$\mathcal{Z}_A = \mathbb{E}_C \text{Tr}\left((C|\psi\rangle\langle\psi|C^\dagger)^{\otimes nm+1}P_{n,A}^{\otimes m}\right), \quad \mathcal{Z}_0 = \mathbb{E}_C \text{Tr}\left((C|\psi\rangle\langle\psi|C^\dagger)^{\otimes nm+1}\right). \tag{9.1.10}$$

Since $\mathcal{Z}_{A,0} \to 1$ in the $m \to 0$ replica limit, we re-write the whole expression as

$$\overline{S}_A^{(n)}(\rho) = \frac{1}{n-1}\lim_{m\to 0}\frac{F_A - F_0}{m} = \frac{1}{1-n}\lim_{m\to 0}\frac{\ln\left(\mathcal{Z}_A/\mathcal{Z}_0\right)}{m}, \tag{9.1.11}$$

where F_A is the free-energy cost of the domain wall corresponding to various the boundary conditions in the entanglement region stemming from $P_{n,A}$ permutation operator.
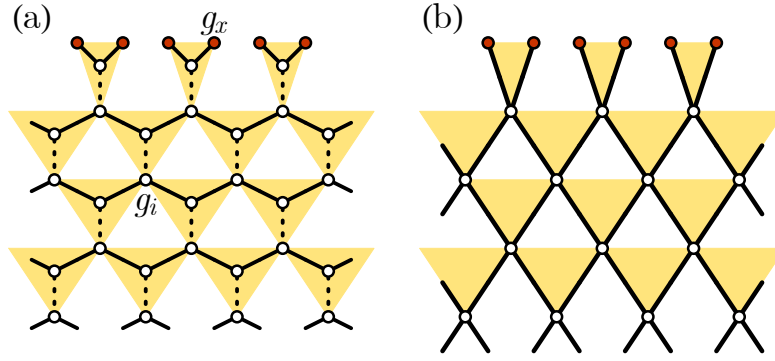
FIGURE 9.2: (a) The geometry of a statistical mechanics model of interacting permutation group S_Q elements. The dotted lines $\mathcal{E}_d$ correspond to the Weingarten functions (stemming from the averaged Haar unitary gates), while the solid lines $\mathcal{E}_s$ originate from the generalized measurements. (b) $d = 0$ limit, corresponding to $Q!$ color Potts on a square lattice. Red circles in both figures correspond to the pinned boundary degrees of freedom. Figure extracted from [145].

Using the well studied methods of taking the ensemble averages over Haar measures [237, 238], one can exactly calculate the circuit averages $\mathbb{E}_C$. Since the measurement and unitary evolution parts are decoupled, one can split the ensemble average of trajectories into the averages over independent measurements and unitary evolutions. Below we will simply state the know results for arbitrary value of $Q = nm + 1$ case. For the two-site unitary gate $U_{i,i+1}$ acting on sites i and $i + 1$, the average of the tensor product $U_{i,i+1}^{\otimes Q}$ and $(U^\dagger)_{i,i+1}^{\otimes Q}$ is [237, 239]

$$\mathbb{E}_{U_{i,i+1}} U_{i,i+1}^{\otimes Q} \otimes (U^\dagger)_{i,i+1}^{\otimes Q} = \sum_{(g_1,g_2)\in S_Q} \text{Wg}_{d^2}(g_1^{-1}g_2)\tau_{g_1,i}^\dagger \tau_{g_1,i+1}^\dagger \tau_{g_2,i}\tau_{g_2,i+1} {}^1 \tag{9.1.12}$$

where $\text{Wg}_{d^2}(g_1^{-1}g_2)$ are the so-called Weingarten function of the permutation $g_1^{-1}g_2$ [237]. Similarly, each generalized measurement will yield a factor $\mathbb{E}_{K\in\mathcal{M}}W(g_1, g_2)$, however it depends on which set of Kraus operators K are used. For $\mathcal{M} = M_p$ and $\mathcal{M} = M_p'$, we get

$$\mathbb{E}_{K\in M_p}W(g_1, g_2) = (1-p)d^{|g_1^{-1}g_2|} + pd$$
$$\mathbb{E}_{K\in M_p'}W(g_1, g_2) = (1-p)d^{|g_1^{-1}g_2|} + pd^Q \equiv W_p(g_1^{-1}g_2) \tag{9.1.13}$$

and thus these two results match if one takes $Q \to 1$ limit first, if one considers $d \to \infty$ limit at the end of the calculations. Using these constructions, one maps the problem of the calculation of $\overline{S}_A^{(n)}(\rho)$ onto a problem of a statistical mechanics of interacting permutation group elements $g_i \in S_Q$ on an anisotropic honeycomb lattice (see Fig.(9.2a))

$$\mathcal{Z}_A = \sum_{\{g_i\}\in S_Q} \prod_{\langle ij\rangle\in\mathcal{E}_s} W_p(g_i^{-1}g_j) \prod_{\langle ij\rangle\in\mathcal{E}_d} \text{Wg}_{d^2}(g_i^{-1}g_j) \tag{9.1.14}$$

In $d = \infty$ case, the model reduces to a $Q!$ color Potts model on a square lattice (see Fig.(9.2b)), where the weight $\omega = e^{-E_{ik}}$ of a local $\langle ik\rangle$ bond is governed by the energy function E_{ik}

$$E_{ik} = -\ln\left(p + (1-p)\delta_{g_i^{-1}g_k}\right), \tag{9.1.15}$$

---

[1]In the literature, authors usually pass to the superoperator formalism [240]: $\tau_g \to |\tau_g\rangle\rangle$ and thus $\tau_{g_1,i}^\dagger \tau_{g_1,i+1}^\dagger \tau_{g_2,i}\tau_{g_2,i+1} \to |\tau_{g_2}\rangle\rangle_i|\tau_{g_2}\rangle\rangle_{i+1}\langle\langle\tau_{g_1}|_i\langle\langle\tau_{g_1}|_{i+1}$.

where $\delta_{g_i^{-1}g_k} = 1$ only if $g_i^{-1}g_k$ is an identity operation. This way, the partition function $\mathcal{Z}_a$ can undergo a phase transition from ordered $(p < p_c)$ to a disordered $(p > p_c)$ regime and will host a critical point $(p = p_c)$ with an underlying conformal field theory description. The critical point resides at $p_c = \frac{1}{2}$. Moreover, for $d \to \infty$ limit, E_{ik} acquires $1/d$ corrections as

$$E_{ik} = -\ln\left(p + (1-p)\left(\delta_{g_i^{-1}g_k} + \frac{1}{d}\delta'_{g_i^{-1}g_k}\right)\right), \tag{9.1.16}$$

where $\delta'_{g_i^{-1}g_k} = 1$ only if $g_i^{-1}g_k$ is a transposition. The inclusion of $1/d$ corrections breaks the $S_{Q!}$ symmetry group of the model down to $S_Q \times S_Q$.

This way, we have mapped the calculation of the entanglement content of RUC model onto a model statistical physics model. From Eq.(9.1.16), we can simply analyse two extreme cases. For $p = 0$ case we have $E_{ik} = -\ln\left(\delta_{g_i^{-1}g_k} + \frac{1}{d}\delta'_{g_i^{-1}g_k}\right)$, which favours the alignment of the group elements g_i and g_k. This renders the state to be ferromagnetically ordered. In this regimes, the free-energy cost $F_A - F_0$ of pinning the spins in l_A region at the boundary scales as $\sim l_A$. This in turn translates to the volume-law phase $\overline{S}_A^{(n)} \sim l_A$, for sufficiently long evolution time $t \to \infty$. This picture remains valid even for $p \ll 1$ small measurement probability. On the other extreme, when $p = 1$ then we have $E_{ik} = 0$. This corresponds to the infinite temperature regime, where the thermal fluctuations completely destroy any possible order in the system. In this case, $F_A - F_0$ scales as the size of the boundary of l_A, thus $F_A - F_0 \sim$ const.. In terms of entanglement entropy, this means that for $p \to 1$ we have an area-law phase $\overline{S}_A^{(n)} \sim$ const..

The critical point p_c that separates the area- and volume-law phases of the entanglement corresponds to order to disorder transition in the corresponding statistical-mechanics model. By assuming that the transition is of second order, then it should be described by a 2D conformal field theory (CFT) with $c = 0$ central charge in $Q \to 1$ limit. Such CFTs with central charge $c = 0$ are known to be non-unitary, a feature shared between statistical mechanics model and the original RUC model. Despite such theories being hard to investigate, it has been shown that $d = \infty$ limit corresponds to the percolation model [145]. In this case, for the $Q \to 1$ replica limit, one can show that that the transition occurs for $p_c = 1/2$ and as one approaches the critical point, correlation length diverges as $\xi \sim |p - p_c|^{-4/3}$.

The problem becomes increasingly complex as one reduces the size of the local Hilbert space. The problem stems from the non-trivial expression for Weingarten function Wg_{d^2}. Thus, if one wants to study the entanglement content of projectively measured RUC model for small local hilbert space dimension, it becomes more convenient to rely on numerical approach. In the following subsection, we present the Monte-Carlo simulations of the statistical mechanics model, corresponding to the RUC model with $d = 10$ dimensional local hilbert space.

9.1.1 Monte Carlo simulation

To corroborate some of the theoretical predictions presented in [145], we perform Monte Carlo simulations. In Eq.(10.3.8) the number of replicas can be expressed as $Q = nm + 1$, with $m \to 0$ an integer; we notice that in practice we cannot actually use the limit $m = 0$ because otherwise the numerics would be trivial. Similarly, we cannot use $n = 1$ because we would not be calculating an entanglement entropy (or in other words the boundary conditions would be trivial). Therefore the lowest number of replicas we can consider is $Q = 3$ ($n = 2$ and $m = 1$), corresponding to a Potts model with six states.

We perform Monte Carlo simulations on a lattice of size $L_x = 40$ and $L_y = 50$ sites (corresponding to a time evolution of L_y time periods), with periodic boundary conditions in the x direction,
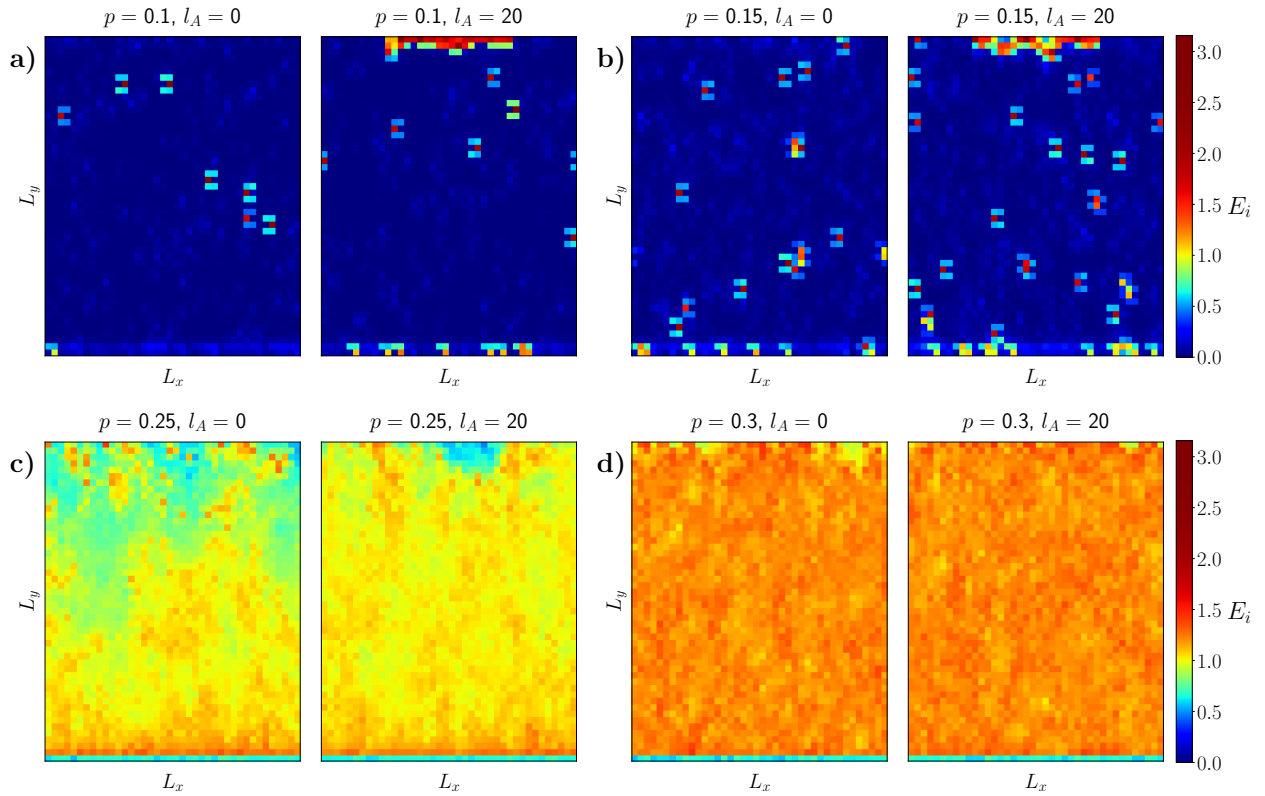
FIGURE 9.3: Colormap of the energy E_i of each spin, calculated including the next neighbors contribution and the boundary contribution for the spins at the top of the chain. The size of the Monte Carlo system is $L_x = 40$ and $L_y = 50$. Each panel shows $l_A = 0$ or $l_A = 20$ for (a) $p = 0.1$, (b) $p = 0.15$, (c) $p = 0.25$, (d) $p = 0.3$. Lower energy corresponds to aligned spins, i.e. ferromagnetic regions, while larger energy corresponds to paramagnetic spins. The labels L_y in the vertical direction correspond to the time direction in the physical system. a-b) The system is completely ferromagnetic and the energy cost of having a boundary is clearly visible at the top of the right plot, but small paramagnetic droplets are forming. c) The system is switching to a paramagnetic phase and the higher energy cost of the boundary is barely visible. d) The system is entirely paramagnetic and the energy cost of the boundary vanishes. Note that the bottom boundary has lower energy because it has less next neighbors than the spins in the bulk.

and boundary conditions at the top in the vertical direction dictated by the value of the partition size l_A.

In this model the identity permutation is $(0)(1)(2)$, while the transposition dictated by the boundary conditions is $(01)(2)$ because ($n = 2$ and $m = 1$). We can naturally map the permutations onto spin states: $\{(0)(1)(2), (0)(12), (01)(2), (021), (012), (02)(1)\} \rightarrow s = \{0, 1, 2, 3, 4, 5\}$. Therefore the boundary conditions of a partition of size l_A are given by l_A sites occupied by the spin $s = 2$ and $L_x - l_A$ sites with the spin $s = 0$. We choose the partition to be centered in the middle of the boundary.

We employ the Wolff cluster algorithm [241, 242] for the update of the lattice configuration. The probability of adding a site to the cluster built by the Wolff algorithm is the usual one, and based on the interaction energy with the neighbors. Whenever a site on the top vertical boundary is added to the cluster, we add its interaction energy with the fixed boundary to the boundary energy E_b. When the cluster is built, we update it with probability $\min(1, e^{-E_b})$, in order to take into account the fact that configurations that have a high interaction energy with the cluster are less probable.

We first thermalize the lattice by updating it with $N_{\text{therm}} = 25000$ Wolff steps. To avoid autocorrelations, we then sample the configuration of the lattice every $N_{\text{sample}} = 50$ steps and
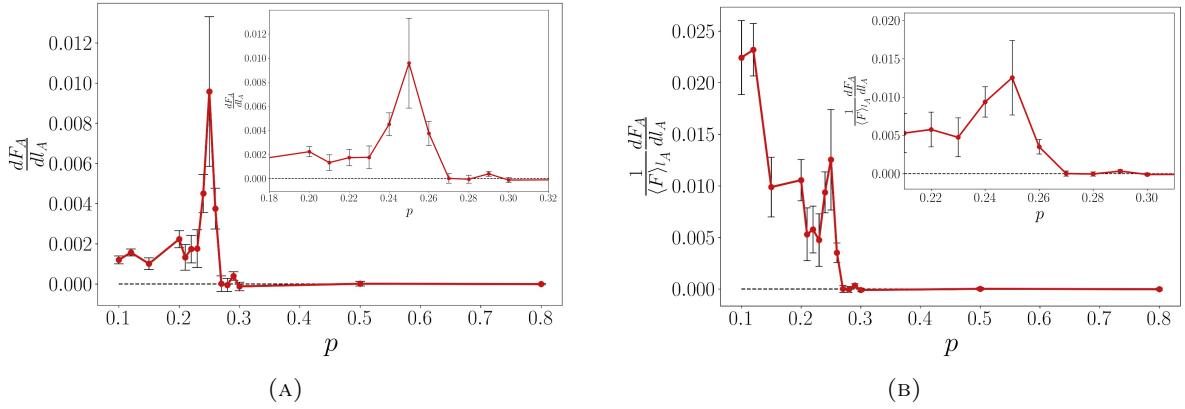
FIGURE 9.4: Behavior of the slope of the normalized energy $F_A/\langle F_A \rangle_{l_A}$ with respect to l_A as function of p. The inset shows the slope of F_A as function of p. The Monte Carlo calculations were performed for $\Gamma/\omega = 0.2$, $L_x = 40$, $L_y = 50$ and $l_A = 0, 2, 4, ..., 20$.

calculate the observables of interest.

Markovian Monte Carlo – We start by considering the Markovian case. For different values of the probability p we consider different sizes of the boundary ranging from $l_A = 0$ to $l_A = L_x/2$, and for each calculate the free energy $F(l_A)$. We may also consider the local energy of each lattice sites due to the interaction with its next neighbors (and with the boundary). Since aligned spins have zero interaction energy while spins oriented in different directions contribute an energy $E_i \sim -\ln p$, we are immediately able to identify the ferromagnetic and the paramagnetic regions by plotting a color map of the local energy.

We notice that at $p = p_c \approx 0.25$, the phase of the system changes from ferromagnetic to paramagnetic, as indicated by the increase in energy over the entire lattice, see Fig.(9.3). Simultaneously, the energy cost of having boundary conditions with $l_A \neq 0$ is large – Fig.(9.3a-b) – at low p, decreases significantly for $p \to p_c$ (see Fig.(9.3c)) and becomes negligible above the critical probability, as in a paramagnetic phase the boundary can be accommodated with very little increase in energy, see Fig.(9.3d).

The transition is also observed by performing a linear fit of the total energy $F_A = F(p, l_A)$ as function of l_A and plotting the behavior of the slope dF_A/dl_A as function of p. When $dF_A/dl_A \neq 0$ the energy of the Potts model, and thus the entanglement entropy of the circuit, scales with the size of the partition subsystem, i.e. it obeys a volume law; when $dF_A/dl_A = 0$, the circuit entanglement is in an area law.

We observe a sharp transition of the slope from non zero values for $p < p_c$ to very small values for $p > p_c$, see Fig.(9.4a). This is also the case if we perform the linear fit analysis on the energy normalized to its average value over l_A at fixed p – i.e. $F_A/\langle F_A \rangle_{l_A}$ – see Fig.(9.4b). This procedure may be necessary to avoid large fluctuations, since at high p the total energy becomes large and analyzing the normalized energy may be more sensible. From both fitting methods we find $p_c \approx 0.25$.

We also observe a local peak of dF_A/dl_A and $\frac{1}{\langle F_A \rangle_{l_A}} \frac{dF_A}{dl_A}$ at $p = p_c$, see the insets in Fig.(9.4). This may be explained as a consequence of the large fluctuations occurring in proximity of the transition: the subsystem at the boundary may act as a nucleation surface that facilitates the appearance of large scale paramagnetic domain that extends deep into the system instead of being confined near the boundary.

9.2   Free fermion model

An interesting setup, where one can numerically investigate the measurement induced phase transition in the free fermionic model has been studied in [169]. In this setup, a 1D chain is populated by spinless fermions, with unitary part of the dynamics constrained to be a simple tight binding Hamiltonian

$$
\mathrm{H} = -\frac{1}{2} \sum_{n=1}^{N-1} \left(c_{n+1}^{\dagger} c_n + \mathrm{h.c.} \right).
\tag{9.2.1}
$$

During the unitary evolution, the state of the system evolves as

$$
|\psi_0\rangle \rightarrow |\psi_t\rangle = e^{-it\mathrm{H}} |\psi_0\rangle
\tag{9.2.2}
$$

The non-unitary part of the evolution is stemming from the coupling of the system to the environment. The interaction between these two lasts for time δt and is characterized with the interaction rate $1/\tau$. One can introduce a dimensionless number $p = \delta t/\tau$, which characterizes the rate by which the environment affects the system. One can mimic the interaction by introducing a set of normalized projective measurement operators $\{P^{(k)}\}_j$ acting on j^{th} site of the system. In practice, one generates a random number p_j for every site and compares it to the aforementioned p to decide whether one performs the measurement or not

1. if $p_j > p$, then the measurement at site j is performed

2. if $p_j < p$, then the measurement at site j is not performed

If the the first option is satisfied, then the system moves to the next step. For our purposes, we assume that the measuring operators are $P_j^{(0)} = n_j$ and $P_j^{(1)} = 1 - n_j$, where n_j is the fermion occupation number at site j. After the measurement of $P_j^{(0,1)}$ observables, the state of the system is projected according to the Born rule with probability $p_j^{(0,1)} = \langle \psi_t | P_j^{(0,1)} | \psi_t \rangle$. To choose whether one should act with $P_j^{(0)}$ or $P_j^{(1)}$ operators, corresponding $p_j^{(0)}$ and $p_j^{(1)}$ numbers are compared to a randomly extracted number $p_j \in (0, 1]$:

$$
|\psi_t\rangle \rightarrow \frac{P_j^{(0,1)} |\psi_t\rangle}{\sqrt{p_j^{(0,1)}}} \quad p_j^{(0,1)} > p_j.
\tag{9.2.3}
$$

The unitary evolution is governed by a quadratic model H, thus the Gaussianity of the state is preserved [169]. Moreover, the projective operators under consideration also preserve the Gaussianity of the state and thus one can use Wick's theorem to describe how two-point correlation function $\mathcal{D}_{nm}(t) = \langle \psi_t | c_n^{\dagger} c_m | \psi_t \rangle$ should be updated after every projective measurement $P_i^{(0,1)}$. The protocol that governs the update of $\mathcal{D}_{nm}(t)$ correlation matrix after the measurements is the following:

1. If we measure n_j, then

$$
\mathcal{D}_{nm} \rightarrow \mathcal{D}_{nm} + \delta_{nj}\delta_{mj} - \frac{\mathcal{D}_{nj}\mathcal{D}_{jm}}{\mathcal{D}_{jj}};
\tag{9.2.4}
$$

2. If we measure $1 - n_j$, then

$$
\mathcal{D}_{nm} \rightarrow \mathcal{D}_{nm} - \delta_{nj}\delta_{mj} + \frac{(\delta_{nj} - \mathcal{D}_{nj})(\delta_{mj} - \mathcal{D}_{jm})}{1 - \mathcal{D}_{jj}}.
\tag{9.2.5}
$$
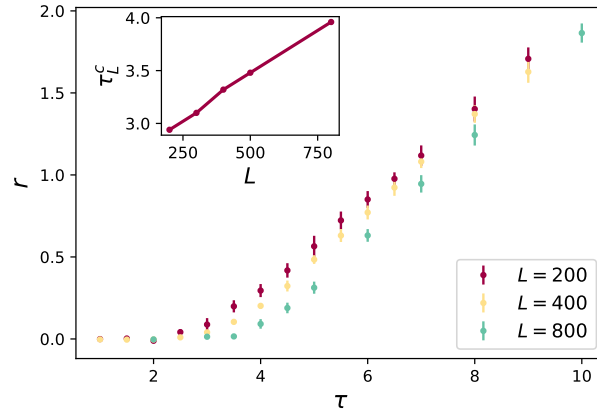
FIGURE 9.5: The main figure shows the dependence of the slope of logarithmic scaling of $\overline{\mathcal{S}}_A$ for various values of measurement rate τ and system size L. The inset shows a finite-size scaling of the critical value τ^c, showing that τ^c increases for larger values of the system size L. Figure extracted from [169].

On the other side, the unitary evolution of the state for time t_{u} corresponds to $\mathcal{D}(t + t_{\mathrm{u}}) = U^\dagger(t_{\mathrm{u}})\mathcal{D}(t)U(t_{\mathrm{u}})$, with

$$U_{nm}(t_{\mathrm{u}}) = \frac{1}{L}\sum_{p=-L/2}^{L/2-1} e^{-i2\pi(n-m)p/L-it_{\mathrm{u}}\epsilon_p}, \tag{9.2.6}$$

where $\epsilon_p = -\cos(2\pi p/L)$ is the spectrum of the tight binding model. Since the measurement and the hermitian part of the evolution operators do not contain any temporal correlations between the present and the past state of the system, the evolution is purely Markovian.

Using the structure of $U_{nm}(t_{\mathrm{u}})$ and protocol of updating the correlation matrix after each measurement, one can easily simulate the ensemble of quantum trajectories for different values of measurement rate and calculate various trajectory averaged expectation values of observables. The Gaussianity of the state of the system allows us to easily access the entanglement content of the system directly via $\mathcal{D}_{nm}$. The bipartite entanglement entropy at time t for a subsystem A can be expressed as

$$\mathcal{S}_A(t) = -\sum_{\lambda_A(t)} \left[\lambda_A(t)\log\lambda_A(t) + (1-\lambda_A(t))\log\left(1-\lambda_A(t)\right)\right], \tag{9.2.7}$$

where $\lambda_A(t)$ are the eigenvalues of the reduced correlation matrix $\tilde{\mathcal{D}}_{nm} = \mathrm{Tr}_B\mathcal{D}_{nm}(t)$. To extract the trajectory averaged entanglement entropy at time t is, one simulates the evolution of the system along many $\alpha \in [1,...,N_{traj}]$, calculates $\mathcal{S}_A^{(\alpha)}(t)$ for each trajectory and then takes the ensemble average

$$\overline{\mathcal{S}}_A(t) = \frac{1}{N_{traj}}\sum_{\alpha=1}^{N_{traj}} \mathcal{S}_A^{(\alpha)}(t). \tag{9.2.8}$$

Initiating every trajectory in some pure-state, say Néel-like configuration of fermions, one can make few intuitive statement about two limiting cases of τ. If $\tau \to \infty$, being equivalent to $p \to 0$, then the system evolves unitarily. Due to this, at later times the bipartite entanglement entropy saturates to some steady state value shows an extensive growth with respect to the size of the bipartition, $\overline{\mathcal{S}}_A(t) \sim l$. In the transient regime, the entanglement entropy will grow linearly in time. The opposite limit $\tau \to 0$, equivalent to persistent measurement of every site at every time-step, drive the system towards Zeno-like regime, where entanglement buildup is maximally suppressed and the system remains in the pure state.

In such setups, one could anticipate that there could exist be an intermediate regime of the

measurement rate, where the scaling of ensemble averaged bipartite entanglement entropy scales logarithmically with respect to the subsystem size. Motivated by Eq.(8.1.4) scaling of entanglement entropy for critical theories described by CFT, one refers to such measurement rates as a critical value of τ^c. To precisely pinpoint τ^c, one can extract $\overline{\mathcal{S}}_A$ at late times and numerically fit it along the logarithmic fitting function $r \ln(l_A) + k$. As it is demonstrated in [169], Fig.(9.5), the scaling of trajectory averaged bipartite entanglement entropy at late times acquires non-zero contribution in logarithmic scaling as soon as one crosses the critical value of τ^c. The precise value of τ^c can in general depend on the system size L. As the finite size analysis in the inset of Fig.(9.5) suggests, the critical value of the measurement rate diverges as one increases the system size. This hints to the fact that in the thermodynamic limit $L \to \infty$, only the area law phase survives for any non-zero value of τ.

This result is in agreement with [186], where authors analytically show that in a 1-dimensional free fermion model with U(1) symmetry and projective measurements, logarithmic growth of entanglement always saturates to an area law-phase even for rare measurements. It must be noted, that other scenarios of monitored free fermions has also been explored, where the logarithmic scaling of entanglement is not related to finite size effects. Namely, authors in [162] have studied free fermionic U(1) chain, albeit with continuous monitoring. In this setup, it was shown that the entanglement scales logarithmically for weak measurement rate $\gamma \ll 1$. For $\gamma \gg 1$, the system collapses in the area-law phase, while logarithmic finite size corrections have been extracted for the critical value $\gamma = \gamma_c$ – indicating to a BKT mechanism of the transition.

Chapter 10

Many-body Non-Markovian Quantum Jumps: Diagrammatic method and Random Unitary Circuit

In this section study the quantum dynamics of a many-body system subject to coherent evolution and coupled to a non-Markovian bath. We propose a technique to unravel the non-Markovian dynamics in terms of quantum jumps, a connection that was so far only understood for single-body systems. We develop a systematic method to calculate the probability of a quantum trajectory, and formulate it in a diagrammatic structure. We find that non-Markovianity renormalizes the probability of realizing a quantum trajectory, and that memory effects can be interpreted as a perturbation on top of the Markovian dynamics. We show that the diagrammatic structure is akin to that of a Dyson equation, and that the probability of the trajectories can be calculated analytically. We then apply our results to study the measurement-induced entanglement transition in random unitary circuits. We find that non-Markovianity does not significantly shift the transition, but stabilizes the volume law phase of the entanglement by shielding it from transient strong dissipation.

10.1 Many-body non-Markovian quantum jumps

We consider a many-body system subjected to coherent time evolution. For simplicity, we focus on a Hamiltonian dynamics, with Hamilton operator H: most of our reasoning also applies to stroboscopic time evolution as realized, for example, in random unitary circuits (on which we will elaborate further in the next sections).

Let us now suppose for simplicity that only one jump operator a acts on the system; the generalization to many decay channels is straightforward.

When the system does not jump, it undergoes a deterministic evolution which is governed by the Hamiltonian H plus a non-Hermitian contribution arising from the back-action of the jump operator, which we can write as $H_{eff} = H - i\Delta(t)a^\dagger a/2$. Over a time δt the quantum state of the system then evolves as [200, 201]

$$|\psi(t + \delta t)\rangle = \frac{(1 - iH_{\text{eff}}\delta t)|\psi(t)\rangle}{||(1 - iH_{\text{eff}}\delta t)|\psi(t)\rangle||} \tag{10.1.1}$$

For book-keeping simplicity, we incorporate all these operations into an operator $\mathcal{U}(t, t')$ that represents the deterministic evolution between t and t', so that $|\psi(t')\rangle = \mathcal{U}(t, t')|\psi(t)\rangle$.

As mentioned, the many-body system can jump at any time and as many times as possible, and the times at which the jump operator is applied matter since the jump operator and the unitary evolution may compete with each other.

The detailed way in which a NJ or a RJ act is shown in Fig.(7.2) and Fig.(10.1). Let us suppose that at time t a jump operator a is applied to the quantum state $|\psi\rangle$ of the system. The system

jumps into $|\psi'\rangle = a|\psi\rangle/||a|\psi\rangle||$, but the bath retains memory of the state $|\psi\rangle$ before the jump. From t to t' the system then evolves with $\mathcal{U}$, $|\psi'\rangle \rightarrow \mathcal{U}|\psi'\rangle$. At time t' a RJ occurs: the system does not jump back into $|\psi\rangle$, but into $|\psi''\rangle = \mathcal{U}|\psi\rangle$. In other words, the RJ brings the system back to the state it would have (unitarily) evolved into if it had never normal jumped at time t. The memory effect is here: the bath remembers the state of the system before the NJ and once the RJ occurs this information flows back into the system in the form of bringing it back to $|\psi''\rangle$. The operatorial definition of the RJ is $|\psi''\rangle\langle\psi'| = \mathcal{U}|\psi\rangle\langle\psi'|$; we stress that it implicitly includes the unitary evolution $\mathcal{U}$, which was absent in the single-body case.
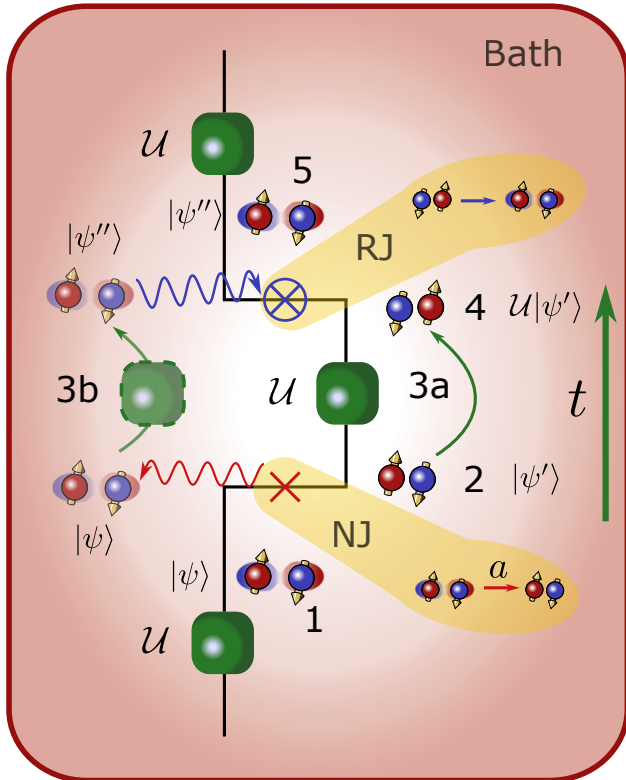
FIGURE 10.1: Example of normal jump (NJ) and reverse jump (RJ) processes in a system coupled to a non-Markovian bath. 1) A system of two spins starts in an entangled Bell pair state $(|\uparrow\downarrow\rangle + |\downarrow\uparrow\rangle)/\sqrt{2}$. 2) The spins undergo a NJ process (red cross) that destroys the coherence and collapses the spins onto a separable state; the information lost in the process is "stored" into the bath (wavy red line). 3a) The system evolves with unitary $\mathcal{U}$ (green square), for example a spin flip $\sigma_1^-\sigma_2^+ + \sigma_1^+\sigma_2^-$; 3b) the bath "remembers" the state before 2 and evolves it with $\mathcal{U}$ (transparent green square) – in this particular case the entangled state is not changed by the spin flip. 4) The system undergoes a reverse jump (blue crossed circle): the information stored in the bath flows back (blue wavy line) into the system that 5) ends up back into the entangled state, regaining its coherence.

The fact that we can reverse the last jump independently of the time it passed since its occurrence is a consequence of the infinite-time memory that we assumed for the non-Markovian bath interacting with the system. On the other end of the "memory spectrum", a Markovian bath has a zero time memory, so that a jump can never be erased. In the middle of the spectrum, there are baths that have a finite but non-zero time memory, so it becomes more and more unlikely to reverse a jump that occurred a long time in the past.

We note an important point: evolving the system from t to t' with just $\mathcal{U}$ or with the sequence RJ $\circ$ $\mathcal{U}$ $\circ$ NJ produces the same quantum state $|\psi''\rangle$ by definition, but along two different trajectories. These two trajectories are equivalent at time t', in the sense that they correspond to the same quantum state and exhibit the same physical properties.

We can therefore group different trajectories into a *class of trajectories* (labeled by the index α) that all exhibit the same quantum state $|\psi_\alpha(t)\rangle$ at time t. We observe that $|\psi_\alpha(t)\rangle$ is completely specified by the initial state $|\psi\rangle$ and by the sequence of times at which normal jumps are performed without being reversed later. In other words, if we label a trajectory class with $\alpha = (t_1, t_2, ..., t_n)$ (see Fig.(10.2)), the quantum state associated to it is given by the unitary evolution, punctuated by the jump operators at the times specified by α:

$$|\psi_\alpha(t)\rangle \equiv \frac{\mathcal{U}(t_n,t)a\,\mathcal{U}(t_{n-1},t_n)a...a\,\mathcal{U}(0,t_1)|\psi\rangle}{||\mathcal{U}a\mathcal{U}a...a\,\mathcal{U}|\psi\rangle||}.$$

(10.1.2)

We remark that using this categorization into trajectory classes, the application of the NMQJ recipe is quite straightforward.
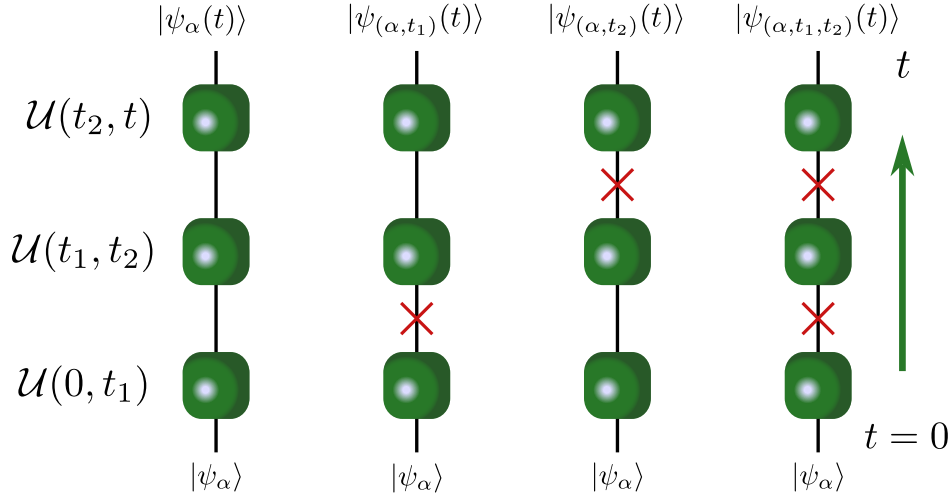
FIGURE 10.2: Different trajectory classes labeled based on the number and time of jumps.
The green squares represent the periods of unitary evolution, while the red crosses represent
normal quantum jumps.

Performing a normal jump at time t simply takes the state of the system from the class $\alpha = (t_1, t_2, ..., t_n)$ to $\alpha' = (t_1, t_2, ..., t_n, t) = (\alpha, t)$. The NJ process and its probability $p^+_{\alpha \to \alpha'}$ are

$$|\psi_\alpha(t)\rangle \to |\psi_{(\alpha,t)}(t)\rangle = \frac{a|\psi_\alpha(t)\rangle}{||a|\psi_\alpha(t)\rangle||}; \tag{10.1.3}$$

$$p^+_{\alpha \to \alpha'} = \Delta(t)\delta t \langle \psi_\alpha(t)|a^\dagger a|\psi_\alpha(t)\rangle. \tag{10.1.4}$$

Conversely, performing a reverse jump from the class $\alpha = (t_1, t_2, ..., t_n) = (\alpha', t_n)$ erases the last NJ performed by the system and takes it into the class $\alpha' = (t_1, t_2, ..., t_{n-1})$:

$$|\psi_\alpha(t)\rangle \to |\psi_{\alpha'}(t)\rangle; \tag{10.1.5}$$

$$\mathcal{U}(t_n, t)\frac{a|\psi_{\alpha'}(t_n)\rangle}{||a|\psi_{\alpha'}(t_n)\rangle||} \to \mathcal{U}(t_{n-1}, t)|\psi_{\alpha'}(t_{n-1})\rangle. \tag{10.1.6}$$

The operator describing the RJ in Eq.(10.1.5) is $|\psi_{\alpha'}(t)\rangle\langle\psi_\alpha(t)|$, which again includes implicitly the unitary evolution operator. The RJ in Eq.(10.1.6) effectively erases the jump that occurred at time t_n, but any trajectory that jumped at a time $t_{n-1} < t' < t$ can reverse jump from $(t_1, t_2, ..., t_{n-1}, t')$ back to α'. Therefore we have to account for these possibilities in the definition of the probability to perform the reverse jump, which is given by

$$p^-_{\alpha \to \alpha'}(t) = \frac{N_{\alpha'}}{\sum\limits_{t_{n-1} < t' < t} N_{(\alpha',t')}} |\Delta(t)|\delta t \langle a^\dagger a \rangle_{\alpha'}(t), \tag{10.1.7}$$

where $\langle a^\dagger a \rangle_\alpha(t) \equiv \langle \psi_\alpha(t)|a^\dagger a|\psi_\alpha(t)\rangle$ and N_α is the probability for the system to be in trajectory α.

The RJ probability is independent of the starting state, in the sense that it is independent of the time t' at which the last jump was performed: every trajectory that originates by normal jumping from the same α' has the same probability of performing a reverse jump back into α'. This property may seem counter intuitive, but actually makes sense since the system does not care when the last jump occurred. For baths with a finite time memory, this is not true anymore, since the probability to reverse jump from (α', t') back to α' decreases as the time difference $t - t'$ increases. This could

be quantified by introducing a memory kernel $K(t', t)$ in the fraction of Eq.(10.1.7):

$$p^{-}_{(\alpha', t_n) \to \alpha'}(t) \sim \frac{N_{\alpha'} K(t_n, t)}{\sum\limits_{t_{n-1} < t' < t} N_{(\alpha', t')} K(t', t)}.$$

We stress that the sum in the denominator is essential for the quantum jump prescription to be consistent with the master equation for the density matrix. It can be proven that averaging the dynamics described by Eqs.(7.5.8, 10.1.3–10.1.7) correctly recovers the master equation. The calculation is tedious but straightforward if the density matrix is written as

$$\rho(t) = \sum_{n=0}^{\infty} \sum_{\{\alpha = (t_1, ..., t_n)\}} \frac{N_\alpha(t)}{N} |\psi_\alpha(t)\rangle\langle\psi_\alpha(t)|, \tag{10.1.8}$$

where the sum over n and over all the times at which the jumps can be performed exhausts all the trajectory classes generated by the evolution.

As expected, the extension of the NMQJ method to a many-body system makes the problem very hard to solve numerically. Not only the number of trajectory classes is exponential $\sim 2^{N_t}$ (with N_t the number of time steps in the evolution) for each decay channel, but it is not even possible to do a statistical sampling of the ensemble as in MCWF, due to the crosstalk between trajectories. Since both the individual trajectories and classes of trajectories are *not* independent of each other as they are in the Markovian case, all of them are needed to compute the probability of reverse jumps.

However, we observe that a class of trajectories is completely identified by α, i.e. the times at which the *normal* jumps occur. This is also true in the Markovian case, where the probability of the system ending up in the state associated to $\alpha = (t_1, t_2, ..., t_n)$ can be calculated at once by multiplying the probability of jumping at times $t_1, t_2, ..., t_n$ with the probability of not jumping at the other times.

In the non-Markovian case, the Markovian probability is modified – borrowing a field theory term, we could say it gets "dressed" or renormalized – by all the trajectories equivalent to α, in which m other normal jumps were performed but later cancelled out by an equal number of reverse jumps, see Figs.(10.2,10.3). If we can find a way to express this additional contribution we can drastically simplify the treatment of the non-Markovian dynamics. This is the topic of the next section.

10.2 Diagrammatics of trajectories

Our goal in this section is to calculate the "dressed" contributions that affect the probability of realizing each state $|\psi_\alpha\rangle$ due to the presence of equivalent trajectories that feature a series of reverse jumps. In particular, we need to evaluate how the latter ones sum up to modify the probability of a given trajectory class.

For the sake of concreteness, we assume that the system is evolved between $t = 0$ and $t = t_f$ and consider the class $\alpha = (t_1, ..., t_n)$. In the Markovian regime, there is only one trajectory contributing to this class, while in the non-Markovian regime, many trajectories contribute to the population of this class. For example any trajectory performing normal jumps at times $t_1, ..., t_n$ plus any number of additional pairs of NJ plus the relative RJ are valid trajectories contributing to the population of α. We note that the normal and reverse jumps must occur at times t_m and t'_m comprised between the times of two successive normal jumps in α, i.e. such that $t_j < t_m, t'_m < t_{j+1}$, with $j = 0, ..., n$ and $t_0 = 0$ and $t_{n+1} = t_f$. These pairs of normal + reverse jumps constitute sort of "loops" (to borrow another term from field theory) that renormalize and increase the probability of realizing
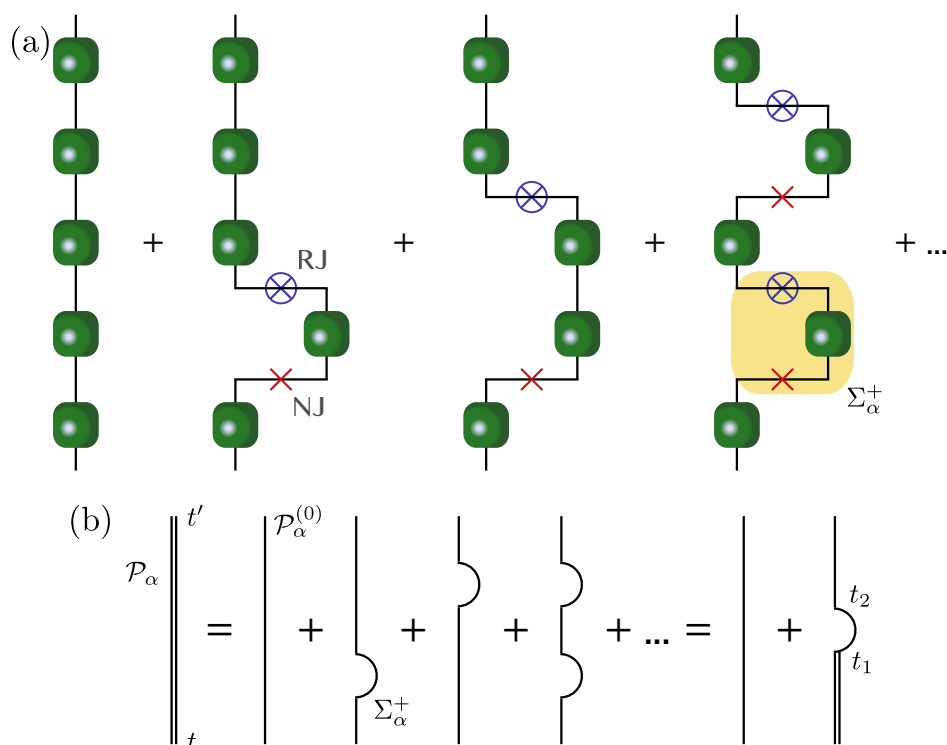
FIGURE 10.3: (a) The trajectories shown in the panel are different since they have different normal + reverse jumps sequences, but all lead to the same final quantum state. Their probabilities must then be summed. (b) Diagrammatic method to calculate the dressed propagator.

the trajectory class $\alpha = (t_1, ..., t_n)$, see Fig.(10.3). It is the contribution of these loops that we want to calculate.

It is useful to write $\Delta(t) = \Delta_+(t) + \Delta_-(t) = \Delta_+(t) - |\Delta_-(t)|$, where $\Delta_\pm(t)$ is the positive/negative part of the decay rate. We also define $\mathcal{P}_\alpha(t, t')$ as the conditional probability that the system is in the state labeled by α at time t and is again found in the same state α at a later time t'. Such probability essentially corresponds to the probability that no additional normal jumps are performed between t and t', or that all the normal jumps performed are cancelled by an equal number of reverse jumps.

In the limit where the dynamics is Markovian, the "bare" probability $\mathcal{P}_\alpha^{(0)}(t, t')$ is given by

$$\mathcal{P}_\alpha^{(0)}(t, t') = \exp\left(-\int_t^{t'} d\tau \Delta_+(\tau) \langle a^\dagger a \rangle_\alpha(\tau)\right). \tag{10.2.1}$$

Equation 10.2.1 arises from the fact that the unitary evolution does not change the probability of the system being in a certain class, and that the product of the probabilities of performing no jumps between t and t' is an exponential in the continuum limit.

10.2.1 No jump trajectory

We start from the simpler case in which the class we consider is the no jump trajectory, i.e. $\alpha = \varnothing$, see Fig.(10.3a). The conditional probability of staying in such trajectory is corrected (with respect to the Markovian case) only by loops of the type normal jump + reverse jump, because no reverse jump can occur first since the system has not jumped at all to begin with.

We indicate with $\Sigma_\alpha^+(t, t')$ the probability of performing a normal jump from the class α at time t and then going back to α with a reverse jump at time t'. Then we can write $\mathcal{P}_\varnothing$ as a perturbative series in Σ^+:

$$\mathcal{P}_\varnothing = \mathcal{P}_\varnothing^{(0)} + \mathcal{P}_\varnothing^{(0)} \circ \Sigma^+ \circ \mathcal{P}_\varnothing^{(0)} + \mathcal{P}_\varnothing^{(0)} \circ \Sigma^+ \circ \mathcal{P}_\varnothing^{(0)} \circ \Sigma^+ \circ \mathcal{P}_\varnothing^{(0)} + ...;$$

$$\downarrow$$

$$\mathcal{P}_\varnothing = \mathcal{P}_\varnothing^{(0)} + (\mathcal{P}_\varnothing^{(0)} + \mathcal{P}_\varnothing^{(0)} \circ \Sigma^+ \circ \mathcal{P}_\varnothing^{(0)} + ...) \circ \Sigma^+ \circ \mathcal{P}_\varnothing^{(0)};$$

$$\downarrow$$

$$\mathcal{P}_\varnothing = \mathcal{P}_\varnothing^{(0)} + \mathcal{P}_\varnothing \circ \Sigma^+ \circ \mathcal{P}_\varnothing^{(0)}, \tag{10.2.2}$$

where $\circ$ represents the convolution over all times between t and t', i.e.

$$(A \circ B)(t, t') = \int_t^{t'} (dt_1/\delta t) A(t, t_1) B(t_1, t'),$$

in the continuum limit we divide the integration over steps of length δt. The resummation formula contained in Eq.(10.2.2) is depicted graphically in Fig.(10.3b).

Writing explicitly the convolutions we find

$$\mathcal{P}_\varnothing(t, t') = \mathcal{P}_\varnothing^{(0)}(t, t') + \int_t^{t'} \frac{dt_2}{\delta t} \int_t^{t_2} \frac{dt_1}{\delta t} \mathcal{P}_\varnothing(t, t_1) \Sigma_\varnothing^+(t_1, t_2) \mathcal{P}_\varnothing^{(0)}(t_2, t').$$

The integration limits express the causality of the jumps: the normal and reverse jumps must occur between t and t' at times such that $t < t_1 < t_2 < t'$.

It is worth noticing that, within this picture, the no-click limit takes the role of a mother trajectory: indeed, a large number of trajectories is represented by the dressed no-click case. This may suggest that the latter is particularly informative about the system dynamics, as already noted in some Markovian cases [150, 243].

10.2.2   Generic trajectory

Eq.(10.2.3) can be extended to a generic conditional probability $\mathcal{P}_\alpha$. In principle, there exist also reverse loops, where a reverse jump occurs first and is then followed by a normal jump. However, the action of such loops on $\mathcal{P}_\alpha$ is ill-defined, in the sense that it is not an actual loop since it does not bring the system back to the same trajectory class.

To be more specific, let us assume that $\alpha = (t_1, .., t_m)$; a reverse jump at $t > t_m$ brings the system into the state labeled by $(t_1, .., t_{m-1})$ and a successive normal jump closing the reverse loop takes the system into the state labeled by $(t_1, .., t_{m-1}, t') \neq \alpha$. Therefore "reverse loops" should not be taken into account when renormalizing $\mathcal{P}_\alpha^{(0)}$ since they always bring the system into a different trajectory class [1].

It is then straightforward to generalize Eq.(10.2.3)

$$\mathcal{P}_\alpha(t, t') = \mathcal{P}_\alpha^{(0)}(t, t') + \int \frac{dt_2}{\delta t} \frac{dt_1}{\delta t} \mathcal{P}_\alpha(t, t_1) \Sigma_\alpha^+(t_1, t_2) \mathcal{P}_\alpha^{(0)}(t_2, t').$$

Borrowing some more terminology from field theory, we can regard the conditional probability $\mathcal{P}_\alpha$ as a sort of propagator of the class α. We observe that the "dressed" propagator is related to the "bare" propagator $\mathcal{P}_\alpha^{(0)}$ by a relation very similar to the Dyson equation for the Green function of interacting systems, where the loop probability Σ^+ plays the role of the self-energy.

---

[1] We exclude the limiting case $t' = t_n$ where the reverse and normal jumps occur at the same time.

We write the loop probability $\Sigma^+(t_1, t_2)$ as the probability to perform a normal jump at time t_1, times the conditional probability to stay in the new trajectory class (α, t_1), times the probability to reverse jump at time t_2.

$$\Sigma^+_\alpha(t_1, t_2) = p^+_{\alpha \to (\alpha, t_1)}(t_1) \mathcal{P}_{(\alpha, t_1)}(t_1, t_2) p^-_{(\alpha, t_1) \to \alpha}(t_2). \tag{10.2.3}$$

We stress that in Eq.(10.2.3) the conditional probability to stay in (α, t_1) is "dressed" because we have to allow for the possibility of "nested" sequences of jumps, e.g. of the type NJ+NJ+RJ+RJ, in which the system jumps further away from (α, t_1) and then comes back to it with reverse jumps before t_2.

Using Eqs.(7.5.8,7.6.2) we write

$$p^+_{\alpha \to (\alpha, t_1)}(t_1) = \Delta_+(t_1) \delta t \langle a^\dagger a \rangle_\alpha(t_1); \tag{10.2.4}$$

$$p^-_{(\alpha, t_1) \to \alpha}(t_2) = \frac{N_\alpha(t_2)|\Delta_-(t_2)|\delta t}{\int_t^{t_2} \frac{d\tau}{\delta t} N_{(\alpha, \tau)}(t_2)} \langle a^\dagger a \rangle_\alpha(t_2). \tag{10.2.5}$$

In the ratio of populations of the target and sources states, we switched to the continuum limit and replaced the summation by an integration. An important point is that the integration in the denominator runs from t to t_2. The upper limit obviously follows from causality, since we can only reverse at time t_2 trajectories that underwent a normal jump from α before t_2. The lower limit is a consequence of the conditional probability $\mathcal{P}_\alpha(t, t')$: we condition the system to be in the state α at time t and we have to only take into account trajectories that normal jumped from α after that time.

The ratio of populations is essentially a ratio of probabilities, and both numerator and denominators can factorize into the probability to be in the state α at time t times the probability to stay in α (or to jump into (α, τ) for the denominator):

$$\frac{N_\alpha(t_2)}{\int_t^{t_2} \frac{d\tau}{\delta t} N_{(\alpha, \tau)}(t_2)} = \frac{\mathcal{P}_\alpha(t, t_2)}{\int_t^{t_2} \frac{d\tau}{\delta t} \mathcal{P}_\alpha(t, \tau) p^+_{\alpha \to (\alpha, \tau)}(\tau) \mathcal{P}_{(\alpha, \tau)}(\tau, t_2)}$$

The denominator arises from the fact that the conditional probability of being in a trajectory eligible to reverse jump is the sum over all times τ between t and t_2 of the probability $\mathcal{P}_\alpha(t, \tau)$ to propagate the state α from t to τ times the probability $p^+_{\alpha \to (\alpha, \tau)}(\tau)$ of jumping at time τ times the probability $\mathcal{P}_{(\alpha, \tau)}(\tau, t_2)$ to propagate in (α, τ) from τ to t_2.

Substituting into Eq.(10.2.5) and Eq.(10.2.3), the integral in the denominator simplifies when integrating over t_1

$$\int \frac{dt_1}{\delta t} \mathcal{P}_\alpha(t, t_1) \Sigma^+_\alpha(t_1, t_2) = \int \frac{dt_1}{\delta t} \mathcal{P}_\alpha(t, t_1) p^+_{\alpha \to (\alpha, t_1)}(t_1) \cdot$$

$$\frac{\mathcal{P}_{(\alpha, t_1)}(t_1, t_2) \mathcal{P}_\alpha(t, t_2)|\Delta_-(t_2)|\delta t \langle a^\dagger a \rangle_\alpha(t_2)}{\int_t^{t_2} d\tau / \delta t \mathcal{P}_\alpha(t, \tau) p^+_{\alpha \to (\alpha, \tau)}(\tau) \mathcal{P}_{(\alpha,)}(\tau, t_2)} = \mathcal{P}_\alpha(t, t_2)|\Delta_-(t_2)|\delta t \langle a^\dagger a \rangle_\alpha(t_2). \tag{10.2.6}$$

This result is remarkable, as after integrating over the starting time of the loop, the specific trajectory class into which the system jumps does not matter. This is a consequence of the fact that all trajectories eligible to perform a reverse jump have the same probability to do so. Combining Eq.(10.2.4,10.2.3) we obtain

$$\mathcal{P}_\alpha(t, t') = \mathcal{P}_\alpha^{(0)}(t, t') + \int_t^{t'} dt_2 \mathcal{P}_\alpha(t, t_2)|\Delta_-(t_2)|\delta t \langle \psi_\alpha(t_2)|a^\dagger a|\psi_\alpha(t_2)\rangle \mathcal{P}_\alpha^{(0)}(t_2, t'); \tag{10.2.7}$$

$$\mathcal{P}_\alpha(t,t') = \exp\left(-\int_t^{t'} d\tau (\Delta_+(\tau) - |\Delta_-(\tau)|)\langle\psi_\alpha(\tau)|a^\dagger a|\psi_\alpha(\tau)\rangle\right)$$

$$= \exp\left(-\int_t^{t'} d\tau \Delta(\tau)\langle a^\dagger a\rangle_\alpha(\tau)\right). \tag{10.2.8}$$

Eq.(10.2.8) is particularly telling. It implies that the regions of non-Markovianity in the decay rate renormalize the probability of staying in a certain trajectory class α. It is also similar to the probability of staying in the excited state of a non-Markovian two level system (as obtained form solving the master equation [201]); however, it shows that this simple expression for the probability of staying in the same state is also valid for a generic many-body system, provided that the state $|\psi_\alpha\rangle$ associated to the label α changes in time according to the unitary and jump evolutions.

10.2.3 Probability of a generic outcome

We now want to calculate what is the probability of performing a certain number of normal jumps between an initial time $t = 0$ and a final time t.

Let us start from the case of one jump, in which we go from the class $\alpha = \varnothing$ to the class $\alpha = (t_1)$ within a small time interval of width δt and centered around time t_1. The probability $\mathcal{P}_\varnothing^{(t_1)}$ of ending up in this state is then given by:

$$\mathcal{P}_\varnothing^{(t_1)}(0,t) = \mathcal{P}_\varnothing(0,t_1)\Delta_+(t_1)\delta t\langle a^\dagger a\rangle_\varnothing(t_1)\mathcal{P}_{(t_1)}(t_1,t).$$

In other words the probability of the evolution realizing the outcome (t_1) is given by the probability to not jump between 0 and t_1, times the probability to perform a normal jump in a δt interval around t_1 times the probability to not jump between t_1 and t and stay in the (t_1) outcome.

We note that we can write $\Delta_+(t_1)$ as $\Delta(t_1)$ since normal jumps only occur in the Markovian regions of the evolution. In this sense we observe $\mathcal{P}_\varnothing^{(t_1)}(0,t) = (-\partial_{t_1}\mathcal{P}_\varnothing(t,t_1))\delta t\mathcal{P}_{(t_1)}(t_1,t)$, or in other words the probability to jump out of the $\varnothing$ outcome at time t_1 is minus the time derivative of the probability to stay into that outcome.

Generalizing the above, we write the probability to jump from outcome α at time t to outcome $(\alpha, t_1, t_2, ..., t_n)$ at time t' by performing n jumps at times $t < t_1 < t_2 < ... < t_n < t'$ as:

$$\mathcal{P}_{(\alpha)}^{(\alpha,t_1,...,t_n)}(t,t') = \mathcal{P}_{(\alpha)}(t,t_1)\Delta_+(t_1)\delta t\langle a^\dagger a\rangle_{(\alpha)}(t_1)\times$$
$$\times\mathcal{P}_{(\alpha,t_1)}(t_1,t_2)\times...\times\Delta_+(t_n)\delta t\langle a^\dagger a\rangle_{(\alpha,t_1,...,t_{n-1})}(t_n)\times \tag{10.2.9}$$
$$\times\mathcal{P}_{(\alpha,t_1,...,t_n)}(t_n,t');$$

$$\mathcal{P}_{(\alpha)}^{(\alpha,t_1,...,t_n)}(t,t') = \prod_{j=0}^n \mathcal{P}_{(\alpha,t_1,...,t_j)}(t_j,t_{j+1})\times\prod_{j=1}^n\Delta_+(t_j)\delta t\langle a^\dagger a\rangle_{(\alpha,t_1,...,t_{j-1})}(t_j). \tag{10.2.10}$$

with the identifications $t_0 = t$ and $t_{n+1} = t'$.

In the case of many decay channels – each with an associated jump operator a_s and decay rate $\Delta_s(t)$ – we can write a vector of labels $\vec{\alpha} = (\alpha_1, \alpha_2, ..., \alpha_{n_\text{channels}})$, where each $\alpha_s = (t_{s,1}, t_{s,2}, ...t_{s,n_s})$ describes the times at which the system undergoes a jump through channel s. Since the channels are independent, the total propagator probability of no jump is the product of the propagator

probability for each channel:

$$\mathcal{P}_{\vec{\alpha}}(t, t') = \exp\left(-\int_t^{t'} d\tau \sum_s \Delta_s(\tau)\langle a_s^\dagger a_s \rangle_{\vec{\alpha}}(\tau)\right). \tag{10.2.11}$$

A similar generalization of Eq.(10.2.10) can be written down.

10.2.4 Advantages and limitations of the diagrammatic renormalization method

In this section we have shown that it is possible to obtain an analytic expression for the probability of a non-Markovian system realizing a certain sequence α of normal quantum jumps and ending up in the corresponding state $|\psi_\alpha\rangle$. This is a remarkable result, as it generalizes known results for the dynamics of Markovian systems to non-Markovian many-body systems.

However, there are some limitations to the applicability of this formula. One limit is that the results we presented are technically exact in the limit in which the system is able to jump an infinite number of times. In fact, in writing the expression for the Σ^+ loops and their corrections, we assumed that the state in which the system jumps is again eligible to jump itself, which is not the case if the system is only able to jump a finite number of times.

The comparison with the extreme example, in which the system may only jump once, shows that our equations correctly predict the probability to perform zero jumps, see Eq.(B5) in Ref. [201], but differ from the probability of performing one jump, see Eq.(B6) in [201]. However, this is not a fatal issue, as our analytic results are more and more a good approximation as the maximum number of jumps increases, and are essentially indistinguishable from the exact results when considering large enough systems and long enough time evolutions.

Another practical issue is that applying Eqs.(10.2.9-10.2.11) to real system still generally requires the knowledge of the quantum state of the system $|\psi_\alpha(t)\rangle$, which implies solving the dynamics of a many-body system, which is exponentially complex in the system size. Note that in a usual non-Markovian setting, the simulation of all possible trajectories is required, meaning the complexity is still exponential in the system size *and* in the evolution time. However, there are some special cases in which the physics of a system can be studied without needing to know the quantum state of the system at all times; one of them is the case of the mapping of random unitary circuits into a statistical model [145], which we analyze in detail in the next section.

10.3 Non-Markovian measurement induced transition

In this section we apply the results obtained in Sec.(10.2) to investigate the dynamics of the entanglement and the transition induced by measurements in non-Markovian systems. We specialize to the case of random unitary (Haar) circuits for a number of reasons. They have been extensively studied in the literature, so there is an abundance of study cases to use for comparison; moreover, random circuits can be mapped to a classical Potts model on which either analytical or Monte Carlo calculations can be performed. And most importantly, the measurement protocol usually implemented on such circuits is such that the exponent in Eq.(10.2.11) simplifies and does not contain the quantum state of the system, greatly simplifying further analytical calculations.

10.3.1 Random Unitary Circuits

We consider a random unitary circuit similar to the model studied in Ref. [145]. The system is composed of L q-dits, i.e. spins with a d-dimensional Hilbert space. Every time step the q-dits evolve according to random unitary gates coupling the odd or even pairs alternatively, and then undergo random local measurements, see Fig.(10.4). The unitary evolution does not affect the
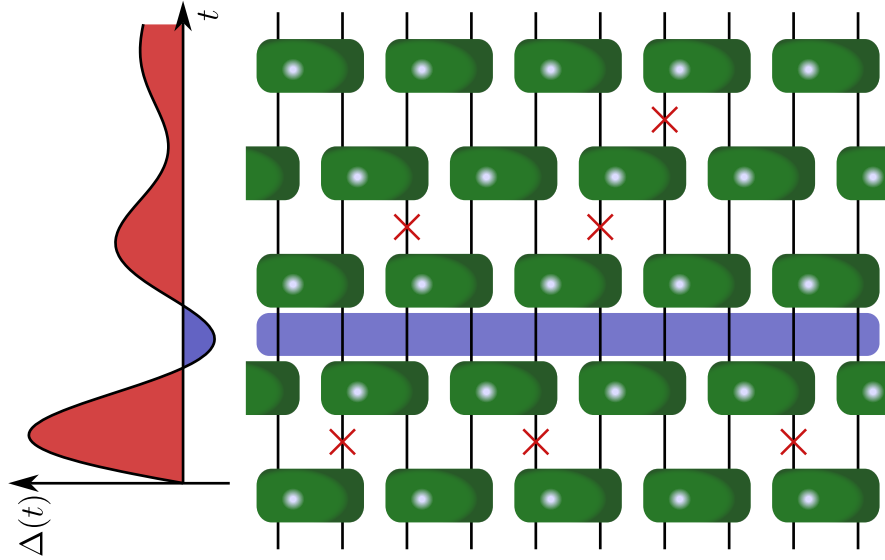
FIGURE 10.4: Diagram of a non-Markovian random unitary circuit. Layers of two-qudits unitary gates (green rectangles) alternate with layers of local random measurements (red crosses). Whenever the decay rate becomes negative (blue shaded region), no normal jump measurements are allowed; this corresponds to a "frozen" layer where the Potts spins behave ferromagnetically.

probability of being in a certain sequence α of quantum jumps in any way other than changing the state of the system.

Similarly to Eq.(10.1.2), we describe the state of the system at time t_i by a sequence of random unitaries $\mathcal{U}$ and local normal quantum jumps a applied to the initial state:

$$|\psi(t)\rangle = \frac{\mathcal{C}(t)|\psi\rangle}{||\mathcal{C}(t)|\psi\rangle||}; \tag{10.3.1}$$

$$\mathcal{C}(t) = \mathcal{U}(t_n, t) a\, \mathcal{U}(t_{n-1}, t_n) a ... a\, \mathcal{U}(0, t_1) \tag{10.3.2}$$

where $\mathcal{C}(t)$ is the circuit operator, $\alpha = (t_1, ..., t_n)$ and with the obvious generalization to multiple channels of decay.

The probability $P_{\mathcal{C}}$ of realizing a particular $\mathcal{C}$ depends on the probability $P_{\mathcal{C}}^{\mathcal{U}}$ associated to the random unitaries and the probability $P_{\mathcal{C}}^{\mathcal{M}}$ of performing the sequence of normal jumps specified by $\mathcal{C}$. Note that $P_{\mathcal{C}}^{\mathcal{U}}$ and $P_{\mathcal{C}}^{\mathcal{M}}$ are independent, so we may only focus on the probability associated to the quantum jumps, which is essentially a discretized version of Eq.(10.2.9).

We now specify the protocol for the measurement: we choose Kraus operators that have equal weight and that constitute a resolution of the identity. For example, for each site we may have d quantum channels, each corresponding to a projector on every state of the local Hilbert space $a_s = |s\rangle\langle s|$ (for $s = 1, ..., d$); alternatively, we may have a continuous set of jump operators obtained by transforming with random unitaries the projector on one of the states $a_s = |s\rangle\langle s|$. We only require that each jump operator in this set has an equal weight, i.e. $\Delta_s = \Delta$. This is a crucial assumption, since it simplifies the sum over the decay channels in Eq.(10.2.11):

$$\sum_s \Delta_s(\tau)\langle\psi(\tau)|s\rangle\langle s|s\rangle\langle s|\psi(\tau)\rangle = \Delta(\tau)\langle\psi(\tau)|\sum_s |s\rangle\langle s|\psi(\tau)\rangle = \Delta(\tau) \tag{10.3.3}$$

since $\sum_s |s\rangle\langle s| = \mathbb{I}$. With this simplification, the probability of no jump becomes independent of the quantum state of the system, and it is possible to calculate it without having to study the many-body dynamics of the system.

10.3.2 Probability of a circuit realization

We discretize the evolution: for any measurement time t_i we define $p_i = \Delta(t_i)\delta t$. During the Markovian regions $\Delta(t_i) > 0$ this is a real probability of performing a jump. During the non-Markovian regions p_i is negative and is not a physical probability, but still makes sense with the interpretation that when $p_i < 0$ there is no normal jump and there is an increase of the weight associated to the no jump trajectory.

Indeed, the probability of performing no jumps on a certain site from time t_i to time $t_{i'}$ is obtained by discretizing the propagator probability Eq.(10.2.11):

$$\mathcal{P}_\alpha(t_i, t_{i'}) = \exp\left(-\int_{t_i}^{t_{i'}} d\tau \Delta(\tau)\right) \to \prod_{j=i}^{i'}(1 - p_j). \tag{10.3.4}$$

i.e. the probability to not perform any normal jump is given by the probability to not undergo jumps at any of the intermediate times. Regions of non-Markovianity increase this probability, which is intuitively and formally correct, since non-Markovianity makes information flow back into the no jump outcome.

We now consider the probability of performing a normal jump and split it into two parts: one associated to the probability of performing a jump and one associated to the weight of the trajectory where the jump is $a_s = |s\rangle\langle s|$:

$$\Delta_+(t_i)\delta t \langle a_s^\dagger a_s\rangle(t_i) = p_i \|a_s|\psi(t_i)\rangle\|^2 = p_i \frac{\|a_s\mathcal{C}(t_i^-)|\psi\rangle\|^2}{\|\mathcal{C}(t_i^-)|\psi\rangle\|^2} = p_i \frac{\|\mathcal{C}(t_i^+)|\psi\rangle\|^2}{\|\mathcal{C}(t_i^-)|\psi\rangle\|^2},$$

where $\mathcal{C}(t_i^\pm)$ is the circuit operator immediately after/before the normal jump. We have used that $|\psi(t_i)\rangle = \mathcal{C}(t_i^-)|\psi\rangle/\|\mathcal{C}(t_i^-)|\psi\rangle\|$ and $a_s\mathcal{C}(t_i^-) = \mathcal{C}(t_i^+)$. We have split the probability associated to the decay rate, i.e. $p_i = \Delta(t_i)\delta t$, from the probabilities associated to the weight of the trajectory, i.e $\mathcal{C}(t)|\psi\rangle$. We are now able to write the discretized form of Eq.(10.2.10).

We assume that the system evolves from time $t_0 = 0$ to time $t_m = t$, and that the circuit operator $\mathcal{C}$ describes n normal jumps at times $t_{i_1}, ..., t_{i_n}$, no jumps at times $t_j \neq t_{i_1}, ..., t_{i_n}$ and a certain realization of random unitaries in between described by the probability $P_\mathcal{C}^{\mathcal{U}}$. We can then write the probability of realizing $\mathcal{C}$ associated to the quantum jumps as

$$P_\mathcal{C} = P_\mathcal{C}^{\mathcal{U}} \prod_{i \neq i_1, ..., i_n}(1 - p_i) \prod_{a=1}^{n} p_{i_a} \frac{\|\mathcal{C}(t_{i_a}^+)|\psi\rangle\|^2}{\|\mathcal{C}(t_{i_a}^-)|\psi\rangle\|^2}. \tag{10.3.5}$$

The circuit operators between two successive jump times only differ by a sequence of unitary operators: $\mathcal{C}(t_{i_{a+1}}^-) = \left(\prod_{j=i_a+1}^{i_{a+1}}\mathcal{U}_j\right)\mathcal{C}(t_{i_a}^+)$. Since the unitaries do not change the norm of the state we have $\|\mathcal{C}(t_{i_{a+1}}^-)|\psi\rangle\| = \|\mathcal{C}(t_{i_a}^+)|\psi\rangle\|$. Therefore, the product of the ratio of the norms simplifies

$$\prod_{a=1}^{n} \frac{\|\mathcal{C}(t_{i_a}^+)|\psi\rangle\|}{\|\mathcal{C}(t_{i_a}^-)|\psi\rangle\|} = \prod_{a=1}^{n} \frac{\|\mathcal{C}(t_{i_{a+1}}^-)|\psi\rangle\|}{\|\mathcal{C}(t_{i_a}^-)|\psi\rangle\|} = \frac{\|\mathcal{C}(t_{i_{n+1}}^-)|\psi\rangle\|^2}{\|\mathcal{C}(t_{i_1}^-)|\psi\rangle\|^2},$$

which reduces to $\|\mathcal{C}(t)|\psi\rangle\|^2$ because $\|\mathcal{C}(t_{i_{n+1}}^-)|\psi\rangle\|^2 = \|\mathcal{C}(t)|\psi\rangle\|^2$ and $\|\mathcal{C}(t_{i_1}^-)|\psi\rangle\|^2 = 1$.

Therefore we write

$$P_{\mathcal{C}} = ||\mathcal{C}\,|\psi\rangle\,||^2 P_{\mathcal{C}}^{\mathcal{U}} \prod_{a=1}^{n} p_{i_a} \prod_{i \neq i_1, \dots, i_n} (1 - p_i); \tag{10.3.6}$$

$$P_{\mathcal{C}} = ||\mathcal{C}\,|\psi\rangle\,||^2 P_{\mathcal{C}}^{\mathcal{U}} P_{\mathcal{C}}^{\mathcal{M}};$$

$$P_{\mathcal{C}}^{\mathcal{M}} = \prod_{l=1}^{L} \left(\prod_{a_l=1}^{n_l} p_{i_{a_l}}^l \prod_{i \neq i_1, \dots, i_{n_l}} (1 - p_i^l) \right). \tag{10.3.7}$$

Equation 10.3.7 is the generalization to the multiple sites case, with p_i^l the probability for a quantum jump to occur at site l at time t_i.

The total probability is $P_{\mathcal{C}} = ||\mathcal{C}\,|\psi\rangle\,||^2 P_{\mathcal{C}}^{\mathcal{U}} \mathcal{P}_{\mathcal{C}}^{\mathcal{M}}$. The first factor is the norm of the state after applying the circuit operator, and accounts for the probability of the state to be eligible to perform a jump. The second factor is the probability of a specific realization of random unitaries.

The third factor in the product is associated to the weight for the random measurements. This crucial factorization allows us to separate the contributions that depend on the quantum state (and that thus require exponentially complex numerical calculations) from the contributions that depend on the decay rates of the quantum channels. In other words, the average over the random measurements factorizes – as in the Markovian case – as the product of the averages over measurements for each time of the evolution and for each site.

We reiterate that one important difference is that for the non-Markovian regions the probability to perform a jump is zero (since no normal jumps can be performed). This is a consequence of the fact that the state of the system is not affected by reverse jumps, in the sense that the final quantum state is only determined by the sequence of normal jumps; the system only cares about reverse jumps to the extent that they renormalize the probability of the system being in a certain quantum state. Indeed, a second difference of the non-Markovian regions is that the probability to not perform any jump is larger than one – meaning a renormalization of the no jump weight. While the meaning of this probability being greater than one is apparently not very physical, this recipe is formally correct and can be employed to map the system to a classical Potts model amenable to Monte Carlo simulations.

10.3.3   Mapping to a Potts model

We use the formal mapping machinery of Ref. [145]. The n-th Renyi entanglement entropy of a partition A of the system is expressed in terms of the free energy F of a replicated system where Q replicas live on each site:

$$S_n^A = \frac{n}{n-1} \lim_{Q \to 1} \frac{F_A - F_0}{Q - 1} \tag{10.3.8}$$

where the free energy is calculated averaging over $P_{\mathcal{C}}^{\mathcal{U}} P_{\mathcal{C}}^{\mathcal{M}}$;

$$F = -\ln \mathcal{Z} = -\ln \sum_{\mathcal{C}} P_{\mathcal{C}}^{\mathcal{U}} P_{\mathcal{C}}^{\mathcal{M}}. \tag{10.3.9}$$

F_A is calculated for boundary conditions (in the physical and replica space) dictated by the partition A and the order n of the Renyi entropy, while F_0 corresponds to a replica system with no partition of the system. Without going too much into the details of the mapping (which are discussed extensively in the literature [142, 145]), the 1+1 quantum model is mapped onto a 2+0 dimensional classical model, where each site is associated to a permutation of the replicas. Thus the classical model is essentially a $Q!$-states Potts model, where neighboring Potts spins are coupled via the unitary gates or via the measurements.

We can split the sum over unitaries and over measurements in Eq.(10.3.9). The sum over the unitaries immediately factorizes into the sum over unitaries for each site [142, 145], yielding terms proportional to the Weingarten functions. The sum over the random measurements also factorizes as (Eq.(13) of [145])

$$\sum_{\mathcal{C}} P_{\mathcal{C}}^{\mathcal{M}} = \prod_{\langle j,l \rangle} \sum_{g_j, g_l \in S_Q} W_p(g_j^{-1}(t_i) g_l(t_{i+1})). \tag{10.3.10}$$

where S_Q is the set of permutations of Q elements. The weight W_p is the average over the possible outcomes of a random jump occurring on site j (associated to a Potts spin g_j) at time t_i and coupling to the next neighbor site l at time t_{i+1} (with associated Potts spin g_l).

The expression of W_p depends on the local Hilbert space dimension d, on the probability of jumping p_i and on whether the set of normal jump operators is a discrete – i.e. $\mathcal{M}_p = \{\mathbb{I}, a_1, ..., a_d\}$ with $a_s = |s\rangle\langle s|$ and weights $\{1 - p, p, ..., p\}$ – or a continuous set of randomly generated projectors $\mathcal{M}_p = \{\mathbb{I}\} \cup \{\sqrt{d} a_U | U \in U(d)\}$, with $a_U = U^\dagger a_1 U$ and U a random unitary matrix. For computational convenience we focus on the second option and find

$$W_p(g) = (1 - p_i) d^{|g|} + p_i d^Q \qquad p_i \geq 0; \tag{10.3.11}$$

$$W_p(g) = (1 - p_i) d^{|g|} \qquad p_i < 0 \tag{10.3.12}$$

where $|g| \leq Q$ is the number of cycles in the permutation g.

The average over unitaries and measurements can be written in terms of the product over triangular plaquettes of the integrated weight $J_p(g_i, g_j; g_k)$.

$$\sum_{\mathcal{C}} P_{\mathcal{C}}^{\mathcal{M}} P_{\mathcal{C}}^{\mathcal{U}} = \sum_{\{g_i \in S_Q\}} \prod_{\langle ijk \rangle \in \triangledown} J_p(g_i, g_j; g_k); \tag{10.3.13}$$

$$J_p(g_i, g_j; g_k) = \sum_{g_l \in S_Q} W_p(g_i^{-1} g_l) W_p(g_j^{-1} g_l) \mathrm{Wg}_{d^2}(g_l^{-1} g_k),$$

where Wg_{d^2} is the Weingarten function that expresses the weight associated to the random unitary evolution. In other terms, we integrate out the contribution of the unitary evolution in order to obtain a reduced average over the random measurements only.

We remark that the factorizations Eqs.(10.3.10,10.3.13) only work if we want to calculate the average of operators local in time and space; however this is the case for the entanglement entropy.

In the large d limit we have [145]

$$J_p(g_i, g_j; g_k) = e^{-E_i(g_i^{-1} g_k)} e^{-E_j(g_j^{-1} g_k)}; \tag{10.3.14}$$

$$E_i(g) = -\ln\left((1 - p_i)\left(\delta_g + \frac{\delta_g'}{d}\right) + \theta_{p_i} p_i \right), \tag{10.3.15}$$

where θ_{p_i} is equal to 1 for Markovian regions $p_i > 0$ and equal to 0 for non-Markovian regions $p_i < 0$, and δ_g (δ_g') is one if g is the identity (a transposition) and zero otherwise.

Eq.(10.3.15) is the basis for our subsequent analysis. Given any decay rate $\Delta(t)$ we can compute the inhomogeneous couplings between different sites on the Potts model. This allows us to perform numerical Monte Carlo simulations as well as do a qualitative analysis of the effect of non-Markovianity on the entanglement transition.

In particular we know from the Markovian case that low p are associated to a ferromagnetic configurations of the Potts spins and to a volume law scaling of the entanglement, i.e. a linear dependence of $F_A - F_0$ with the size l_A of A. In fact, from Eq.(10.3.15) we observe that if spins are aligned (i.e. $g_i^{-1} g_k$ is the identity) the energy E_i vanishes while it is approximately $E_i = -\ln p$ when
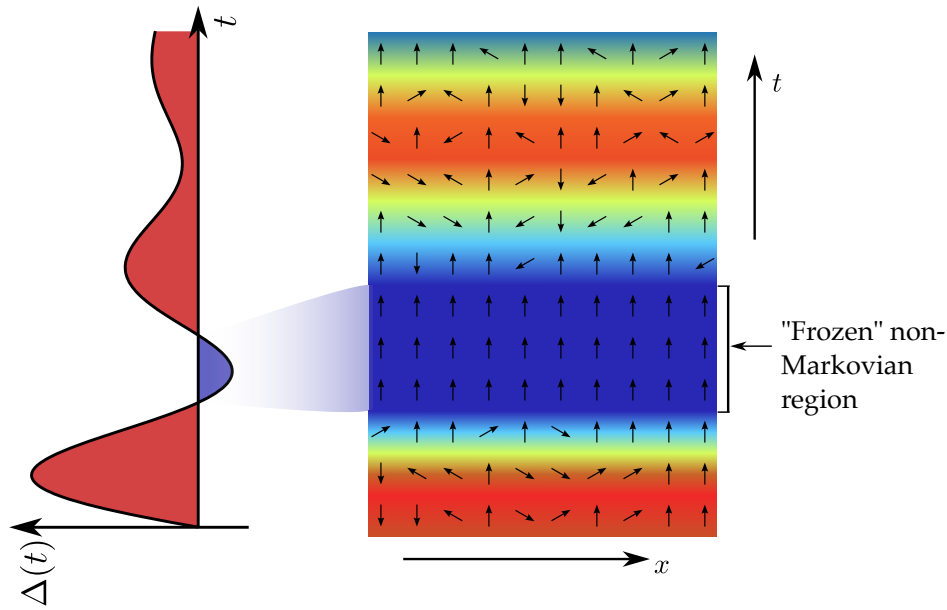
FIGURE 10.5: Sketch of the time-dependent rate $\Delta(t)$ with the non-Markovian region shaded in blue. This region corresponds to a ferromagnetic region in the Potts model, (shaded in blue on the right). The Markovian regions (shaded in red in the left plot) allow for paramagnetic regions in the Potts model, with neighboring spins not aligned.

they are different; thus, at low p, spins tend to align while at larger p paramagnetic configurations with the spins aligned in random directions are possible.

In the non-Markovian regions, the energy is $-\ln(1 - p_i) < 0$ for aligned spins and infinite otherwise (technically the energy is finite due to $\mathcal{O}(1/d^a)$ corrections, but still very large); therefore regions of non-Markovianity are essentially strips of "frozen" spins all aligned to each other (see Fig.(10.5)), which means that they favor a volume law entanglement. This is equivalent to saying that memory effects do in fact slow down the effect of noise, and strengthen the role of coherent dynamics.

Non-Markovian Monte Carlo – We now turn to the study of a prototypical non-Markovian system.

As already mentioned in Sec.(7.7), we will use the decay rate $\Delta(t)$ that originates from a bath whose spectral density is described by a Lorentzian centered around ω and with bandwidth Γ:

$$\Delta(t) = \Delta_0 \left[\frac{\Gamma}{\omega} + e^{-\Gamma t} \left(\sin(\omega t) - \frac{\Gamma}{\omega} \cos(\omega t) \right) \right]. \tag{10.3.16}$$

This is a good approximation of a system of qudits, where each qudit level couples through its occupation number to a cavity mode with detuning ω and bandwidth Γ.

The rate decays to $\Delta_0 \Gamma / \omega$ over a timescale $\sim 1/\Gamma$ and has minima at $\omega t = 3\pi/2 + 2\pi n$. The first (and lower) minimum is negative for $\Gamma/\omega < 0.274$, meaning that Γ sets the non-Markovianity of the dynamics.

The normalization constant Δ_0 depends on the interaction strength. We choose each discrete time step in the L_y direction to correspond to $\omega t = 1/2$. We then set Δ_0 so that the probability associated to the asymptotic value of $\Delta(t)$ is p

$$p_i = p \left[1 + e^{-\Gamma t_i} \left(\frac{\sin(\omega t_i)}{\Gamma/\omega} - \cos(\omega t_i) \right) \right]. \tag{10.3.17}$$
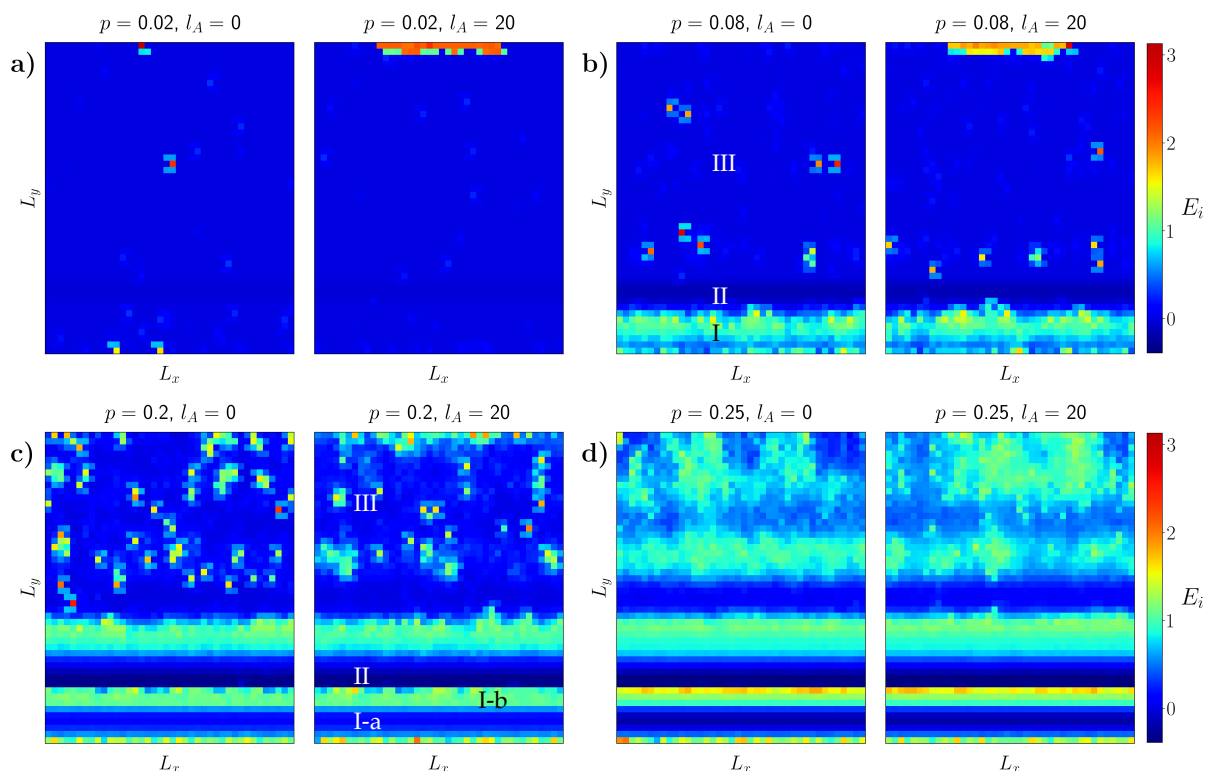
FIGURE 10.7: Colormap of the energy E_i of each spin. Each panel shows $l_A = 0$ or $l_A = 20$ for (a) $p = 0.1$, (b) $p = 0.3$, (c) $p = 0.4$, (d) $p = 1$. Lower energy corresponds to aligned spins, i.e. ferromagnetic regions, while larger energy corresponds to paramagnetic spins. The labels L_y in the vertical direction correspond to the time direction in the physical system. a) The system is completely ferromagnetic and the energy cost of having a boundary is clearly visible at the top of the right plot. b) The system is still ferromagnetic at later times (with the energy cost of the boundary still clearly visible) but small paramagnetic domains start to form at earlier times (when the peak value is $p_i \sim 0.3 \gtrsim p_{hom}^c$). c) The system is paramagnetic at early times since $p \sim 0.4 > p_{hom}^c$ contributing to the total energy, but the successive non-Markovian region is highly ferromagnetic and confines paramagnetism to early times. d) At late times $p_i \sim p_{hom}^c$, causing paramagnetic domains to appear after the non-Markovian region; the energy cost of the boundary is now small.

We remark that the value of p_i in Eq.(10.3.17) cannot be immediately mapped to the measurement probability p of the Markovian case. They can only be compared in a sensible way at large times, where p_i converges to a constant (and Markovian) measurement probability. We thus refrain from calling p_i explicitly a probability. However, the earlier times behavior of the non-Markovian p_i still affects the behavior of the system – as we shall see in detail – in a way that an analogy with the Markovian case cannot really be made.

We also note that depending on p and Γ/ω, p_i can exceed one for certain times. This may seem weird, but is mathematically correct and corresponds to a coupling that favors a paramagnetic phase, since it gives a zero energy for aligned spins and an energy $\sim -\ln p_i < 0$ for paramagnetic spins. This intuitively makes sense, since for very large p_i – i.e. very large decay rates – the system tends to be paramagnetic rather than ferromagnetic.

We perform Monte Carlo simulations for $\Gamma/\omega = 0.2$, which means the rate is negative for $3.77 < \omega t < 5.80$. Thus for a system with $L_y = 50$ spins and ωt_i this means that the spins with

$8 \leq i_y \leq 11$ have $p_i < 0$, i.e. experience a non-Markovian coupling. The non-Markovian region is indicated with the label II in Fig.(10.7).
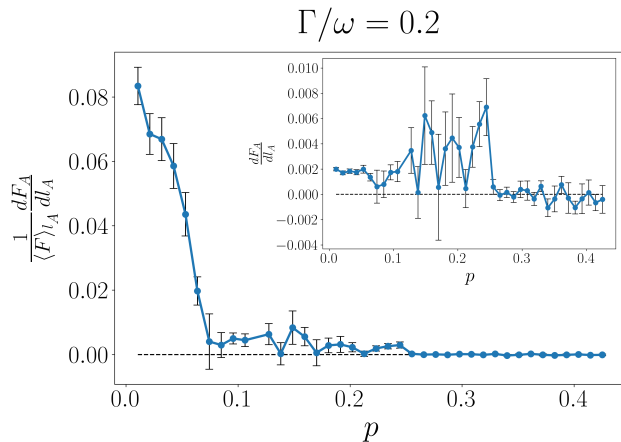
FIGURE 10.6: Behavior of the slope of the normalized energy $F_A/\langle F_A \rangle_{l_A}$ with respect to l_A as function of p. The inset shows the slope of F_A as function of p. The Monte Carlo calculations were performed for $\Gamma/\omega = 0.2$, $L_x = 40$, $L_y = 50$ and $l_A = 0, 2, 4, ..., 20$.

Our results are reported in Figs.(10.6,10.7). We can immediately observe several similarities and some differences with the Markovian case, shown on Figs.(9.3,9.4).

The normalized slope $\frac{1}{\langle F_A \rangle_{l_A}} \frac{dF_A}{dl_A}$ drops from very large values to smaller values (but non zero) around $p = p_{c1} \approx 0.08$; this corresponds to an increase of the fluctuations and of the slope $\frac{dF_A}{dl_A}$. For $p > p_{c2} \approx 0.25$ both slopes decrease to zero, signalling an entanglement phase transition from volume to area law.

The strange phase between p_{c1} and p_{c2} corresponds to an emergence of paramagnetic domains at earlier times, before the non-Markovian region, indicated by the label I in Fig.(10.7). Indeed, p_{c1} corresponds to a peak value in the I-a region approximately equal to $p_i \sim 0.4$, which is sufficient to turn paramagnetic the bottom region at early times, see Fig.(10.7b). Consequently the energy of the system increases, which explains the drop in $\frac{1}{\langle F_A \rangle_{l_A}} \frac{dF_A}{dl_A}$, and the system is more susceptible to different boundary conditions, thus explaining the increase in $\frac{dF_A}{dl_A}$. However, the value of p_i at later times (region III in Fig.(10.7)) is still too small to turn paramagnetic the top region, so that the system still exhibits a volume law behavior, as it is evident by the boundary energy cost in Fig.(10.7c).

For larger values $p \sim p_{c2}$ also the late times regions of the system start to turn paramagnetic, explaining the decrease of both slopes, see Fig.(10.6) and Fig.(10.7c). For p larger than p_{c2}, the entire system turns paramagnetic, except for the non-Markovian region which is constrained to be ferromagnetic, see Fig.(10.7d).

We also notice that for $p \gtrsim 0.15$ the region I at earlier times exhibits two energy subregions I-a and I-b, see Fig.(10.7c). These subregions are both paramagnetic, but I-a has a lower energy because p_i exhibits its peak in I-a; this large probability lowers the energy of the paramagnetic phase. In I-b, p_i decreases and eventually vanishes before becoming negative in region II; thus the energy of the paramagnetic phase increases as p_i decreases, explaining the different energy behavior inside of region I.

The phase between p_{c1} and p_{c2} is still volume law despite exhibiting large energy fluctuations. The width of this region is likely size dependent, since evolving the system for longer times would suppress the influence of the paramagnetic region (I) and of the non-Markovian region (II) at early times on the late times (III) region.

Indeed, the transition from volume law to area law is mostly determined by the late times values of p_i and only occurs at $p_{c2} \approx 0.25$, similarly to the Markovian transition. This confirms the intuition that the late times non-Markovian dynamics, when the rate is always positive $\Delta(t) > 0$, is equivalent to a Markovian dynamics.

An interesting result is that the volume law phase still survives even when the peak value of p_i becomes *significantly* larger than the Markovian critical probability. This occurs because while the peak p_i is large enough to turn paramagnetic the early times region (I), the successive non-Markovian region (II) is always ferromagnetic and shields the rest of the evolution from the effects of this large peak value.

We conclude that, while non-Markovianity does not affect the volume law phase at late times, when most of the dynamics has become Markovian, it stabilizes the volume law phase at early times and protects it from regions of strong measurements, provided they occur before the non-Markovian region.

We remark that while the numerical results obtained with our Monte Carlo simulations display fluctuations, especially near the transition, they still provide a qualitative (and somewhat quantitative) picture of the Markovian and non-Markovian transition. Precision can be improved by increasing the system size and the number of sampling steps, but this has a somehow high computational cost, particularly since we have to utilize boundary conditions that make Monte Carlo simulations slower compared to a system with periodic boundary conditions.

Chapter 11

Measurement induced transitions in non-Markovian free fermion ladders

In Sec.(10.3) we have analyzed the entanglement transition in system with a non-Markovian dissipative processes. We investigated the entanglement in random unitary circuits by unravelling the many-body dynamics and calculating analytically the effect of non-Markovianity on the probability of dissipative measurements. This study is a step forward in the field of transition induced by external baths, since most environments display memory effects and thus can be better described by a non-Markovian dynamics.

In this chapter we study the non-Markovian entanglement transition using a fundamentally different approach which can be better extended to many-body interacting systems. We reproduce a non-Markovian dynamics by considering two coupled fermionic chains: the first one is the system under cosideration, while the second one acts as a bath with a non-trivial dynamics. The bath chain is also subject to a Markovian dissipative dynamics; thanks to the bath internal dynamics, which introduces memory effects, the system chain is effectively subject to a non-Markovian dissipation. By including explicitly the bath in our analysis, we pay a price in doubling the degrees of freedom, but are able to numerically simulate the quantum trajectories of the dynamics of the system and bath chain, which is purely Markovian. This approach is akin to the techniques exploiting an auxiliary extension of the Hilbert space of the system [244, 245, 246, 247], which are also used in quantum thermodynamics under the name of super-bath approach [248, 249, 250].

More specifically, we consider a model of free fermions with next neighbors hopping within each chain and inter-chain hopping, see Fig.(11.1a). We assume the dissipative dynamics on the bath chain to be given by local projective measurements of the particle number. Both unitary and dissipative dynamics preserve the Gaussianity of the state of the system, thus allowing to express all the relevant observables in terms of two-point correlation functions and to perform efficient numerical simulations up to system sizes of hundreds of sites [251, 252, 165, 169, 253, 224, 162].

We study the evolution of both chains until a steady state is reached, and then integrate out the bath chain, resulting in an effective non-Markovian dynamics for the remaining chain, see Fig.(11.1b). We then consider suitable partitions of the system chain and compute the average over the quantum trajectories of entanglement witnessing operators, such as entropy, mutual information [139, 162, 254] and negativity [178, 255]. Relative to what is shown in Sec.(9.2) based on [169], in the current situation the U(1) symmetry is absent in the inner chain and thus the scaling of entanglement is not bound to be an area-law [186].

For example, we find that even in the extreme regime in which the bath chain is always subject to measurements, the non-area-law phase still survives in the system chain. This is due to the coupling and internal hopping structure of the two chains: for example the coupling between the two chains can be weak enough that the system chain does not feel the measurements on the baths; or the hopping in the bath is good enough at scrambling information after measurements, so that entanglement loss in the system is very small.

We study the size scaling of entanglement entropy in the non-area-law phase, and find that it exhibits a logarithmic scaling compatible with a conformal field theory phase. At larger values of the bath chain hopping we observe linear corrections, which are likely due to a finite size effect and not an indicator of a volume law phase. In fact, an analysis of the mutual information indicates the presence of long-range correlations for all values of the bath chain hopping, which is not compatible with a volume law phase.

We also study the regime where the measurement probability is smaller than one. This case is fundamentally different, as the system chain is always in a mixed state. Thus the entropy and the mutual information are no longer good observables to study entanglement, as they also track classical correlations. We thus employ the fermionic negativity [223, 224, 225] to perform an analysis of the phase transition as function of the measurement probability. We find that the area law disappears for sufficiently weak measurements, and that the non-area-law phase exhibits a scaling behavior qualitatively similar to that of the entanglement entropy, with a mixture of linear and logarithmic contributions. Since in this case the negativity is the only observable at our disposal, we cannot attribute in a definitive way its scaling behavior to one scaling or the other (even if, in certain regimes, a volume scaling appears considerably more likely).

We then study how much the dynamics of the system is non-Markovian using already tested non-Markovianity measures [193, 192, 256, 257, 189, 258, 259, 260, 261, 262, 195, 191]. This analysis is quite complex to perform as we need to use exact diagonalization techniques and simulate the dynamics many times, and thus the maximum system sizes that we can consider are limited. We find that the dynamics is non-Markovian in all the regions of the phase diagram as a function of the system and bath parameters, and that the degree of non-Markovianity changes and displays a pattern similar to that of the entanglement phase. In particular, we observe that a stronger degree of non-Markovianity is associated to a larger entanglement within the system.

11.1   The model

Our goal is to study a model whose partitioning into a bath component and a system component can give us insights into the non-Markovian dynamics of the system component. We focus on a model of two coupled chains of free and spinless fermions, with an approach that may be reminiscent of those based on doubling the Hilbert space for non-Markovian systems [244, 245, 246, 247]. We consider periodic boundary conditions so that the geometry is that of a circular ladder. The legs of the ladder are the intrachain hoppings, while the rungs represent the interchain coupling, as shown in Fig.(11.1a). The outer chain is the bath, while the inner chain is the system under study.

The ladder is at half filling [1] and evolves with a stroboscopic dynamics of time period τ_u. Each cycle is constituted by a unitary evolution that lasts for the entire period τ_u and is governed by the Hamiltonian $\hat{H}$, and by projective measurements of the particle occupation on the outer chain, that occur at the end of the cycle. This simulates a non-Markovian dissipation when the degrees of freedom of the outer chain are traced out, pictorially represented on Fig.(11.1b).

The model Hamiltonian governing the unitary part of the evolution during time τ_u is

$$\hat{H} = \sum_{i,\sigma} t_\sigma \hat{c}^\dagger_{i,\sigma} \hat{c}_{i+1,\sigma} + t_{12} \sum_{i=1}^{L} \hat{c}^\dagger_{i,1} \hat{c}_{i,2} + \text{h.c.}, \qquad (11.1.1)$$

where $\hat{c}^\dagger_{j,\sigma}, \hat{c}_{j,\sigma}$ are the fermionic creation and destruction operators on site j of chain $\sigma = 1, 2$. We impose periodic boundary conditions as $\hat{c}_{L+n,\sigma} = \hat{c}_{n,\sigma}$.

---

[1]Note that the total number of fermions in the ladder is conserved, but the number of fermions in each chain can change during the evolution.
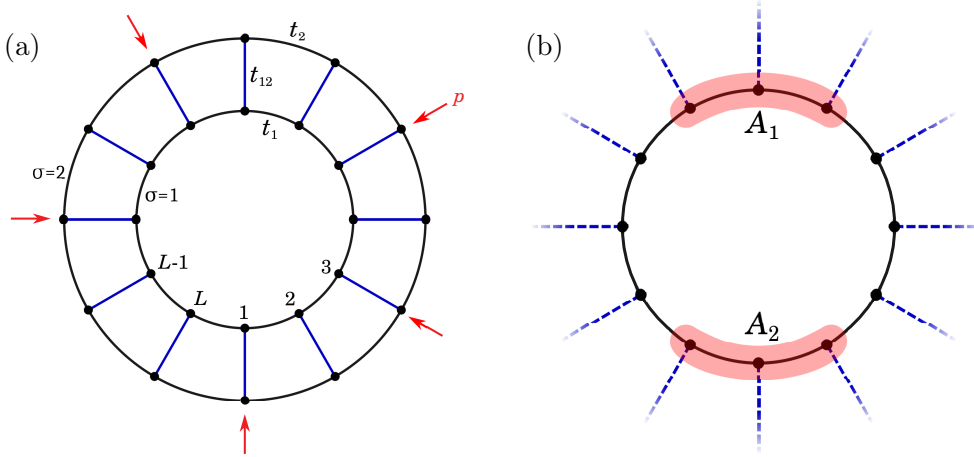
FIGURE 11.1: (a) A pictorial representation of a fermionic ladder with the periodic boundary conditions. The tunneling amplitude within the outer ($\sigma = 2$) and the inner chain ($\sigma = 1$) is t_2 and t_1, respectively. t_{12} is the inter-chain tunneling amplitude. The red arrows indicate the temporally and spatially random projective measurements of the particle occupation at the corresponding sites. p is the probability of performing such measurement. (b) After integrating out the degrees of freedom of the outer chain, the inner chain is partitioned into segments $\{A_j\}$. The residual correlations between outer and inner chain is pictorially represented by dashed blue lines. The size and location of $\{A_j\}$ segments can be arbitrary. Here we show a tri-partition of the inner chain into segments A_1, A_2 and the rest of the chain, labeled as B throughout the paper.

The Hamiltonian can be diagonalized in Fourier space, where it is written as

$$\hat{H} = \sum_k \hat{\psi}_k^\dagger H_k \hat{\psi}_k; \qquad H_k = \begin{pmatrix} 2t_1 \cos k & t_{12} \\ t_{12} & 2t_2 \cos k, \end{pmatrix} \tag{11.1.2}$$

with $\hat{\psi}_k \equiv \begin{pmatrix} \hat{c}_{k,1} \\ \hat{c}_{k,2} \end{pmatrix}$ and $\hat{c}_{k,\sigma} = \sum_j e^{-ijk} \hat{c}_{j,\sigma} / \sqrt{L}$.

The unitary evolution operator over one cycle factorizes as $\hat{U} = \bigotimes_k \hat{U}_k$, where $\hat{U}_k = e^{-i\tau_u H_k}$ is the evolution operator on the subspace with momentum k:

$$\hat{U}_k = e^{-it\cos k\tau_u} \left[\cos\left(\sqrt{t_{12}^2 + \delta^2 \cos^2 k}\,\tau_u\right) - i\frac{t_{12}\sigma^x + \delta\cos k\sigma^z}{\sqrt{t_{12}^2 + \delta^2 \cos^2 k}} \sin\left(\sqrt{t_{12}^2 + \delta^2 \cos^2 k}\,\tau_u\right) \right], \tag{11.1.3}$$

where $t = t_1 + t_2$ and $\delta = t_1 - t_2$. The identity and the Pauli matrices $\sigma^{x,z}$ operate in the chain index space. We work in the units of $\hbar = 1$ and fix $t_1 = 1$.

From Eq.11.1.3 we recognize the periodic structure of $\hat{U}_k$ in t_{12}. In particular, we see that only the term proportional to σ^x couples the two chains. Therefore when $t_{12} = 0$ the two chains are decoupled, as expected. This also occurs when $\sin\left(\sqrt{t_{12}^2 + \delta^2 \cos^2 k}\,\tau_u\right) = 0$, which in general cannot be satisfied at once for all values of k. However, when $\delta = 0$ (i.e. when the intrachain hoppings are equal), the decoupling condition reduces to $t_{12}\tau_u = n\pi$ showing the periodicity in t_{12} of the dynamics on the special line $t_2 = t_1$. For small values of δ around this special line, the two chains are "quasi-decoupled" for $t_{12}\tau_u \approx n\pi, n \in \mathbb{Z}$ in the sense that the off-diagonal matrix elements in $\hat{U}_k$ are very small for every k.

Since the Hamiltonian is quadratic, the Gaussianity of the state is intact during the unitary

evolution and Wick's theorem is applicable. After a time τ_u, the unitary evolution of the state $|\Psi(t)\rangle \to |\Psi(t+\tau_u)\rangle = \hat{U}|\Psi(t)\rangle$ is interrupted and the system interacts with a local measuring apparatus. The random local measurements occur within a very short time, so that they may be considered instantaneous. The local particle occupation number on the outer chain, i.e. $\hat{n}_{i,2} = \hat{c}^\dagger_{i,2}\hat{c}_{i,2}$, is randomly measured with probability p for each site of the outer chain.

In general, the projective measurements can spoil the Gaussianity of the state, however the type of the measurements that we consider does not [169]. This allows us to extract all relevant information regarding the state of the system from the two-point correlation matrix $\mathcal{D}_{ij,\sigma\sigma'}(t) = \langle\Psi(t)|\hat{c}^\dagger_{i,\sigma}\hat{c}_{j,\sigma'}|\Psi(t)\rangle$. During the measurement process, the correlation matrix changes according to the following protocol:

1. Extract a random number $p_l \in (0,1]$ for each site l in the top chain. If $p_l \le p$ then the measurement is performed, otherwise the site is left intact.

2. If the measurement has to be performed, extract a second random number $q_l \in (0,1]$.

3. If $q_l \le \mathcal{D}_{ll,22} = \langle c^\dagger_{l,2}c_{l,2}\rangle$, then the operator $\hat{n}_{l,2}$ is applied to the state $|\Psi\rangle \to \hat{n}_{l,2}|\Psi\rangle$ which results into the following change of the correlation matrix

$$\mathcal{D}_{ij,\sigma\sigma'} \to \mathcal{D}_{ij,\sigma\sigma'} + \delta_{il}\delta_{jl}\delta_{\sigma2}\delta_{\sigma'2} - \frac{\mathcal{D}_{il,\sigma2}\mathcal{D}_{lj,2\sigma'}}{\mathcal{D}_{ll,22}} \tag{11.1.4}$$

4. If $q_l \ge \mathcal{D}_{ll,22}$, then the operator $1 - \hat{n}_{l,2}$ is applied to the state which results into

$$\mathcal{D}_{ij,\sigma\sigma'} \to \mathcal{D}_{ij,\sigma\sigma'} - \delta_{il}\delta_{jl}\delta_{\sigma2}\delta_{\sigma'2} + \frac{(\delta_{il,\sigma2} - \mathcal{D}_{il,\sigma2})(\delta_{lj,2\sigma'} - \mathcal{D}_{lj,2\sigma'})}{(1 - \mathcal{D}_{ll,22})} \tag{11.1.5}$$

After the measurement process is complete, the cycle of unitary evolution and measurements is repeated for a number of times t_{st}.

11.2   Measurement induced transition

To investigate the properties of the entanglement transition, we unravel the dynamics of the system by using the quantum trajectory approach [196, 197, 198]. Along each quantum trajectory α the system evolves with a circuit operator $\hat{C}_\alpha$ given by the sequence of unitaries and measurement operations. Different trajectories α and α' differ from each other by the location and time of the measurements. We start from an initial state of the system $|\Psi(0)\rangle$ with a random distribution of particles and let the system evolve along some trajectory α. After reaching the steady state $|\Psi^\alpha(t_{st})\rangle = \hat{C}_\alpha|\Psi(0)\rangle$, we calculate the expectation value of some operator $\mathcal{O}$ on the αth trajectory as $\langle\mathcal{O}^{(\alpha)}\rangle_{t_{st}} = \langle\Psi(0)|\hat{C}^\dagger_\alpha\hat{\mathcal{O}}\hat{C}_\alpha|\Psi(0)\rangle$. For each trajectory, the corresponding observable is averaged over next m timesteps as

$$\langle\langle\mathcal{O}^{(\alpha)}\rangle\rangle_{t_{st}} = \frac{1}{m}\sum_{s=1}^m \langle\mathcal{O}^{(\alpha)}\rangle_{t_{st}+s\tau_u}. \tag{11.2.1}$$

This process is repeated for N_{traj} trajectories, yielding the steady state trajectory averaged value of operator $\mathcal{O}$

$$\overline{\mathcal{O}} = \frac{1}{N_{traj}}\sum_{\alpha=1}^{N_{traj}} \langle\langle\mathcal{O}^{(\alpha)}\rangle\rangle_{t_{st}}. \tag{11.2.2}$$

Throughout this paper, we drop the notation for additional averaging over t_{avg} times and fix $m = 5$ for all observables.

11.2.1 Regime of persistent measurements

We first consider the limiting case of persistent measurements, i.e. $p = 1$, which corresponds to always measuring every site of the outer chain. In such regime, the state of the inner chain is always pure, because at every round of measurements the state is separable as the product of the state on the outer chain and the state on the inner chain. Thus, upon tracing out the outer chain we obtain a pure state for the inner chain, and we can use the entanglement entropy as a true measure of entanglement within the inner chain, since it only carries quantum correlation and does not include any classical contribution. This is not true anymore in the $p < 1$ case, where the state is not separable, and after integrating out the outer chain degrees of freedom we obtain a mixed state for the inner chain.

Thus in this section, we employ the entanglement entropy and the mutual information as entanglement measures.

When calculating the bipartite entanglement entropy, we choose $A = A_1$ and $A_2 = \varnothing$ (see Fig.(11.1b)), and divide the system into A and its corresponding complement segment $\bar{A} = B$. The von Neumann entanglement entropy of subsystem A is defined as

$$\mathcal{S}_A = -\mathrm{Tr}\left(\rho_A \log \rho_A\right), \tag{11.2.3}$$

where $\rho_A = \mathrm{Tr}_B \rho_{A \cup B}$, Tr_B being the trace over the degrees of freedom of the complement subsystem B.

The Gaussianity of the state of the system allows us to extract the entanglement properties along some trajectory α at the steady state directly from $\mathcal{D}_{ij,\sigma\sigma'}^{(\alpha)} = \mathcal{D}_{ij,\sigma\sigma'}^{(\alpha)}(t_{st})$:

$$\mathcal{S}_A^{(\alpha)}(t_{st}) = -\sum_{\lambda_A^{(\alpha)}} \left[\lambda_A^{(\alpha)} \log \lambda_A^{(\alpha)} + \left(1 - \lambda_A^{(\alpha)}\right) \log \left(1 - \lambda_A^{(\alpha)}\right)\right] \tag{11.2.4}$$

where $\lambda_A^{(\alpha)}$ are the eigenvalues of the reduced correlation matrix $\mathrm{Tr}_B \mathcal{D}_{ij,\sigma\sigma'}^{(\alpha)}(t_{st})$. In Appendix (A) we study in detail the convergence of $\mathcal{S}_A^{(\alpha)}$ to the steady state as function of t_{st} for various system sizes.

The trajectory averaged steady state entanglement entropy is:

$$\overline{\mathcal{S}}_A = \frac{1}{N_{traj}} \sum_{\alpha=1}^{N_{traj}} \frac{1}{m} \sum_{s=1}^{m} \mathcal{S}_A^{(\alpha)}(t_{st} + s\tau_{\mathrm{u}}). \tag{11.2.5}$$

In Appendix (B) we study the convergence of $\overline{\mathcal{S}}_A$ as function of the number of trajectories for various system sizes. We find that convergence is typically achieved for $t_{st} = 100\tau_{\mathrm{u}}$ and $N_{traj} = 150$, so that we employ these values throughout the rest of the paper, unless stated otherwise. For simplicity, we set $\tau_{\mathrm{u}} = 1$ for the rest of the paper.

The mutual information between two subsystems A_1 and A_2 quantifies the correlations between them. It is defined as $\mathcal{I}_{A_1,A_2} = \mathcal{S}_{A_1} + \mathcal{S}_{A_2} - \mathcal{S}_A$, where $A = A_1 \cup A_2$. The quantity of interest is the trajectory averaged steady state mutual information:

$$\overline{\mathcal{I}}_{A_1,A_2} = \overline{\mathcal{S}}_{A_1} + \overline{\mathcal{S}}_{A_2} - \overline{\mathcal{S}}_A, \tag{11.2.6}$$

following the definition Eq.(11.2.5). Various known scaling forms of the entanglement entropy and of the mutual information are summarized in Tbl.(11.1).

	$\mathcal{S}_{L/2}(L) \sim$	$\mathcal{I}_{L/4}(L) \sim$	$\mathcal{I}_{L/8}(L) \sim$
Area-law	const> 0	0	0
CFT	$\log(L)$	const> 0	const> 0
Volume-law	L	$L^{1/3}$	0

TABLE 11.1: Known scaling behavior of the bipartite entanglement entropy $\mathcal{S}_{L/2}$, and of the mutual information $\mathcal{I}_{L/8}$ and $\mathcal{I}_{L/4}$ as function of L for the area-law phase, for the critical (CFT) phase and for the volume-law phase [140, 162, 254].
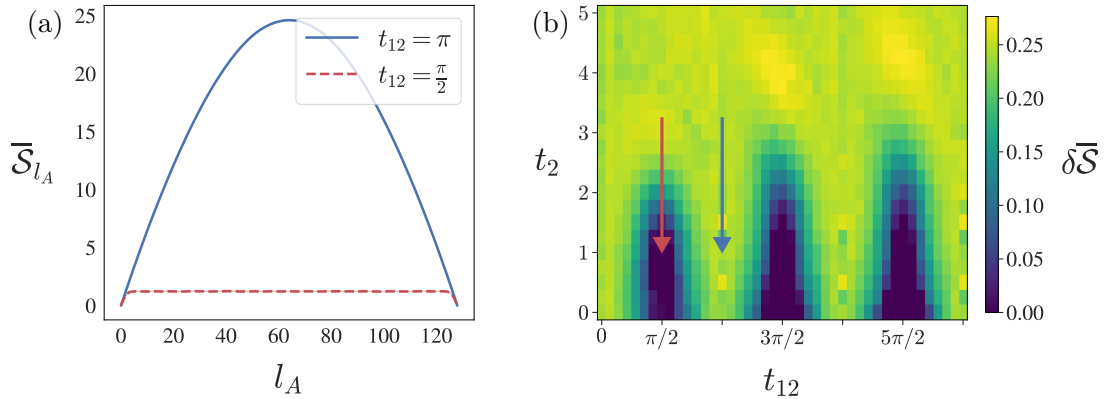
FIGURE 11.2: (a) Scaling of $\overline{\mathcal{S}}_{l_A}$ with respect to the partition size l_A, for $t_2 = 1$ and $L = 128$. Here the error bar obtained from the 95% confidence interval is smaller than the line width. (b) Colour plot of $\delta\overline{\mathcal{S}} = 1 - \overline{\mathcal{S}}_{L/4}/\overline{\mathcal{S}}_{L/2}$ as a function of t_{12} and t_2 with $L = 16$. The red and blue arrows correspond to the values of t_2 and t_{12} shown in panel (a), with the corresponding color labeling.

Entanglement Entropy

In this subsection we report the numerical results for the entanglement entropy.

Some of the features of $\overline{\mathcal{S}}_A$ can already be understood from the properties of Eq.(11.1.3). As already explained in Sec.(11.1), at the resonance $t_1 = t_2$, a shift of the transverse tunneling amplitude $t_{12} \to t_{12} + n\pi/\tau_u$ $(n \in Z)$ leaves the unitary evolution operator invariant (up to a sign)

$$\hat{U}_k\left(\delta = 0, t_{12} + \frac{n\pi}{\tau_u}\right) = (-1)^n \hat{U}_k\left(\delta = 0, t_{12}\right). \tag{11.2.7}$$

We expect the entanglement entropy of the system chain to have the same periodic behavior. The σ^x term in $\hat{U}_k$, Eq.(11.1.3), is responsible for mixing and entangling the degrees of freedom of the two chains; it vanishes for $t_{12} = n\pi$ and is maximum for $t_{12} = (n + 1/2)\pi$. When the two chains are decoupled, the entanglement in the inner chain grows thanks to the scrambling action of t_1 and is insensitive to the measurements in the outer chain. Hence, we expect the non-area-law phase to still persist in the vicinity of $t_{12} = n\pi$ and $t_1 = t_2$. On the contrary, for $t_{12} = \pi/2 + n\pi$ the coupling between the chains is maximum, increasing the sensitivity of the entanglement within the inner chain to measurements in the outer chain. In this regime, the area-law emerges.

These considerations are confirmed by the numerical simulations. We calculate the entanglement entropy $\overline{\mathcal{S}}_{l_A}$ as function of the partition size l_A, see Fig.(11.2a). In all figures, the error bar corresponds to a 95% confidence interval obtained from the distribution of $\mathcal{S}_{l_A}$ over trajectories (see Appendix B); if not visible, it is smaller compared to line width or symbols.

For $t_{12} = \pi/2$ we expect an area-law phase: the entanglement saturates quickly with l_A and shows a nearly flat behavior. On the other hand for $t_{12} = \pi$ we do not expect an area-law and in
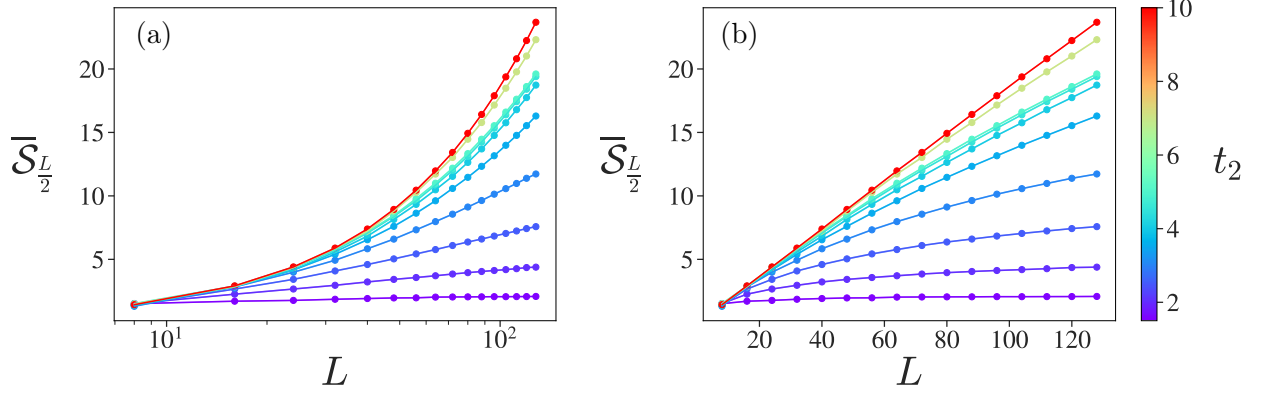
FIGURE 11.3: The trajectory averaged entanglement entropy for $l_A = L/2$, for various system sizes and tunneling amplitude t_2, with $t_{12} = \pi/2$ fixed, with logarithmic (a) and linear (b) scales

fact $\overline{\mathcal{S}}_{l_A}$ exhibits a dome shape reminiscent of volume law phases.

In Fig.(11.2b) we plot a colormap of $\delta\overline{\mathcal{S}} = 1 - \overline{\mathcal{S}}_{L/4}/\overline{\mathcal{S}}_{L/2}$ as function of t_{12} and t_2. This quantity vanishes when the entanglement obeys an area-law (because $\overline{\mathcal{S}}_{l_A}$ behaves constantly in l_A), while it is non zero for non-area-law phases, and is thus a good indicator to distinguish between the two phases. The periodical structure of area and non-area-law phases, due to the periodicity of Eq.(11.2.7), emerges in a very clear way in the colormap.

We now characterize more in detail the non-area law phase. In Tbl.(11.1) we report the scaling behaviors of the bipartite entanglement entropy $\overline{\mathcal{S}}_{L/2}$, and of the mutual information as function of the system size L, for different types of phases. These scaling behaviors can be used to probe the features of the non-area law phase and distinguish between volume-law scaling and critical (CFT) behavior (which has a logarithmic scaling).

We vary t_2 along the fixed line $t_{12} = \pi/2$, and study the scaling with L of $\overline{\mathcal{S}}_{L/2}$, which we report in Fig.(11.3). Based on Fig.(11.3), we see that the entropy exhibits different behaviors with changing t_2. In particular, $\overline{\mathcal{S}}_{L/2}$ displays a clear logarithmic scaling for $t_2 \sim 1.5 \div 3$, while its scaling seems more linear (i.e. volume law) in L for large t_2, see Fig.(11.3), respectively.

In order to quantify the different behaviors, we fit our results with the ansatz

$$\overline{\mathcal{S}}_{L/2} = \gamma L + \frac{c}{3}\log(L) + \beta \tag{11.2.8}$$

within a range $L_{\min} \leq L \leq L_{\max}$, for different ranges $[L_{\min}, L_{\max}]$. We calculate γ and c and compare $\gamma L_{\max}$ with $c/3 \ln L_{\max}$. We observe a crossover between the logarithmic contribution (dominant at small t_2) and the linear contribution, which dominates at larger t_2 but is very small below a threshold value of t_2. The detailed results and plots are reported in Appendix C. However, as we increase for $L_{\max}$, both the threshold for γ and the crossover value of t_2 increase, suggesting that the logarithmic scaling is the dominant contribution in the thermodynamic limit and that the presence of linear corrections is a finite size effect.

In order to assess whether this is an artifact of boundary effects from which the entanglement entropy suffers, we also consider the mutual information, where finite size effects are less prominent.

Mutual Information

In this subsection, we study the mutual information to further investigate the non-area regime.

We look at the behavior of $\overline{\mathcal{I}}_{L/4}$, i.e. the mutual information between diametrically opposing subsystems A_1 and A_2 with $l_{A_1} = l_{A_2} = L/4$, and plot its behavior in Fig.(11.4a). Comparing
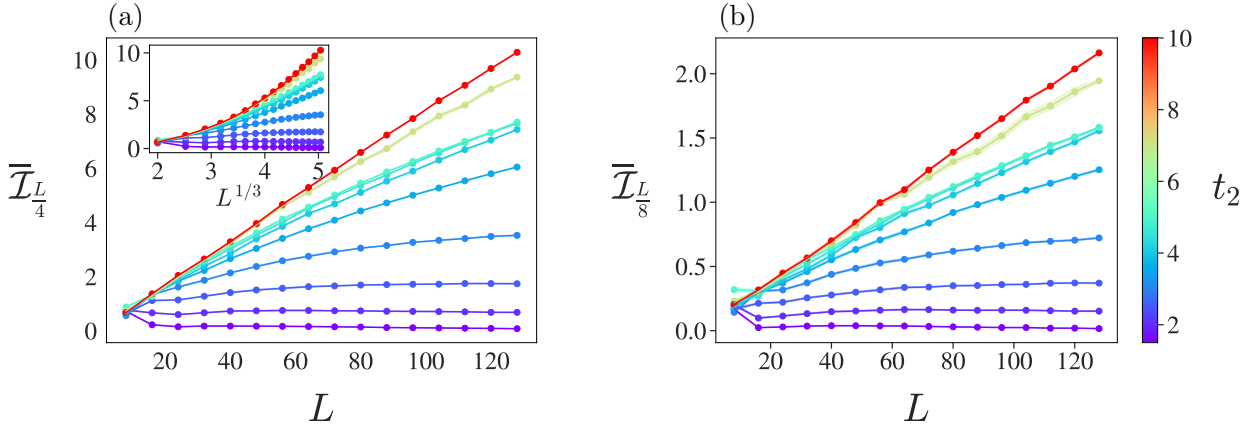
FIGURE 11.4: The trajectory averaged mutual information for various system sizes and t_2, for $l_A = l_B = l$, with $l = L/4$ for (a) and $l = L/8$ for (b), with fixed $t_{12} = \pi/2$. For the sake of comparison with expected volume law scaling, the inset on panel (a) shows the scaling of $\overline{\mathcal{I}}_{L/4}$ on $L^{1/3}$ scale.

Tbl.(11.1) and Fig.(11.4a), the behavior of $\overline{\mathcal{I}}_{L/4}$ is clearly consistent with an area law for $t_2 = 1.5$ and with a CFT phase for $t_2 \lesssim 3.0$. At larger t_2, $\overline{\mathcal{I}}_{L/4}$ does not saturate to a constant, but keeps increasing. This is compatible with a CFT phase for which the saturation size of $\overline{\mathcal{I}}_{L/4}$ is larger than the sizes we can access, but does not completely exclude a volume law phase for which $\overline{\mathcal{I}}_{L/4} \sim L^{1/3}$.

Another useful witness of a phase transition is the behavior of $\overline{\mathcal{I}}_{L/8}$, i.e. the mutual information between diametrically opposing subsystems A_1 and A_2 with $l_{A_1} = l_{A_2} = L/8$. $\overline{\mathcal{I}}_{L/8}$ vanishes in the area and volume law phases, and is enhanced at the critical point, due to long-range correlations developing between the subsystems [140, 143]. As shown in Fig.(11.4b), $\overline{\mathcal{I}}_{L/8}$ is very close to zero for $t_2 = 1.5$, indicating an area law. For $t_2 \lesssim 3.0$, $\overline{\mathcal{I}}_{L/8}$ saturates to a constant values, thus agreeing with the presence of a CFT phase. Similarly to $\overline{\mathcal{I}}_{L/4}$, the value of $\overline{\mathcal{I}}_{L/8}$ keeps increasing as t_2 gets larger. This is not compatible with a volume law phase, suggesting that also at large t_2 the system is in a CFT phase, but due to stronger finite size effects the entanglement entropy displays a linear scaling contribution and the mutual information saturates to values of L larger than the system sizes we can access.

In order to better discriminate the presence of an underlying CFT description of the phase, we study the dependence of the mutual information on the cross ratio η. Suppose that the system of fixed size L is bipartitioned into two subsystems of length l_A and l_B, with the boundaries of the l_A segment located at sites x_1 and x_2 and the boundaries of segment l_B located at x_3 and x_4. The cross ratio for such a bipartition is defined as $\eta = \frac{x_{12}x_{34}}{x_{13}x_{24}}$, with $x_{ij} = L/\pi \sin(\pi|x_i - x_j|/L)$. In a CFT regime, the mutual information collapses onto a single line and for small cross ratios shows a power-law growth, i.e. $\mathcal{I}(\eta) \sim \eta^\Delta$.

The inset in Fig.(11.5a) shows the behavior of the trajectory averaged steady state mutual information with respect to η for $L = 64$. The data points for $\eta \ll 1$ collapse onto a single line for $t_2 = 1.5$ and for $t_2 = 3.0$, but in the first case they show a larger spread.

In order to reduce the fluctuations due to the spread of the data points and perform a fit for Δ, we restrict our analysis to the special case of diametrically opposite segments $|A| = |B| \sim \sqrt{\eta}L$, for which $I_{A,B} \sim \eta^\Delta$. The fitted data for $L = 128$ in Fig.(11.5a) would suggest that the $t_2 = 3$ and $t_2 = 5$ regimes correspond to a CFT. We observe that for these regimes, the scaling exponent Δ is very close to 1. For $t_2 = 1.5$ the data points have larger deviation from the η^Δ curve at larger η, meaning that the fit for Δ is not very reliable. In order to obtain a more precise results in the latter case, computationally costly simulations with a larger number of trajectories are needed. By
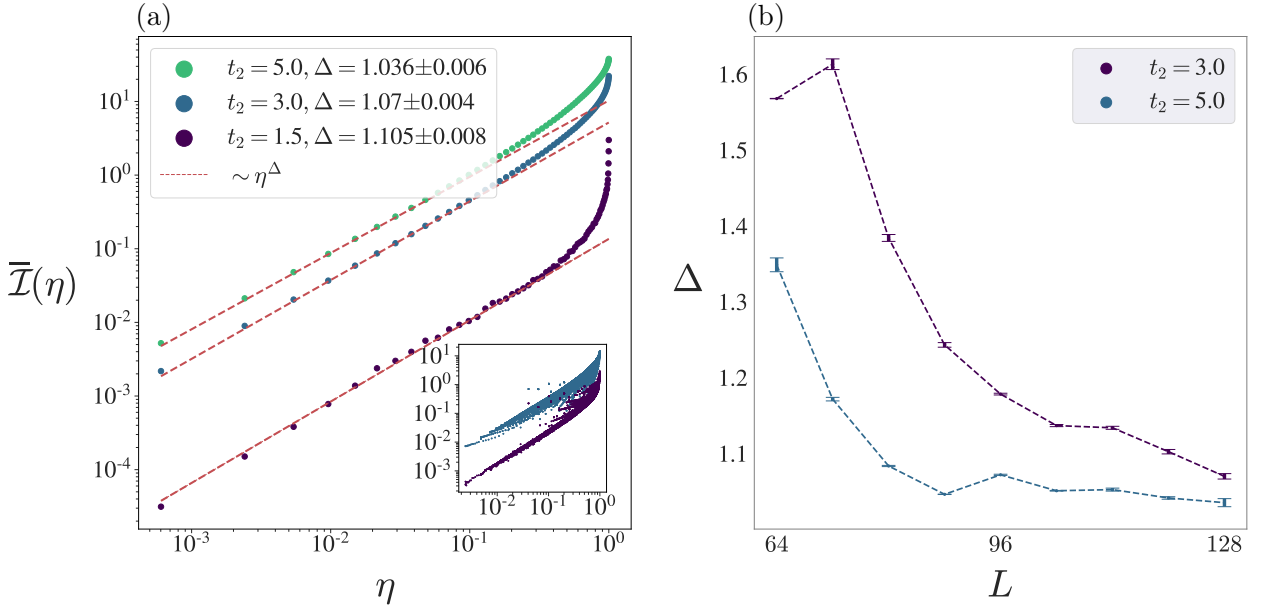
FIGURE 11.5: (a) Trajectory averaged mutual information with $L = 128$, with fixed $t_{12} = \pi/2$ and $t_2 = 1.5, 3$ and 5, for $l_A = l_B$ and $r_{AB} = L/2$. The red dashed lines correspond to $\sim \eta^\Delta$ fit along the data-points. The fitting curve is $I(\eta) = a(e^{b\eta^c} - 1)^d$, which for $\eta \ll 1$ reduces to $I(\eta) \approx ab^d\eta^{cd}$ and thus $\Delta = cd$. The inset shows the mutual information for $L = 64$, for every tripartitions, with $t_{12} = \pi/2$ and $t_2 = 1.5$ and 3. The collapse of the data points onto a single curve is evident for smaller values of η and $t_2 = 1.5$, while there is a significant spread at larger η or for $t_2 = 3$. (b) The scaling behavior of Δ exponent, for $t_{12} = \pi/2$ and $t_2 = 3$ and 5.

calculating Δ for various t_2 and system sizes Fig.(11.5b), we see that $\Delta \to 1$ for the regimes far away from the area-law phases ($t_2 = 3$ and 5).

Thus our analysis points to the presence of a CFT phase for all values of $t_2 \geq 1.5$. The linear scaling of the entanglement entropy at large t_2 seems to be a finite size effect, since the presence of a volume law phase is in contradiction with the large long-range correlations indicated by the large values of $\overline{\mathcal{I}}_{L/8}$. This behavior is reminiscent of what found in [162], where the entanglement entropy displays linear finite size corrections below a saturation size L that depends on the measurement rate.

However, without access to larger system sizes we cannot definitively exclude a volume law phase. We point out that for a single free fermion chain, the underlying unitary dynamics is expected to contribute logarithmically [152] – indeed the ground state of the unmonitored chain is a CFT phase – so that one would expect to observe an area-to-log transition. This is no longer guaranteed for a ladder, where the entanglement entropy within one leg may scale linearly with size.

We also remark that the presence of bigger long-range correlations at larger t_2 makes intuitively sense. In fact, when t_2 is large, information spreading in the outer chain is fast, meaning that a local measurement can still affect the neighboring sites, and the range of this effect increases with t_2. In other words, the time correlations between measurements due to the internal dynamics of the bath chain translate into space correlations at the level of the system chain. In a sense, this can be interpreted as non-Markovian effects inducing long-range correlations within the system chain.

11.2.2   Regime of sporadic measurements

For measurement probabilities that are smaller than one, the Von Neumann entropy and the mutual information are not valid measures of quantum entanglement, since they also include classical

correlations, given that the reduced state of the inner chain is now mixed.

To properly quantify the entanglement properties of the inner chain, we use the logarithmic fermionic negativity [223, 224, 225], not to be confused with the logarithmic negativity, which is used for systems of commuting particles. Negativity is an entanglement monotone for mixed states, whose bosonic version has already found use in the context of measurement induced transitions [178, 255].

Suppose the inner chain, described by the corresponding reduced density matrix ρ_{sys}, is further bipartitioned into A and B (as in Fig.(11.1a) with $A = A_1$ and $A_2 = \varnothing$). The logarithmic fermionic negativity $\mathcal{E}_A$ of subsystem A is defined as

$$\mathcal{E}_A = \log \text{Tr} |\rho_{\text{sys}}^{\tilde{T}_A}|, \tag{11.2.9}$$

with

$$\rho_{\text{sys}}^{\tilde{T}_A} = \rho_{\text{sys}}^{T_A} (-1)^{F_A}, \tag{11.2.10}$$

where $\rho_{\text{sys}}^{\tilde{T}_A}$ and $\rho_{\text{sys}}^{T_A}$ are the twisted and untwisted partial transpose of the reduced density matrix, respectively. Both operations are performed only on the A sub-system, leaving B intact. F_A is the number of fermions in the sub-system A.

Thanks to the Gaussianity of the state, the fermionic logarithmic negativity can be extracted from the correlation matrix $\mathcal{D}$ [263, 264]. Since in our model $\langle c_{j,\sigma}^\dagger c_{j',\sigma'}^\dagger \rangle = 0$ for all times, the computation of the negativity is simpler than in Ref. [223] and the passage to the Majorana fermions can be avoided. Given a reduced correlation matrix $\mathcal{D}_{\text{sys}}$ of an entire inner chain, we define $(\Gamma_{\text{sys}})_{ij,\sigma\sigma'} = 2(\mathcal{D}_{\text{sys}})_{ij,\sigma\sigma'} - \delta_{ij}\delta_{\sigma\sigma'}$. For a bipartition of the inner chain to A and B, the $(\Gamma_{\text{sys}})_{ij,\sigma\sigma'}$ matrix is expressed as

$$\Gamma_{\text{sys}} = \begin{pmatrix} \Gamma_{AA} & \Gamma_{AB} \\ \Gamma_{BA} & \Gamma_{BB} \end{pmatrix}, \tag{11.2.11}$$

where each block corresponds to the correlations between the segments indicated in the subscript. From the block structure of Γ_{sys}, we introduce the transformed matrices

$$\Gamma_\pm = \begin{pmatrix} \Gamma_{AA} & \pm i\Gamma_{AB} \\ \pm i\Gamma_{BA} & -\Gamma_{BB} \end{pmatrix} \tag{11.2.12}$$

and

$$\Gamma_* = \frac{1}{2} \left[1 - (1 + \Gamma_+\Gamma_-)^{-1}(\Gamma_+ + \Gamma_-) \right]. \tag{11.2.13}$$

Using these matrices, the calculation of the Fermionic negativity is straightforward

$$\mathcal{E}_{A_1} = \sum_j \left[\ln \left(\sqrt{\mu_j} + \sqrt{1 - \mu_j} \right) + \frac{1}{2} \ln \left(1 - 2\lambda_j + 2\lambda_j^2 \right) \right], \tag{11.2.14}$$

where μ_j and λ_j are the eigenvalues of Γ_* and $\mathcal{D}_{\text{sys}}$, respectively.

We calculate the logarithmic fermionic negativity for the steady state and average it over different trajectories, yielding $\overline{\mathcal{E}}_A$.

We have analyzed the scaling properties of the fermionic negativity, for fixed system size $L = 64$ and different values of p and t_2, shown in Fig.(11.6). Figure (11.6a) corresponds to the fine-tuned resonance regime $t_2 = 1$ and $t_{12} = \pi/2$. The peak of the negativity at $l_A = L/2$ is reduced as the measurement probability p increases and the curve is progressively flattened out. This behaviour is expected, since for $t_1 = t_2$ and $t_{12} = \pi/2$ the two chains exhibit maximum coupling and thus, the entanglement content within the inner chain is reduced when the outer chain is frequently measured. The flattening of $\overline{\mathcal{E}}_{l_A}$ for larger p indicates the onset of the area-law regime.
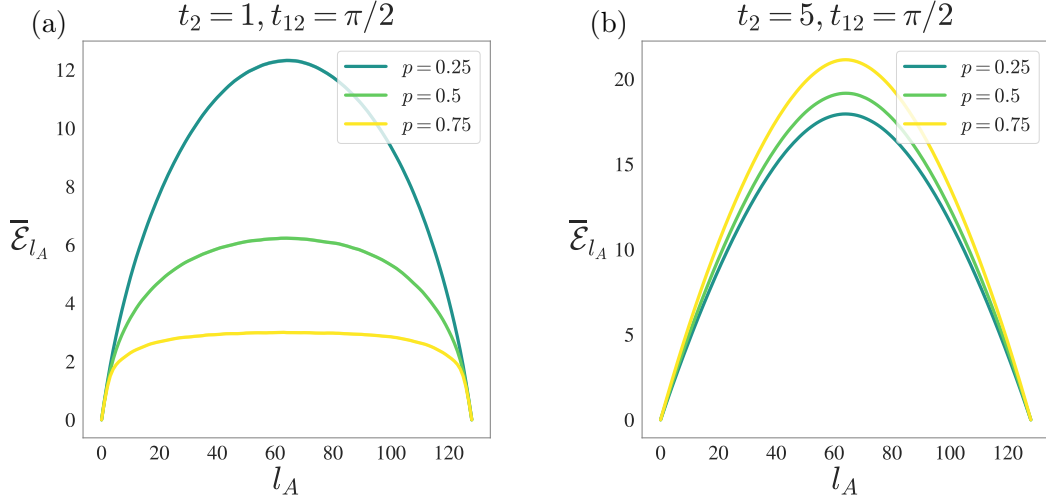
FIGURE 11.6: Figures show the scaling of $\overline{\mathcal{E}}_{l_A}$ with respect to l_A with $L = 64$, for various values of p.

Figure (11.6b) corresponds to the case of parameters far away from the resonant regime. Contrary to the previous case, now the peak of the negativity becomes larger as p increases. This surprisingly counterintuitive behavior can be explained in terms of entanglement monogamy [230, 231, 232]. The relatively large value of t_2 quickly spreads the entanglement throughout the outer chain, before the next measurement occurs, while the coupling between the degrees of freedom of the inner and outer chains, is maximal. For low measurement probability, more entanglement is spread within the outer chain and between the outer chain and the inner chain, leaving less entanglement available to be distributed within two partitions of the inner chain, which thus shows a lower value of the fermionic negativity. This occurs because the total amount of entanglement that can be shared within a tripartite system (in our case the outer chain and two partitions of the inner chain) is limited, so that the more information two subsystems share with the third subsystems, the less information they will share after tracing it out. Conversely for large p, the entanglement between the two chains is smaller due to frequent measurements. This means less information is discarded when performing the partial trace over the outer chain, and more entanglement content is shared within the inner chain.

Similarly to what was done for the entanglement entropy in Fig.(11.2), we extract the phase diagram of the system for $p < 1$. We characterize the phases using $\delta\overline{\mathcal{E}} = 1 - \overline{\mathcal{E}}_{L/4}/\overline{\mathcal{E}}_{L/2}$ as function of t_{12} and t_2, and find that again a periodic structure of the phase diagram emerges Fig.(11.7). For smaller p, the faint remnants of the area-law lobes are still present. As p is increased, these lobes become more prominent and visible.

We then study the scaling of $\overline{\mathcal{E}}_{L/2}$ for various values of p and t_2, which shows different scaling properties. For $p = 0.75$ we clearly see an area law behavior at small t_2 and a logarithmic behavior at larger t_2; the area law at $t_2 = 1.5$ disappears for $p = 0.25$, in agreement with Fig.(11.7). We also observe that for large $t_2 \sim 5 \div 10$, the negativity exhibits a linear behavior at small sizes and a seemingly logarithmic behavior at large sizes $L \gtrsim 128$. To confirm this claim, we fit the data along $\overline{\mathcal{E}}_{L/2} = c/2\ln(L) + \gamma L + \beta$ [223] curve and extract the corresponding coefficients. Figures (11.8b,d,f) show the behavior of $\gamma L_{\max}$ and $c/2\ln(L_{\max})$ for different fitting ranges (with $L_{\max}$ the maximum size of each range). The plot show that the logarithmic contribution clearly dominates for small t_2, while it is comparable with the linear term for large t_2; however, increasing the sizes in the fitting range, the logarithmic contribution increases faster than the linear one at all values of t_2. This suggests that the linear contribution is a finite size effect, which is stronger at small L and large t_2 but becomes negligible as larger and larger system sizes are considered. This behavior
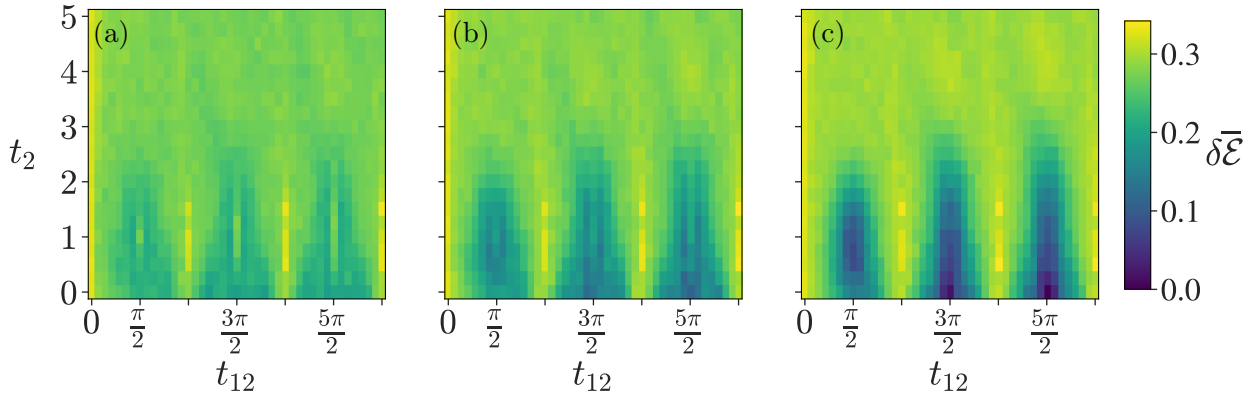
FIGURE 11.7: Color-maps of the negativity difference $\delta\overline{\mathcal{E}} = 1 - \overline{\mathcal{E}}_{L/4}/\overline{\mathcal{E}}_{L/2}$ for $L = 16$, with $p = 0.25$ in panel (a), $p = 0.5$ in panel (b) and $p = 0.75$ in panel (c).

is qualitatively similar to what we found for the $p = 1$ case, confirming the rich variety of phases present in this model.

The trend of the logarithmic and linear contributions with the range of the fit and an analogy with the behavior of the entanglement entropy, suggest that the linear contribution at large t_2 is due to finite size effects. However we cannot make a definitive claim and exclude completely a volume law phase, since we only have the negativity at our disposal to quantify the entanglement, and cannot cross-check it with a second observable such as the mutual information for the $p = 1$ case.

11.3   Quantifying the non-Markovianity of the dynamics

In this Section we assess how non-Markovian the dynamics of the inner chain is, and we show that the model we study is indeed a good platform to simulate non-Markovian systems.

In order to quantify the degree of non-Markovianity, we use the measure $\mathcal{N}(\mathcal{W})$ defined in Ref. [192], where $\mathcal{W}$ is a dynamical map acting in the space of density matrices such that $\mathcal{W} : \rho(0) \to \rho(t) = \mathcal{W}(t)\rho(0)$. Here $\mathcal{W}$ may represent for example the map generated by a master equation $\dot{\rho} = \mathcal{L}\rho$, such that $\mathcal{W}(t) = e^{\mathcal{L}t}$.

We measure the degree of non-Markovianity by tracking the temporal change of the trace distance, introduced in Sec.(7.7). The calculation of $\mathcal{N}(\mathcal{W})$ is demanding, since it involves calculating the distance between density matrices, and the Gaussian state formalism employed in the previous sections cannot be applied. Moreover, calculating the maximum over the pairs of initial density matrices, means sampling a space whose dimension scales exponentially with the size of the system.

We use exact diagonalization (ED) techniques to numerically simulate the dynamics of the model defined in Sec.(11.1). We calculate the evolution of the total density matrix of the two chains according to the Lindblad master equation that results from averaging over trajectories Eqs.(11.1.3-11.1.5). Since we already calculate the average dynamics, we do not need to perform the evolution over different trajectories and then average. We choose $L = 4$ and for each time step we trace out the outer chain in order to obtain the density matrix of the inner chain as function of time. We sample over a number of pairs of random initial density matrices $N_{\text{pairs}} \sim 100$. This sampling is the largest source of fluctuations in our simulations: especially for small values of non-Markovianity, the number of initial pairs that we need to sample to get a non zero value is rather large – as it scales exponentially with the size of the system.

Our results are reported in Figs.(11.9,11.10). In Fig.(11.9) we plot the color maps of $\mathcal{N}(\mathcal{W})$ and $\mathcal{N}_{\text{norm}}(\mathcal{W})$ as function of t_2 and t_{12} for $p = 1$. Here we have defined the normalized non-Markovianity
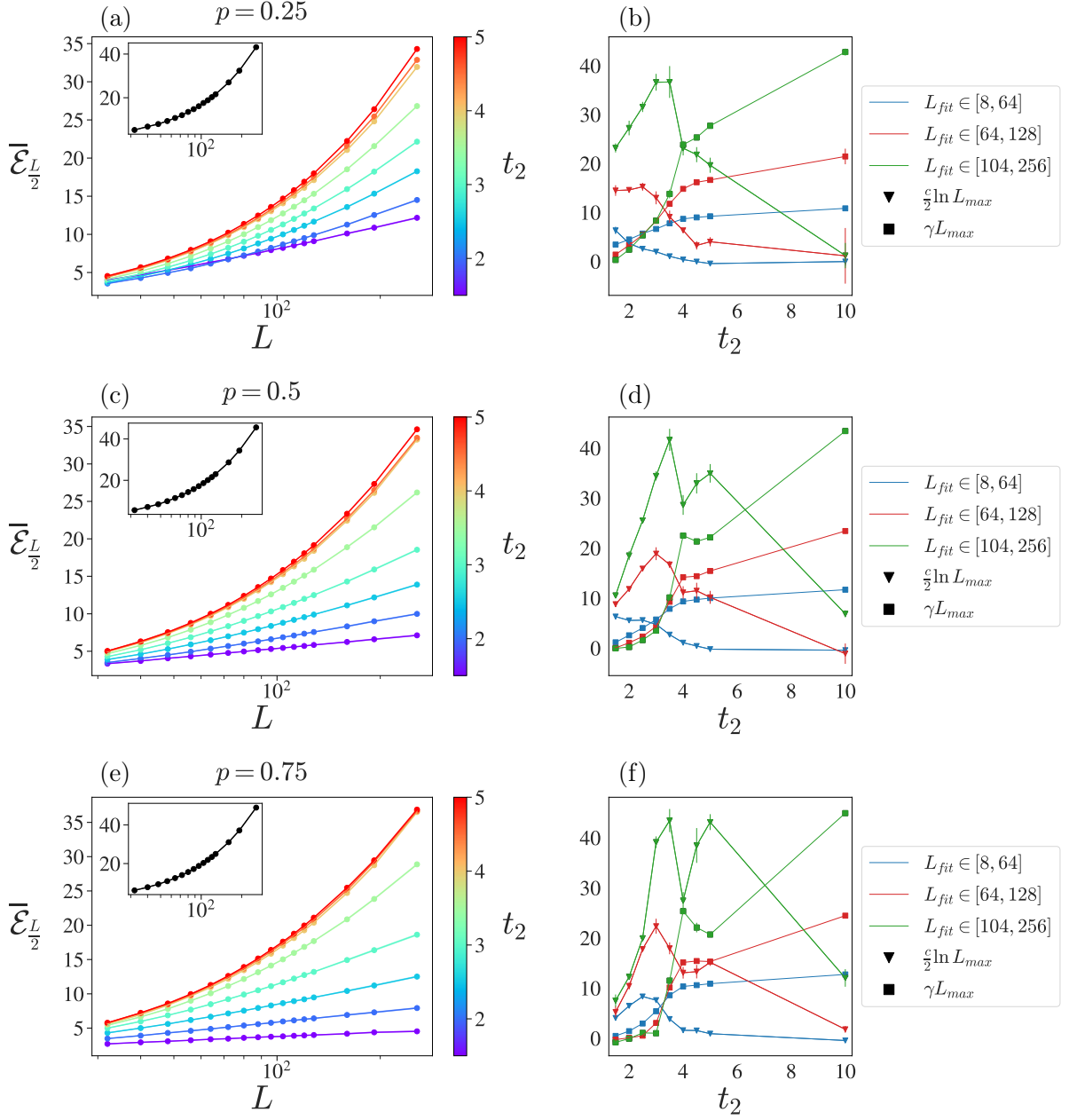
FIGURE 11.8: Panels (a,c,e) correspond to the trajectory averaged fermionic negativity for $l_A = L/2$, for various system sizes, tunneling amplitude t_2 and measurement probability p. The value of the inter-chain tunneling amplitude is fixed to $t_{12} = \pi/2$. The insets correspond to $t_2 = 10$ regime. Panels (b,d,f) are the plots of γL_{max} and $c/2 \ln(L_{max})$ versus t_2 tunneling amplitudes. The points is extracted from fitting the data along $\overline{\mathcal{E}}_{L/2} = c/2 \ln(L) + \gamma L + \beta$ curve.

measure $\mathcal{N}_{\text{norm}}(\mathcal{W})$ by dividing the integral over the regions of non-Markovianity with the integral over time of $|\sigma|$ and then maximizing over the pairs of initial density matrices, i.e.

$$\mathcal{N}_{\text{norm}}(\mathcal{W}) = \max_{\rho_{1,2}(0)} \frac{\int_{\sigma_{\mathcal{W}} > 0} dt \sigma_{\mathcal{W}}(t, \rho_{1,2}(0))}{\int dt |\sigma_{\mathcal{W}}(t, \rho_{1,2}(0))|} \tag{11.3.1}$$

The integral of $|\sigma|$ is typically of order one, so that $\mathcal{N}(\mathcal{W})$ and $\mathcal{N}_{\text{norm}}(\mathcal{W})$ have usually the same
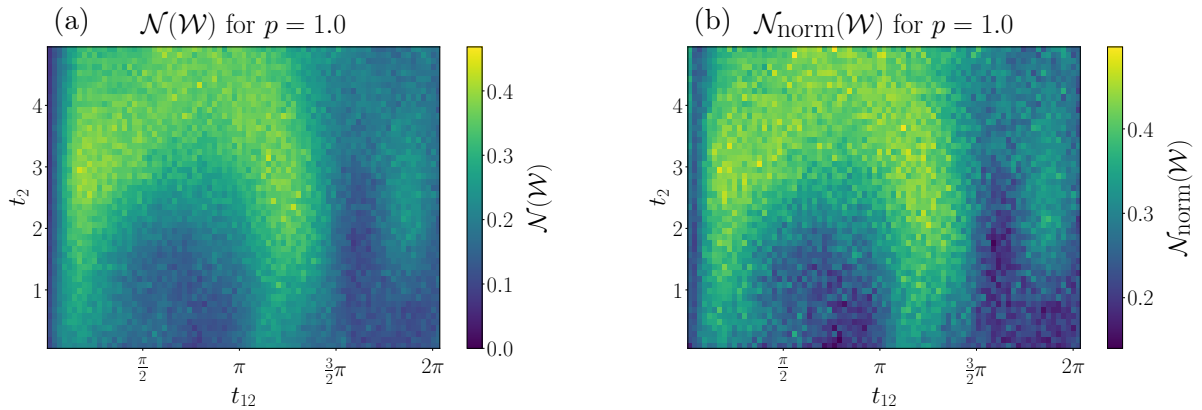
FIGURE 11.9: (a) Colormap of the non-Markovianity measure $\mathcal{N}(\mathcal{W})$ for the process defined by the map $\mathcal{W}(t)$, as function of t_2 and t_{12} for probability measurement $p = 1$ and for system size $L = 4$. (b) Colormap of the normalized non-Markovianity measure $\mathcal{N}_{\mathrm{norm}}(\mathcal{W})$ calculated for the same parameters of (a).
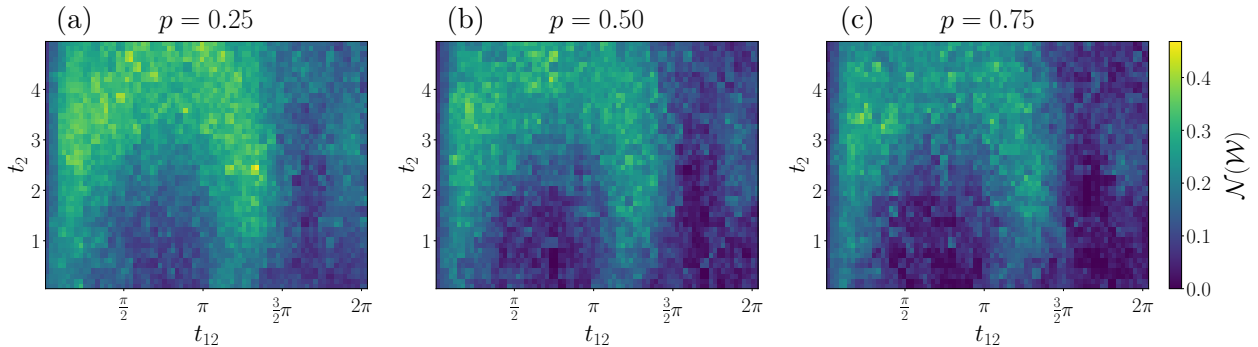
FIGURE 11.10: Colormap of the non-Markovianity measure $\mathcal{N}(\mathcal{W})$, as function of t_2 and t_{12}, calculated for system size $L = 4$ and for measurement probabilities $p = 0.25$ (a), $p = 0.5$ (b), $p = 0.75$ (c). The color scale is the same as Fig.(11.9a).

order of magnitude. However, the normalized measure is still useful to identify non-Markovianity in regimes where the decay of the density matrix towards its equilibrium value is slow, such as in the small t_{12} regime, see Fig.(11.9b).

We find that the dynamics of the inner chain is always non-Markovian. The degree of non-Markovianity is not uniform in the t_{12}–t_2 plane, and $\mathcal{N}(\mathcal{W})$ exhibits a behavior similar to that of the entanglement entropy and of the negativity. Except for the region of very small t_{12}, where we expect $\mathcal{N}(\mathcal{W})$ to be small due to the weak interchain coupling, the regions of strong non-Markovianity coincide qualitatively with the regions of non-area-law entanglement, see Fig.(11.2). This makes intuitive sense; for example, at $p = 1$ one would always expect an area law, but for large t_2 this does not occur because the internal dynamics of the bath (outer chain) scrambles the effects of the measurements, meaning that there are strong non-Markovian effects [2]. This is indeed reflected in the behavior of $\mathcal{N}(\mathcal{W})$. The phase diagrams of Fig.(11.2) and Fig.(11.9) do not coincide exactly, since the periodicity of $\mathcal{N}(\mathcal{W})$ in t_{12} seems to be larger than π as found for entanglement. This is likely due to finite size effects, given the very small system size we use to calculate $\mathcal{N}(\mathcal{W})$.

We also calculate $\mathcal{N}(\mathcal{W})$ for $p = 0.25$, 0.5, 0.75, see Fig.(11.10). We do not find any qualitative difference with the $p = 1$ case. We observe that the degree of non-Markovianity is generally smaller for $p = 0.5$ and $p = 0.75$, while it increases again for $p = 0.25$. This non-monotonous behavior of

---

[2]We point out that this is not true for arbitrary large t_2; for $t_2 \to \infty$ one expects the dynamics of the bath to be so fast that it results in a Markovian behavior.
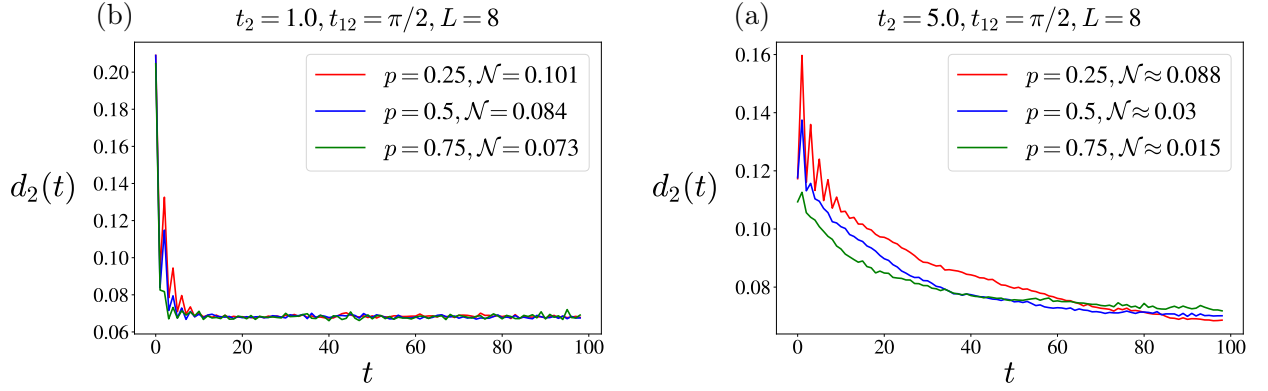
FIGURE 11.11: The time evolution of quadratic trace distance $d_2(\rho_1, \rho_2)$, for various values of t_2 and measurement probability p, with fixed $t_{12} = \pi/2$ and $L = 8$. The curves correspond to the pair initial conditions ρ_1 and ρ_2 that maximize the non-Markovianity measure $\mathcal{N}$.

$\mathcal{N}(\mathcal{W})$ as function of p is akin to what we found in Fig.(11.6b) because of entanglement monogamy. However, given the large fluctuations and the small system sizes of these simulations, we do not have enough accuracy to speculate further on the meaning of this result.

Note that we need to use ED techniques to calculate d since we cannot take advantage of the Gaussianity of the state. In fact the average density matrix $\rho(t)$ of the two chains is obtained as the average over trajectories of the pure (Gaussian) state density matrices

$$\rho(t) = \frac{1}{N_{traj}} \sum_\alpha |\psi(t)\rangle \langle \psi(t)|^{(\alpha)},$$

and Gaussianity is not an additive property so that $\rho(t)$ cannot be expressed as a Gaussian state. The same problem is encountered if the relative entropy $d_{\log}(\rho_1, \rho_2) \equiv \text{Tr}(\rho_1(\log \rho_1 - \log \rho_2))$ is used as trace distance, since $\log \rho_1$ cannot be written as a Gaussian state. On the other hand, one can take advantage of the Gaussianity of the state if the $\mathbb{L}_2$ quadratic trace distance [215] is used:

$$d_2(\rho_1, \rho_2) = \sqrt{\text{Tr}|\rho_1 - \rho_2|^2}. \tag{11.3.2}$$

In fact $\text{Tr}(\rho_1^2) = \text{Tr} \sum_{\alpha,\alpha'} |\psi_1\rangle \langle \psi_1|^{(\alpha)} |\psi_1\rangle \langle \psi_1|^{(\alpha')} / N_{traj}^2$, i.e. it is a double average of the product of two Gaussian states, which is still a Gaussian state whose trace can be calculated in terms of the two-points correlation matrix [251]. The same is true for ρ_2^2 and $\rho_1 \rho_2$, so that $\text{Tr}|\rho_1 - \rho_2|^2$ can be calculated from the behavior of the correlation matrix averaged twice over trajectories.

In order to evaluate the degree of non-Markovianity we will need to maximize it over different pairs of initial conditions ρ_1 and ρ_2, i.e.

$$\mathcal{N} = \max_{1,2} \int_{\partial_t d_2 > 0} dt \partial_t d_2(t). \tag{11.3.3}$$

Though the calculation of $d_2(\rho_1, \rho_2)$ from the two-point correlation function of the system $\mathcal{D}_{sys} = \text{Tr}_{\sigma=2} \mathcal{D}$ is straightforward, it comes with a large computational cost. In fact, while all the operations to be performed have a polynomial cost in the system size, there is a large overhead originating from the double average over trajectories, which is completely absent for ED numerics. Moreover, the calculation of the product of two Gaussian states in each of the terms of the double average, requires inverting the correlation matrices, an operation that becomes expensive when the system size increases. This actually makes calculations of $d_2(\rho_1, \rho_2)$ rather expensive for large system sizes.

Method	ED	Hybrid (Gaussian+ED)	Gaussian
Complexity	$a2^{6L}t_{st}N_{pairs}$	$((2L)^3 + 2^{6L})t_{st}N_{traj}N_{pairs}$	$(2L)^3 t_{st}N_{traj}N_{pairs}$

TABLE 11.2: Scaling of the computational complexity to calculate $\mathcal{N}(\mathcal{W})$ for different methods. a is the number of matrix multiplication performed in one time step during the ED simulations (typically $a \sim 3$), t_{st} is the number of time steps, N_{pairs} is the number of different initial conditions and N_{traj} is the number of trajectories. 2^{6L} is the typical computational cost of the multiplication of the density matrix of a system of size $2L$.

For this reason, we have restricted ourselves with $L = 8$ system size, with $N_{pairs} \sim 300$ number of pairs of initial conditions and $N_{traj} = 50$ trajectories per initial condition. The total running time for a single trajectory is fixed to $T_{max} = 100$ time-steps.

We present the results in Fig.(11.11), where the non-Markovianity of the dynamics (increasing trace distance) can be clearly seen. Similarly to ED simulations, for $t_2 = 5$ we observe that the degree of non-Markovianity is enhanced for smaller values of p. For a fine-tuned regime $t_2 = t_1 = 1$, the degree of non-Markovianity increases with increasing p. It should be noted, that the trace distance does not saturate to zero, likely due to small Hilbert space size of the model with $L = 8$. Moreover, we see that for $p = 0.5$ and $p = 0.75$, Fig.(11.11) shows that the degree of non-Markovianity is larger for $t_2 = 1$ and smaller for $t_2 = 5$, however the opposite trend is visible on Figs.(11.10b,c). These differences allows us to only conclude that the dynamics is always non-Markovian and do not allow us to make any further statements regarding the degree of non-Markovianity for various regimes of tunneling amplitudes $t_{2,12}$ and measurement probability p.

A third (hybrid) method that could be used consists in simulating the time evolution of the correlation matrix using Gaussian states, calculating the corresponding density matrix for each trajectory and time step, and averaging them over trajectories to obtain the average density matrix given a certain initial condition. However, this method results more costly than using only Gaussian states and performing all necessary calculations on the correlation matrices, since it involves calculating the exponential of a matrix of size $2^{2L} \times 2^{2L}$ which scales like a matrix multiplication and thus $\sim (2^{2L})^3$. A brief comparison of the computational complexity of each method is reported in Tbl.(11.2).
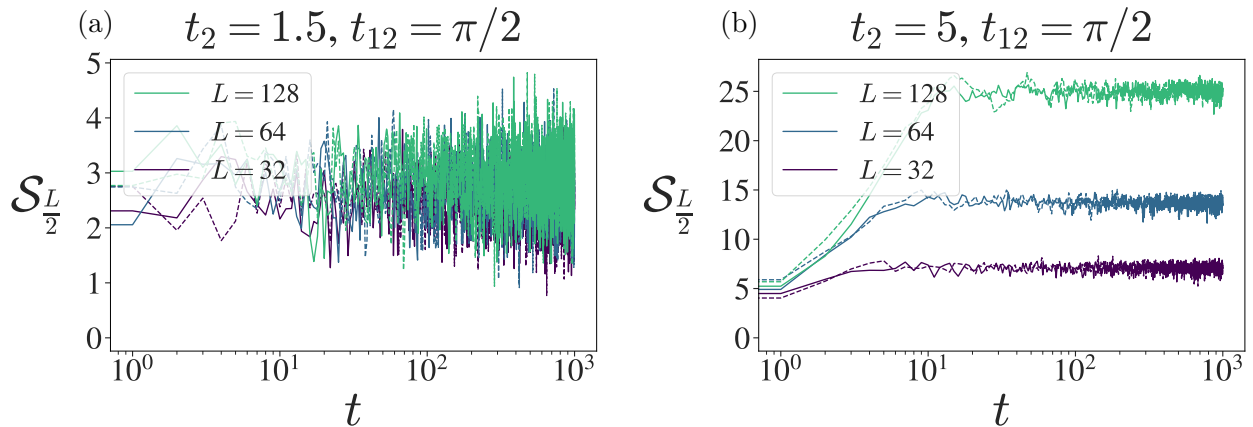
FIGURE 11.12: The time-scaling of entanglement entropy of A, with $l_A = L/2$. The solid and dashed lines correspond to random and Neel-like pure state initial conditions.

Appendix

A   Evolution towards the steady state for a single trajectory

In this section, we estimate the time it take for the system to reach the steady state along a single trajectory. After a transient regime of duration $\sim t_{st}$, an observable that evolves along a single trajectory converges to a steady state value around which it fluctuates. The magnitude of these fluctuations depend on the system size and model parameters, but we can typically truncate the evolution of the trajectory at $t = t_{st}$.

The time evolution of a single trajectory entanglement entropy for $l_A = L/2$ bipartition is shown on Fig.(11.12). The dashed and solid lines correspond to an initial pure state with Néel-like (i.e. antiferromagnetic fermionic populations) and random configuration of fermions, respectively. As seen on the figure, the dynamics of both initial conditions yield the same transient and stationary states. For this reason, all of the simulations are performed with random initial conditions, different for every trajectory. The figures show that larger systems take more time to reach the steady state, but for both $t_2 = 1.5$ and $t_2 = 5$, the saturation time for $S_{L/2}$ does not exceed 100 time-steps.

Fig.(11.13) shows the dynamics of a single trajectory mutual information, between regions A and B (with $l_A = l_B = L/8$) located opposite to each other, as in Fig.(11.1). Since the mutual information is a very non-linear function of the density matrix, it is more prone to fluctuations. In the vicinity of the area-law phase, the situation is qualitatively the same as for the entanglement entropy - the mutual information quickly reaches small but non-zero values and rapidly oscillates around it.

The time evolution of a single trajectory mutual information, between regions A and B, with $l_A = l_B = L/4$, is shown in Fig.(11.14). The picture is qualitatively the same as in Fig.(11.13). A difference we observe is that the values of mutual information for both $t_2 = 5$ and $t_2 = 1.5$ are reduced and stronger fluctuations are present. Also, for larger systems, the time it takes for the system to saturate to a steady state seems to exceed 100 time-steps.
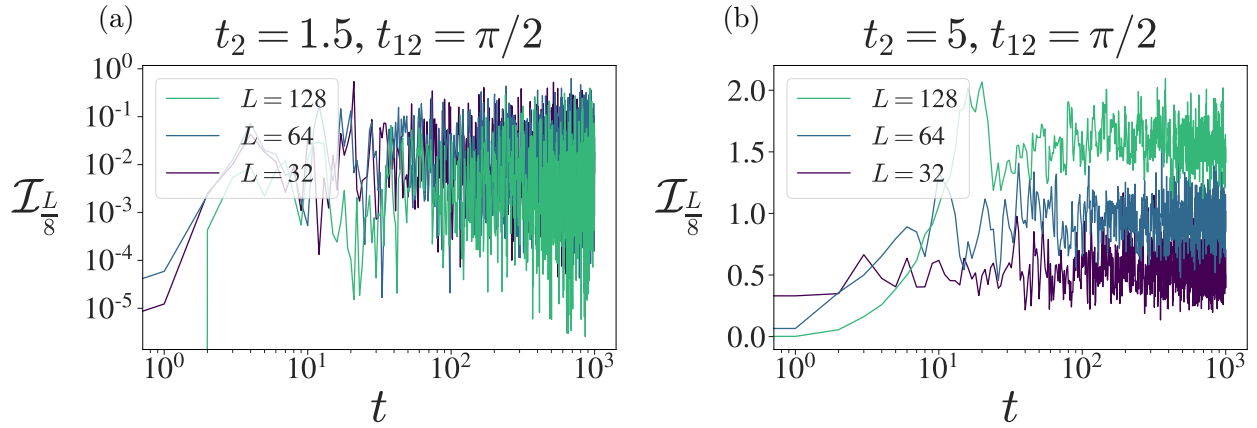
FIGURE 11.13: The time-scaling of mutual information between A and B, for $l_A = l_B = L/8$ and $r_{AB} = L/2$ distance between them.
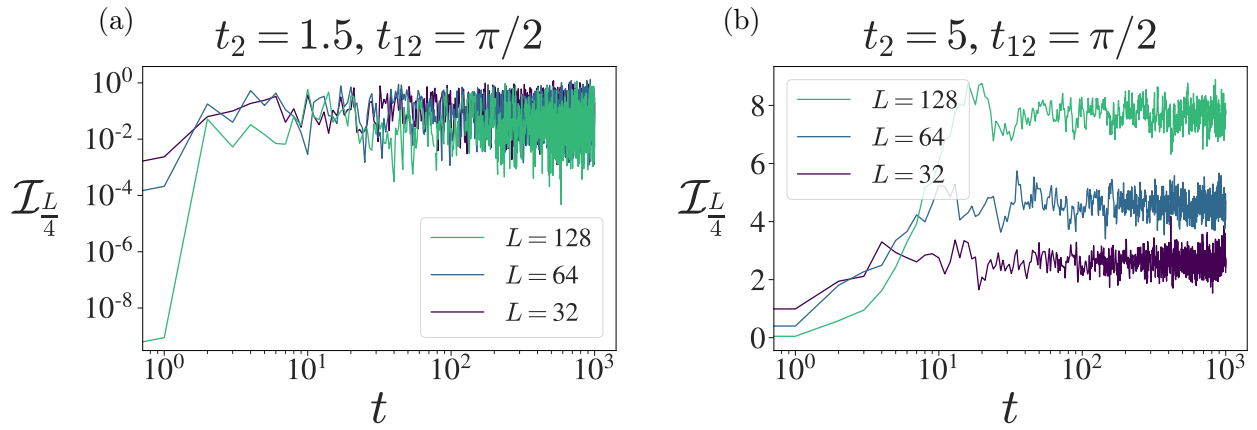
FIGURE 11.14: The time-scaling of mutual information between A and B, for $l_A = l_B = L/4$ and $r_{AB} = L/2$ distance between them.
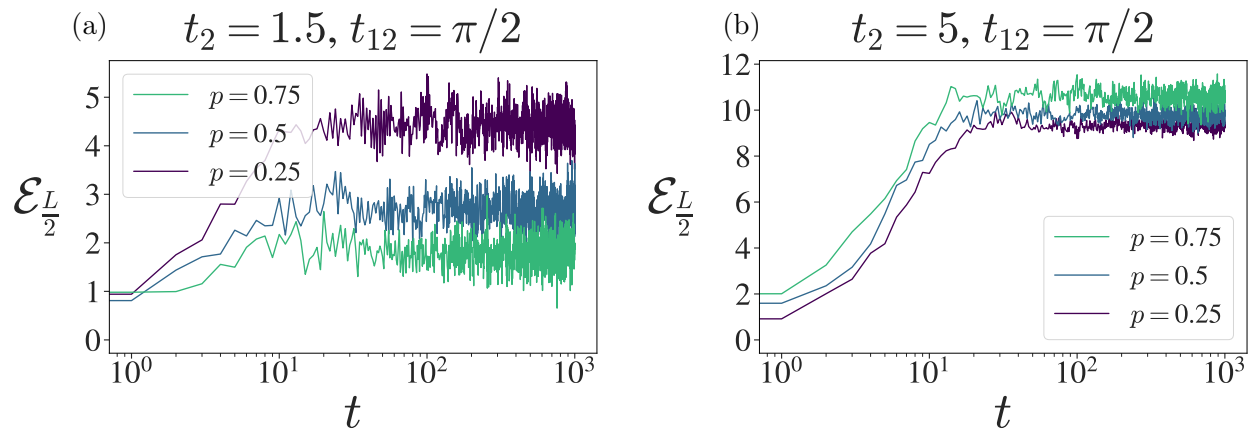
FIGURE 11.15: The time-scaling of bipartite negativity of A, with $l_A = L/2$.

Considering these results, we conclude that for $p = 1$, a safe estimate for the amount of time it takes to achieve convergence is $t_{st} = 100$ for small systems ($L \leq 64$) and $t_{st} = 1000$ for larger systems ($L > 64$).

In Fig.(11.15) we present the dynamics of the fermionic negativity for a single trajectory, for
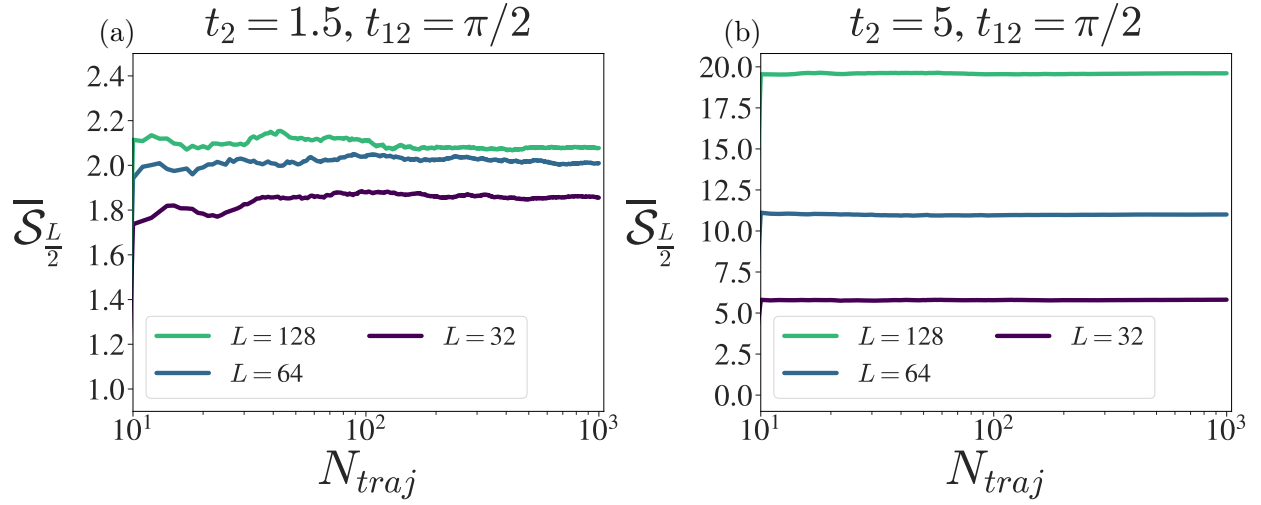
FIGURE 11.16: The figures (a) and (b) show the convergence of $\overline{\mathcal{S}}_{L/2}$ with respect to number of trajectories N_{traj}.

$l_A = L/2$ bipartition. The results correspond to a single fixed system size of $L = 128$ and $p = 0.25, 0.5, 0.75$ measurement probabilities. As explained in Sec.(11.2.2), the peculiar growth of fermionic negativity with respect to p for $t_2 = 5$ is already evident on a single trajectory level, Fig.(11.15b).

Based on these results, it is safe to fix $t_{st} = 100$ as the time when the system reaches the steady state.

B   The convergence of the ensemble averages with respect to the number of trajectories

In this section we study the convergence of the steady state value of an observables with respect to the number of trajectories N_{traj}, with $t_{st} = 100$ for $L \leq 64$ and $t_{st} = 1000$ for $L > 64$. Each trajectory has a different random initial condition.

Fig.(11.16) shows how $\overline{\mathcal{S}}_{L/2}$ converges with respect to N_{traj}. The solid lines represent the average value of the observable, while the shaded regions correspond to a 95% confidence interval calculated from the distribution of $\mathcal{S}_{L/2}$ over the quantum trajectories. The parameters are chosen to be $t_2 = 1.5$ and 5, with fixed $t_{12} = \pi/2$. As it is seen, for a proper convergence, a bigger N_{traj} is needed for larger system sizes and for values of t_2 close to the area-law regime $t_2 = 1$.

The convergence of the mutual informations $\overline{\mathcal{I}}_{L/4}$ and $\overline{\mathcal{I}}_{L/8}$ with respect to N_{traj} is illustrated on Figs.(11.17,11.18). For $t_2 = 5$, both quantities rapidly saturate to the corresponding average values. However for $t_2 = 1.5$, as Figs.(11.17a,11.18a) shows, the mutual informations are more sensitive due to the proximity of an area-law regime and it takes more trajectories for a proper convergence.

Considering these results, we assume that for $p = 1$ and for the regimes far away from the area law-regimes (i.e. for $t_2 > 1.5$), $N_{traj} = 400$ is sufficient for the convergence of the trajectory averaged quantities for $L \leq 64$ and we use $N_{traj} = 1000$ for $L > 64$. For the regions with $t_2 \leq 1.5$, we take $N_{traj} = 1000$ for all system sizes.

Fig.(11.19) shows how $\overline{\mathcal{E}}_{L/2}$ converges with respect to N_{traj}, for various values of measurement probability p and fixed system size $L = 128$. As it is seen, for $p = 0.25, 0.5$ and 0.75, $N_{traj} \approx 100$ is already sufficient number of trajectories. Thus in order to ensure a proper convergence of our simulations, we set $N_{traj} = 1000$ for $L > 64$ and $N_{traj} = 400$ for $L \leq 64$, regardless of values of t_2 and p.
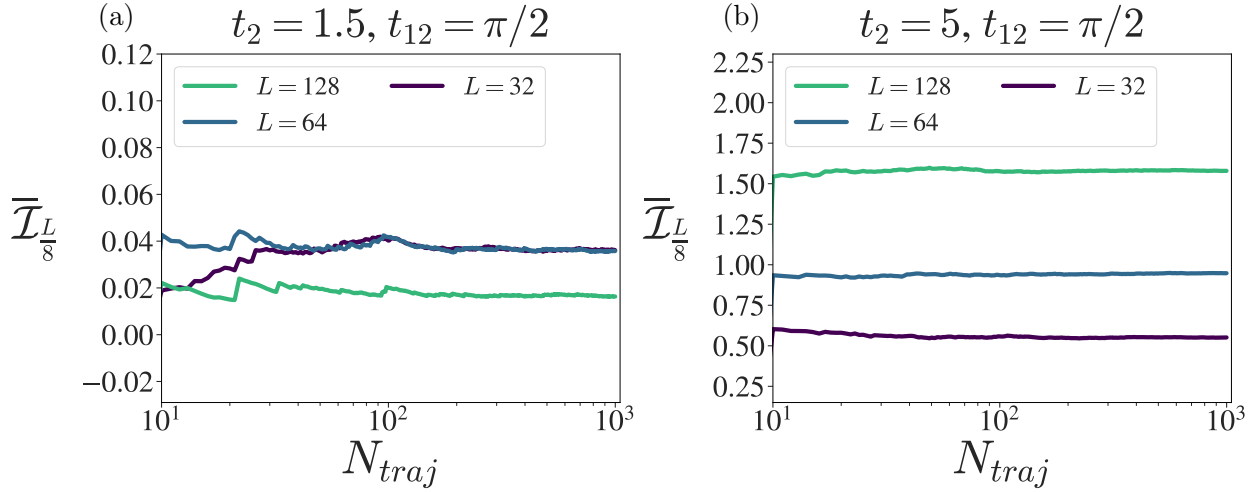
FIGURE 11.17: The figures shows the convergence of $\overline{\mathcal{I}}_{L/8}$ with respect to number of trajectories N_{traj}.
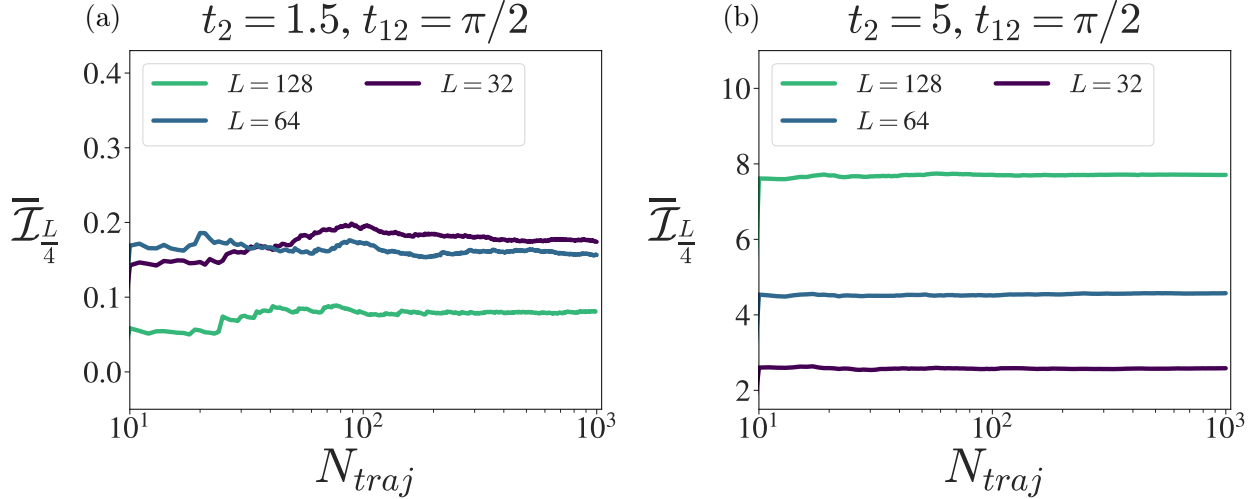
FIGURE 11.18: The figures shows the convergence of $\overline{\mathcal{I}}_{L/4}$ with respect to number of trajectories N_{traj}.

C   Finite size effects on the scaling of the entanglement entropy

In this Appendix we show the details of the scaling fit for the entanglement entropy $\overline{\mathcal{S}}_{L/2}$. We fit with the function $\overline{\mathcal{S}}_{L/2} = \gamma L + c/3 \log(L) + \beta$ within a range $L_{\min} \leq L \leq L_{\max}$, for three different intervals $L \in [8, 64]$, $L \in [32, 80]$ and $L \in [72, 128]$. We plot the behavior of $c/3 \log(L_{\max})$ and $\gamma L_{\max}$ as function of t_2 for the three different intervals in Fig.(11.20).

We observe that $\gamma L_{\max}$ is very small below a threshold value $t_2^{\lin}$ and displays a sharp increase after such value. Simultaneously $c/3 \log(L_{\max})$ displays a peak around $t_2^{\lin}$.

We find that the value of $t_2^{\lin}$ increases as $L_{\max}$ is increased, meaning that the region where the linear contribution becomes comparable with the logarithmic contribution is pushed to larger and larger values of t_2. Moreover, the maximum value of $\gamma L_{\max}$, observed at larger values of t_2, does not change significantly when the fitting interval changes. On the other hand, the peak value of $c/3 \log(L_{\max})$, as well as its value at large t_2 increases significantly when $L_{\max}$ is increased. This suggests that in the thermodynamic limit the logarithmic contribution will always dominate, and
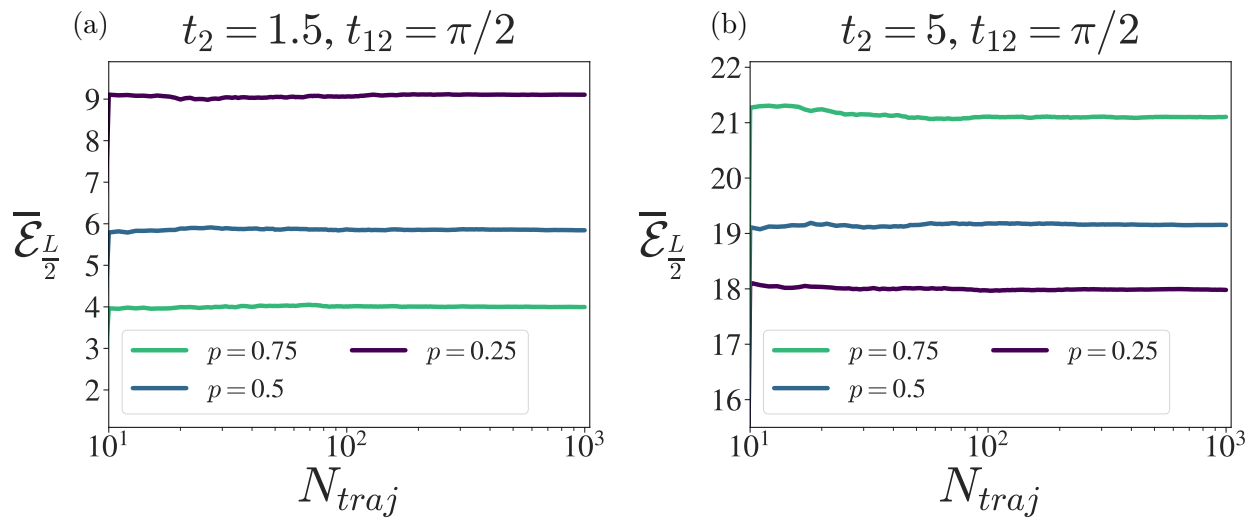
FIGURE 11.19: The figures (a) and (b) show the convergence of bipartite logarithmic negativity $\overline{\mathcal{E}}_{L/2}$ with respect to number of trajectories N_{traj}, for various p and fixed $L = 128$.
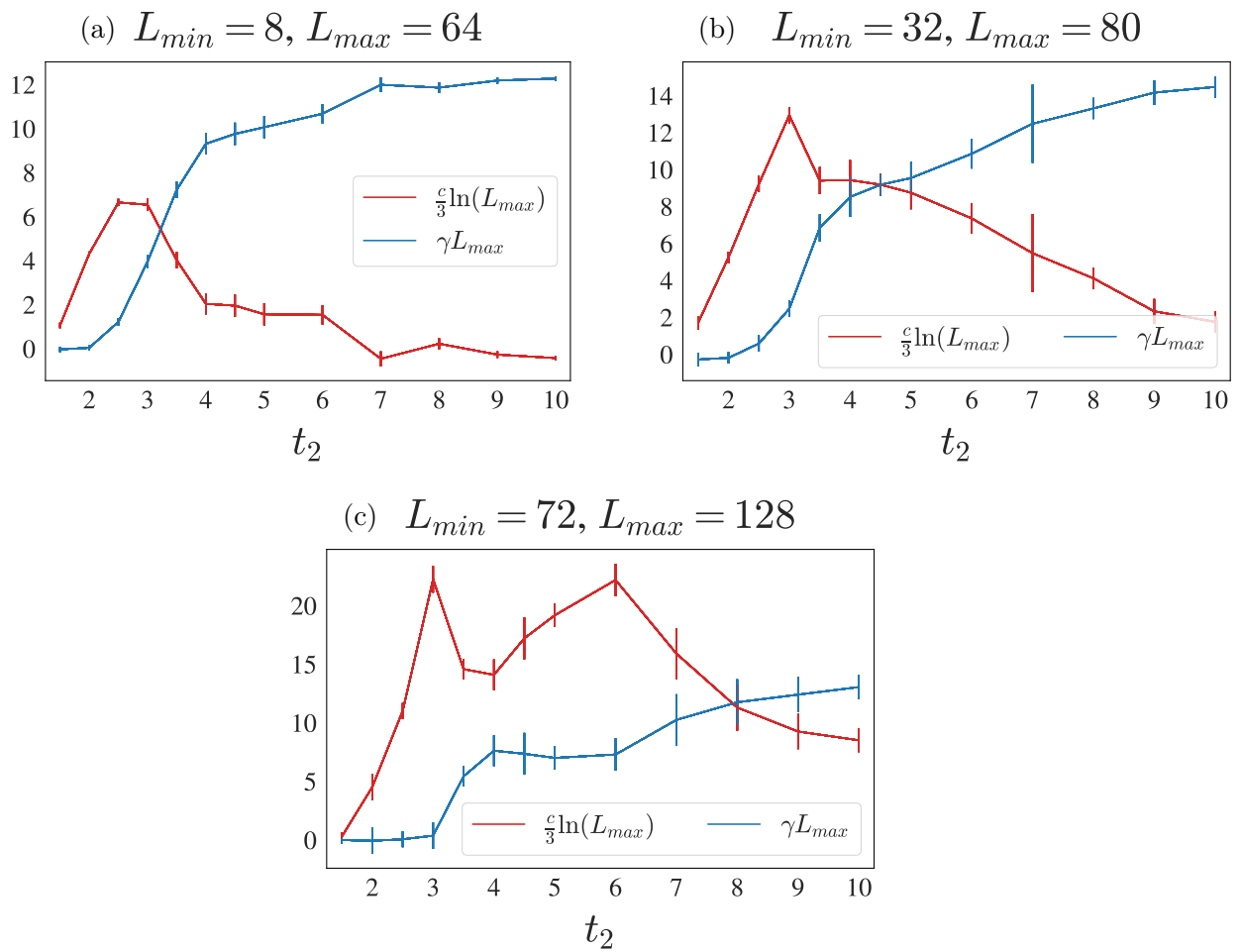
FIGURE 11.20: Plot of $c/3 \log(L_{max})$ and γL_{max} as function of t_2 for the three fitting intervals $L \in [8, 64]$ (a), $L \in [32, 80]$ (b) and $L \in [72, 128]$ (c).
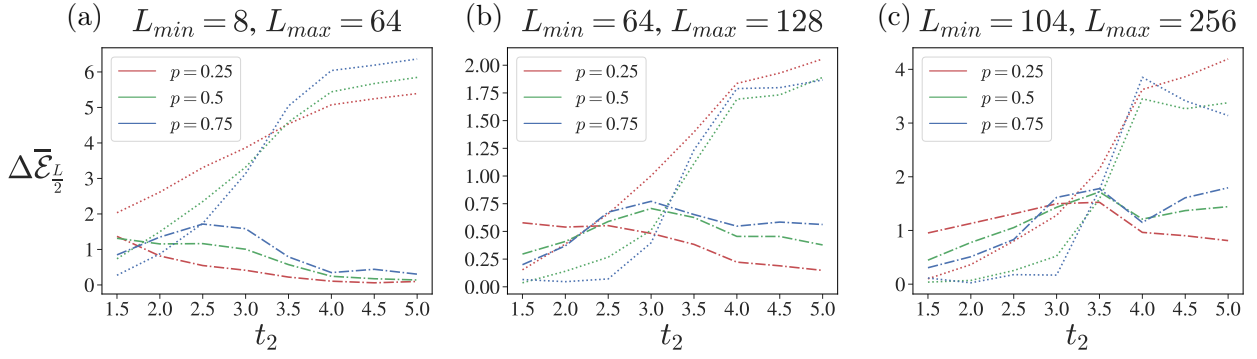
FIGURE 11.21

that the linear contribution is a finite size effect. The crossover size L^* above which the logarithmic contribution is dominant seems to be dependent on t_2, with larger crossover sizes needed to observe the logarithmic scaling as t_2 is increased.

D   Residual Analysis of the data fit for Negativity

In this section, we analyse the residuals of the data fit for $\overline{\mathcal{E}}_{L/2}$ vs L, for fixed $t_{12} = \pi/2$, with various t_2 and p. We compare the total residual $\Delta\overline{\mathcal{E}}_{L/2} = \sum_{L \in L_{\text{fit}}} \left(\overline{\mathcal{E}}_{L/2}^{(\text{data})} - \overline{\mathcal{E}}_{L/2}^{(\text{fit})} \right)$ for linear and logarithmic fitting curves, for L in fitting range $L_{\text{fit}} = [L_{\text{min}}, L_{\text{max}}]$.

Fig.(11.21) shows the residuals for linear (dash-dot lines, with $\overline{\mathcal{E}}_{L/2}^{(\text{fit})} = \gamma L + \beta$ fitting curve) and logarithmic (dotted lines, with $\overline{\mathcal{E}}_{L/2}^{(\text{fit})} = c\log(L) + \beta$ fitting curve). As the figures show, for smaller values of t_2, the logarithmic fit yields smaller residuals and thus is a better fit, compared to linear. On the other hand, for larger t_2, linear fit seems to be more accurate compared to the logarithmic.

It should be noted that the shift of the crossing point between dash-dot and dotted lines by variation of L_{fit} is attributed to the finite-size effects.

Chapter 12

Conclusion

In this part of thesis we have explored the concept of Coherence and Decoherence in quantum dynamics. Specifically, we demonstrate that the decoherence in the system induced by the interaction with the environment can be interpreted as a measurement effect. By deriving the time-local Lindblad master equation and using the trace-distance measure of non-Markovianity, we show that time-dependent Lindblad master equations is Markovian if the corresponding decay rates are always positive. Contrary to this case, if the decay rates become negative, then the dynamics becomes non-Markovian. It was shown that during non-Markovian regions, the system regains the coherences that it has lost to the environment in the past. This creates the memory effect of the time evolution and renders the dynamics non-Markovian. Due to this, already at a single-body level the unraveling of non-Markovian master equation with quantum trajectory approach becomes challenging, although still possible.

To resolve this issue, we have introduced a theoretical framework to unravel the non-Markovian dynamics of quantum many-body systems in terms of quantum trajectories interspersed by quantum jumps. Our technique relies on two methodological innovations: a formulation of many-body quantum jumps applicable to certain classes of non-Markovian dynamics, and a diagrammatic expansion to map the resulting evolution into amenable equations of motion.

Unlike in the Markov case, non-Markovian many-body trajectories are not independent from each other, a direct consequence of the fact that the bath retains finite memory due to non-trivial spectral functions. This feature makes averaging the system dynamics from trajectories practically intractable at the computational level. However, as we have demonstrated, non-Markovian dynamics in the random unitary circuit is still tractable within the framework of proposed diagrammatic expansion.

The Markovian variant of one dimensional random unitary circuit model has been studied previously and was proven that the spatio-temporally random projective measurements can induce a phase transition in the scaling of the entanglement entropy. Specifically, for vanishing measurement rate the unitary evolution will drive the system towards the state with large entanglement content. On the other limit, for large measurement rates, the state of the system is persistently collapsed due to measurement and thus the unitary evolution fails to build up the entanglement in the system. This competition of unitary evolution and projective measurement hosts a critical point, where the growth and the decay of entanglement is in balance, while the scaling of entanglement entropy indicates that the critical point has underlying conformal field theoretical description. It was proven that the random unitary circuit model maps to a two-dimensional classical Potts model, where the couplings between spins are homogeneous and local along the time direction.

The key feature of our framework is that it allows to investigate measurement induced phase transitions in the presence of information back-flow in random unitary circuits - a situation relevant to any system where measurements are realized via coupling to a non-trivial bath. This can be done analytically because, under mild assumptions (i.e. sufficiently large sizes and evolution times), it is possible to write down closed-form equations governing the conditional probability of each trajectory using diagrammatic methods. Remarkably, these equations share the same functional form of the

Dyson equation, and can be manipulated so that the probability of a generic outcome trajectory is given in terms of the time evolution of the expectation value of local observables. Within our framework, this result shows how the highly non-linear effect of non-Markovianity on many-body systems can be cast as a "dressing" over Markovian trajectories, very much like interactions do for single particle wave-functions in electronic systems.

This Dyson equation-like description enables the study of entanglement and measurement induced transitions in the presence of information inflow from the bath back to the system. For the case of one-dimensional Haar circuits, we formulate a classical statistical mechanics model of the system dynamics. The key difference with the memory-less case is that couplings are now time-dependent, and that there are large regions of space-time where magnetic fluctuations are suppressed: these are actually the non-Markovian regions, and their coupling profiles reflects the fact that reverse jumps are included in the statistical mechanics model implicitly via the dressed probability distributions.

The properties of entanglement was studied via numerical simulations of the corresponding Potts model describing the $N = 3$ replica space. We point out that our approach is also applicable to the case of evolution with Clifford gates, where statistical mechanics mappings have been recently proposed [265]. Numerical evidence points to the fact that non-Markovianity does not significantly shift the transition, but stabilizes the volume law phase of the entanglement by shielding it from transient strong dissipation.

Motivated by the robustness of non-Markovian MIPT in RUC and well-known free-fermionic models with measurements, we studied a free fermionic ladder model by directly simulating the quantum trajectories. The inner chain of the ladder acts as the system under study, while the outer chain acts as an environment with an internal dynamics. Measurements are performed on the outer chain, thus inducing an effective non-Markovian dynamics on the inner chain once the outer chain is traced out.

We have investigated the entanglement transition in this system by analyzing several witnesses of entanglement within the inner chain. More specifically, we studied the bipartite entanglement entropy and the mutual information between diametrically opposite partitions when the outer chain is always measured – i.e. when $p = 1$ and the the outer chain is in a pure state – and the fermionic negativity for $p < 1$.

By analyzing the phase diagram as function of the hopping between the chains (t_{12}) and within the bath chain (t_2) at $p = 1$, and were able to distinguish between area-law phase and non-area-law phase by looking at the scale with partition size of the entanglement entropy at fixed L. We found that the non-area law survives even for strong measurements when the scrambling rate of the outer chain (which is proportional to t_2) is large enough. We also found a periodic structure in t_{12} of the phase diagram, with repeating lobes of area-law phases, which arises due to the geometric structure of the ladder.

For a value of t_{12} that maximizes the interchain coupling, we investigated the nature of the non-area law phase to understand whether it is a volume-law phase or a conformally invariant phase. The analysis of the mutual information clearly confirm the presence of the CFT phase at smaller values of t_2, close to the lobes of area-law phases, although larger system sizes would be needed for a definitive assessment.

We also considered the case of $p < 1$ and studied the entanglement transition using the fermionic negativity. We found a qualitatively similar behavior to the $p = 1$ case. A striking result is that for large t_2, the entanglement in the inner chain can be increased by performing more measurements on the outer chain, a phenomenon which we postulate is due to the monogamy of entanglement. Although the behavior of negativity is very similar to that of the entanglement entropy, we cannot in principle make the claim that the linear contributions are due to finite size effects, as we lack the $p < 1$ counterpart of the mutual information to precisely pinpoint the phase of the system.

A remarkably similar phenomenology has been observed in [266], where a single free fermion chain is monitored through measurements of long-range string operators [267]. Changing the range of the measurement operators, the phase changes from area-law (local measurements) to logarithmic (short-range) to what it seems a regime of mixed logarithmic and volume scaling (long-range). This striking resemblance could be interpreted in terms of the same qualitative features exhibited by long-range measurements and by non-Markovian local measurements – i.e. measurements with a long-time memory that translates into a long spatial range at the level of the system chain. This connection is very interesting and deserves to be accurately investigated on its own, although such a study goes well beyond the scope of this work.

By implementing the trace-distance measure of non-Markovianity, we also explicitly showed that the effective dynamics of the inner chain is non-Markovian. Moreover, the dynamics is always non-Markovian, and the strength of non-Markovianity has a qualitative behavior that resembles that of the entanglement transition. In particular, regions of strong non-Markovianity correspond to regions where the entanglement in the system is larger, suggesting a connection between memory effects and an enhancement of entanglement [202, 268]. We remark that we considered a minimal model of non-interacting bath. Indeed it would be interesting to investigate the role of interactions in the bath, and how they can modify non-Markovianity effects.

Our results demonstrate a previously unproved inherent robustness of measurement-induced transition to information backflow in RUC and free fermionic setups. Combined with the, by now established, fact that such transitions can occur for various kinds of coherent dynamics and Kraus operators, this suggests that measurement induced transitions might indeed take place in a variety of settings, including systems where the effects of information back-flow are often non-negligible.

It is worth pointing out a few possible questions that these results raise. In terms of relevance to experiments, it would be important to combine our approach with an inherently open system description of the system (i.e. noise in addition to measurement), that, for the Markovian case, has been recently addressed in Ref. [269]. Moreover, our methods may find application in studying measurement induced transitions in solid state systems, where memory effects are important; for example, the $1/f$ noise is non-Markovian and is the most common type of noise in quantum devices based on solid state platforms [270].

We also remark that the non-Markovian trajectories that we consider can still be realized through a (possibly very complicated) experimental setup, for example through a combination of quantum simulation of the system and a classical memory that stores information about the occurrence of the normal jumps [271, 272]. This classical memory is essential to supply the memory effects of the non-Markovian evolution and allows to provide memory feedback in a controlled way, but it also requires exponentially large resources. Another way of realizing non-Markovian trajectories in a physical system, is by coupling the system of interest to an auxiliary bath with a non trivial dynamics and subjected to Markovian measurements, which results in an effective non-Markovian dynamics of the system. The evolution of system+bath is described by conventional quantum trajectories, and in the case where the measurements act globally on the bath, the system evolves along a pure state trajectory for which the formalism of our paper is directly applicable. Indeed, we have illustrated the above idea within the context of coupled free-fermion chains in Sec.(11) [203], where we also confirmed numerically a key qualitative prediction of the diagrammatic approach – that is the 'stability' of the measurement-induced transition.

Within the context of measurement induced transitions, another question is about the connection between error correction schemes and measurement protocols. Given the fact that memory effects can in principle be precisely quantified in experiments by performing spectroscopy of the bath, it would be interesting to see whether that information can be utilized to improve error correction, or at least, if the presence of a measurement induced transition can at least provide some intrinsic robustness of decoding methods with respect to measurement errors (that can also be seen as a non-Markovian effect in some cases) [268].

Another open question is the formulation of practical numerical procedures to address MIPT in the presence of memory. Here, it might be possible to adapt some methods that have found success in few body systems, at least for a qualitative understanding. Beyond such applications, it would be interesting to see whether our diagrammatic method can provide insights on other many-body phenomena in non-Markovian systems, as well as on recently developed computational techniques to tackle them [273].

Bibliography

[1] Peter Schauß et al. "Observation of spatially ordered structures in a two-dimensional Rydberg gas". In: *Nature* 491.7422 (Oct. 2012), pp. 87–91. DOI: 10.1038/nature11596. URL: https://doi.org/10.1038/nature11596.

[2] Y.-Y. Jau et al. "Entangling atomic spins with a Rydberg-dressed spin-flip blockade". In: *Nature Physics* 12.1 (Oct. 2015), pp. 71–74. DOI: 10.1038/nphys3487. URL: https://doi.org/10.1038/nphys3487.

[3] R. Faoro et al. "van der Waals explosion of cold Rydberg clusters". In: *Phys. Rev. A* 93 (3 Mar. 2016), p. 030701. DOI: 10.1103/PhysRevA.93.030701. URL: https://link.aps.org/doi/10.1103/PhysRevA.93.030701.

[4] Johannes Zeiher et al. "Many-body interferometry of a Rydberg-dressed spin lattice". In: *Nature Physics* 12.12 (Aug. 2016), pp. 1095–1099. DOI: 10.1038/nphys3835. URL: https://doi.org/10.1038/nphys3835.

[5] Hannes Bernien et al. "Probing many-body dynamics on a 51-atom quantum simulator". In: *Nature* 551.7682 (Nov. 2017), pp. 579–584. DOI: 10.1038/nature24622. URL: https://doi.org/10.1038/nature24622.

[6] Daniel Barredo et al. "Synthetic three-dimensional atomic structures assembled atom by atom". In: *Nature* 561.7721 (Sept. 2018), pp. 79–82. DOI: 10.1038/s41586-018-0450-2. URL: https://doi.org/10.1038/s41586-018-0450-2.

[7] J B Balewski et al. "Rydberg dressing: understanding of collective many-body effects and implications for experiments". In: *New Journal of Physics* 16.6 (June 2014), p. 063012. DOI: 10.1088/1367-2630/16/6/063012. URL: https://doi.org/10.1088/1367-2630/16/6/063012.

[8] Sylvain de Léséleuc et al. "Accurate Mapping of Multilevel Rydberg Atoms on Interacting Spin-1/2 Particles for the Quantum Simulation of Ising Models". In: *Phys. Rev. Lett.* 120 (11 Mar. 2018), p. 113602. DOI: 10.1103/PhysRevLett.120.113602. URL: https://link.aps.org/doi/10.1103/PhysRevLett.120.113602.

[9] Antoine Browaeys and Thierry Lahaye. "Many-body physics with individually controlled Rydberg atoms". In: *Nature Physics* 16.2 (Jan. 2020), pp. 132–142. DOI: 10.1038/s41567-019-0733-z. URL: https://doi.org/10.1038/s41567-019-0733-z.

[10] P. Scholl et al. "Microwave Engineering of Programmable XXZ Hamiltonians in Arrays of Rydberg Atoms". In: *PRX Quantum* 3 (2 Apr. 2022), p. 020303. DOI: 10.1103/PRXQuantum.3.020303. URL: https://link.aps.org/doi/10.1103/PRXQuantum.3.020303.

[11] T. Pohl, E. Demler, and M. D. Lukin. "Dynamical Crystallization in the Dipole Blockade of Ultracold Atoms". In: *Phys. Rev. Lett.* 104 (4 Jan. 2010), p. 043002. DOI: 10.1103/PhysRevLett.104.043002. URL: https://link.aps.org/doi/10.1103/PhysRevLett.104.043002.

[12] Alexander Keesling et al. "Quantum Kibble–Zurek mechanism and critical dynamics on a programmable Rydberg simulator". In: *Nature* 568.7751 (Apr. 2019), pp. 207–211. DOI: 10.1038/s41586-019-1070-1. URL: https://doi.org/10.1038/s41586-019-1070-1.

[13]   Sylvain de Léséleuc et al. "Observation of a symmetry-protected topological phase of interacting bosons with Rydberg atoms". In: *Science* 365.6455 (Aug. 2019), pp. 775–780. ISSN: 0036-8075. DOI: 10.1126/science.aav9105. URL: https://doi.org/10.1126/science.aav9105.

[14]   Sepehr Ebadi et al. "Quantum phases of matter on a 256-atom programmable quantum simulator". In: *Nature* 595.7866 (July 2021), pp. 227–232. ISSN: 1476-4687. DOI: 10.1038/s41586-021-03582-4. URL: https://doi.org/10.1038/s41586-021-03582-4.

[15]   Pascal Scholl et al. "Quantum simulation of 2D antiferromagnets with hundreds of Rydberg atoms". In: *Nature* 595.7866 (July 2021), pp. 233–238. ISSN: 1476-4687. DOI: 10.1038/s41586-021-03585-1. URL: https://doi.org/10.1038/s41586-021-03585-1.

[16]   N. Henkel, R. Nath, and T. Pohl. "Three-Dimensional Roton Excitations and Supersolid Formation in Rydberg-Excited Bose-Einstein Condensates". In: *Phys. Rev. Lett.* 104 (19 May 2010), p. 195302. DOI: 10.1103/PhysRevLett.104.195302. URL: https://link.aps.org/doi/10.1103/PhysRevLett.104.195302.

[17]   G. Pupillo et al. "Strongly Correlated Gases of Rydberg-Dressed Atoms: Quantum and Classical Dynamics". In: *Phys. Rev. Lett.* 104 (22 June 2010), p. 223002. DOI: 10.1103/PhysRevLett.104.223002. URL: https://link.aps.org/doi/10.1103/PhysRevLett.104.223002.

[18]   Jens Honer et al. "Collective Many-Body Interaction in Rydberg Dressed Atoms". In: *Phys. Rev. Lett.* 105 (16 Oct. 2010), p. 160404. DOI: 10.1103/PhysRevLett.105.160404. URL: https://link.aps.org/doi/10.1103/PhysRevLett.105.160404.

[19]   T. Macrí and T. Pohl. "Rydberg dressing of atoms in optical lattices". In: *Phys. Rev. A* 89 (1 Jan. 2014), p. 011402. DOI: 10.1103/PhysRevA.89.011402. URL: https://link.aps.org/doi/10.1103/PhysRevA.89.011402.

[20]   Marco Mattioli et al. "Cluster Luttinger Liquids of Rydberg-Dressed Atoms in Optical Lattices". In: *Phys. Rev. Lett.* 111 (16 Oct. 2013), p. 165302. DOI: 10.1103/PhysRevLett.111.165302. URL: https://link.aps.org/doi/10.1103/PhysRevLett.111.165302.

[21]   M. Dalmonte et al. "Cluster Luttinger liquids and emergent supersymmetric conformal critical points in the one-dimensional soft-shoulder Hubbard model". In: *Phys. Rev. B* 92 (4 July 2015), p. 045106. DOI: 10.1103/PhysRevB.92.045106. URL: https://link.aps.org/doi/10.1103/PhysRevB.92.045106.

[22]   Adriano Angelone et al. "Nonequilibrium scenarios in cluster-forming quantum lattice models". In: *Phys. Rev. A* 101 (6 June 2020), p. 063603. DOI: 10.1103/PhysRevA.101.063603. URL: https://link.aps.org/doi/10.1103/PhysRevA.101.063603.

[23]   Adriano Angelone, Fabio Mezzacapo, and Guido Pupillo. "Superglass Phase of Interaction-Blockaded Gases on a Triangular Lattice". In: *Phys. Rev. Lett.* 116 (13 Apr. 2016), p. 135303. DOI: 10.1103/PhysRevLett.116.135303. URL: https://link.aps.org/doi/10.1103/PhysRevLett.116.135303.

[24]   Elmer Guardado-Sanchez et al. "Quench Dynamics of a Fermi Gas with Strong Nonlocal Interactions". In: *Phys. Rev. X* 11 (2 May 2021), p. 021036. DOI: 10.1103/PhysRevX.11.021036. URL: https://link.aps.org/doi/10.1103/PhysRevX.11.021036.

[25]   Mikheil Tsitsishvili et al. "Phase diagram of Rydberg-dressed atoms on two-leg square ladders: Coupling supersymmetric conformal field theories on the lattice". In: *Phys. Rev. B* 105 (15 Apr. 2022), p. 155159. DOI: 10.1103/PhysRevB.105.155159. URL: https://link.aps.org/doi/10.1103/PhysRevB.105.155159.

[26] Pierre Fromholz et al. "Phase diagram of Rydberg-dressed atoms on two-leg triangular ladders". In: *Phys. Rev. B* 106 (15 Oct. 2022), p. 155411. DOI: 10.1103/PhysRevB.106.155411. URL: https://link.aps.org/doi/10.1103/PhysRevB.106.155411.

[27] Philippe Di Francesco, Pierre Mathieu, and David Sénéchal. *Conformal Field Theory*. Graduate Texts in Contemporary Physics. New York: Springer New York, 1997. DOI: 10.1007/978-1-4612-2256-9. URL: https://doi.org/10.1007/978-1-4612-2256-9.

[28] A. O. Gogolin, A. A. Nersesyan, and A. M. Tsvelik. *Bosonization and Strongly Correlated Systems*. Cambridge, 1999. arXiv: cond-mat/9909069 [cond-mat.str-el]. URL: https://www.cambridge.org/it/academic/subjects/physics/condensed-matter-physics-nanoscience-and-mesoscopic-physics/bosonization-and-strongly-correlated-systems?format=PB&isbn=9780521617192.

[29] Eduardo Fradkin. *Field Theories of Condensed Matter Physics*. 2nd ed. Cambridge University Press, 2013.

[30] B. Andrei Bernevig. *Topological Insulators and Topological Superconductors*. Princeton: Princeton University Press, 2013. ISBN: 9781400846733. DOI: doi:10.1515/9781400846733. URL: https://doi.org/10.1515/9781400846733.

[31] T. D. Schultz, D. C. Mattis, and E. H. Lieb. "Two-Dimensional Ising Model as a Soluble Problem of Many Fermions". In: *Rev. Mod. Phys.* 36 (3 July 1964), pp. 856–871. DOI: 10.1103/RevModPhys.36.856. URL: https://link.aps.org/doi/10.1103/RevModPhys.36.856.

[32] A Yu Kitaev. "Unpaired Majorana fermions in quantum wires". In: *Physics-Uspekhi* 44.10S (Oct. 2001), p. 131. DOI: 10.1070/1063-7869/44/10S/S29. URL: https://dx.doi.org/10.1070/1063-7869/44/10S/S29.

[33] Jason Alicea. "New directions in the pursuit of Majorana fermions in solid state systems". In: *Reports on Progress in Physics* 75.7 (June 2012), p. 076501. DOI: 10.1088/0034-4885/75/7/076501. URL: https://dx.doi.org/10.1088/0034-4885/75/7/076501.

[34] R. Jackiw and C. Rebbi. "Solitons with fermion number $\frac{1}{2}$". In: *Phys. Rev. D* 13 (12 June 1976), pp. 3398–3409. DOI: 10.1103/PhysRevD.13.3398. URL: https://link.aps.org/doi/10.1103/PhysRevD.13.3398.

[35] Glen Bigan Mbeng, Angelo Russomanno, and Giuseppe E. Santoro. *The quantum Ising chain for beginners*. 2020. arXiv: 2009.09208 [quant-ph].

[36] Paul Fendley. "Parafermionic edge zero modes inZn-invariant spin chains". In: *Journal of Statistical Mechanics: Theory and Experiment* 2012.11 (Nov. 2012), P11020. ISSN: 1742-5468. DOI: 10.1088/1742-5468/2012/11/p11020. URL: http://dx.doi.org/10.1088/1742-5468/2012/11/P11020.

[37] Leo P. Kadanoff. "Operator Algebra and the Determination of Critical Indices". In: *Phys. Rev. Lett.* 23 (25 Dec. 1969), pp. 1430–1433. DOI: 10.1103/PhysRevLett.23.1430. URL: https://link.aps.org/doi/10.1103/PhysRevLett.23.1430.

[38] A.A. Belavin, A.M. Polyakov, and A.B. Zamolodchikov. "Infinite conformal symmetry in two-dimensional quantum field theory". In: *Nuclear Physics B* 241.2 (1984), pp. 333–380. ISSN: 0550-3213. DOI: https://doi.org/10.1016/0550-3213(84)90052-X. URL: https://www.sciencedirect.com/science/article/pii/055032138490052X.

[39] Thierry Giamarchi. *Quantum Physics in One Dimension*. Oxford: Oxford University Press, Dec. 2003. DOI: 10.1093/acprof:oso/9780198525004.001.0001. URL: https://doi.org/10.1093/acprof:oso/9780198525004.001.0001.

[40] F. D. M. Haldane. "Effective Harmonic-Fluid Approach to Low-Energy Properties of One-Dimensional Quantum Fluids". In: *Phys. Rev. Lett.* 47 (25 Dec. 1981), pp. 1840–1843. DOI: `10.1103/PhysRevLett.47.1840`. URL: `https://link.aps.org/doi/10.1103/PhysRevLett.47.1840`.

[41] Michael Stone. *Bosonization*. Ed. by Michael Stone. Singapore, Singapore: World Scientific Publishing, Jan. 1994.

[42] F Bloch. "Bremsvermögen von Atomen mit mehreren Elektronen". de. In: *Eur. Phys. J. A* 81.5-6 (May 1933), pp. 363–376.

[43] F. Bloch. "Inkohärente Röntgenstreuung und Dichteschwankungen eines entarteten Fermigases". In: *Helvetica Physica Acta* 7.IV (1934), p. 385. ISSN: 0018-0238. DOI: `10.5169/seals-110373`. URL: `https://www.e-periodica.ch`.

[44] P Jordan. "Zur Neutrinotheorie des Lichtes". de. In: *Eur. Phys. J. A* 93.7-8 (July 1935), pp. 464–472.

[45] P Jordan. "Lichtquant und Neutrino". de. In: *Eur. Phys. J. A* 98.11-12 (Nov. 1936), pp. 759–767.

[46] P Jordan. "Zur Herleitung der Vertauschungsregeln in der Neutrinotheorie des Lichtes". de. In: *Eur. Phys. J. A* 99.1-2 (Feb. 1936), pp. 109–113.

[47] P Jordan. "Beiträge zur Neutrinotheorie des Lichtes. I". de. In: *Eur. Phys. J. A* 102.3-4 (Mar. 1936), pp. 243–252.

[48] P Jordan. "Beiträge zur Neutrinotheorie des Lichtes. II". de. In: *Eur. Phys. J. A* 105.1-2 (Jan. 1937), pp. 114–121.

[49] P Jordan. "Beiträge zur Neutrinotheorie des Lichtes. III". de. In: *Eur. Phys. J. A* 105.3-4 (Mar. 1937), pp. 229–231.

[50] S-I Tomonaga. "Remarks on bloch's method of sound waves applied to many-fermion problems". In: *Prog. Theor. Phys.* 5.4 (July 1950), pp. 544–569.

[51] J M Luttinger. "An exactly soluble model of a many-fermion system". en. In: *J. Math. Phys.* 4.9 (Sept. 1963), pp. 1154–1162.

[52] Daniel C Mattis and Elliott H Lieb. "Exact solution of a many-fermion system and its associated boson field". en. In: *J. Math. Phys.* 6.2 (Feb. 1965), pp. 304–312.

[53] A. Luther and I. Peschel. "Single-particle states, Kohn anomaly, and pairing fluctuations in one dimension". In: *Phys. Rev. B* 9 (7 Apr. 1974), pp. 2911–2919. DOI: `10.1103/PhysRevB.9.2911`. URL: `https://link.aps.org/doi/10.1103/PhysRevB.9.2911`.

[54] A. Luther and V. J. Emery. "Backward Scattering in the One-Dimensional Electron Gas". In: *Phys. Rev. Lett.* 33 (10 Sept. 1974), pp. 589–592. DOI: `10.1103/PhysRevLett.33.589`. URL: `https://link.aps.org/doi/10.1103/PhysRevLett.33.589`.

[55] Sidney Coleman. "Quantum sine-Gordon equation as the massive Thirring model". In: *Phys. Rev. D* 11 (8 Apr. 1975), pp. 2088–2097. DOI: `10.1103/PhysRevD.11.2088`. URL: `https://link.aps.org/doi/10.1103/PhysRevD.11.2088`.

[56] S. Mandelstam. "Soliton operators for the quantized sine-Gordon equation". In: *Phys. Rev. D* 11 (10 May 1975), pp. 3026–3030. DOI: `10.1103/PhysRevD.11.3026`. URL: `https://link.aps.org/doi/10.1103/PhysRevD.11.3026`.

[57] Edward Witten. "Non-abelian bosonization in two dimensions". en. In: *Commun. Math. Phys.* 92.4 (Dec. 1984), pp. 455–472.

[58] D. Sénéchal. *An introduction to bosonization*. 1999. arXiv: `cond-mat/9908262 [cond-mat.str-el]`. URL: `https://arxiv.org/abs/cond-mat/9908262`.

[59] R Shankar. "Bosonization: How to make it work for you in condensed matter". In: *Low-Dimensional Quantum Field Theories for Condensed Matter Physicists*. Trieste, Italy: WORLD SCIENTIFIC, Feb. 1995.

[60] Jan von Delft and Herbert Schoeller. "Bosonization for beginners — refermionization for experts". In: *Annalen der Physik* 510.4 (Nov. 1998), pp. 225–305. ISSN: 1521-3889. DOI: 10.1002/andp.19985100401. URL: http://dx.doi.org/10.1002/andp.19985100401.

[61] Alexei M Tsvelik. *Quantum field theory in condensed matter physics*. 2nd ed. Cambridge, England: Cambridge University Press, May 2010.

[62] Steven R. White. "Density matrix formulation for quantum renormalization groups". In: *Phys. Rev. Lett.* 69 (19 Nov. 1992), pp. 2863–2866. DOI: 10.1103/PhysRevLett.69.2863. URL: https://link.aps.org/doi/10.1103/PhysRevLett.69.2863.

[63] Steven R. White. "Density-matrix algorithms for quantum renormalization groups". In: *Phys. Rev. B* 48 (14 Oct. 1993), pp. 10345–10356. DOI: 10.1103/PhysRevB.48.10345. URL: https://link.aps.org/doi/10.1103/PhysRevB.48.10345.

[64] Steven R. White. "Density matrix renormalization group algorithms with a single center site". In: *Phys. Rev. B* 72 (18 Nov. 2005), 180403(R). DOI: 10.1103/PhysRevB.72.180403. URL: https://link.aps.org/doi/10.1103/PhysRevB.72.180403.

[65] Ian P McCulloch. "From density-matrix renormalization group to matrix product states". In: *Journal of Statistical Mechanics: Theory and Experiment* 2007.10 (Oct. 2007), P10014–P10014. DOI: 10.1088/1742-5468/2007/10/p10014. URL: https://doi.org/10.1088/1742-5468/2007/10/p10014.

[66] Richard P. Feynman. "Simulating physics with computers". In: *International Journal of Theoretical Physics* 21.6–7 (June 1982), pp. 467–488. ISSN: 1572-9575. DOI: 10.1007/bf02650179. URL: http://dx.doi.org/10.1007/BF02650179.

[67] M J Seaton. "Quantum defect theory". In: *Rep. Prog. Phys.* 46.2 (Feb. 1983), pp. 167–257.

[68] Thomas F. Gallagher. "Rydberg Atoms". In: *Springer Handbook of Atomic, Molecular, and Optical Physics*. Ed. by Gordon W. F. Drake. Cham: Springer International Publishing, 2023, pp. 231–240. ISBN: 978-3-030-73893-8. DOI: 10.1007/978-3-030-73893-8_15. URL: https://doi.org/10.1007/978-3-030-73893-8_15.

[69] Paul Adrien Maurice Dirac. *The Principles of Quantum Mechanics*. Oxford: Clarendon Press, 1930.

[70] J. J. Sakurai and Jim Napolitano. *Modern Quantum Mechanics*. 3rd ed. Cambridge University Press, 2020.

[71] Pascal Weckesser et al. *Realization of a Rydberg-dressed extended Bose Hubbard model*. 2024. arXiv: 2405.20128 [cond-mat.quant-gas].

[72] David Wei et al. "Observation of Brane Parity Order in Programmable Optical Lattices". In: *Phys. Rev. X* 13 (2 June 2023), p. 021042. DOI: 10.1103/PhysRevX.13.021042. URL: https://link.aps.org/doi/10.1103/PhysRevX.13.021042.

[73] M Valiente and D Petrosyan. "Scattering resonances and two-particle bound states of the extended Hubbard model". In: *Journal of Physics B: Atomic, Molecular and Optical Physics* 42.12 (June 2009), p. 121001. DOI: 10.1088/0953-4075/42/12/121001. URL: https://dx.doi.org/10.1088/0953-4075/42/12/121001.

[74] Anders W. Sandvik. "Computational Studies of Quantum Spin Systems". In: *AIP Conference Proceedings* 1297.1 (2010), pp. 135–338. DOI: 10.1063/1.3518900. URL: https://aip.scitation.org/doi/abs/10.1063/1.3518900.

[75]   Ulrich Schollwöck. "The density-matrix renormalization group in the age of matrix product states". In: *Annals of Physics* 326.1 (Jan. 2011), pp. 96–192. DOI: `10.1016/j.aop.2010.09.012`. URL: `https://doi.org/10.1016/j.aop.2010.09.012`.

[76]   Román Orús. "A practical introduction to tensor networks: Matrix product states and projected entangled pair states". In: *Annals of Physics* 349 (Oct. 2014), pp. 117–158. DOI: `10.1016/j.aop.2014.06.013`. URL: `https://doi.org/10.1016/j.aop.2014.06.013`.

[77]   Lorenzo Gotta et al. "Pairing in spinless fermions and spin chains with next-nearest neighbor interactions". In: *Physical Review Research* 3.1 (2021), p. 13114. ISSN: 26431564. DOI: `10.1103/PhysRevResearch.3.013114`. URL: `https://doi.org/10.1103/PhysRevResearch.3.013114`.

[78]   L. Dixon, P. Ginsparg, and J. Harvey. "Superconformal field theory". In: *Nuclear Physics B* 306.3 (Aug. 1988), pp. 470–496. DOI: `10.1016/0550-3213(88)90011-9`. URL: `https://doi.org/10.1016/0550-3213(88)90011-9`.

[79]   Thomas Botzung et al. *One-dimensional extended Hubbard model with soft-core potential.* eprint: `arXiv:1909.12168`.

[80]   Masaaki Nakamura. "Tricritical behavior in the extended Hubbard chains". In: *Phys. Rev. B* 61 (24 June 2000), pp. 16377–16392. DOI: `10.1103/PhysRevB.61.16377`. URL: `https://link.aps.org/doi/10.1103/PhysRevB.61.16377`.

[81]   C. Dziurzik et al. "Triplet superconductivity in a 1D itinerant electron system with transverse spin anisotropy". In: *The European Physical Journal B* 51.1 (May 2006), pp. 41–51. DOI: `10.1140/epjb/e2006-00193-x`. URL: `https://doi.org/10.1140/epjb/e2006-00193-x`.

[82]   Bela Bauer et al. "Supersymmetric multicritical point in a model of lattice fermions". In: *Phys. Rev. B* 87 (16 Apr. 2013), p. 165145. DOI: `10.1103/PhysRevB.87.165145`. URL: `https://link.aps.org/doi/10.1103/PhysRevB.87.165145`.

[83]   Paolo Zanardi and Nikola Paunković. "Ground state overlap and quantum phase transitions". In: *Phys. Rev. E* 74 (3 Sept. 2006), p. 031123. DOI: `10.1103/PhysRevE.74.031123`. URL: `https://link.aps.org/doi/10.1103/PhysRevE.74.031123`.

[84]   SHI-JIAN GU. "Fidelity approach to quantum phase transitions". In: *International Journal of Modern Physics B* 24.23 (Sept. 2010), pp. 4371–4458. DOI: `10.1142/s0217979210056335`. URL: `https://doi.org/10.1142/s0217979210056335`.

[85]   David Schwandt, Fabien Alet, and Sylvain Capponi. "Quantum Monte Carlo Simulations of Fidelity at Magnetic Quantum Phase Transitions". In: *Phys. Rev. Lett.* 103 (17 Oct. 2009), p. 170501. DOI: `10.1103/PhysRevLett.103.170501`. URL: `https://link.aps.org/doi/10.1103/PhysRevLett.103.170501`.

[86]   G. Sun, A. K. Kolezhuk, and T. Vekua. "Fidelity at Berezinskii-Kosterlitz-Thouless quantum phase transitions". In: *Phys. Rev. B* 91 (1 Jan. 2015), p. 014418. DOI: `10.1103/PhysRevB.91.014418`. URL: `https://link.aps.org/doi/10.1103/PhysRevB.91.014418`.

[87]   I. P. McCulloch. *Infinite size density matrix renormalization group, revisited.* 2008. arXiv: `0804.2509 [cond-mat.str-el]`. URL: `https://arxiv.org/abs/0804.2509`.

[88]   Gregory M. Crosswhite, A. C. Doherty, and Guifré Vidal. "Applying matrix product operators to model systems with long-range interactions". In: *Phys. Rev. B* 78 (3 July 2008), p. 035116. DOI: `10.1103/PhysRevB.78.035116`. URL: `https://link.aps.org/doi/10.1103/PhysRevB.78.035116`.

[89]   G. Vidal. "Classical Simulation of Infinite-Size Quantum Lattice Systems in One Spatial Dimension". In: *Phys. Rev. Lett.* 98 (7 Feb. 2007), p. 070201. DOI: `10.1103/PhysRevLett.98.070201`. URL: `https://link.aps.org/doi/10.1103/PhysRevLett.98.070201`.

[90]   Jonas A. Kjäll et al. "Phase diagram of the anisotropic spin-2 XXZ model: Infinite-system density matrix renormalization group study". In: *Phys. Rev. B* 87 (23 June 2013), p. 235106. DOI: 10.1103/PhysRevB.87.235106. URL: https://link.aps.org/doi/10.1103/PhysRevB.87.235106.

[91]   G. Giudici et al. "Diagnosing Potts criticality and two-stage melting in one-dimensional hard-core boson models". In: *Phys. Rev. B* 99 (9 Mar. 2019), p. 094434. DOI: 10.1103/PhysRevB.99.094434. URL: https://link.aps.org/doi/10.1103/PhysRevB.99.094434.

[92]   Sukhwinder Singh, Robert N. C. Pfeifer, and Guifré Vidal. "Tensor network decompositions in the presence of a global symmetry". In: *Phys. Rev. A* 82 (5 Nov. 2010), p. 050301. DOI: 10.1103/PhysRevA.82.050301. URL: https://link.aps.org/doi/10.1103/PhysRevA.82.050301.

[93]   Sukhwinder Singh, Robert N. C. Pfeifer, and Guifre Vidal. "Tensor network states and algorithms in the presence of a global U(1) symmetry". In: *Phys. Rev. B* 83 (11 Mar. 2011), p. 115125. DOI: 10.1103/PhysRevB.83.115125. URL: https://link.aps.org/doi/10.1103/PhysRevB.83.115125.

[94]   L. Tagliacozzo et al. "Scaling of entanglement support for matrix product states". In: *Phys. Rev. B* 78 (2 July 2008), p. 024410. DOI: 10.1103/PhysRevB.78.024410. URL: https://link.aps.org/doi/10.1103/PhysRevB.78.024410.

[95]   Frank Pollmann et al. "Theory of Finite-Entanglement Scaling at One-Dimensional Quantum Critical Points". In: *Phys. Rev. Lett.* 102 (25 June 2009), p. 255701. DOI: 10.1103/PhysRevLett.102.255701. URL: https://link.aps.org/doi/10.1103/PhysRevLett.102.255701.

[96]   B. Pirvu et al. "Matrix product states for critical spin chains: Finite-size versus finite-entanglement scaling". In: *Phys. Rev. B* 86 (7 Aug. 2012), p. 075117. DOI: 10.1103/PhysRevB.86.075117. URL: https://link.aps.org/doi/10.1103/PhysRevB.86.075117.

[97]   Curtis Callan and Frank Wilczek. "On geometric entropy". In: *Physics Letters B* 333.1-2 (July 1994), pp. 55–61. DOI: 10.1016/0370-2693(94)91007-3. URL: https://doi.org/10.1016/0370-2693(94)91007-3.

[98]   G. Vidal et al. "Entanglement in Quantum Critical Phenomena". In: *Phys. Rev. Lett.* 90 (22 June 2003), p. 227902. DOI: 10.1103/PhysRevLett.90.227902. URL: https://link.aps.org/doi/10.1103/PhysRevLett.90.227902.

[99]   Pasquale Calabrese and John Cardy. "Entanglement entropy and quantum field theory". In: *Journal of Statistical Mechanics* 2004.06 (June 2004), P06002. DOI: 10.1088/1742-5468/2004/06/p06002. URL: https://doi.org/10.1088/1742-5468/2004/06/p06002.

[100] Louis Villa, Julien Despres, and Laurent Sanchez-Palencia. "Unraveling the excitation spectrum of many-body systems from quantum quenches". In: *Phys. Rev. A* 100 (6 Dec. 2019), p. 063632. DOI: 10.1103/PhysRevA.100.063632. URL: https://link.aps.org/doi/10.1103/PhysRevA.100.063632.

[101] L. Villa et al. "Local quench spectroscopy of many-body quantum systems". In: *Phys. Rev. A* 102 (3 Sept. 2020), p. 033337. DOI: 10.1103/PhysRevA.102.033337. URL: https://link.aps.org/doi/10.1103/PhysRevA.102.033337.

[102] Alexander W. Glaetzle et al. "Designing Frustrated Quantum Magnets with Laser-Dressed Rydberg Atoms". In: *Phys. Rev. Lett.* 114 (17 Apr. 2015), p. 173002. DOI: 10.1103/PhysRevLett.114.173002. URL: https://link.aps.org/doi/10.1103/PhysRevLett.114.173002.

[103] S. Diehl et al. "Quantum states and phases in driven open quantum systems with cold atoms". In: *Nature Physics* 4 (11 2008), pp. 878–883. DOI: 10.1038/nphys1073.

[104] Frank Verstraete, Michael M Wolf, and J Ignacio Cirac. "Quantum computation and quantum-state engineering driven by dissipation". In: *Nature physics* 5.9 (2009), pp. 633–636.

[105] L M Sieberer, M Buchhold, and S Diehl. "Keldysh field theory for driven open quantum systems". In: *Reports on Progress in Physics* 79.9 (Aug. 2016), p. 096001. DOI: 10.1088/0034-4885/79/9/096001. URL: https://doi.org/10.1088/0034-4885/79/9/096001.

[106] Tony E. Lee, Sarang Gopalakrishnan, and Mikhail D. Lukin. "Unconventional Magnetism via Optical Pumping of Interacting Spin Systems". In: *Phys. Rev. Lett.* 110 (25 June 2013), p. 257204. DOI: 10.1103/PhysRevLett.110.257204. URL: https://link.aps.org/doi/10.1103/PhysRevLett.110.257204.

[107] Jiasen Jin et al. "Cluster Mean-Field Approach to the Steady-State Phase Diagram of Dissipative Spin Systems". In: *Phys. Rev. X* 6 (3 July 2016), p. 031011. DOI: 10.1103/PhysRevX.6.031011. URL: https://link.aps.org/doi/10.1103/PhysRevX.6.031011.

[108] Mohammad F. Maghrebi and Alexey V. Gorshkov. "Nonequilibrium many-body steady states via Keldysh formalism". In: *Physical Review B* 93.1 (Jan. 2016), p. 014307. ISSN: 2469-9969. URL: https://doi.org/10.1103/PhysRevB.93.014307.

[109] Michael Foss-Feig et al. "Solvable Family of Driven-Dissipative Many-Body Systems". In: *Phys. Rev. Lett.* 119 (19 Nov. 2017), p. 190402. DOI: 10.1103/PhysRevLett.119.190402. URL: https://link.aps.org/doi/10.1103/PhysRevLett.119.190402.

[110] J. M. Fink et al. "Observation of the Photon-Blockade Breakdown Phase Transition". In: *Phys. Rev. X* 7 (1 Jan. 2017), p. 011012. DOI: 10.1103/PhysRevX.7.011012. URL: https://link.aps.org/doi/10.1103/PhysRevX.7.011012.

[111] Mattias Fitzpatrick et al. "Observation of a Dissipative Phase Transition in a One-Dimensional Circuit QED Lattice". In: *Phys. Rev. X* 7 (1 Feb. 2017), p. 011016. DOI: 10.1103/PhysRevX.7.011016. URL: https://link.aps.org/doi/10.1103/PhysRevX.7.011016.

[112] N. Fläschner et al. "Observation of dynamical vortices after quenches in a system with topology". In: *Nature Physics* 14 (3 2018), pp. 265–268. DOI: 10.1038/s41567-017-0013-8.

[113] N. Syassen et al. "Strong Dissipation Inhibits Losses and Induces Correlations in Cold Molecular Gases". In: *Science* 320.5881 (2008), pp. 1329–1331. ISSN: 0036-8075. DOI: 10.1126/science.1155309.

[114] Jamir Marino and Sebastian Diehl. "Driven Markovian Quantum Criticality". In: *Phys. Rev. Lett.* 116 (7 Feb. 2016), p. 070407. DOI: 10.1103/PhysRevLett.116.070407. URL: https://link.aps.org/doi/10.1103/PhysRevLett.116.070407.

[115] Riccardo Rota et al. "Quantum Critical Regime in a Quadratically Driven Nonlinear Photonic Lattice". In: *Phys. Rev. Lett.* 122 (11 Mar. 2019), p. 110405. DOI: 10.1103/PhysRevLett.122.110405. URL: https://link.aps.org/doi/10.1103/PhysRevLett.122.110405.

[116] Jeremy T. Young et al. "Nonequilibrium Fixed Points of Coupled Ising Models". In: *Phys. Rev. X* 10 (1 Feb. 2020), p. 011039. DOI: 10.1103/PhysRevX.10.011039. URL: https://link.aps.org/doi/10.1103/PhysRevX.10.011039.

[117] Matteo Marcuzzi et al. "Universal Nonequilibrium Properties of Dissipative Rydberg Gases". In: *Phys. Rev. Lett.* 113 (21 Nov. 2014), p. 210401. DOI: 10.1103/PhysRevLett.113.210401. URL: https://link.aps.org/doi/10.1103/PhysRevLett.113.210401.

[118] Kushal Seetharam et al. *Correlation engineering via non-local dissipation*. 2021. arXiv: 2101.06445.

[119] Dario Poletti et al. "Interaction-Induced Impeding of Decoherence and Anomalous Diffusion". In: *Phys. Rev. Lett.* 109 (4 July 2012), p. 045302. DOI: 10.1103/PhysRevLett.109.045302. URL: https://link.aps.org/doi/10.1103/PhysRevLett.109.045302.

[120] Dario Poletti et al. "Emergence of Glasslike Dynamics for Dissipative and Strongly Interacting Bosons". In: *Phys. Rev. Lett.* 111 (19 Nov. 2013), p. 195301. DOI: 10.1103/PhysRevLett.111.195301. URL: https://link.aps.org/doi/10.1103/PhysRevLett.111.195301.

[121] L. M. Sieberer et al. "Dynamical Critical Phenomena in Driven-Dissipative Systems". In: *Phys. Rev. Lett.* 110 (19 May 2013), p. 195301. DOI: 10.1103/PhysRevLett.110.195301. URL: https://link.aps.org/doi/10.1103/PhysRevLett.110.195301.

[122] Bruno Sciolla, Dario Poletti, and Corinna Kollath. "Two-Time Correlations Probing the Dynamics of Dissipative Many-Body Quantum Systems: Aging and Fast Relaxation". In: *Phys. Rev. Lett.* 114 (17 Apr. 2015), p. 170401. DOI: 10.1103/PhysRevLett.114.170401. URL: https://link.aps.org/doi/10.1103/PhysRevLett.114.170401.

[123] M. Schirò et al. "Exotic Attractors of the Nonequilibrium Rabi-Hubbard Model". In: *Phys. Rev. Lett.* 116 (14 Apr. 2016), p. 143603. DOI: 10.1103/PhysRevLett.116.143603. URL: https://link.aps.org/doi/10.1103/PhysRevLett.116.143603.

[124] Giuliano Chiriacò, Andrew J. Millis, and Igor L. Aleiner. "Transient superconductivity without superconductivity". In: *Phys. Rev. B* 98 (22 Dec. 2018), 220510(R). DOI: 10.1103/PhysRevB.98.220510. URL: https://link.aps.org/doi/10.1103/PhysRevB.98.220510.

[125] Giuliano Chiriacò, Andrew J. Millis, and Igor L. Aleiner. "Negative absolute conductivity in photoexcited metals". In: *Phys. Rev. B* 101 (4 Jan. 2020), p. 041105. DOI: 10.1103/PhysRevB.101.041105.

[126] Giuliano Chiriacò and Andrew J. Millis. "Polarity dependent heating at the phase interface in metal-insulator transitions". In: *Phys. Rev. B* 102 (8 Aug. 2020), p. 085116. DOI: 10.1103/PhysRevB.102.085116.

[127] Zhiyuan Sun and Andrew J. Millis. "Transient Trapping into Metastable States in Systems with Competing Orders". In: *Phys. Rev. X* 10 (2 May 2020), p. 021028. DOI: 10.1103/PhysRevX.10.021028. URL: https://link.aps.org/doi/10.1103/PhysRevX.10.021028.

[128] D. A. Lidar, I. L. Chuang, and K. B. Whaley. "Decoherence-Free Subspaces for Quantum Computation". In: *Phys. Rev. Lett.* 81 (12 Sept. 1998), pp. 2594–2597. DOI: 10.1103/PhysRevLett.81.2594.

[129] D. A. Lidar, D. Bacon, and K. B. Whaley. "Concatenating Decoherence-Free Subspaces with Quantum Error Correcting Codes". In: *Phys. Rev. Lett.* 82 (22 May 1999), pp. 4556–4559. DOI: 10.1103/PhysRevLett.82.4556.

[130] M. B. Plenio, V. Vedral, and P. L. Knight. "Quantum error correction in the presence of spontaneous emission". In: *Phys. Rev. A* 55 (1 Jan. 1997), pp. 67–71. DOI: 10.1103/PhysRevA.55.67. URL: https://link.aps.org/doi/10.1103/PhysRevA.55.67.

[131] D. Bacon et al. "Universal Fault-Tolerant Quantum Computation on Decoherence-Free Subspaces". In: *Phys. Rev. Lett.* 85 (8 Aug. 2000), pp. 1758–1761. DOI: 10.1103/PhysRevLett.85.1758.

[132] Almut Beige et al. "Quantum Computing Using Dissipation to Remain in a Decoherence-Free Subspace". In: *Phys. Rev. Lett.* 85 (8 Aug. 2000), pp. 1762–1765. DOI: 10.1103/PhysRevLett.85.1762. URL: https://link.aps.org/doi/10.1103/PhysRevLett.85.1762.

[133] Paul G. Kwiat et al. "Experimental Verification of Decoherence-Free Subspaces". In: *Science* 290.5491 (2000), pp. 498–501. DOI: 10.1126/science.290.5491.498.

[134] Sergio De Filippo. "Quantum computation using decoherence-free states of the physical operator algebra". In: *Phys. Rev. A* 62 (5 Oct. 2000), p. 052307. DOI: 10.1103/PhysRevA.62.052307. URL: https://link.aps.org/doi/10.1103/PhysRevA.62.052307.

[135] Alireza Shabani and Daniel A. Lidar. "Theory of initialization-free decoherence-free subspaces and subsystems". In: *Phys. Rev. A* 72 (4 Oct. 2005), p. 042303. DOI: 10.1103/PhysRevA.72.042303.

[136] Daniel A. Lidar and K. Birgitta Whaley. "Decoherence-Free Subspaces and Subsystems". In: *Irreversible Quantum Dynamics*. Ed. by Fabio Benatti and Roberto Floreanini. Berlin, Heidelberg: Springer Berlin Heidelberg, 2003, pp. 83–120. ISBN: 978-3-540-44874-7. DOI: 10.1007/3-540-44874-8_5.

[137] Shrabanti Dhar and Subinay Dasgupta. "Measurement-induced phase transition in a quantum spin system". In: *Phys. Rev. A* 93 (5 May 2016), p. 050103. DOI: 10.1103/PhysRevA.93.050103. URL: https://link.aps.org/doi/10.1103/PhysRevA.93.050103.

[138] Adam Nahum et al. "Quantum Entanglement Growth under Random Unitary Dynamics". In: *Phys. Rev. X* 7 (3 July 2017), p. 031016. DOI: 10.1103/PhysRevX.7.031016. URL: https://link.aps.org/doi/10.1103/PhysRevX.7.031016.

[139] Yaodong Li, Xiao Chen, and Matthew P. A. Fisher. "Quantum Zeno effect and the many-body entanglement transition". In: *Phys. Rev. B* 98 (20 Nov. 2018), p. 205136. DOI: 10.1103/PhysRevB.98.205136. URL: https://link.aps.org/doi/10.1103/PhysRevB.98.205136.

[140] Yaodong Li, Xiao Chen, and Matthew P.A. Fisher. "Measurement-driven entanglement transition in hybrid quantum circuits". In: *Physical Review B* 100.13 (2019), p. 134306. DOI: 10.1103/PhysRevB.100.134306.

[141] Yaodong Li and Matthew P. A. Fisher. "Statistical mechanics of quantum error correcting codes". In: *Phys. Rev. B* 103 (10 Mar. 2021), p. 104306. DOI: 10.1103/PhysRevB.103.104306. URL: https://link.aps.org/doi/10.1103/PhysRevB.103.104306.

[142] Tianci Zhou and Adam Nahum. "Emergent statistical mechanics of entanglement in random unitary circuits". In: *Phys. Rev. B* 99 (17 May 2019), p. 174205. DOI: 10.1103/PhysRevB.99.174205.

[143] Brian Skinner, Jonathan Ruhman, and Adam Nahum. "Measurement-Induced Phase Transitions in the Dynamics of Entanglement". In: *Phys. Rev. X* 9 (3 July 2019), p. 031009. DOI: 10.1103/PhysRevX.9.031009. URL: https://link.aps.org/doi/10.1103/PhysRevX.9.031009.

[144] Yimu Bao, Soonwon Choi, and Ehud Altman. "Theory of the phase transition in random unitary circuits with measurements". In: *Physical Review B* 101.10 (2020), p. 104301. DOI: 10.1103/PhysRevB.101.104301.

[145] Chao-Ming Jian et al. "Measurement-induced criticality in random quantum circuits". In: *Physical Review B* 101.10 (10 Mar. 2020), p. 104302. DOI: 10.1103/physrevb.101.104302. URL: https://link.aps.org/doi/10.1103/PhysRevB.101.104302.

[146] Michael J. Gullans and David A. Huse. "Scalable Probes of Measurement-Induced Criticality". In: *Phys. Rev. Lett.* 125 (7 Aug. 2020), p. 070606. DOI: 10.1103/PhysRevLett.125.070606. URL: https://link.aps.org/doi/10.1103/PhysRevLett.125.070606.

[147] Michael J. Gullans and David A. Huse. "Dynamical Purification Phase Transition Induced by Quantum Measurements". In: *Phys. Rev. X* 10 (4 Oct. 2020), p. 041020. DOI: 10.1103/PhysRevX.10.041020. URL: https://link.aps.org/doi/10.1103/PhysRevX.10.041020.

[148] Sarang Gopalakrishnan and Michael J. Gullans. "Entanglement and Purification Transitions in Non-Hermitian Quantum Mechanics". In: *Phys. Rev. Lett.* 126 (17 Apr. 2021), p. 170503. DOI: 10.1103/PhysRevLett.126.170503. URL: https://link.aps.org/doi/10.1103/PhysRevLett.126.170503.

[149] Xhek Turkeshi, Rosario Fazio, and Marcello Dalmonte. "Measurement-induced criticality in (2+1)-dimensional hybrid quantum circuits". In: *Phys. Rev. B* 102 (1 July 2020), p. 014315. DOI: 10.1103/PhysRevB.102.014315. URL: https://link.aps.org/doi/10.1103/PhysRevB.102.014315.

[150] Xhek Turkeshi et al. "Measurement-induced entanglement transitions in the quantum Ising chain: From infinite to zero clicks". In: *Phys. Rev. B* 103 (22 June 2021), p. 224210. DOI: 10.1103/PhysRevB.103.224210. URL: https://link.aps.org/doi/10.1103/PhysRevB.103.224210.

[151] Matteo Ippoliti et al. "Entanglement Phase Transitions in Measurement-Only Dynamics". In: *Phys. Rev. X* 11 (1 Feb. 2021), p. 011030. DOI: 10.1103/PhysRevX.11.011030. URL: https://link.aps.org/doi/10.1103/PhysRevX.11.011030.

[152] M. Buchhold et al. "Effective Theory for the Measurement-Induced Phase Transition of Dirac Fermions". In: *Phys. Rev. X* 11 (4 Oct. 2021), p. 041004. DOI: 10.1103/PhysRevX.11.041004. URL: https://link.aps.org/doi/10.1103/PhysRevX.11.041004.

[153] Takaaki Minato et al. "Fate of Measurement-Induced Phase Transition in Long-Range Interactions". In: *Phys. Rev. Lett.* 128 (1 Jan. 2022), p. 010603. DOI: 10.1103/PhysRevLett.128.010603. URL: https://link.aps.org/doi/10.1103/PhysRevLett.128.010603.

[154] Maxwell Block et al. "Measurement-Induced Transition in Long-Range Interacting Quantum Circuits". In: *Phys. Rev. Lett.* 128 (1 Jan. 2022), p. 010604. DOI: 10.1103/PhysRevLett.128.010604. URL: https://link.aps.org/doi/10.1103/PhysRevLett.128.010604.

[155] Shraddha Sharma et al. "Measurement-induced criticality in extended and long-range unitary circuits". In: *SciPost Phys. Core* 5 (2022), p. 023. DOI: 10.21468/SciPostPhysCore.5.2.023.

[156] Xiao Chen et al. "Emergent conformal symmetry in nonunitary random dynamics of free fermions". In: *Phys. Rev. Research* 2 (3 July 2020), p. 033017. DOI: 10.1103/PhysRevResearch.2.033017. URL: https://link.aps.org/doi/10.1103/PhysRevResearch.2.033017.

[157] Alberto Biella and Marco Schirò. "Many-Body Quantum Zeno Effect and Measurement-Induced Subradiance Transition". In: *Quantum* 5 (Aug. 2021), p. 528. ISSN: 2521-327X. DOI: 10.22331/q-2021-08-19-528. URL: https://doi.org/10.22331/q-2021-08-19-528.

[158] Qicheng Tang, Xiao Chen, and W. Zhu. "Quantum criticality in the nonunitary dynamics of $(2+1)$-dimensional free fermions". In: *Phys. Rev. B* 103 (17 May 2021), p. 174303. DOI: 10.1103/PhysRevB.103.174303. URL: https://link.aps.org/doi/10.1103/PhysRevB.103.174303.

[159] Shao-Kai Jian et al. "Measurement-Induced Phase Transition in the Monitored Sachdev-Ye-Kitaev Model". In: *Phys. Rev. Lett.* 127 (14 Sept. 2021), p. 140601. DOI: 10.1103/PhysRevLett.127.140601. URL: https://doi.org/10.1103/PhysRevLett.127.140601.

[160] T. Müller, S. Diehl, and M. Buchhold. "Measurement-Induced Dark State Phase Transitions in Long-Ranged Fermion Systems". In: *Phys. Rev. Lett.* 128 (1 Jan. 2022), p. 010605. DOI: 10.1103/PhysRevLett.128.010605. URL: https://link.aps.org/doi/10.1103/PhysRevLett.128.010605.

[161] Oliver Lunt, Marcin Szyniszewski, and Arijeet Pal. "Measurement-induced criticality and entanglement clusters: A study of one-dimensional and two-dimensional Clifford circuits". In: *Phys. Rev. B* 104 (15 Oct. 2021), p. 155111. DOI: 10.1103/PhysRevB.104.155111. URL: https://link.aps.org/doi/10.1103/PhysRevB.104.155111.

[162] O. Alberton, M. Buchhold, and S. Diehl. "Entanglement Transition in a Monitored Free-Fermion Chain: From Extended Criticality to Area Law". In: *Phys. Rev. Lett.* 126 (17 Apr. 2021), p. 170602. DOI: 10.1103/PhysRevLett.126.170602. URL: https://link.aps.org/doi/10.1103/PhysRevLett.126.170602.

[163] Adam Nahum et al. "Measurement and Entanglement Phase Transitions in All-To-All Quantum Circuits, on Quantum Trees, and in Landau-Ginsburg Theory". In: *PRX Quantum* 2 (1 Mar. 2021), p. 010352. DOI: 10.1103/PRXQuantum.2.010352. URL: https://link.aps.org/doi/10.1103/PRXQuantum.2.010352.

[164] Piotr Sierant et al. "Dissipative Floquet Dynamics: from Steady State to Measurement Induced Criticality in Trapped-ion Chains". In: *Quantum* 6 (Feb. 2022), p. 638. ISSN: 2521-327X. DOI: 10.22331/q-2022-02-02-638. URL: https://doi.org/10.22331/q-2022-02-02-638.

[165] Xiangyu Cao, Antoine Tilloy, and Andrea De Luca. "Entanglement in a fermion chain under continuous monitoring". In: *SciPost Phys.* 7 (2 2019), p. 24. DOI: 10.21468/SciPostPhys.7.2.024. URL: https://scipost.org/10.21468/SciPostPhys.7.2.024.

[166] M. Szyniszewski, A. Romito, and H. Schomerus. "Universality of Entanglement Transitions from Stroboscopic to Continuous Measurements". In: *Phys. Rev. Lett.* 125 (21 Nov. 2020), p. 210602. DOI: 10.1103/PhysRevLett.125.210602. URL: https://link.aps.org/doi/10.1103/PhysRevLett.125.210602.

[167] Nicolai Lang and Hans Peter Büchler. "Exploring quantum phases by driven dissipation". In: *Phys. Rev. A* 92 (1 July 2015), p. 012128. DOI: 10.1103/PhysRevA.92.012128. URL: https://link.aps.org/doi/10.1103/PhysRevA.92.012128.

[168] T. Botzung, S. Diehl, and M. Müller. "Engineered dissipation induced entanglement transition in quantum spin chains: From logarithmic growth to area law". In: *Phys. Rev. B* 104 (18 Nov. 2021), p. 184422. DOI: 10.1103/PhysRevB.104.184422. URL: https://link.aps.org/doi/10.1103/PhysRevB.104.184422.

[169] Michele Coppola et al. "Growth of entanglement entropy under local projective measurements". In: *Phys. Rev. B* 105 (9 Mar. 2022), p. 094303. DOI: 10.1103/PhysRevB.105.094303. URL: https://link.aps.org/doi/10.1103/PhysRevB.105.094303.

[170] A Osterloh et al. "Scaling of entanglement close to a quantum phase transition". In: *Nature* 416.6881 (Apr. 2002), pp. 608–610.

[171] Luigi Amico et al. "Entanglement in many-body systems". In: *Rev. Mod. Phys.* 80 (2 May 2008), pp. 517–576. DOI: 10.1103/RevModPhys.80.517. URL: https://link.aps.org/doi/10.1103/RevModPhys.80.517.

[172] Thomas Iadecola et al. *Dynamical entanglement transition in the probabilistic control of chaos.* 2022. arXiv: 2207.12415 [cond-mat.dis-nn].

[173] Brian Skinner. *Lecture Notes: Introduction to random unitary circuits and the measurement-induced entanglement phase transition.* 2023. arXiv: 2307.02986 [cond-mat.stat-mech].

[174] Adam Nahum, Sagar Vijay, and Jeongwan Haah. "Operator Spreading in Random Unitary Circuits". In: *Phys. Rev. X* 8 (2 Apr. 2018), p. 021014. DOI: 10.1103/PhysRevX.8.021014. URL: https://link.aps.org/doi/10.1103/PhysRevX.8.021014.

[175] Kyungjoo Noh, Liang Jiang, and Bill Fefferman. "Efficient classical simulation of noisy random quantum circuits in one dimension". In: *Quantum* 4 (Sept. 2020), p. 318. ISSN: 2521-327X. DOI: 10.22331/q-2020-09-11-318. URL: https://doi.org/10.22331/q-2020-09-11-318.

[176] John C. Napp et al. "Efficient Classical Simulation of Random Shallow 2D Quantum Circuits". In: *Phys. Rev. X* 12 (2 Apr. 2022), p. 021021. DOI: 10.1103/PhysRevX.12.021021. URL: https://link.aps.org/doi/10.1103/PhysRevX.12.021021.

[177] Ali Lavasani, Yahya Alavirad, and Maissam Barkeshli. "Measurement-induced topological entanglement transitions in symmetric random quantum circuits". In: *Nature Physics* 17.3 (Mar. 2021), pp. 342–347. ISSN: 1745-2481. DOI: 10.1038/s41567-020-01112-z. URL: https://doi.org/10.1038/s41567-020-01112-z.

[178] Shengqi Sang et al. "Entanglement Negativity at Measurement-Induced Criticality". In: *PRX Quantum* 2 (3 July 2021), p. 030313. DOI: 10.1103/PRXQuantum.2.030313. URL: https://link.aps.org/doi/10.1103/PRXQuantum.2.030313.

[179] Piotr Sierant et al. "Measurement-induced phase transitions in $(d+1)$-dimensional stabilizer circuits". In: *Phys. Rev. B* 106 (21 Dec. 2022), p. 214316. DOI: 10.1103/PhysRevB.106.214316. URL: https://link.aps.org/doi/10.1103/PhysRevB.106.214316.

[180] Shiyu Zhou et al. "Single T gate in a Clifford circuit drives transition to universal entanglement spectrum statistics". In: *SciPost Phys.* 9 (2020), p. 087. DOI: 10.21468/SciPostPhys.9.6.087. URL: https://scipost.org/10.21468/SciPostPhys.9.6.087.

[181] Shane P. Kelly et al. *Coherence requirements for quantum communication from hybrid circuit dynamics*. 2023. arXiv: 2210.11547 [quant-ph].

[182] Nicolai Lang and Hans Peter Büchler. "Entanglement transition in the projective transverse field Ising model". In: *Phys. Rev. B* 102 (9 Sept. 2020), p. 094204. DOI: 10.1103/PhysRevB.102.094204. URL: https://link.aps.org/doi/10.1103/PhysRevB.102.094204.

[183] Giulia Piccitto, Angelo Russomanno, and Davide Rossini. "Entanglement transitions in the quantum Ising chain: A comparison between different unravelings of the same Lindbladian". In: *Phys. Rev. B* 105 (6 Feb. 2022), p. 064305. DOI: 10.1103/PhysRevB.105.064305. URL: https://link.aps.org/doi/10.1103/PhysRevB.105.064305.

[184] Youenn Le Gal, Xhek Turkeshi, and Marco Schirò. "Volume-to-area law entanglement transition in a non-Hermitian free fermionic chain". In: *SciPost Phys.* 14 (2023), p. 138. DOI: 10.21468/SciPostPhys.14.5.138. URL: https://scipost.org/10.21468/SciPostPhys.14.5.138.

[185] B. Ladewig, S. Diehl, and M. Buchhold. "Monitored open fermion dynamics: Exploring the interplay of measurement, decoherence, and free Hamiltonian evolution". In: *Phys. Rev. Research* 4 (3 July 2022), p. 033001. DOI: 10.1103/PhysRevResearch.4.033001. URL: https://link.aps.org/doi/10.1103/PhysRevResearch.4.033001.

[186] Igor Poboiko et al. "Theory of Free Fermions under Random Projective Measurements". In: *Phys. Rev. X* 13 (4 Dec. 2023), p. 041046. DOI: 10.1103/PhysRevX.13.041046. URL: https://link.aps.org/doi/10.1103/PhysRevX.13.041046.

[187] Giulia Piccitto, Davide Rossini, and Angelo Russomanno. *The impact of different unravelings in a monitored system of free fermions*. 2024. arXiv: 2402.06597 [quant-ph].

[188] Heinz-Peter Breuer et al. "Colloquium: Non-Markovian dynamics in open quantum systems". In: *Rev. Mod. Phys.* 88 (2 Apr. 2016), p. 021002. DOI: 10.1103/RevModPhys.88.021002. URL: https://link.aps.org/doi/10.1103/RevModPhys.88.021002.

[189] Ángel Rivas, Susana F. Huelga, and Martin B. Plenio. "Entanglement and Non-Markovianity of Quantum Evolutions". In: *Phys. Rev. Lett.* 105 (5 July 2010), p. 050403. DOI: 10.1103/PhysRevLett.105.050403. URL: https://link.aps.org/doi/10.1103/PhysRevLett.105.050403.

[190] Simon Milz et al. "Entanglement, non-Markovianity, and causal non-separability". In: *New Journal of Physics* 20.3 (Mar. 2018), p. 033033. DOI: 10.1088/1367-2630/aaafee. URL: https://dx.doi.org/10.1088/1367-2630/aaafee.

[191] Paolo Abiuso et al. "Characterizing (non-)Markovianity through Fisher information". In: *SciPost Physics* 15.1 (July 2023). DOI: 10.21468/scipostphys.15.1.014. URL: https://doi.org/10.21468%2Fscipostphys.15.1.014.

[192] Heinz-Peter Breuer, Elsi-Mari Laine, and Jyrki Piilo. "Measure for the Degree of Non-Markovian Behavior of Quantum Processes in Open Systems". In: *Phys. Rev. Lett.* 103 (21 Nov. 2009), p. 210401. DOI: 10.1103/PhysRevLett.103.210401. URL: https://link.aps.org/doi/10.1103/PhysRevLett.103.210401.

[193] M. M. Wolf et al. "Assessing Non-Markovian Quantum Dynamics". In: *Phys. Rev. Lett.* 101 (15 Oct. 2008), p. 150402. DOI: 10.1103/PhysRevLett.101.150402. URL: https://link.aps.org/doi/10.1103/PhysRevLett.101.150402.

[194] Chu Guo, Kavan Modi, and Dario Poletti. "Tensor-network-based machine learning of non-Markovian quantum processes". In: *Phys. Rev. A* 102 (6 Dec. 2020), p. 062414. DOI: 10.1103/PhysRevA.102.062414. URL: https://link.aps.org/doi/10.1103/PhysRevA.102.062414.

[195] Chu Guo. "Quantifying Non-Markovianity in Open Quantum Dynamics". In: *SciPost Phys.* 13 (2022), p. 028. DOI: 10.21468/SciPostPhys.13.2.028. URL: https://scipost.org/10.21468/SciPostPhys.13.2.028.

[196] Klaus Mølmer, Yvan Castin, and Jean Dalibard. "Monte Carlo wave-function method in quantum optics". In: *Journal of the Optical Society of America B* 10 (3 1993), pp. 524–538. DOI: 10.1364/JOSAB.10.000524. URL: https://doi.org/10.1364/JOSAB.10.000524.

[197] Jean Dalibard, Yvan Castin, and Klaus Mølmer. "Wave-function approach to dissipative processes in quantum optics". In: *Phys. Rev. Lett.* 68 (5 Feb. 1992), pp. 580–583. DOI: 10.1103/PhysRevLett.68.580. URL: https://link.aps.org/doi/10.1103/PhysRevLett.68.580.

[198] Andrew J. Daley. "Quantum trajectories and open many-body quantum systems". In: *Advances in Physics* 63.2 (2014), pp. 77–149. DOI: 10.1080/00018732.2014.933502.

[199] H. P. Wiseman and G.J. Milburn. *Quantum measurement and control.* University Printing House Shaftesbury Road Cambridge: Cambridge University Press, 2009. DOI: https://doi.org/10.1017/CBO9780511813948.

[200] Jyrki Piilo et al. "Non-Markovian Quantum Jumps". In: *Phys. Rev. Lett.* 100 (18 May 2008), p. 180402. DOI: 10.1103/PhysRevLett.100.180402. URL: https://link.aps.org/doi/10.1103/PhysRevLett.100.180402.

[201] J. Piilo et al. "Open system dynamics with non-Markovian quantum jumps". In: *Phys. Rev. A* 79 (6 June 2009), p. 062112. DOI: 10.1103/PhysRevA.79.062112. URL: https://link.aps.org/doi/10.1103/PhysRevA.79.062112.

[202] Giuliano Chiriacò et al. "Diagrammatic method for many-body non-Markovian dynamics: Memory effects and entanglement transitions". In: *Phys. Rev. B* 108 (7 Aug. 2023), p. 075151. DOI: 10.1103/PhysRevB.108.075151. URL: https://link.aps.org/doi/10.1103/PhysRevB.108.075151.

[203] Mikheil Tsitsishvili et al. "Measurement induced transitions in non-Markovian free fermion ladders". In: *SciPost Phys. Core* 7 (2024), p. 011. DOI: 10.21468/SciPostPhysCore.7.1.011. URL: https://scipost.org/10.21468/SciPostPhysCore.7.1.011.

[204] Ryszard Horodecki et al. "Quantum entanglement". In: *Rev. Mod. Phys.* 81 (2 June 2009), pp. 865–942. DOI: `10.1103/RevModPhys.81.865`. URL: `https://link.aps.org/doi/10.1103/RevModPhys.81.865`.

[205] K. Hornberger. "Introduction to Decoherence Theory". In: *Entanglement and Decoherence: Foundations and Modern Trends*. Ed. by Andreas Buchleitner, Carlos Viviescas, and Markus Tiersch. Berlin, Heidelberg: Springer Berlin Heidelberg, 2009, pp. 221–276. ISBN: 978-3-540-88169-8. DOI: `10.1007/978-3-540-88169-8_5`. URL: `https://doi.org/10.1007/978-3-540-88169-8_5`.

[206] Maximilian Schlosshauer. *The quantum-to-classical transition and decoherence*. 2019. arXiv: `1404.2635 [quant-ph]`. URL: `https://arxiv.org/abs/1404.2635`.

[207] Ulrich Weiss. *Quantum Dissipative Systems (Fourth Edition)*. 4th ed. Singapore, Singapore: World Scientific Publishing, Mar. 2012.

[208] Fabrizio Minganti and Alberto Biella. *Open quantum systems – A brief introduction*. 2024. arXiv: `2407.16855 [quant-ph]`. URL: `https://arxiv.org/abs/2407.16855`.

[209] Walter Wyss. *Two Non-Commutative Binomial Theorems*. 2017. arXiv: `1707.03861 [math.RA]`.

[210] Inés de Vega and Daniel Alonso. "Dynamics of non-Markovian open quantum systems". In: *Rev. Mod. Phys.* 89 (1 Jan. 2017), p. 015001. DOI: `10.1103/RevModPhys.89.015001`. URL: `https://link.aps.org/doi/10.1103/RevModPhys.89.015001`.

[211] Michael J. W. Hall et al. "Canonical form of master equations and characterization of non-Markovianity". In: *Phys. Rev. A* 89 (4 Apr. 2014), p. 042120. DOI: `10.1103/PhysRevA.89.042120`. URL: `https://link.aps.org/doi/10.1103/PhysRevA.89.042120`.

[212] M. B. Plenio and P. L. Knight. "The quantum-jump approach to dissipative dynamics in quantum optics". In: *Rev. Mod. Phys.* 70 (1 Jan. 1998), pp. 101–144. DOI: `10.1103/RevModPhys.70.101`. URL: `https://link.aps.org/doi/10.1103/RevModPhys.70.101`.

[213] Howard M. Wiseman and J. M. Gambetta. "Pure-State Quantum Trajectories for General Non-Markovian Systems Do Not Exist". In: *Phys. Rev. Lett.* 101 (14 Sept. 2008), p. 140401. DOI: `10.1103/PhysRevLett.101.140401`. URL: `https://link.aps.org/doi/10.1103/PhysRevLett.101.140401`.

[214] H. P. Breuer and F. Petruccione. *The theory of open quantum systems*. Great Clarendon Street: Oxford University Press, 2002.

[215] Giuliano Chiriacò. *To be Published*.

[216] Bassano Vacchini et al. "Markovianity and non-Markovianity in quantum and classical systems". In: *New Journal of Physics* 13.9 (Sept. 2011), p. 093004. DOI: `10.1088/1367-2630/13/9/093004`. URL: `https://dx.doi.org/10.1088/1367-2630/13/9/093004`.

[217] Shunlong Luo, Shuangshuang Fu, and Hongting Song. "Quantifying non-Markovianity via correlations". In: *Phys. Rev. A* 86 (4 Oct. 2012), p. 044101. DOI: `10.1103/PhysRevA.86.044101`. URL: `https://link.aps.org/doi/10.1103/PhysRevA.86.044101`.

[218] Heinz-Peter Breuer. "Foundations and measures of quantum non-Markovianity". In: *Journal of Physics B: Atomic, Molecular and Optical Physics* 45.15 (July 2012), p. 154001. DOI: `10.1088/0953-4075/45/15/154001`. URL: `https://dx.doi.org/10.1088/0953-4075/45/15/154001`.

[219] Martin B. Plenio and Shashank Virmani. "An introduction to entanglement measures". In: *Quantum Info. Comput.* 7.1 (Jan. 2007), pp. 1–51. ISSN: 1533-7146.

[220] J. Eisert. *Entanglement in quantum information theory*. 2006. arXiv: `quant-ph/0610253 [quant-ph]`. URL: `https://arxiv.org/abs/quant-ph/0610253`.

[221]   Matthew J. Donald, Michał Horodecki, and Oliver Rudolph. "The uniqueness theorem for entanglement measures". In: *Journal of Mathematical Physics* 43.9 (Sept. 2002), pp. 4252–4272. ISSN: 1089-7658. DOI: 10.1063/1.1495917. URL: http://dx.doi.org/10.1063/1.1495917.

[222]   Pasquale Calabrese and John Cardy. "Entanglement entropy and conformal field theory". In: *Journal of Physics A: Mathematical and Theoretical* 42.50 (Dec. 2009), p. 504005. DOI: 10.1088/1751-8113/42/50/504005. URL: https://doi.org/10.1088/1751-8113/42/50/504005.

[223]   Hassan Shapourian et al. "Twisted and untwisted negativity spectrum of free fermions". In: *SciPost Phys.* 7 (2019), p. 037. DOI: 10.21468/SciPostPhys.7.3.037. URL: https://scipost.org/10.21468/SciPostPhys.7.3.037.

[224]   Hassan Shapourian and Shinsei Ryu. "Entanglement negativity of fermions: Monotonicity, separability criterion, and classification of few-mode states". In: *Phys. Rev. A* 99 (2 Feb. 2019), p. 022310. DOI: 10.1103/PhysRevA.99.022310. URL: https://link.aps.org/doi/10.1103/PhysRevA.99.022310.

[225]   Sara Murciano et al. "Negativity Hamiltonian: An Operator Characterization of Mixed-State Entanglement". In: *Phys. Rev. Lett.* 128 (14 Apr. 2022), p. 140502. DOI: 10.1103/PhysRevLett.128.140502. URL: https://link.aps.org/doi/10.1103/PhysRevLett.128.140502.

[226]   Pasquale Calabrese, John Cardy, and Erik Tonni. "Entanglement Negativity in Quantum Field Theory". In: *Phys. Rev. Lett.* 109 (13 Sept. 2012), p. 130502. DOI: 10.1103/PhysRevLett.109.130502. URL: https://link.aps.org/doi/10.1103/PhysRevLett.109.130502.

[227]   Valerie Coffman, Joydip Kundu, and William K. Wootters. "Distributed entanglement". In: *Phys. Rev. A* 61 (5 Apr. 2000), p. 052306. DOI: 10.1103/PhysRevA.61.052306. URL: https://link.aps.org/doi/10.1103/PhysRevA.61.052306.

[228]   Yong-Cheng Ou and Heng Fan. "Monogamy inequality in terms of negativity for three-qubit states". In: *Phys. Rev. A* 75 (6 June 2007), p. 062308. DOI: 10.1103/PhysRevA.75.062308. URL: https://link.aps.org/doi/10.1103/PhysRevA.75.062308.

[229]   Xiao-Lan Zong et al. "Monogamy of Quantum Entanglement". In: *Frontiers in Physics* 10 (2022). ISSN: 2296-424X. DOI: 10.3389/fphy.2022.880560. URL: https://www.frontiersin.org/articles/10.3389/fphy.2022.880560.

[230]   W. Dür, G. Vidal, and J. I. Cirac. "Three qubits can be entangled in two inequivalent ways". In: *Phys. Rev. A* 62 (6 Nov. 2000), p. 062314. DOI: 10.1103/PhysRevA.62.062314. URL: https://link.aps.org/doi/10.1103/PhysRevA.62.062314.

[231]   Dong Yang. "A simple proof of monogamy of entanglement". In: *Physics Letters A* 360.2 (2006), pp. 249–250. ISSN: 0375-9601. DOI: https://doi.org/10.1016/j.physleta.2006.08.027. URL: https://www.sciencedirect.com/science/article/pii/S0375960106012801.

[232]   Gian Luca Giorgi. "Monogamy properties of quantum and classical correlations". In: *Phys. Rev. A* 84 (5 Nov. 2011), p. 054301. DOI: 10.1103/PhysRevA.84.054301. URL: https://link.aps.org/doi/10.1103/PhysRevA.84.054301.

[233]   Michael Foss-Feig et al. "Solvable Family of Driven-Dissipative Many-Body Systems". In: *Phys. Rev. Lett.* 119 (19 Nov. 2017), p. 190402. DOI: 10.1103/PhysRevLett.119.190402. URL: https://link.aps.org/doi/10.1103/PhysRevLett.119.190402.

[234]   Berislav Buča et al. "Bethe ansatz approach for dissipation: exact solutions of quantum many-body dynamics under loss". In: *New Journal of Physics* 22.12 (Dec. 2020), p. 123040. DOI: 10.1088/1367-2630/abd124. URL: https://dx.doi.org/10.1088/1367-2630/abd124.

[235] Alice Marché et al. *Universality and two-body losses: lessons from the effective non-Hermitian dynamics of two particles.* 2024. arXiv: 2405.04789 [cond-mat.quant-gas]. URL: https://arxiv.org/abs/2405.04789.

[236] Matthew P.A. Fisher et al. "Random Quantum Circuits". In: *Annual Review of Condensed Matter Physics* 14.Volume 14, 2023 (2023), pp. 335–379. ISSN: 1947-5462. DOI: https://doi.org/10.1146/annurev-conmatphys-031720-030658. URL: https://www.annualreviews.org/content/journals/10.1146/annurev-conmatphys-031720-030658.

[237] Kyle Poland, Kerstin Beer, and Tobias J. Osborne. *No Free Lunch for Quantum Machine Learning.* 2020. arXiv: 2003.14103 [quant-ph].

[238] Antonio Anna Mele. "Introduction to Haar Measure Tools in Quantum Information: A Beginner's Tutorial". In: *Quantum* 8 (May 2024), p. 1340. ISSN: 2521-327X. DOI: 10.22331/q-2024-05-08-1340. URL: https://doi.org/10.22331/q-2024-05-08-1340.

[239] Adam Nahum, Sagar Vijay, and Jeongwan Haah. "Operator Spreading in Random Unitary Circuits". In: *Phys. Rev. X* 8 (2 Apr. 2018), p. 021014. DOI: 10.1103/PhysRevX.8.021014. URL: https://link.aps.org/doi/10.1103/PhysRevX.8.021014.

[240] Man-Duen Choi. "Completely positive linear maps on complex matrices". en. In: *Linear Algebra Appl.* 10.3 (June 1975), pp. 285–290.

[241] Ulli Wolff. "Collective Monte Carlo Updating for Spin Systems". In: *Phys. Rev. Lett.* 62 (4 Jan. 1989), pp. 361–364. DOI: 10.1103/PhysRevLett.62.361. URL: https://link.aps.org/doi/10.1103/PhysRevLett.62.361.

[242] Jaron Kent-Dobias and James P. Sethna. "Cluster representations and the Wolff algorithm in arbitrary external fields". In: *Phys. Rev. E* 98 (6 Dec. 2018), p. 063306. DOI: 10.1103/PhysRevE.98.063306. URL: https://link.aps.org/doi/10.1103/PhysRevE.98.063306.

[243] Xhek Turkeshi et al. "Entanglement transitions from stochastic resetting of non-Hermitian quasiparticles". In: *Physical Review B* 105.24 (2022), p. L241114.

[244] A. Imamoglu. "Stochastic wave-function approach to non-Markovian systems". In: *Phys. Rev. A* 50 (5 Nov. 1994), pp. 3650–3653. DOI: 10.1103/PhysRevA.50.3650. URL: https://link.aps.org/doi/10.1103/PhysRevA.50.3650.

[245] B. M. Garraway and P. L. Knight. "Cavity modified quantum beats". In: *Phys. Rev. A* 54 (4 Oct. 1996), pp. 3592–3602. DOI: 10.1103/PhysRevA.54.3592. URL: https://link.aps.org/doi/10.1103/PhysRevA.54.3592.

[246] Heinz-Peter Breuer, Bernd Kappler, and Francesco Petruccione. "Stochastic wave-function method for non-Markovian quantum master equations". In: *Phys. Rev. A* 59 (2 Feb. 1999), pp. 1633–1643. DOI: 10.1103/PhysRevA.59.1633. URL: https://link.aps.org/doi/10.1103/PhysRevA.59.1633.

[247] Heinz-Peter Breuer. "Genuine quantum trajectories for non-Markovian processes". In: *Phys. Rev. A* 70 (1 July 2004), p. 012106. DOI: 10.1103/PhysRevA.70.012106. URL: https://link.aps.org/doi/10.1103/PhysRevA.70.012106.

[248] Shigeru Ajisaka et al. "Nonequilibrium particle and energy currents in quantum chains connected to mesoscopic Fermi reservoirs". In: *Phys. Rev. B* 86 (12 Sept. 2012), p. 125111. DOI: 10.1103/PhysRevB.86.125111. URL: https://link.aps.org/doi/10.1103/PhysRevB.86.125111.

[249] Patrick Haughian, Massimiliano Esposito, and Thomas L. Schmidt. "Quantum thermodynamics of the resonant-level model with driven system-bath coupling". In: *Phys. Rev. B* 97 (8 Feb. 2018), p. 085435. DOI: 10.1103/PhysRevB.97.085435. URL: https://link.aps.org/doi/10.1103/PhysRevB.97.085435.

[250]   Wenjie Dou et al. "Universal approach to quantum thermodynamics in the strong coupling regime". In: *Phys. Rev. B* 98 (13 Oct. 2018), p. 134306. DOI: 10.1103/PhysRevB.98.134306. URL: https://link.aps.org/doi/10.1103/PhysRevB.98.134306.

[251]   Maurizio Fagotti and Pasquale Calabrese. "Entanglement entropy of two disjoint blocks in XY chains". In: *Journal of Statistical Mechanics: Theory and Experiment* 2010.04 (Apr. 2010), P04016. DOI: 10.1088/1742-5468/2010/04/P04016. URL: https://dx.doi.org/10.1088/1742-5468/2010/04/P04016.

[252]   Jacopo Surace and Luca Tagliacozzo. "Fermionic Gaussian states: an introduction to numerical approaches". In: *SciPost Phys. Lect. Notes* (2022), p. 54. DOI: 10.21468/SciPostPhysLectNotes.54. URL: https://scipost.org/10.21468/SciPostPhysLectNotes.54.

[253]   Jens Eisert, Viktor Eisler, and Zoltán Zimborás. "Entanglement negativity bounds for fermionic Gaussian states". In: *Phys. Rev. B* 97 (16 Apr. 2018), p. 165123. DOI: 10.1103/PhysRevB.97.165123. URL: https://link.aps.org/doi/10.1103/PhysRevB.97.165123.

[254]   Aidan Zabalo et al. "Critical properties of the measurement-induced transition in random quantum circuits". In: *Phys. Rev. B* 101 (6 Feb. 2020), p. 060301. DOI: 10.1103/PhysRevB.101.060301. URL: https://link.aps.org/doi/10.1103/PhysRevB.101.060301.

[255]   Zack Weinstein et al. *Scrambling Transition in a Radiative Random Unitary Circuit*. 2022. arXiv: 2210.14242 [quant-ph].

[256]   S. C. Hou et al. "Alternative non-Markovianity measure by divisibility of dynamical maps". In: *Phys. Rev. A* 83 (6 June 2011), p. 062115. DOI: 10.1103/PhysRevA.83.062115. URL: https://link.aps.org/doi/10.1103/PhysRevA.83.062115.

[257]   A. R. Usha Devi, A. K. Rajagopal, and Sudha. "Open-system quantum dynamics with correlated initial states, not completely positive maps, and non-Markovianity". In: *Phys. Rev. A* 83 (2 Feb. 2011), p. 022109. DOI: 10.1103/PhysRevA.83.022109. URL: https://link.aps.org/doi/10.1103/PhysRevA.83.022109.

[258]   B. Bylicka, D. Chruściński, and S. Maniscalco. "Non-Markovianity and reservoir memory of quantum channels: a quantum information theory perspective". In: *Scientific Reports* 4.1 (2014), p. 5720.

[259]   Carlos Pineda et al. "Measuring and using non-Markovianity". In: *Phys. Rev. A* 93 (2 Feb. 2016), p. 022117. DOI: 10.1103/PhysRevA.93.022117. URL: https://link.aps.org/doi/10.1103/PhysRevA.93.022117.

[260]   Zhi He et al. "Non-Markovianity measure based on the relative entropy of coherence in an extended space". In: *Phys. Rev. A* 96 (2 Aug. 2017), p. 022106. DOI: 10.1103/PhysRevA.96.022106. URL: https://link.aps.org/doi/10.1103/PhysRevA.96.022106.

[261]   Wen Xu, Zhu-Jun Zheng, and Shao-Ming Fei. "The quantum Markovianity criterion based on correlations under random unitary qudit dynamical evolutions". In: *Quantum Information Processing* 21.6 (2022), p. 221.

[262]   Andreas Ask and Göran Johansson. "Non-Markovian Steady States of a Driven Two-Level System". In: *Phys. Rev. Lett.* 128 (8 Feb. 2022), p. 083603. DOI: 10.1103/PhysRevLett.128.083603. URL: https://link.aps.org/doi/10.1103/PhysRevLett.128.083603.

[263]   Xhek Turkeshi, Lorenzo Piroli, and Marco Schirò. "Enhanced entanglement negativity in boundary-driven monitored fermionic chains". In: *Phys. Rev. B* 106 (2 July 2022), p. 024304. DOI: 10.1103/PhysRevB.106.024304. URL: https://link.aps.org/doi/10.1103/PhysRevB.106.024304.

[264] Hassan Shapourian and Shinsei Ryu. "Finite-temperature entanglement negativity of free fermions". In: *Journal of Statistical Mechanics: Theory and Experiment* 2019.4 (Apr. 2019), p. 043106. DOI: `10.1088/1742-5468/ab11e0`. URL: `https://dx.doi.org/10.1088/1742-5468/ab11e0`.

[265] Yaodong Li et al. *Statistical Mechanics Model for Clifford Random Tensor Networks and Monitored Quantum Circuits*. 2021. arXiv: `2110.02988 [cond-mat.stat-mech]`.

[266] Angelo Russomanno, Giulia Piccitto, and Davide Rossini. "Entanglement transitions and quantum bifurcations under continuous long-range monitoring". In: *Phys. Rev. B* 108 (10 Sept. 2023), p. 104313. DOI: `10.1103/PhysRevB.108.104313`. URL: `https://link.aps.org/doi/10.1103/PhysRevB.108.104313`.

[267] Giulia Piccitto, Angelo Russomanno, and Davide Rossini. "Entanglement dynamics with string measurement operators". In: *SciPost Phys. Core* 6 (2023), p. 078. DOI: `10.21468/SciPostPhysCore.6.4.078`. URL: `https://scipost.org/10.21468/SciPostPhysCore.6.4.078`.

[268] Pradeep Niroula, Sarang Gopalakrishnan, and Michael J. Gullans. *Error Mitigation Thresholds in Noisy Quantum Circuits*. 2023. arXiv: `2302.04278 [quant-ph]`.

[269] Zack Weinstein, Yimu Bao, and Ehud Altman. "Measurement-Induced Power-Law Negativity in an Open Monitored Quantum Circuit". In: *Phys. Rev. Lett.* 129 (8 Aug. 2022), p. 080501. DOI: `10.1103/PhysRevLett.129.080501`. URL: `https://link.aps.org/doi/10.1103/PhysRevLett.129.080501`.

[270] E. Paladino et al. "$1/f$ noise: Implications for solid-state quantum information". In: *Rev. Mod. Phys.* 86 (2 Apr. 2014), pp. 361–418. DOI: `10.1103/RevModPhys.86.361`. URL: `https://link.aps.org/doi/10.1103/RevModPhys.86.361`.

[271] Crystal Noel et al. "Measurement-induced quantum phases realized in a trapped-ion quantum computer". In: *Nature Physics* 18.7 (2022), pp. 760–764. DOI: `10.1038/s41567-022-01619-7`. URL: `https://doi.org/10.1038/s41567-022-01619-7`.

[272] Jin Ming Koh et al. "Measurement-induced entanglement phase transition on a superconducting quantum processor with mid-circuit readout". In: *Nature Physics* (2023). DOI: `10.1038/s41567-023-02076-6`. URL: `https://doi.org/10.1038/s41567-023-02076-6`.

[273] Ángel Rivas, Susana F Huelga, and Martin B Plenio. "Quantum non-Markovianity: characterization, quantification and detection". In: *Reports on Progress in Physics* 77.9 (Aug. 2014), p. 094001. DOI: `10.1088/0034-4885/77/9/094001`. URL: `https://dx.doi.org/10.1088/0034-4885/77/9/094001`.